

DE GRUYTER

CHEMICAL SCIENCES IN THE FOCUS

VOLUME 3: THEORETICAL AND COMPUTATIONAL
CHEMISTRY ASPECTS

Edited by Ponnadurai Ramasami

Copyright 2021. De Gruyter. All rights reserved. May not be reproduced in any form without permission from the publisher, except fair uses permitted under U.S. or applicable copyright law.

Ponnadurai Ramasami (Ed.)
Chemical Sciences in the Focus

Also of interest



Chemical Sciences in the Focus
Volume 1: Pharmaceutical Applications
Ponnadurai Ramasami (Ed.), 2021
ISBN 978-3-11-071072-4, e-ISBN 978-3-11-072659-6



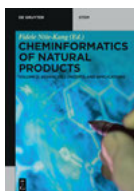
Chemical Sciences in the Focus
Volume 2: Green and Sustainable Processing
Ponnadurai Ramasami (Ed.), 2021
ISBN 978-3-11-072659-6, e-ISBN 978-3-11-072614-5



Computational Chemistry Methods.
Applications
Ponnadurai Ramasami (Ed.), 2020
ISBN 978-3-11-062906-4, e-ISBN 978-3-11-063162-3



Chemoinformatics of Natural Products
Volume 1: Fundamental Concepts
Fidele Ntie-Kang (Ed.), 2020
ISBN 978-3-11-057933-8, e-ISBN 978-3-11-057935-2



Chemoinformatics of Natural Products
Volume 2: Advanced Concepts and Applications
Fidele Ntie-Kang (Ed.), 2021
ISBN 978-3-11-066888-9, e-ISBN 978-3-11-066889-6



Physical Sciences Reviews.
e-ISSN 2365-659X

Chemical Sciences in the Focus

Volume 3: Theoretical and Computational Chemistry Aspects

Edited by
Ponnadurai Ramasami

DE GRUYTER

Editor

Prof. Dr. Ponnadurai Ramasami
Computational Chemistry Group,
Department of Chemistry, Faculty of Science,
University of Mauritius,
Reduit 80837,
Mauritius

Department of Chemistry,
College of Science, Engineering and Technology,
University of South Africa,
P.O. Box 392, Pretoria 0003,
South Africa
E-mail address: p.ramasami@uom.ac.mu

ISBN 978-3-11-073974-9

e-ISBN (PDF) 978-3-11-073976-3

e-ISBN (EPUB) 978-3-11-073980-0

Library of Congress Control Number: 2021940642

Bibliographic information published by the Deutsche Nationalbibliothek

The Deutsche Nationalbibliothek lists this publication in the Deutsche Nationalbibliografie;
detailed bibliographic data are available on the Internet at <http://dnb.dnb.de>.

© 2021 Walter de Gruyter GmbH, Berlin/Boston

Cover image: BlackJack3D/E+/Getty Images

Typesetting: TNQ Technologies Pvt. Ltd.

Printing and binding: CPI books GmbH, Leck

www.degruyter.com

Preface of the Book of Proceedings of the Virtual Conference on Chemistry and its Applications (VCCA-2020)

A virtual conference on chemistry and its applications (VCCA-2020) was organized online from 1st to 31st August 2020. The theme of the virtual conference was “Research and Innovations in Chemical Sciences: Paving the Way Forward”.

There were 190 presentations for the virtual conference with 300 participants from 50 countries. A secured platform was used for virtual interactions of the participants. After the virtual conference, there was a call for full papers to be considered for publication in the conference proceedings. Manuscripts were received and they were processed and reviewed as per the policy of De Gruyter.

This book, volume 3, is a collection of the ten accepted manuscripts incorporating theoretical and computational chemistry aspects.

Saha and Bhattacharyya studied the effect of heteroatoms Boron-Nitrogen and substituents namely methyl, hydroxyl, amine, carboxyl and cyano on the structural parameters, global reactivity, aromaticity and UV-visible spectra of pyrene with the help of density functional theory. Tetteh and Ofori reported on the effect of delocalization of nonbonding electron density on the stability of the M-C_{carbene} bond in main group metal-imidazol-2-ylidene complexes based on a computational and structural database study. Mammino focussed on the educational aspects of mentoring chemistry postgraduate students, analysing the challenges encountered by students in the transition from undergraduate to postgraduate learning, and throughout the postgraduate projects up to completion of PhD level, and discussing the design of suitable addressing options by the mentor. Nedyalkova presented a study dealing with the interpretation and modeling of clinical data for patients with diabetes mellitus type 2 additionally diagnosed with complications of the disease by the use of multivariate statistical methods. Edim et al presented an electronic structure theory study of the reactivity and structural molecular properties of halo-substituted (F, Cl, Br) and heteroatom (N, O, S) doped cyclobutane. Bisong et al focussed on the reactivity, stability, and electronic interaction of pyridinium hydrogen nitrate PHN based ionic liquids and the influence of methyl substituent on this class of ionic liquids. Banerjee and Samanta reviewed the use of modern computational modeling methods to optimize the surfactant at the oil-water interfaces from the perspective of its applications in enhanced oil recovery using molecular dynamic simulation, dissipative particle dynamics and density functional theory. Oshakuade and Awe determined the bulk and surface properties of liquid Bi-Sn alloys using an improved quasi-lattice theory. Adewole et al reported on the identification of potential histone deacetylase inhibitory biflavonoids from *Garcinia Kola* (Guttiferae) using in silico protein-ligand interaction. Osundiya et al

<https://doi.org/10.1515/9783110739763-201>

carried out a conductometric study to derive the thermodynamic parameters of the micellization of quarternary based cationic surfactants in triethanolamine-water media.

I hope that these chapters of this volume 3 will add to literature and they will be useful references for researchers.

To conclude, VCCA-2020 was a successful event and I would like to thank all those who have contributed. I would also like to thank the Organising and International Advisory committee members, the participants and the reviewers.

Prof. Ponnadurai Ramasami

Contents

Preface — V

List of contributing authors — XI

Bapan Saha and Pradip Kumar Bhattacharyya

1 Role of heteroatoms and substituents on the structure, reactivity, aromaticity, and absorption spectra of pyrene: a density functional theory study — 1

- 1.1 Introduction — 1
- 1.2 Theoretical and computational details — 2
- 1.3 Results and discussions — 3
 - 1.3.1 Geometry of the chosen systems — 4
 - 1.3.2 HOMO shapes and HOMO perspectives — 6
 - 1.3.3 Variations in global hardness and philicity, and dipole moment — 10
 - 1.3.4 Variations in aromatic character — 13
 - 1.3.5 Variations in UV visible spectra — 14
- 1.4 Conclusions — 16
- References — 17

Samuel Tetteh and Albert Ofori

2 Effect of delocalization of nonbonding electron density on the stability of the M–C_{carbene} bond in main group metal-imidazol-2-ylidene complexes: a computational and structural database study — 21

- 2.1 Introduction — 21
- 2.2 Methods — 23
 - 2.2.1 CSD Analyses — 23
 - 2.2.2 Computational Details — 24
- 2.3 Results and discussion — 24
 - 2.3.1 Binding energy — 28
 - 2.3.2 Natural bond orbital (NBO) analyses — 29
 - 2.3.3 Thermodynamic stability — 30
- 2.4 Conclusions — 31
- References — 32

Liliana Mammino

3 Educational components in the supervision of chemistry postgraduate students: experiences and reflections — 35

- 3.1 Introduction — 36
 - 3.1.1 Background information — 36
 - 3.1.2 Continuity aspects and novel components in postgraduate mentoring — 37

- 3.1.3 General and specific features of learning how to do research in computational chemistry — **37**
- 3.2 Approaches selected for educational research focusing on the postgraduate level — **38**
- 3.3 Mentoring and learning in postgraduate studies — **40**
- 3.3.1 The main operations in postgraduate work — **40**
- 3.3.2 The literature review operation — **41**
- 3.3.3 Designing a project — **42**
- 3.3.4 Performing the planned activities — **42**
- 3.3.5 Preparation of presentations — **43**
- 3.3.6 Writing: the most challenging operation — **44**
- 3.3.7 Planning a thesis and organising its material — **54**
- 3.3.8 Fostering independence — **56**
- 3.4 Discussion and conclusions — **57**
- References — **58**

Miroslava Nedyalkova, Ralitsa Robeva, Atanaska Elenkova and Vasil Simeonov

4 Chemometric exploratory data analysis for patients with diabetes type 2 and diabetic complications — 61

- 4.1 Introduction — **61**
- 4.2 Methods and results — **62**
- 4.2.1 Input data — **62**
- 4.3 Results and discussion — **64**
- 4.3.1 Clustering of the parameters (HCA) — **66**
- 4.4 Conclusions — **76**
- References — **76**

Moses M. Edim, Hitler Louis, Emmanuel A. Bisong, Apebende G. Chioma, Obieze C. Enudi, Tomsmith O. Unimuke, Asuquo B. Basse, David Prince, Queen O. Sam, Emmanuel I. Ubana and Tiyati H. Mujong

5 Electronic structure theory study of the reactivity and structural molecular properties of halo-substituted (F, Cl, Br) and heteroatom (N, O, S) doped cyclobutane — 79

- 5.1 Introduction — **80**
- 5.2 Computational details — **80**
- 5.3 Results and discussion — **85**
- 5.3.1 Vibrational analysis — **85**
- 5.3.2 Bond Polarity Index (BPI) — **87**
- 5.3.3 Intrinsic Bond Strength Index (IBSI) — **88**
- 5.3.4 CDFT results using Fukui function on cyclobutane and its associated halogenated and doped-ringed structures — **90**

- 5.3.5 Quantum chemical descriptors — 92
- 5.3.6 Natural bond orbital analysis (NBO) — 95
- 5.3.7 Atomic charge analysis — 96
- 5.3.8 Molecular electrostatic potential (MEP) — 97
- 5.4 Conclusions — 99
- References — 100

Emmanuel A. Bisong, Hitler Louis, Tomsmith O. Unimuke, Victoria M. Bassey,
John A. Agwupuye, Linda I. Peter, Francis O. Ekpen and Aderemi T. Adeleye

6 Theoretical investigation of the stability, reactivity, and the interaction of methyl-substituted peridinium-based ionic liquids — 103

- 6.1 Introduction — 104
- 6.2 Computational details — 105
- 6.3 Results and discussion — 105
 - 6.3.1 Natural bond orbital (NBO) analysis — 105
 - 6.3.2 Analysis of HOMO–LUMO — 110
 - 6.3.3 Atomic dipole moment corrected Hirshfeld (ADCH) atomic charge analysis of pyridinium ion and its interaction with hydrogen nitrate: emphasis on the nitrogen charge — 112
 - 6.3.4 The electrostatic molecular potential (ESP) plot — 112
 - 6.3.5 Binding energy — 113
 - 6.3.6 Atoms-in-molecules (AIM) descriptors and H-atom binding energies — 114
- 6.4 Conclusions — 115
- References — 115

Tandrima Banerjee and Abhijit Samanta

7 Chemical computational approaches for optimization of effective surfactants in enhanced oil recovery — 119

- 7.1 Introduction — 119
- 7.2 Fundamentals of use of surfactant in EOR — 121
- 7.3 Chemical computational approaches for surfactant — 122
 - 7.3.1 Molecular dynamics (MD) simulation — 122
 - 7.3.2 Dissipative particle dynamics (DPD) simulation — 126
- 7.4 Application of chemical computational approaches — 130
 - 7.4.1 Application of MD and DFT Simulation in EOR — 130
 - 7.4.2 Application of DPD simulation in EOR — 138
- 7.5 Conclusions — 141
- References — 142

Olugbenga Morayo Oshakuade and Oluseyi Ezekiel Awe

8 Determination of bulk and surface properties of liquid Bi-Sn alloys using an improved quasi-lattice theory — 149

- 8.1 Introduction — 149
- 8.2 Theoretical framework — 150
 - 8.2.1 Average coordination number (\hat{Z}) — 150
 - 8.2.2 Quasi-lattice theory for compound forming liquid alloys (QLT) — 152
 - 8.2.3 Surface concentration and surface tension — 158
- 8.3 Results and discussion — 159
 - 8.3.1 Enthalpy and entropy of mixing — 159
 - 8.3.2 Concentration-concentration fluctuations in the long-wavelength limit and Warren-Cowley short-range-order parameter — 160
 - 8.3.3 Surface concentration and surface tension — 161
- 8.4 Conclusions — 162
- References — 163

Kayode E. Adewole, Ahmed A. Ishola and Blessing O. Omolaso

9 Identification of potential histone deacetylase inhibitory biflavonoids from *Garcinia kola* (Guttiferae) using *in silico* protein-ligand interaction — 165

- 9.1 Introduction — 165
- 9.2 Materials and methods — 167
 - 9.2.1 Ligand preparation — 167
 - 9.2.2 Protein preparation — 167
 - 9.2.3 Molecular docking — 167
- 9.3 Results — 167
- 9.4 Discussion and conclusions — 174
 - 9.4.1 Discussion — 174
 - 9.4.2 Conclusions — 176
- References — 176

Medinat O. Osundiya, Segun E. Olaseni, Rasaq A. Olowu, and Olanrewaju Owoyomi

10 Thermodynamics of the micellization of quaternary based cationic surfactants in triethanolamine-water media: a conductometry study — 181

- 10.1 Introduction — 182
- 10.2 Materials and methods — 184
 - 10.2.1 Materials — 184
- 10.3 Results and discussion — 185
 - 10.3.1 Results — 185
 - 10.3.2 Mixed micelle formation. And Solvent Effect — 187
 - 10.3.3 Effect of Temperature on the Mixed micelle formation — 188
 - 10.3.4 Thermodynamics of Mixed-Micelles — 189
- 10.4 Conclusion — 190
- References — 191

Index — 195

List of contributing authors

Aderemi T. Adeleye

Beingin

China

aderemi4crown@yahoo.com

John A. Agwupuye

University of Calabar

Pure and Applied Chemistry

Calabar, Calabar 540221

Nigeria

agwupuye.john@yahoo.com

Gloria Chioma Apebende

University of Calabar

Pure and Applied Chemistry

Calabar, Calabar 540221

Nigeria

gloriaapebende@yahoo.com

Bassey B. Asuquo

University of Calabar

Pure and Applied Chemistry

Calabar, Calabar 540221

Nigeria

basseyasuquo123@gmail.com

Oluseyi Ezekiel Awe

University of Ibadan

Physics

Ibadan, Oyo

Nigeria

oluseyi.awe@ui.edu.ng

Tandrima Banerjee

Indian Institute of Science Education and

Research Kolkata

Mohanpur, West Bengal

India

tandrima.samanta10@gmail.com

Victoria Mfon Bassey

University of Calabar

Pure and Applied Chemistry

Calabar, Calabar 540221

Nigeria

victoriaanyia@yahoo.com

Pradip Kumar Bhattacharyya

Arya Vidyapeeth College

Guwahati, Assam

India

prdpbhatta@yahoo.co.in

Emmanuel Asu Asu Bisong

University of Calabar

Pure and Applied Chemistry

Calabar, Calabar 540221

Nigeria

bisongea@unical.edu.ng

Prince David

University of Calabar

Pure and Applied Chemistry

Calabar, Calabar 540221

Nigeria

princedaavid@gmail.com

Moses Mbeh Edim

University of Calabar

Pure and Applied Chemistry

Calabar, Calabar 540221

Nigeria

moses.edim@yahoo.com

Francis Ogar Ekpen

University of Calabar

Pure and Applied Chemistry

Calabar, Calabar 540221

Nigeria

pafrank2016@gmail.com

Atanaska Elenkova

Medical University-Sofia Faculty of Medicine

Sofia, Sofiã

Bulgaria

atanaska@gmail.com

Obieze C. Enudi

University of Calabar

Pure and Applied Chemistry

Calabar, Calabar 540221

Nigeria

enudij@gmail.com

<https://doi.org/10.1515/9783110739763-202>

XII — List of contributing authors

Adewole Kayode Ezekiel
University of Medical Sciences Ondo City -
Biochemistry
Ondo, Ondo State
Nigeria
kayowolemi@gmail.com

Ahmed Adebayo Ishola
Central Research Laboratories Limited,
University Road Ilorin - Biochemistry
Ilorin, Kwara State
Nigeria
djmedite@gmail.com

Hitler Louis
University of Calabar
Pure and Applied Chemistry
Calabar, Calabar 540221
Nigeria
louismuzong@gmail.com

Liliana Mammio
University of Venda
Thohoyandou, Limpopo
South Africa
sasdestria@yahoo.com

Tiyati H. Mujong
University Claude Bernard Lyon 1
Villeurbanne, Auvergne-Rhône-Alpes
France
tiyato-humwapwa.mujong@etu.univ-lyon1.fr

Miroslava Nedyalkova
Medical University-Sofia Faculty of Medicine
Sofia, Sofiã
Bulgaria
mici345@yahoo.com

Albert Ofori
University of Cape Coast School of Physical
Sciences
Department of Chemistry
Cape Coast, Central
Ghana
albert.ofori1@ucc.edu.gh

Osundiya Medinat Olubunmi
1 Lagos State University - Chemistry
Ojo, Lagos
Nigeria
2 Adekunle Ajasin University - Chemistry
Akungba-Akoko, Ondo
Nigeria
3 Obafemi Awolowo University - Chemistry
Ile-Ife, Osun
Nigeria
medinat.osundiya@lasu.edu.ng

Blessing O. Omolaso
University of Medical Sciences Ondo City -
Physiology
Ondo, Ondo State
Nigeria
bomolaso@unimed.edu.ng

Olugbenga Morayo Oshakuade
University of Ibadan
Physics
Ibadan, Oyo
Nigeria
om.oshakuade@ui.edu.ng

Linda I. Peter
University of Calabar
Pure and Applied Chemistry
Calabar, Calabar 540221
Nigeria
ifedioralinda@gmail.com

Ralitsa Robeva
Medical University-Sofia Faculty of Medicine
Sofia, Sofiã
Bulgaria
rali_robeva@abv.bg

Bapan Saha
Handique Girls' College - Chemistry
Guwahati, Assam
India
bapan.chem@gmail.com

Queen O. Sam
University of Calabar
Pure and Applied Chemistry
Calabar, Calabar 540221
Nigeria
queensam21@gmail.com

Abhijit Samanta
The Neotia University - School of Engineering and
Applied Sciences
Kolkata, West Bengal
India
abhijit.ism08@hotmail.com

Vasil Simeonov
Medical University-Sofia Faculty of Medicine
Sofia, Sofia
Bulgaria
vsimeonov@chem.uni-sofia.bg

Samuel Tetteh
University of Cape Coast School of Physical
Sciences
Department of Chemistry
Cape Coast, Central
Ghana
samuel.tetteh@ucc.edu.gh

Emmanuel I. Ubana
University of Calabar
Pure and Applied Chemistry
Calabar, Calabar 540221
Nigeria
emmanuelubana@gmail.com

Tomsmith O. Unimuke
University of Calabar
Pure and Applied Chemistry
Calabar, Calabar 540221
Nigeria
Ojtomtsm@gmail.com

Bapan Saha* and Pradip Kumar Bhattacharyya

1 Role of heteroatoms and substituents on the structure, reactivity, aromaticity, and absorption spectra of pyrene: a density functional theory study

Abstract: Effect of heteroatoms viz. BN and substituents viz. –Me (methyl), –OH (hydroxyl), –NH₂ (amine), –COOH (carboxyl), and –CN (cyano) on the structural parameters, global reactivity, aromaticity, and UV-visible spectra of pyrene are studied with the help of density functional theory (DFT). Global reactivity parameters such as global hardness (η) and electrophilicity (ω) are calculated using density functional reactivity theory (DFRT). Time dependent density functional theory (TD-DFT) is explored for interpreting the UV-visible absorption spectra. Aromaticity of the pyrene rings are predicted from the nucleus independent chemical shift (NICS) values. Presence of BN unit and substituent induces reasonable impact on the studied parameters. The observed absorption spectra lie predominantly within the UV-region (both blue and red shifts are observed in presence of BN and substituent). HOMO energy and absorption spectra are affected nominally in solvent phase.

Keywords: absorption spectra; aromaticity; BN doped pyrene; DFT; Pyrene; TD-DFT.

1.1 Introduction

Polycyclic aromatic compounds (PACs) play substantial role in organic electronics, chemosensors, and electroluminescent materials [1–4]. Besides, their excellent fluorescent properties have been attributed to their extended delocalized π -electrons [5]. Besides, these electrons are also responsible for different kinds of π -interactions via their unique bonding modes [6–9]. However, their low solubility and nonexistence of suitable methods for chemical transformations have constrained their widespread use as materials. Nevertheless, PACs with four membered (fused) rings have attracted the scientific community because of their unique nature [10–13] and suitably explored as energy related applications and in organic electronics [14–16].

Pyrene can be considered as the molecular fragments of carbon nano allotropes viz. graphene and carbon nanotubes [17, 18]. Owing to the conjugated macrocyclic

*Corresponding author: Bapan Saha, Department of Chemistry, Handique Girls' College, Guwahati, 781001, Assam, India, E-mail: bapan.chem@gmail.com

Pradip Kumar Bhattacharyya, Arya Vidyapeeth College, Guwahati, 781016, Assam, India, E-mail: prdpbhatta@yahoo.co.in

This article has previously been published in the journal *Physical Sciences Reviews*. Please cite as: B. Saha and P. K. Bhattacharyya "Role of heteroatoms and substituents on the structure, reactivity, aromaticity, and absorption spectra of pyrene: a density functional theory study" *Physical Sciences Reviews* [Online] 2021, 7. DOI: 10.1515/psr-2020-0086 | <https://doi.org/10.1515/9783110739763-001>

π -delocalized structure, pyrene-based materials have been explored in developing light emitting (organic electronics) and charge transport materials [11, 14]. Recently, pyrene-based molecules are being extensively used for functionalization of carbon nanotubes and in anchoring of foreign molecules such as polymers, proteins, small biomolecules and many more [19–21]. Besides, their use in studying protein and nucleic acids, such materials has also been explored in sensing oxygen, intercalating DNA, and solar cells [22–24]. Studies revealed that functionalized pyrenes have different optical, electrical, and mechanical properties than the pyrene molecule [25]. Presence of substituents and their position also play significant roles in geometrical parameters and molecular orbital energy level of pyrene counterparts or pyrene-based materials [11, 26]. As the focus has been on their spectroscopic properties, quantum chemical studies could be handy in understanding the structural relationship with electronic properties.

B and N doped/co-doped PACs have been of fundamental interest because of their usefulness in chemosensing and developing optoelectronic materials [27–29]. Heteroatoms such as B and/or N significantly tailor their photophysical and electronic properties, keeping the structural features intact. Although a good number of reports on B and/or N doped pyrene are available in literature, those devoted to understanding the structure and molecular properties of doped substituted pyrene are relatively sparse. It is thus expected to be very fascinating to study and compare different properties of doped and substituted pyrene-based materials. In this study, gas and solvent phase reactivity, aromaticity, and absorption spectra of BN doped substituted pyrene system are studied. For the purpose, both electron donating (methyl, hydroxyl and amino) and electron withdrawing (carboxyl and cyano) groups are taken into consideration. Moreover, position of dopants is also varied and its effect on the aforesaid properties is scrutinized. Moreover, heteroaromatic rings possess unique electronic structure and modulated distribution of electron density that facilitates variety of interactions which could be of key importance in organic electronics [30]. The study is expected to be handy in designing novel pyrene-based materials with tailored molecular properties.

1.2 Theoretical and computational details

In this study, all density functional calculations are performed with the help of Gaussian 09 programme [31]. All calculations are performed at B3LYP/6-311+G(d,p) level of theory. Presence of real minima is ensured by frequency (all real) calculation for the chosen systems. Literatures are also in favor of using B3LYP functional for understanding molecular properties of polyaromatic compounds [32, 33]. Energy of the highest occupied molecular orbital (E_{HOMO}), global hardness (η), and global electrophilicity (ω) are calculated for rationalizing the global reactivity. The working formulae for η and ω are given by $\eta = (E_{\text{LUMO}} - E_{\text{HOMO}})/2$ and $\omega = \mu^2/2\eta$, respectively. E_{LUMO} is energy the of lowest unoccupied molecular orbital and $\mu = (E_{\text{HOMO}} + E_{\text{LUMO}})/2$ [34, 35]. Since LUMO is a virtual orbital, its energy obtained from Koopman's theorem is somewhat questionable and

therefore, η values are again calculated adopting Δ SCF method and compared with the corresponding results obtained using Koopman's theorem [36]. According to Δ SCF method, ionization potential/energy, $IP = E_{N-1} - E_N$, and electron affinity, $EA = E_N - E_{N+1}$. E_N , E_{N-1} and E_{N+1} are the ground state energies of systems with N , $N-1$ and $N+1$ electron respectively. Accordingly, η values are defined as $\eta = (IP - EA)/2$.

Reorganization energies for holes (λ_h) and electrons (λ_e) are calculated by the relationship $\lambda_{h/e} = (E_3 - E_2) + (E_4 - E_1)$ [37] where E_1 is the energy of neutral optimized molecule, E_2 is the energy of the corresponding cation/anion obtained from single point calculation, and E_3 is the energy of the optimized cation/anion and E_4 is the energy of the neutral molecule obtained from single point calculation.

Aromaticity of the chosen systems is predicted from NICS (nucleus independent chemical shift) values [38]. For calculation of NICS values, gauge independent atomic orbital (GIAO) method is used. UV-visible absorption spectra of chosen pyrene moieties are calculated using the TDDFT method ($N = 6$ states) [39]. For solvent phase calculation, polarizable continuum model (PCM) is used [40] with cyclohexane ($\epsilon = 2.02$), ethanol ($\epsilon = 24.85$), and water ($\epsilon = 78.35$) as model solvent systems.

1.3 Results and discussions

Herein, BN is doped at the centre (in between two rings keeping naphthalene unit in either side) (Figure 1.1b) and at the edge (Figure 1.1c). The position of the substituent is

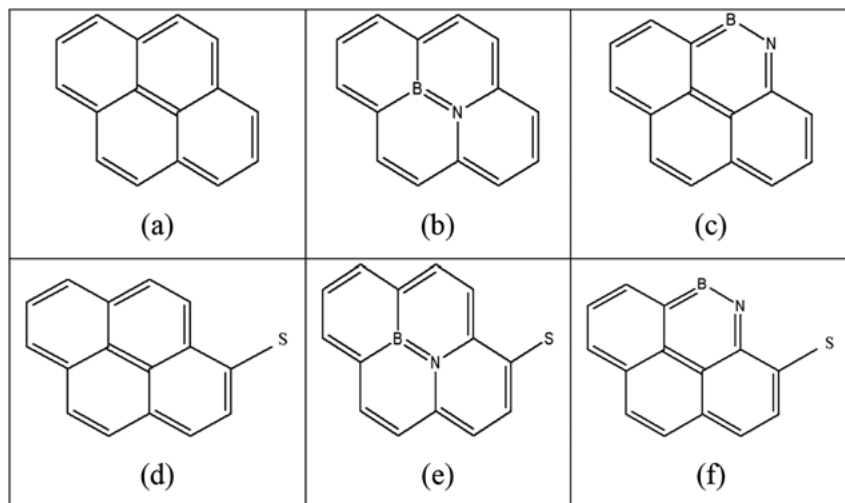


Figure 1.1: The chosen systems (a) undoped Pyr, (b) BN doped Pyr at the centre, (c) BN doped Pyr at the edge, and substituted (d) undoped Pyr, (e) BN doped Pyr at the centre, and (f) BN doped Pyr at the edge.

considered at the positions shown in Figure 1.1d–f (S is the position of the substituent). All throughout the manuscript, the undoped, BN unit at the centre and BN unit at the edge are represented as Pyr and Pyr_(BN) and Pyr_(BNe), respectively. The substituted pyrene unit is represented with the symbol of substituent such as –Me (methyl), –OH (hydroxyl), –NH₂ (amine), –COOH (carboxyl), and –CN (cyano). For example, methyl and hydroxyl substituted pyrenes are represented as Me–Pyr and OH–Pyr, respectively.

In molecular electrostatic potential surface (MESP), a site with poor electron distribution is susceptible to nucleophilic attack whereas an electron rich site is preferred by an electrophile [41, 42]. MESP diagram are widely used in understanding the mechanism of chemical reactions along with some understanding about the bonding and reactivity trends in fused aromatic systems [43]. The MESP surfaces are studied and shown in Figure 1.2. MESP surface of Pyr is symmetrical with electron rich sites (red color) distributed on the surface and electron poor sites (blue color) distributed around the edge, Figure 1.2a. Upon doping, there occurs a perturbation in the electron density distribution (intensity of red and blue color changes) around the dopants (Figure 1.2b and c) indicating a charge separation on the respective sites/species. Similar results in distribution of electron density in presence of dopants are previously reported for larger fused arene systems [32, 42].

Moreover, position of the dopant also plays significant role on the distribution of electron density (intensity of the color varies) of the chosen systems, Figure 1.2b and c. In presence of substituents, further perturbation in electron density distribution is observed (Figure 1.2d–r). Presence of the BN unit in the aromatic framework; resulting in charge separation on the surface of Pyr unit thereby, modulating its electronic structure and molecular properties. As expected, distribution of electron density also varies on varying the substituent (intensity of the colour varies), Figure 1.2d–r. Thus, presence and position of dopant and nature of the substituent would be crucial in tailoring their chosen molecular properties.

1.3.1 Geometry of the chosen systems

Optimized geometries of the chosen systems are shown in Figure 1.3. As expected, the geometry of Pyr is planar with unperturbed π -electron delocalization, with unequal C–C distances, (1.36–1.44 Å), Figure 1.3a. The calculated bond lengths corroborate well with the experimental results (1.39 Å) and thus validate the suitability of used computational method for the study [44]. For substituted Pyr, nominal effect on the bond parameters are observed, Figure 1.3b–f. On doping BN, irrespective of its position, the planarity of the systems remained intact with some perturbation in distribution of π -electron nearby the dopant, Figure 1.3g–r. Variations observed in the C–C bond distances are insignificant (<0.02 Å) and B–C, B–N, C–N distances are within 1.42–1.51, 1.37–1.48, and 1.37–1.40 Å, respectively. The C–C bonds are unaffected (<0.02 Å) in case

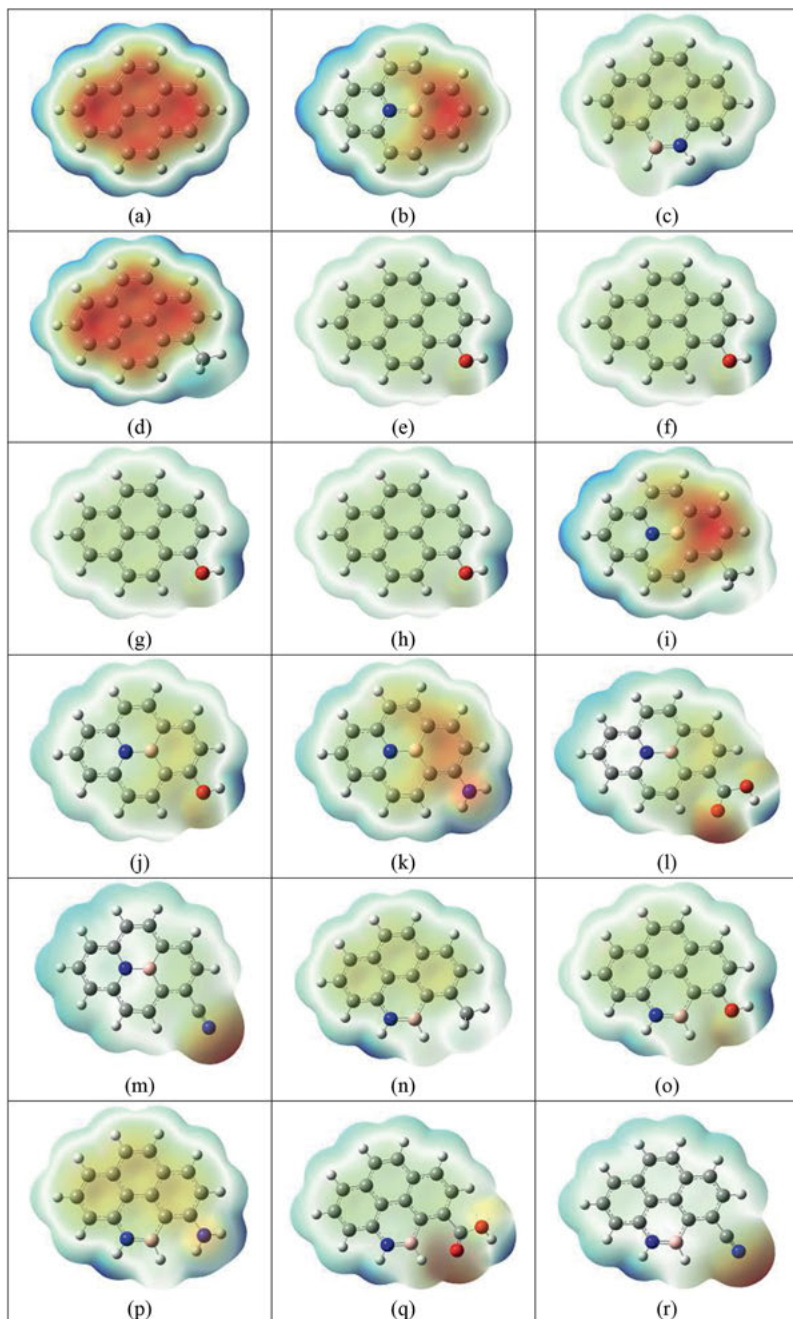


Figure 1.2: MESP surface of (a) Pyr, (b) Pyr_(BN), (c) Pyr_(BNe), (d) Me-Pyr, (e) OH-Pyr, (f) NH₂-Pyr, (g) COOH-Pyr, (h) CN-Pyr, (i) Me-Pyr_(BN), (j) OH-Pyr_(BN), (k) NH₂-Pyr_(BN), (l) COOH-Pyr_(BN), (m) CN-Pyr_(BN), (n) Me-Pyr_(BNe), (o) OH-Pyr_(BNe), (p) NH₂-Pyr_(BNe), (q) COOH-Pyr_(BNe), and (r) CN-Pyr_(BNe).

on substituted BN doped Pyr. The observed variation in bond parameters also predicts transformation of molecular properties resulting from presence of dopants and substituents.

1.3.2 HOMO shapes and HOMO perspectives

From the viewpoint of its importance in understanding the reactivity (donor sites, stability, and band gap) patterns, the shapes of HOMO and E_{HOMO} are obtained for the chosen systems and the results are presented in Figure 1.4 and Table 1.1 respectively. Referring to Figure 1.4a, HOMO of Pyr is distributed symmetrically over the entire molecule. In presence of substituents, in addition to the molecular surface, HOMO is also associated with the substituent irrespective of their nature, Figure 1.4b–f. Similarly, a nominal variation (except nearby the ring with substituents) in the shapes of HOMO is observed in case of BN doped counterparts (Figure 1.4g–r) irrespective of position of the dopants. Since BN is isoelectronic with CC, its presence does not disturb the electron distribution significantly. Although nominal, the shapes of HOMO indicate towards some variations in molecular properties of the chosen systems.

E_{HOMO} value for Pyr is obtained at $-130.79 \text{ kcal mol}^{-1}$. In presence of substituent, E_{HOMO} values are varied, within the range -124.76 to $-141.56 \text{ kcal mol}^{-1}$, Table 1.1. For electron donating substituents, E_{HOMO} values are raised while for electron withdrawing substituents, the E_{HOMO} values are dropped. Electron withdrawing substituent reduces the electron density from the Pyr surface thereby lowering the E_{HOMO} values. Exactly opposite phenomena would operate in case of electron donating substituent. For example, E_{HOMO} values for Me–Pyr, OH–Pyr, NH_2 –Pyr, COOH–Pyr and CN–Pyr are -128.12 , -124.76 , -128.44 , -137.32 , and $-141.56 \text{ kcal mol}^{-1}$, respectively. Thus, in view of E_{HOMO} values, COOH–Pyr and CN–Pyr are more stable than the rest of undoped substituted Pyr.

Presence of BN unit causes some variation in E_{HOMO} values depending upon the position of dopants, the E_{HOMO} values for $\text{Pyr}_{(\text{BN})}$ and $\text{Pyr}_{(\text{BNe})}$ are -129.15 and $-133.90 \text{ kcal mol}^{-1}$, respectively. BN unit at the centre of Pyr raises the HOMO energy while at the edge it drops the HOMO energy. Therefore, reactivity of $\text{Pyr}_{(\text{BN})}$ is more than that of Pyr which, in turn, is more than $\text{Pyr}_{(\text{BNe})}$. Similar results are also observed in case of substituted BN doped pyrene irrespective of the position of the dopants (lie within the range -121.79 to $-143.68 \text{ kcal mol}^{-1}$), Table 1.1. In comparison to their undoped counterparts, in case of BN doped substituted Pyr at the centre, the E_{HOMO} values are raised by upto $3.69 \text{ kcal mol}^{-1}$ (NH_2 – $\text{Pyr}_{(\text{BN})}$, $-124.75 \text{ kcal mol}^{-1}$). However, for BN doped substituted Pyr at the edge, the E_{HOMO} values dropped by upto $3.02 \text{ kcal mol}^{-1}$ (Me– $\text{Pyr}_{(\text{BNe})}$, $-131.12 \text{ kcal mol}^{-1}$). Ishibashi et al., has indicated key role of position of BN unit on the HOMO shapes and E_{HOMO} values of BN doped linear acenes [12]. Nonetheless, the effect of nature of substituent (raised E_{HOMO} values for electron donating substituent and dropped E_{HOMO} values for electron withdrawing

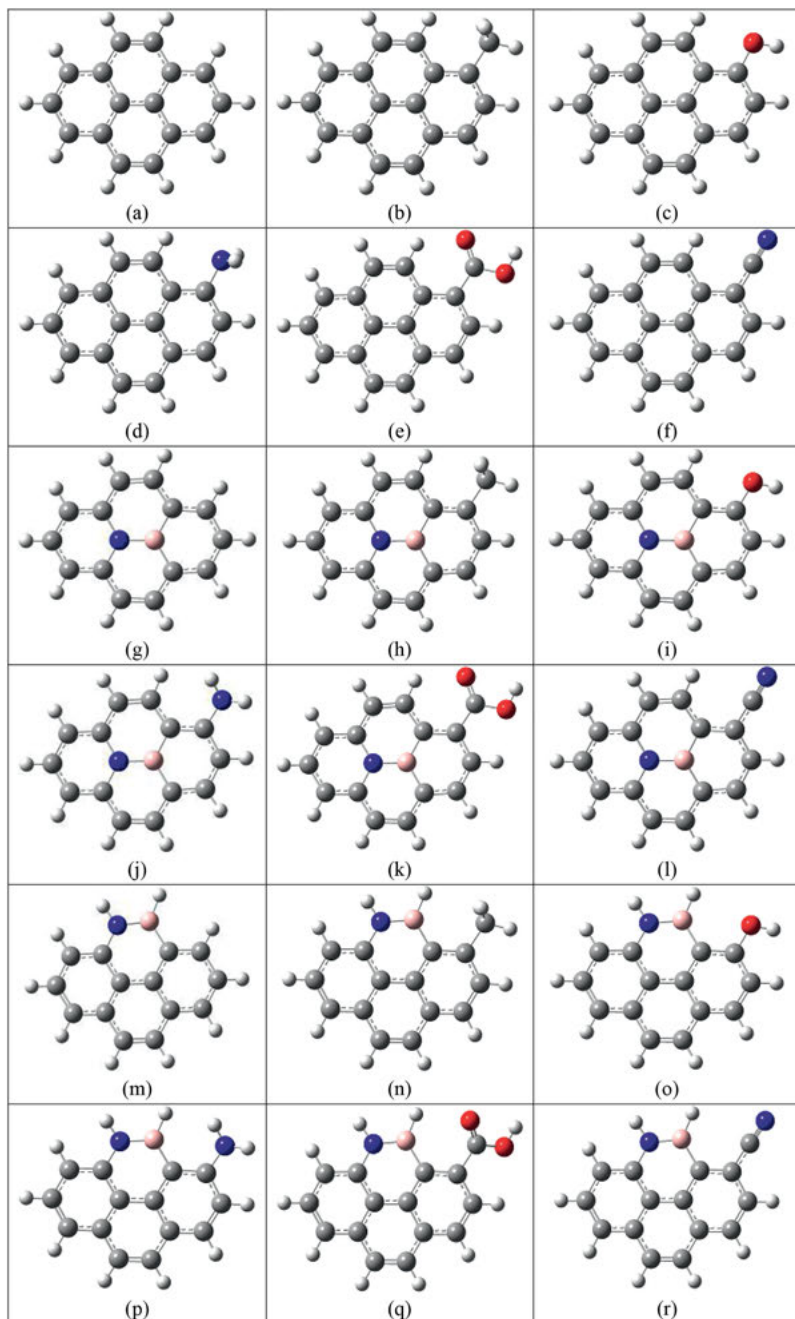


Figure 13: Optimized geometry of (a) Pyr, (b) Me-Pyr, (c) OH-Pyr, (d) NH₂-Pyr, (e) COOH-Pyr, (f) CN-Pyr (g) Pyr_(BN), (h) Me-Pyr_(BN), (i) OH-Pyr_(BN), (j) NH₂-Pyr_(BN), (k) COOH-Pyr_(BN), (l) CN-Pyr_(BN), (m) Pyr_(BNe), (n) Me-Pyr_(BNe), (o) OH-Pyr_(BNe), (p) NH₂-Pyr_(BNe), (q) COOH-Pyr_(BNe), and (r) CN-Pyr_(BNe).

Table 1.1: Variation in E_{HOMO} values in gas ($E_{\text{HOMO(gas)}}$), cyclohexane ($E_{\text{HOMO(ch)}}$), ethanol ($E_{\text{HOMO(eth)}}$), and water ($E_{\text{HOMO(wat)}}$), and reorganization energies for hole (λ_h) and electron (λ_e) (in kcal mol⁻¹).

| Systems | $E_{\text{HOMO(gas)}}$ | $E_{\text{HOMO(ch)}}$ | $E_{\text{HOMO(eth)}}$ | $E_{\text{HOMO(wat)}}$ | λ_h | λ_e |
|---------------------------------------|------------------------|-----------------------|------------------------|------------------------|-------------|-------------|
| Pyr | -130.79 | -131.53 | -133.36 | -133.57 | 0.0067 | 0.0005 |
| Me-Pyr | -128.12 | -129.05 | -130.98 | -131.22 | 0.0065 | 0.0092 |
| OH-Pyr | -124.76 | -125.82 | -127.99 | -128.22 | 0.0077 | 0.0136 |
| NH ₂ -Pyr | -128.44 | -129.64 | -131.80 | -132.03 | 0.0312 | 0.0199 |
| COOH-Pyr | -137.32 | -137.61 | -138.82 | -138.96 | 0.0105 | 0.0266 |
| CN-Pyr | -141.56 | -140.59 | -140.37 | -140.39 | 0.0140 | 0.0442 |
| Pyr _(BN) | -129.15 | -130.02 | -131.95 | -132.16 | 0.0184 | 0.0094 |
| Me-Pyr _(BN) | -125.98 | -126.93 | -128.96 | -129.18 | 0.0044 | 0.0066 |
| OH-Pyr _(BN) | -121.79 | -122.91 | -125.15 | -125.39 | 0.0039 | 0.0052 |
| NH ₂ -Pyr _(BN) | -124.75 | -125.91 | -126.40 | -128.55 | 0.0913 | 0.0568 |
| COOH-Pyr _(BN) | -135.94 | -136.32 | -137.68 | -137.84 | 0.0465 | 0.6341 |
| CN-Pyr _(BN) | -140.29 | -139.51 | -139.50 | -139.55 | 0.0098 | 0.0198 |
| Pyr _(BNe) | -133.90 | -134.48 | -136.05 | -136.23 | 0.0530 | 0.0375 |
| Me-Pyr _(BNe) | -131.12 | -131.91 | -133.68 | -133.88 | 0.0533 | 0.0496 |
| OH-Pyr _(BNe) | -127.78 | -128.73 | -130.73 | -130.95 | 0.0053 | 0.0071 |
| NH ₂ -Pyr _(BNe) | -130.67 | -131.73 | -133.96 | -134.22 | 1.2925 | 0.0652 |
| COOH-Pyr _(BNe) | -138.18 | -138.84 | -139.70 | -139.82 | 0.0581 | 0.7767 |
| CN-Pyr _(BNe) | -143.68 | -142.38 | -141.73 | -141.72 | 0.0369 | 0.0165 |

substituent) on the E_{HOMO} values remained similar irrespective of presence of dopants, Table 1.1. Thus, in addition to substituents, position of dopants is also important in controlling the stability of chosen systems.

Charge transport behavior is validated by calculating reorganization energies for the hole and electrons are calculated and the obtained values are shown in Table 1.1. Referring to Table 1.1, it is observed that, both λ_h and λ_e values are significantly small (<1.5 kcal mol⁻¹) which is very significant from the view point of charge transport properties. In some cases, $\lambda_h < \lambda_e$ (hole transport) while for others $\lambda_h > \lambda_e$ (electron transport), Table 1.1. Thus, the chosen systems are either exhibit hole transport capacity or exhibit electron transport capacity. Owing to presence of substituents variation charge transport properties are induced in the chosen systems. Pyrene based materials are also reported to be suitable as both hole injection and transport materials in earlier literature [45].

E_{HOMO} values are also calculated in different solvent phase, results are shown in Table 1.1. Presence of solvent phase causes drop in the E_{HOMO} values by 0.29–3.8 kcal mol⁻¹ with the exception of cyano substituted undoped/doper Pyr, Table 1.1. E_{HOMO} values are increased (by upto 1.96 kcal mol⁻¹) irrespective of solvent dielectrics, Table 1.1. The electron donating tendency of cyano substituted systems (undoped/doped) are increased with incorporation of solvent phase. The drop in E_{HOMO} values

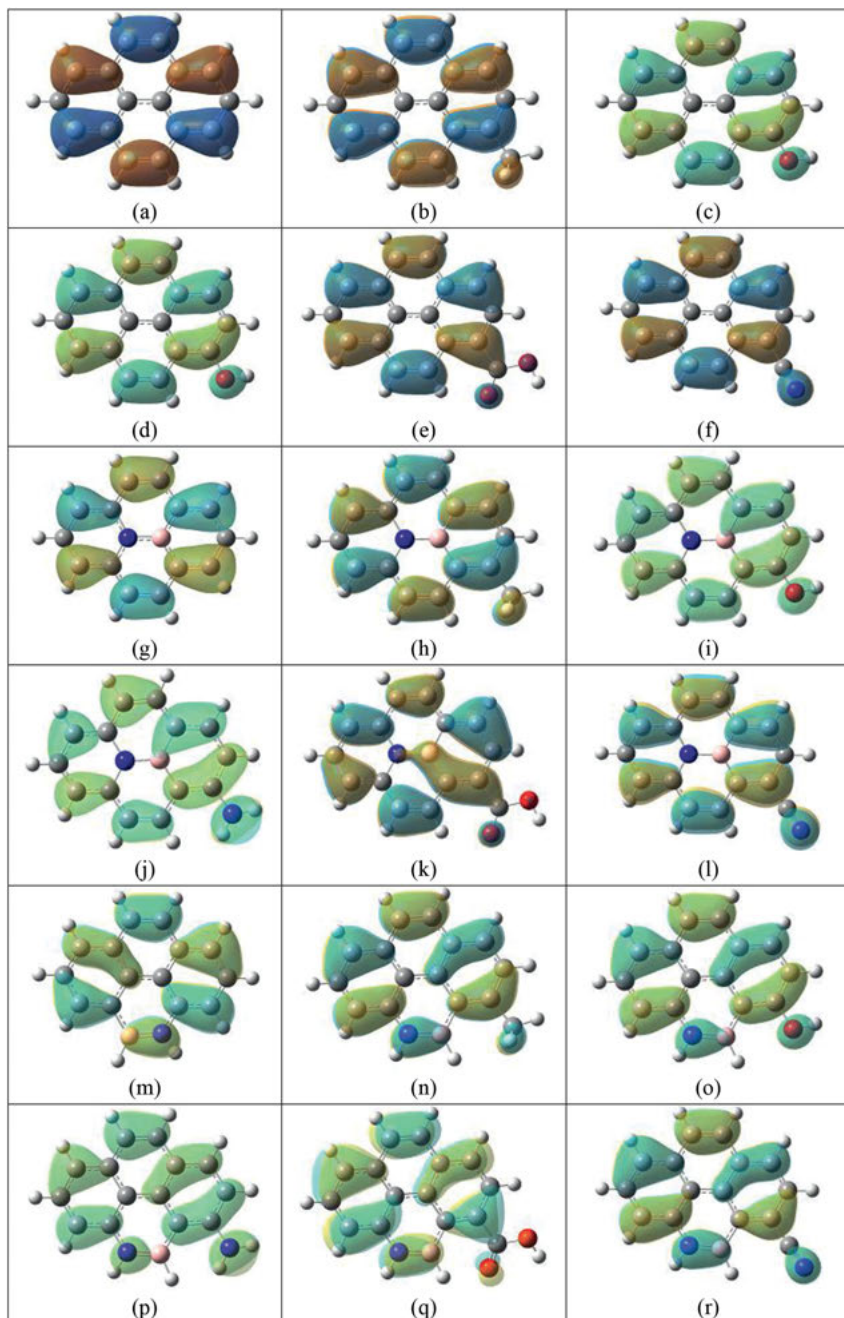


Figure 1.4: HOMO shapes of (a) Pyr, (b) Me-Pyr, (c) OH-Pyr, (d) NH₂-Pyr, (e) COOH-Pyr, (f) CN-Pyr (g) Pyr_(BN), (h) Me-Pyr_(BN), (i) OH-Pyr_(BN), (j) NH₂-Pyr_(BN), (k) COOH-Pyr_(BN), (l) CN-Pyr_(BN), (m) Pyr_(BNe), (n) Me-Pyr_(BNe), (o) OH-Pyr_(BNe), (p) NH₂-Pyr_(BNe), (q) COOH-Pyr_(BNe), and (r) CN-Pyr_(BNe).

follows the order: $E_{\text{HOMO}(\text{ch})} < E_{\text{HOMO}(\text{eth})} < E_{\text{HOMO}(\text{wat})}$. The drop in E_{HOMO} values for the chosen systems (undoped/doped) are more pronounced (by up to $1.20 \text{ kcal mol}^{-1}$ in cyclohexane, $3.36 \text{ kcal mol}^{-1}$ in ethanol and $3.80 \text{ kcal mol}^{-1}$ in water) in case of solvents with higher dielectrics. For example, E_{HOMO} values for Pyr in gas, cyclohexane, ethanol, and water are -130.79 , -131.53 , -133.36 , and $-133.57 \text{ kcal mol}^{-1}$, respectively. Therefore, incorporation of solvent exerts some role in controlling solution phase chemistry of the chosen systems.

1.3.3 Variations in global hardness and philicity, and dipole moment

To have some insight about chemical stability, η (larger the value, higher is the stability) and ω (smaller the value, higher is the stability), and dipole moment for the chosen systems are calculated and the results are shown in Table 1.2. η value for Pyr is estimated to be $43.95 \text{ kcal mol}^{-1}$ and in presence of substituents decrease in η values are observed (40.22 – $42.94 \text{ kcal mol}^{-1}$) and thereby indicating their higher reactivity. In case of $\text{Pyr}_{(\text{BN})}$ and $\text{Pyr}_{(\text{BNe})}$, the η values are 41.29 and $47.29 \text{ kcal mol}^{-1}$, respectively. Thus, reactivity of the doped systems depends on the position of dopants, reactivity increased in the order: $\text{Pyr}_{(\text{BNe})} < \text{Pyr} < \text{Pyr}_{(\text{BN})}$. Presence of substituent also effects the η values of the BN doped Pyr, Table 1.2. For BN unit at the centre, the η values lie within the range 36.70 – $39.85 \text{ kcal mol}^{-1}$ and at the edge, η values lie within the range 43.32 – $46.01 \text{ kcal mol}^{-1}$. Similar to their undoped counterparts, presence of substituent increases the reactivity of BN doped Pyr irrespective of its position. Similar trends in stability were also predicted from the HOMO energies of the corresponding systems. In case of COOH-Pyr and CN-Pyr , the decrease in η values are significant (by $>3.50 \text{ kcal mol}^{-1}$), indicating their higher reactivities. In case of dopant at the centre, the variation in η values are more significant (by up to $4.59 \text{ kcal mol}^{-1}$) for electron donating substituents. For the systems with BN at the edge, the stability order is reversed and follows the trend exactly similar to undoped counterparts, i.e., electron-withdrawing $\text{COOH-Pyr}_{(\text{BNe})}$ and $\text{CN-Pyr}_{(\text{BNe})}$ are more reactive than $\text{Pyr}_{(\text{BNe})}$. Therefore, presence of dopant, substituent, and position of dopant is imperative from the view point of reactivity of pyrene systems.

Moreover, η values can also be used for predicting HOMO–LUMO gap (parallel) for the chosen systems. Presence of substituents reduces the η values, thereby reducing the HOMO–LUMO gap. Lowest HOMO–LUMO gap is observed for Pyr with electron withdrawing substituents *viz.*, $-\text{CN}$ and $-\text{COOH}$. Also, presence of BN unit at the centre of pyrene reduced the HOMO–LUMO gap. Thus, BN doped pyrene and $-\text{CN}$ and $-\text{COOH}$ substituted pyrene could be suitably used in dye sensitized solar cells. Kathiravan et al., has also echoed similarly and suggested that pyrene with weak electron withdrawing substituent possess larger HOMO–LUMO gap while the same for strong electron withdrawing substituent are relatively smaller [46].

Table 1.2: Variation in η , ω values (in kcal mol⁻¹), and dipole moment (in Debye).

| Systems | η | ω | Dipole moment |
|---------------------------------------|--------|----------|---------------|
| Pyr | 43.95 | 81.76 | 0 |
| Me-Pyr | 42.94 | 84.45 | 0.51 |
| OH-Pyr | 42.46 | 85.78 | 1.62 |
| NH ₂ -Pyr | 43.63 | 82.43 | 1.32 |
| COOH-Pyr | 40.22 | 117.15 | 2.36 |
| CN-Pyr | 41.31 | 121.64 | 5.52 |
| Pyr _(BN) | 41.29 | 93.48 | 2.55 |
| Me-Pyr _(BN) | 38.74 | 98.24 | 2.18 |
| OH-Pyr _(BN) | 39.09 | 97.47 | 1.25 |
| NH ₂ -Pyr _(BN) | 36.70 | 92.98 | 1.61 |
| COOH-Pyr _(BN) | 39.21 | 126.58 | 4.25 |
| CN-Pyr _(BN) | 39.85 | 119.32 | 7.71 |
| Pyr _(BNe) | 47.29 | 78.74 | 0.83 |
| Me-Pyr _(BNe) | 46.01 | 79.30 | 0.58 |
| OH-Pyr _(BNe) | 45.51 | 74.38 | 0.91 |
| NH ₂ -Pyr _(BNe) | 43.32 | 79.05 | 1.65 |
| COOH-Pyr _(BNe) | 44.10 | 101.86 | 2.37 |
| CN-Pyr _(BNe) | 43.95 | 113.15 | 5.96 |

ω value for Pyr is estimated to be 81.76 kcal mol⁻¹ and as expected, variation in ω values are observed (lie within the range 82.43–121.64 kcal mol⁻¹), indicating decrease in stability of the substituted undoped Pyr, Table 1.2. In case of Pyr_(BN) and Pyr_(BNe), the ω values are 93.48 and 78.74 kcal mol⁻¹, respectively. Thus, the stability of Pyr_(BN) is less than Pyr which in turn is less than Pyr_(BNe). In presence of substituents, ω values vary with the position of dopants, and are within 102.98–126.58 (dopant at the center) and 79.05–113.15 (dopant at the edge) kcal mol⁻¹, Table 1.2. E_{HOMO} and η values for the corresponding systems also predicted similar stability trends. Thus, the studied reactivity descriptors are consistent enough in predicting the reactivity and/or stability of the chosen systems.

Since, LUMO is a virtual or empty orbital, accurate estimation of its energy is somewhat questionable. To encounter this, use of hybrid functional is recommended [47]. Although hybrid functional B3LYP is used, it would be more scientific to validate the fact (scrutinize the suitability of Koopmans' theorem) for the chosen systems. For this purpose, the ionization potential and η values are further calculated using Δ SCF method. The estimated ionization potential is then plotted against HOMO energy obtained from Koopman's theorem, shown in Figure 1.5a–c. Similarly, the η values obtained by both the methods are also plotted, shown in Figure 1.5d–f. Referring to Figure 1.5a–c, there exists an excellent linear relationship between HOMO energy estimated from Koopman's theorem and ionization potential estimated from Δ SCF method

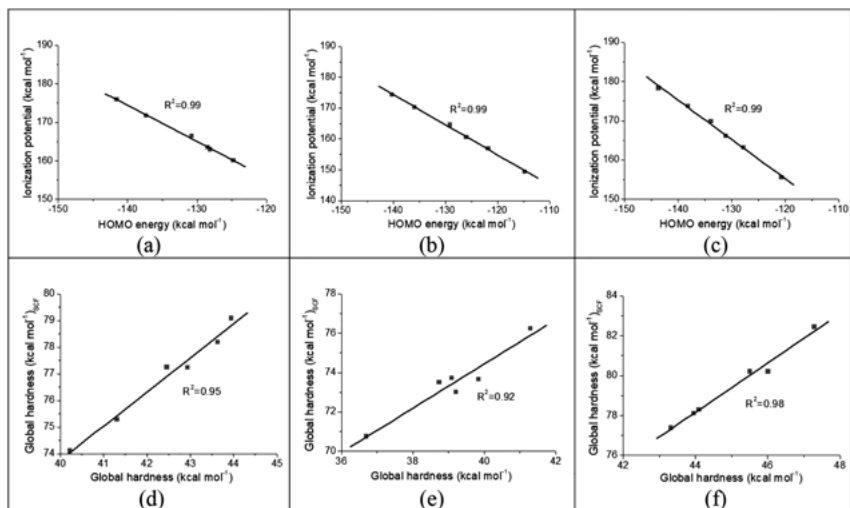


Figure 1.5: HOMO energy vs. Ionization potential for (a) Undoped Pyr (b) BN doped Pyr at centre and (c) BN doped Pyr at edge and Global hardness vs Global hardness_{SCF} for (d) Undoped Pyr (e) BN doped Pyr at centre and (f) BN doped Pyr at edge.

with R^2 values of 0.99. Similarly, linear relationship between global hardness (η) estimated from Koopmans' theorem and Δ SCF method also exists with R^2 values in the range, 0.92–0.98. Presence of linear relationships between the chosen parameters thus validates the suitability of Koopmans' theorem for predicting the reactivity patterns. Similar protocol was adopted in earlier literatures [33].



As expected, Pyr is nonpolar with zero dipole moment. Polarity is induced in presence of substituents with dipole moment values within the range 0.51–5.52 Debye, Table 1.2. Variations in dipole moments are more significant for Pyr with electron withdrawing substituents. The dipole moment values for the undoped pyrene increased in the order: Pyr (0) < Me–Pyr (0.51) < NH₂–Pyr (1.32) < OH–Pyr (1.62) < COOH–Pyr (2.36) < CN–Pyr (5.52), values are in Debye. Presence of BN also induces some polarity with dipole moments 2.55 (for Pyr_(BN)) and 0.83 (for Pyr_(BNe)) Debye. Thus, Pyr_(BN) is more polar than Pyr_(BNe) which in turn is more polar than Pyr. Similar to other reactivity parameters, dipole moment is also position dependent. In presence of solvent phase, the dipole moment values increased with increase in the solvent dielectric. For example, the observed dipole moment for Me–Pyr in cyclohexane, ethanol, and water are 0.62, 0.70, and 0.76 Debye, respectively. Analogous trends are also observed in BN doped substituted pyrene in solvent phase. Similar relationship between dipole moment and solvent dielectrics are also previously reported in literature [48].

1.3.4 Variations in aromatic character

NICS values obtained by GIAO method is one of the most commonly used parameters for predicting the aromaticity [49, 50]. Positive NICS value designates antiaromatic behavior while negative NICS value corresponds to aromatic character. NICS value around zero is described as nonaromatic. Herein, NICS values are estimated for ring with substituent and dopants at the molecular plane. This would enable us to scrutinize the role of substituent and dopants on the aromaticity of the chosen systems [49, 50]. NICS_{zz} values (provides more reliable picture about the π -electron distribution) are obtained for rings with substituent (NICS_{zz(0)sub}) and dopants (NICS_{zz(0)dop}) at the molecular plane, results are shown in Table 1.3.

The NICS_{zz} value for Pyr is found to be -22.20 and 3.33 ; the obtained values correspond to aromatic and antiaromatic character of the rings, which corroborates well with reported values [51]. In presence of substituent, variation in NICS_{zz} values are

Table 1.3: Variation in NICS_{zz(0)sub} and NICS_{zz(0)dop} values.

| Systems | NICS _{zz(0)sub} | NICS _{zz(0)dop} |
|---------------------------------------|--|---|
| |  |  |
| Pyr | -20.20 | 3.33 |
| Me-Pyr | -17.89 | 5.05 |
| OH-Pyr | -18.60 | 3.49 |
| NH ₂ -Pyr | -19.47 | 2.94 |
| COOH-Pyr | -15.78 | 2.65 |
| CN-Pyr | -16.83 | 2.99 |
| Pyr _(BN) | -29.04 | -6.36 |
| Me-Pyr _(BN) | -27.36 | -6.60 |
| OH-Pyr _(BN) | -26.90 | -3.43 |
| NH ₂ -Pyr _(BN) | -24.31 | -1.84 |
| COOH-Pyr _(BN) | -24.42 | -7.90 |
| CN-Pyr _(BN) | -25.71 | -6.87 |
| Pyr _(BNe) | -17.37 | 15.78 |
| Me-Pyr _(BNe) | -15.67 | 15.31 |
| OH-Pyr _(BNe) | -14.60 | 16.03 |
| NH ₂ -Pyr _(BNe) | -10.02 | 16.32 |
| COOH-Pyr _(BNe) | -15.43 | 15.36 |
| CN-Pyr _(BNe) | -15.18 | 14.87 |

observed -15.78 to -19.47 ($\text{NICS}_{zz(0)\text{sub}}$) and 2.65 to 5.05 , Table 1.3. Although, NICS_{zz} values vary, the aromaticity patterns predicted for both the rings are similar. Aromaticity of substituted Pyr is less than Pyr, COOH-Pyr is the least aromatic while $\text{NH}_2\text{-Pyr}$ is the most aromatic, Table 1.3. Thus, presence of substituents does not affect the aromatic properties to a significant level. However, electronic properties are affected for each to some extent.

Presence of dopant significantly affects the aromatic criterion of the chosen systems as NICS_{zz} values vary significantly. NICS_{zz} values for $\text{Pyr}_{(\text{BN})}$ is -29.04 ($\text{NICS}_{zz(0)\text{sub}}$) and -6.36 ($\text{NICS}_{zz(0)\text{dop}}$), indicating aromatic character of both the rings. Thus, presence of BN unit at the ring center increases the aromaticity and transforms antiaromatic ring to aromatic. Ghosh et al., have reported the $\text{NICS}_{zz(0)}$ values of -28.39 and -5.97 for the same [51]. Although presence of substituent lowers the aromaticity, aromaticity pattern is identical with that of $\text{Pyr}_{(\text{BN})}$ with NICS_{zz} values within the range -24.42 to -27.36 ($\text{NICS}_{zz(0)\text{sub}}$). However, the NICS_{zz} values at the ring with substituent are all negative and are within the range -1.84 to -7.90 ($\text{NICS}_{zz(0)\text{dop}}$). Similar to their unsubstituted counterparts, the ring with dopants are aromatic with minimum aromatic character for $\text{NH}_2\text{-Pyr}_{(\text{BN})}$ and maximum aromatic character for $\text{COOH-Pyr}_{(\text{BN})}$, Table 1.3. Moreover, position of the dopants also exerts notable impact on the aromatic character of the chosen rings. For example, the NICS_{zz} values for $\text{Pyr}_{(\text{BNe})}$ are -17.37 ($\text{NICS}_{zz(0)\text{sub}}$) and 15.78 ($\text{NICS}_{zz(0)\text{dop}}$). Thus, one of the ring for $\text{Pyr}_{(\text{BNe})}$ is less aromatic than both Pyr and $\text{Pyr}_{(\text{BN})}$ whereas the other ring is of significantly higher antiaromaticity than both, Table 1.3. The reported $\text{NICS}_{zz(0)}$ values for the same are -16.56 and 16.07 , respectively. Like other two cases, presence of substituents lowers the aromaticity with NICS_{zz} values within the range -10.02 to -15.67 ($\text{NICS}_{zz(0)\text{sub}}$). The antiaromaticity of the substituted ring is comparable with that of the $\text{Pyr}_{(\text{BNe})}$, Table 1.3. Thus, presence of substituent and dopant play some role on the aromaticity and electronic properties and thereby controlling the chemistry of the chosen systems. Position dependence of aromaticity of the ring systems are also illustrated in previously reported literature [51].

1.3.5 Variations in UV visible spectra

UV visible spectra are studied in gas and solvent phase with varying dielectrics; the obtained results are shown in Figure 1.6. In line with the literature, B3LYP functional is used for calculation [46]. UV-visible absorption spectrum of Pyr is calculated using $N = 6$, $N = 10$, $N = 15$, and $N = 20$ methods and the corresponding absorption (primary) maxima in gas phase are obtained at 339 nm (vary after decimal point only) for each. The observed band at this wavelength is ascribed to $\pi \rightarrow \pi^*$ transition ($\text{HOMO} \rightarrow \text{LUMO}$). The experimental absorption maximum has been reported to be at 333 nm [52], which is close to the calculated results thereby validating the suitability of the adopted theoretical methods. Since $N = 6$, $N = 10$, $N = 15$, and $N = 20$ produce

absorption band around same wavelength, the absorption spectra for the chosen systems are calculated using $N = 6$ method (computationally less expensive). In presence of substituents, two absorption maxima for each are observed, which are in the range 275–283 and 342–374 nm, Figure 1.6a. Therefore, significant blue and red shift are observed in presence of substituents. Effect of anchoring group or substituents on the UV-visible absorption spectral pyrene-based materials were also previously reported in literatures [46, 53]. Sahoo et al., have reported the UV-visible spectra of CHO–Pyr (different conditions) within two distinguishable regions viz 250–300 nm and 320–410 nm [53]. The magnitude of blue shifts is almost comparable for all, while for electron withdrawing substituents the observed red shifts are significant, Figure 1.6a.

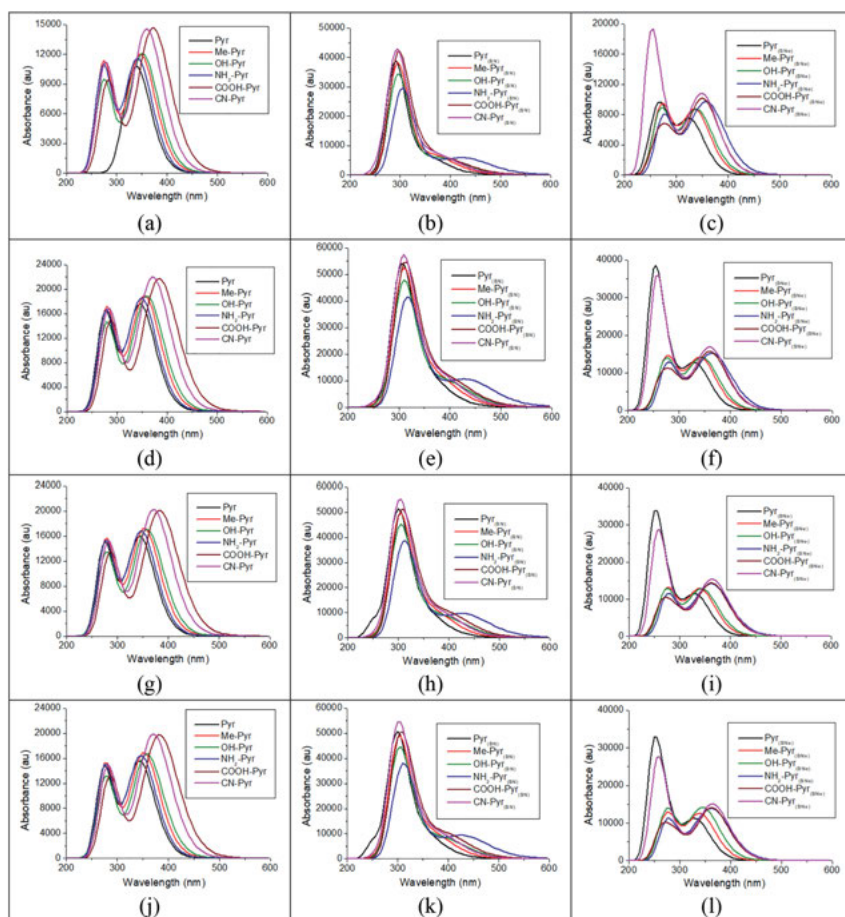


Figure 1.6: UV-visible spectra of (a) undoped Pyr, (b) BN doped Pyr at centre, (c) BN doped Pyr at edge in gas, (d) undoped Pyr, (e) BN doped Pyr at centre, (f) BN doped Pyr at edge in cyclohexane, (g) undoped Pyr, (h) BN doped Pyr at centre, (i) BN doped Pyr at edge in ethanol and (j) undoped Pyr, (k) BN doped Pyr at centre, and (l) BN doped Pyr at edge in water.

For example, the blue shifted absorption maxima for COOH-Pyr and CN-Pyr are obtained at 283 and 277 nm while the red shifted absorption maxima are obtained at 374 and 360 nm, respectively.

For Pyr_(BN), single absorption maximum at 291 nm is observed, ascribed to (HOMO-1 → LUMO+1) transition. Thus, presence of BN unit at the center shifted the maximum to shorter wave length (significant blue shift, high intensity). Unlike substituted Pyr, only single absorption maximum for each is observed in case of substituted Pyr_(BN), Figure 1.6b. A nominal red shift (<10 nm) is observed in most of the cases, Figure 1.6b. NH₂-Pyr_(BN) is an exception to this where two absorption maxima at 305 nm (strong) and 428 nm (broad) are observed. Moreover, significant red shift is also observed in this case, Figure 1.6b. In contrast to BN doped pyrene at the center, two absorption maxima (low intensity) for each are obtained in presence of BN at the edge, Figure 1.6c. For Pyr_(BNe), two absorption maxima are observed at 268 and 332 nm, respectively. Compared to Pyr and Pyr_(BN), the observed blue shift is larger for Pyr_(BNe). In presence of substituents, the absorption maxima for most of the systems are red shifted, Figure 1.6c. However, the observed shift depends on the nature and type of substituents. Absorption maxima at lower wavelength are shifted to around 275 nm while that of the higher wavelength are shifted within the range 340–365 nm, Figure 1.6c. CN-Pyr_(BNe) is an exception to these, with two absorption maxima at 250 (blue shift) and 352 nm are observed. Magnitude of shift is more prominent in case of NH₂-Pyr_(BNe), absorption maxima at 277 and 365 nm are observed. Thus, position of dopant also plays crucial on the electronic properties of chosen systems.

In presence of solvent phase, not much shift in absorption spectra (maxima) is observed except Pyr. Unlike Pyr in gas phase, two absorption maxima around 276 and 345 nm are observed in solvent phase, Figure 1.6d, g, and j. The experimentally reported maxima for dilute solution of Pyr in DCM (dichloromethane) have shown two absorption bands around 274 and 336 nm [54]. Thus, the calculated solvent phase absorption maxima are consistent with the experimentally reported one. For rest of the system (undoped/doped), the number of absorption maxima is identical with gas phase, Figure 1.6. However, nominal red shifts are observed (5–15 nm) for all the chosen systems irrespective of solvent dielectrics, Figure 1.6. Similar trends were also predicted from E_{HOMO} values in solvent phase. Compared to cyclohexane, blue shifts are observed for the corresponding systems in solvent with higher dielectrics i.e., ethanol and water, Figure 1.6. Nominal variations in UV-visible absorption spectra of tetraaryl pyrenes in solvent phase are also reported by Assaad et al. [11].

1.4 Conclusions

The present study enumerates the role of substituent and dopants on the global reactivity descriptors of pyrene systems. Owing to the variation in distribution of electron density, presence of substituents (electron donating and electron

withdrawing), and BN doping exert a reasonable impact on HOMO energy, global hardness, and electrophilicity of the undoped/doped substituted pyrenes. Polarity is induced due to the presence of substituents and maximum polarity is observed for CN–Pyr, CN–Pyr_(BN), and CN–Pyr_(BNe). Different reactivity and polarity induced in the chosen systems might prove to be crucial for their application in multifunctional devices and facilitate further functionalization. Extent of aromaticity varies and depends on the nature of substituents. Substituent and BN doping impart a remarkable impact on the interband transition thereby tuning the optical properties. This indicates their possible role in optoelectronic devices, dye sensitize solar cells and many more. The outcome of the study could possibly be another driving force for experimental investigations in the said area.

Author contributions: All the authors have accepted responsibility for the entire content of this submitted manuscript and approved submission.

Research funding: Authors acknowledge Department of Science and Technology, New Delhi, (Grant No. SB/S1/PC-17/2014) India for providing financial assistance.

Conflict of interest statement: The authors declare no competing financial interests in the current study.

References

1. Takimiya K, Osaka I, Nakano M. π -Building blocks for organic electronics: reevaluation of “inductive” and “resonance” effects of π -electron deficient units. *Chem Mater* 2014;26:587–93.
2. Dou L, You J, Hong Z, Xu X, Li G, Street RA, et al. A decade of organic/polymeric photovoltaic research. *Adv Mater* 2013;25:6642–71.
3. Mei J, Diao Y, Appleton AL, Fang L, Bao Z. Integrated materials design of organic semiconductors for field effect transistors. *J Am Chem Soc* 2013;135:6724–46.
4. Tyagi P, Venkateswararao A, Thomas KRJ. Solution processable indoloquinoline derivatives containing bulky polyaromatic hydrocarbons: synthesis, optical spectra, and electroluminescence. *J Org Chem* 2011;76:4571–81.
5. Facchetti A. π -Conjugated polymers for organic electronics and photovoltaic cell applications. *Chem Mater* 2011;23:733–58.
6. Tehrani ZA, Kim KS. Functional molecules and materials by π -interaction based quantum theoretical design. *Int J Quant Chem* 2016;116:622–33.
7. Schneider HJ. Interactions in supramolecular complexes involving arenes: experimental studies. *Acc Chem Res* 2013;46:1010–19.
8. Salonen LM, Ellermann M, Diederich F. Aromatic rings in chemical and biological recognition: energetics and structures. *Angew Chem Int Ed* 2011;50:4808–42.
9. Saha B, Bhattacharyya PK. B–H δ ... π interaction in borane–graphene complexes: coronene as a case study. *New J Chem* 2017;41:5040–54.
10. Chung YH, Sheng L, Xing X, Zheng L, Bian M, Chen Z, et al. A pure blue emitter (CIE_y≈0.08) of chrysene derivative with high thermal stability for OLED. *J Mater Chem C* 2015;1794–8. <https://doi.org/10.1039/c4tc02669a>.

11. Assaad THE, Auer M, Castaneda R, Hallal KM, Jradi FM, Mosca L, et al. Tetraaryl pyrenes: photophysical properties, computational studies, crystal structures, and application in OLEDs. *J Mater Chem C* 2016;3041–58.
12. Ishibashi JSA, Dargelos A, Darrigan C, Chrostowska A, Liu SY. BN Tetracene: extending the reach of BN/CC isosterism in acenes. *Organometallics* 2017;36:2494–7.
13. Levell JW, Ruseckas A, Henry JB, Wang Y, Stretton AD, Mount AR, et al. Fluorescence enhancement by symmetry breaking in a twisted triphenylene derivative. *J Phys Chem* 2010;114:13291–5.
14. Thomas KRJ, Kapoor N, Bolisetty MNKP, Jou JH, Chen YL, Jou YC. Pyrene fluorene hybrids containing acetylene linkage as color tunable emitting materials for organic light-emitting diodes. *J Org Chem* 2012;77:3921–32.
15. Ionkin AS, Marshall WJ, Fish BM, Bryman LM, Wang Y. A tetra-substituted chrysene: orientation of multiple electrophilic substitution and use of a tetra-substituted chrysene as a blue emitter for OLEDs. *Chem Commun* 2008:2319–22. <https://doi.org/10.1039/b715386d>.
16. Li A, Wena SH, Song JL, Deng WQ. Synthesis of cyanated tetracenes as the organic semiconductors. *Org Electron* 2009;10:1054–9.
17. Hirsch A. The era of carbon allotropes. *Nat Mater* 2010;9:868–71.
18. Mishra PC, Yadav A. Polycyclic aromatic hydrocarbons as finite size models of graphene and graphene nanoribbons: enhanced electron density edge effect. *Chem Phys* 2012;402:56–68.
19. Billing BK, Mayank, Agnihotri PK, Singh N. Development of pyrene-stacked carbon nanotube-based hybrid: measurement of NO_3^- ions using fluorescence spectroscopy. *Analyst* 2018: 3343–52. <https://doi.org/10.1039/c8an00286j>.
20. Meran M, Akkus PD, Kurkcuoglu O, Baysak E, Hizal G, Haciosmanoglu E, et al. Noncovalent pyrene-polyethylene glycol coatings of carbon nanotubes achieve in vitro biocompatibility. *Langmuir* 2018;34:12071–82.
21. Zhou Y, Fang Y, Ramasamy RP. Non-covalent functionalization of carbon nanotubes for electrochemical biosensor development. *Sensors* 2019;19:392.
22. Fujiwara Y, Amao Y. An oxygen sensor based on the fluorescence quenching of pyrene chemisorbed layer onto alumina plates. *Sensor Actuator B Chem* 2003;89:187–91.
23. Jiang Z, Zhang Y, Yu Y, Wang Z, Zhang X, Duan X, et al. Study on intercalations between double-stranded DNA and pyrene by single-molecule force spectroscopy: toward the detection of mismatch in DNA. *Langmuir* 2010;26:13773–9.
24. Jeon NJ, Lee J, Noh JH, Nazeeruddin MK, Gratzel M, Seok SI. Efficient inorganic–organic hybrid perovskite solar cells based on pyrene arylamine derivatives as hole-transporting materials. *J Am Chem Soc* 2013;135:19087–90.
25. Baheti A, Lee CP, Thomas KRJ, Ho KC. Pyrene-based organic dyes with thiophene containing π -linkers for dye-sensitized solar cells: optical, electrochemical and theoretical investigations. *Phys Chem Chem Phys* 2011:17210–21. <https://doi.org/10.1039/c1cp21714c>.
26. Salunke JK, Wong FL, Feron K, Manzhos S, Lo MF, Shinde D, et al. Phenothiazine and carbazole substituted pyrene based electroluminescent organic semiconductors for OLED devices. *J Mater Chem C* 2016;4:1009–18.
27. Wang XY, Wang JY, Pei J. BN heterosuperbenzenes: synthesis and properties. *Chem Eur J* 2014;20: 1–13.
28. Tasseroul J, Mercedes M, Garcia L, Dosso J, Simon F, Velari S, et al. Probing peripheral H-bonding functionalities in BN-doped polycyclic aromatic hydrocarbons. *J Org Chem* 2020;85:3454–64.
29. Farrell JM, Mutzel C, Bialas D, Rudolf M, Menekse K, Krause AM, et al. Tunable low-LUMO boron-doped polycyclic aromatic hydrocarbons by general one-pot C–H borylations. *J Am Chem Soc* 2019; 141:9096–10004.
30. Anthony JE. Functionalized acenes and heteroacenes for organic electronics. *Chem Rev* 2006;106: 5028–48.

31. Frisch MJ, Trucks JW, Schlegel HB, Scuseria GE, Robb MA, Cheeseman JR, et al. Gaussian 09, revision B.01. Wallingford CT: Gaussian, Inc.; 2010.
32. Saha B, Bhattacharyya PK. Understanding reactivity, aromaticity and absorption spectra of carbon cluster mimic to graphene: a DFT study. *RSC Adv* 2016;6:79768–80.
33. Sharma H, Deka BC, Saha B, Bhattacharyya PK. Understanding the structure, reactivity and absorption spectra of borazine doped pillar[5]arene: a DFT study. *Comput Theor Chem* 2018;1139: 82–9.
34. Koopmans, T. Über die Zuordnung von Wellenfunktionen und Eigenwerten zu den einzelnen Elektronen eines Atoms. *Physica* 1934;1:104–13.
35. Parr RG, Szentpaly LV, Liu S. Electrophilicity index. *J Am Chem Soc* 1999;121:1922–4.
36. Parr RG, Yang W. Density-functional theory of atoms and molecules. International Series of Monographs on Chemistry. New York: Oxford University Press; 1989.
37. Ahmed, S. Mushahary, BC. Kalita, DJ. Rational design of bay-annulated indigo (BAI)-Based oligomers for bulk heterojunction organic solar cells: a density functional theory (DFT) study. *ACS Omega* 2020;5:8321–33.
38. Schleyer PV, Maerker C, Dransfeld A, Jiao HJ, Hommes N. Nucleus-independent chemical shifts: a simple and efficient aromaticity probe. *J Am Chem Soc* 1996;118:6317–8.
39. Fabian J. TDDFT-calculations of Vis/NIR absorbing compounds. *Dyes Pigments* 2010;84:36–53.
40. Tomasi J, Mennucci B, Cammi R. Quantum mechanical continuum solvation models. *Chem Rev* 2005;105:2999–3094.
41. Sjoberg P, Politzer P. Use of the electrostatic potential at the molecular surface to interpret and predict nucleophilic processes. *J Phys Chem* 1990;94:3959–62.
42. Remya GS, Suresh CH. Quantification and classification of substituent effects in organic chemistry: a theoretical molecular electrostatic potential study. *Phys Chem Chem Phys* 2016;18:20615–26.
43. Phukan AK, Kalagi RP, Gadre SR, Jemmis ED. Structure, reactivity and aromaticity of acenes and their BN analogues: a density functional and electrostatic investigation. *Inorg Chem* 2004;43: 5824–32.
44. Robertson JM, White JG. The crystal structure of pyrene. A quantitative X-ray investigation. *J Chem Soc* 1947;1:358–68.
45. Duarte TMF, Mullen K. Pyrene-based materials for organic electronics. *Chem Rev* 2011;111: 7260–314.
46. Kathiravan A, Panneerselvam M, Sundaravel K, Pavithra N, Srinivasan V, Anandand S, et al. Unravelling the effect of anchoring groups on the ground and excited state properties of pyrene using computational and spectroscopic methods. *Phys Chem Chem Phys* 2016;13332–45. <https://doi.org/10.1039/c6cp00571c>.
47. Zhang G, Musgrave CB. Comparison of DFT methods for molecular orbital eigenvalue calculations. *J Phys Chem* 2007;111:1554–61.
48. Orucu H, Acar N. Effects of substituent groups and solvent media on pyrene in ground and excited states: a DFT and TDDFT study. *Comput Theor Chem* 2015;1056:11–8.
49. Schleyer PVR, Manoharan M, Wang ZX, Kiran B, Jiao H, Puchta R, et al. Dissected nucleus-independent chemical shift analysis of π -aromaticity and antiaromaticity. *Org Lett* 2001;3:2465–8.
50. Corminboeuf C, Heine T, Seifert G, Schleyer PVR, Weber J. Downfield proton chemical shifts are not reliable aromaticity indicators. *Phys Chem Chem Phys* 2004;6:273–6.
51. Ghosh D, Periyasamy G, Pati SK. Density functional theoretical investigation of the aromatic nature of BN substituted benzene and four ring polyaromatic hydrocarbons. *Phys Chem Chem Phys* 2011; 13:20627–36.
52. Taniguchi M, Lindsey JS. Database of absorption and fluorescence spectra of >300 common compounds for use in Photochem CAD. *Photochem Photobiol* 2018;94:290–327.

53. Sahoo GP, Das D, Sheet PS, Beg H, Moranb GS, Misra A. Morphology directing synthesis of 1-pyrenecarboxaldehyde microstructures and their photophysical properties. *RSC Adv* 2014;4: 10903–11.
54. Qiao Y, Zhang J, Xua W, Zhu D. Novel 2,7-substituted pyrene derivatives: syntheses, solid-state structures and properties. *Tetrahedron* 2011;67:3395–405.

Samuel Tetteh* and Albert Ofori

2 Effect of delocalization of nonbonding electron density on the stability of the M–C_{carbene} bond in main group metal-imidazol-2-ylidene complexes: a computational and structural database study

Abstract: The M–C_{carbene} bond in metal (M) complexes involving the imidazol-2-ylidene (Im) ligand has largely been described using the σ -donor only model with donation of σ electrons from the sp-hybridized orbital of the carbene carbon into vacant orbitals on the metal centre. Analyses of the M–C_{carbene} bond in a series of group IA, IIA and IIIA main group metal complexes show that the M-Im interactions are mostly electrostatic with the M–C_{carbene} bond distances greater than the sum of the respective covalent radii. Estimation of the binding energies of a series of metal hydride/fluoride/chloride imidazol-2-ylidene complexes revealed that the stability of the M–C_{carbene} bond in these complexes is not always commensurate with the σ -only electrostatic model. Further natural bond orbital (NBO) analyses at the DFT/B3LYP level of theory revealed substantial covalency in the M–C_{carbene} bond with minor delocalization of electron density from the lone pair electrons on the halide ligands into antibonding molecular orbitals on the Im ligand. Calculation of the thermodynamic stability of the M–C_{carbene} bond showed that these interactions are mostly endothermic in the gas phase with reduced entropies giving an overall $\Delta G > 0$.

Keywords: Cambridge structural database (CSD), density functional theory (DFT), imidazol-2-ylidenes, main group metal complexes

2.1 Introduction

N-heterocyclic carbenes (NHCs) have gained prominence as ubiquitous ligands in inorganic and coordination chemistry [1, 2]. These cyclic carbenes have at least one α -amino substituent and are highly nucleophilic with tuneable properties which have

*Corresponding author: Samuel Tetteh, Department of Chemistry, School of Physical Sciences, College of Agriculture and Natural Sciences, University of Cape Coast, Cape Coast, Ghana,
E-mail: samuel.tetteh@ucc.edu.gh. <https://orcid.org/0000-0002-8989-6346>

Albert Ofori, Department of Chemistry, School of Physical Sciences, College of Agriculture and Natural Sciences, University of Cape Coast, Cape Coast, Ghana

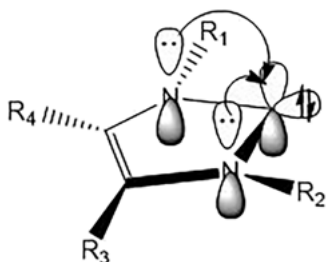
This article has previously been published in the journal *Physical Sciences Reviews*. Please cite as: S. Tetteh and A. Ofori "Effect of delocalization of nonbonding electron density on the stability of the M–C_{carbene} bond in main group metal-imidazol-2-ylidene complexes: a computational and structural database study" *Physical Sciences Reviews* [Online] 2021, 5. DOI: 10.1515/psr-2020-0084 | <https://doi.org/10.1515/9783110739763-002>

been explored in the synthesis of highly selective organometallic catalysts [3–5]. One of the most common NHCs used in catalysis is the five-membered ring, imidazol-2-ylidene (Im) (Scheme 2.1). It has an sp -hybridized carbon between two α -amino groups. Spectroscopically, both electrons on carbon-2 have been found to be localized in the sp -hybridized orbitals leaving the orthogonal $p\pi$ -orbital empty. This gives rise to an $A1$ term with the Im being a strong σ -donor ligand with little or no π^* -backbonding interactions [6]. This σ -electron-donating property allows for very strong M-Im bonds and prevents the decomposition of the formed organometallic compounds [3].

Another interesting property which makes Im ligands unique is the type of electronic stabilization provided by the nitrogen atoms. These σ -electron withdrawing and π -electron donating groups stabilize the electronic structure by inductively withdrawing electrons and lowering the energy of the occupied sp -orbital and simultaneously donating electron density into the empty $p\pi$ -orbital [1]. This stabilization of the sp -orbital also accounts for the σ -only donor ability of the Im ligands. Substituents such as R_1 , R_3 , R_4 and R_5 can also be varied to fine tune the kinetic and electronic stability of the Im ligand in the synthesis of transition metal catalysts [1, 7]. In a recent review [3], imidazole-2-ylidene functionalized ligands have been successfully applied as supporting ligands in the synthesis of catalysts employed in cyclization reactions, polymerization reactions, C–C bond formation and H_2 -mediated hydrogenation reactions.

Bonding in imidazol-2-ylidene complexes is predominantly ligand-to-metal σ -donation with low π^* -backbonding character [6]. Theoretical studies by Penka et al. involving a series of substituted Im group 10 metal complexes have shown that the σ -character in M-Im bonds is considerable stronger than the M-Py bond (where Py = pyridine). They also found a high σ/π ratio in the M-Im bond supporting the σ -donor nature of the M-Im bond in electron rich d metal centres.

The stability of main group and rare earth imidazol-2-ylidene complexes also provide ample evidence of their pure σ -donor character [8, 9]. A number of stable Im complexes of main group and rare earth Im complexes have been reported [9–11]. Natural bond orbital (NBO) analysis has also been used to confirm the view that Im ligands are purely σ -donors in these complexes [12, 13]. Crystallographic and NMR studies of a number of different adducts of N-substituted propylimidazole-2-ylidene



Scheme 2.1: Frontier molecular orbitals of imidazole-2-ylidene.

(IPr) with complexes of Mg, Ca, Sr and Ba have shown that whereas the IPr ligand binds to the metal centre by σ -donation, the M-Im distances were in the order (Mg-Im < Ca-Im < Ba-Im) indicating that the σ -interactions decrease down the group [6, 8]. However, this widely held notion of σ -only donor ability of these ligands is rapidly changing as Meyer et al. have shown that NHCs can accept electron density from electron rich group 11 metal species through a M-L π^* back-donation scheme [14, 15]. Molecular orbital analysis of [Ir(ImBu)₂]PF₆ shows a remarkable π -electron donation from the filled molecular orbital of the imidazol-2-ylidene ligand to empty d-orbitals of the Ir atom through a ligand to metal π -bonding scheme. This property of the Im ligand has been used to rationalize the unusual stability of the 14e complex [Ir(ImBu)₂]PF₆ [16]. Crystallographic studies by Abernethy et al. [17] on an Im adduct of trichloro-oxo- vanadium(V), a high oxidation-state transition-metal carbene complex with no d-electron for π^* -backbonding interactions have shown extremely stable bonding interactions between the C_{carbene} atom and neighbouring chloride ligands on the central vanadium ion. Density functional theory (DFT) calculations have proven that the interactions were mainly due to delocalization of *cis*-chloride electron density into the formally vacant π -orbital situated on the C_{carbene}. In view of the extreme stability of this adduct, the mode of bonding can be considered as a form of backbonding to the C_{carbene} with the electron density originating from lone pairs on the chloride ligands rather than the metal.

In a previous study, we reported the variation in the M-C_{carbene} bond length of a series of groups IA, IIA and IIA imidazole-2-ylidene complexes using crystallographic data obtained from the Cambridge structural database (CSD) [8]. It was observed that the average M-C_{carbene} bond length is largely insensitive to the coordination number around the metal centre but is largely controlled by electrostatic factors. In this current work, the stability of M-C_{carbene} bond will be assessed relative to the type of substituent (H, F, Cl) on the metal ion. As has been shown by Abernethy et al., there is a high probability of electron delocalization from nonbonding orbitals on the halide ion into the formally vacant π -orbital on the C_{carbene} thereby stabilizing the M-Im complex.

2.2 Methods

2.2.1 CSD Analyses

Substructure searches of the main-group metal-imidazol-2-ylidene complexes performed with version 5.40 of the Cambridge Structural Database (November 2018) + 1 update and *ConQuest* [18] version 2.1.0 are similar to those reported elsewhere [8] with minor modifications to the imidazol-2-ylidene ring as follows; one hydrogen atom was attached to each of the atoms except C2 (Scheme 2.1). This was done to prevent complexes with substituted imidazol-2-ylidene ligands from showing up in the retrieved data. The number of bonded atoms was also restricted to three, in agreement with the sp hybridization of the constituent atoms in the ring. The numbers of bonded atoms around the central atom were also restricted to the coordination number in each search. Secondary search criteria such as: 3D coordinates determined; no disorder in crystal structure; no errors; no polymeric structures; no powder structures

and only organometallic structures (according to standard CSD definitions) were also applied. The number of crystal structures retrieved and the respective coordination numbers of the metal complexes are given in Tables 2.1–2.3. Structure visualization and statistical analyses of the retrieved data were done with the CSD program *Mercury* [19] (version 4.1.0).

2.2.2 Computational Details

All calculations were conducted at the DFT level using the Gaussian 09 package [20]. The input and output files were visualized using the GaussView 5.0.8 molecular viewer [21]. The gas-phase structures were fully optimized using Becke's three parameter hybrid method and the Lee-Yang-Parr correlation functional (B3LYP) [22] with the 6-311G(d,p) split basis set to include diffuse functions on all atoms. All stationary points were characterized as minima by calculation of normal modes of vibration and all the complexes were in their ground states [8]. For each group of complexes, the central metal atom was varied accordingly with the substituent on the metal being H, F or Cl.

2.3 Results and discussion

Table 2.1 presents the coordination number (CN), number of entries retrieved from the CSD and the M–C_{carbene} bond lengths of the group IA complexes. Lithium-imidazol-2-ylidene complexes have the highest number (27 entries) with coordination numbers ranging from 2 to 6. More than half of the entries have the lithium ion tetracoordinated to the surrounding ligands. These complexes are largely employed as transmetallation agents in the synthesis of organometallic catalysts such as silver-NHCs [23].

Table 2.1: The coordination number (CN), number of hits and bond lengths of group IA metal-imidazol-2-ylidene complexes.

| Metal | CN | No. of Hits | Range D (M–Im) (Å) | Mean ± St.dev |
|-------|----|-------------|-----------------------|---------------|
| Li | 2 | 2 | 2.129–2.178 | 2.141 ± 0.020 |
| | 3 | 7 | 2.073–2.271 | 2.154 ± 0.056 |
| | 4 | 15 | 2.047–2.290 | 2.180 ± 0.063 |
| | 5 | 1 | | 2.110 |
| | 6 | 2 | 2.094–2.155 | 2.117 ± 0.027 |
| Na | 2 | 4 | 2.439–2.460 | 2.447 ± 0.007 |
| | 3 | 2 | 2.388–2.577 | 2.447 ± 0.074 |
| | 4 | 2 | 2.481–2.551 | 2.551 ± 0.036 |
| K | 2 | 5 | 2.810–3.199 | 2.924 ± 0.168 |
| | 3 | 2 | 2.986–3.029 | 3.008 ± 0.03 |
| | 4 | 1 | | 2.902 |
| | 5 | 2 | 2.921–3.128 | 3.024 ± 0.024 |
| | 6 | 1 | | 2.888 |
| | 7 | 1 | | 2.896 |
| | 9 | 1 | | 2.876 |

Table 2.2: The coordination number (CN), number of hits and bond lengths of group IIA metal-imidazol-2-ylidene complexes.

| Metal | CN | No. of Hits | Range D (M–Im) (Å) | Mean ± St.dev |
|-------|----|-------------|-----------------------|---------------|
| Be | 3 | 8 | 1.768–1.820 | 1.798 ± 0.019 |
| | 4 | 3 | 1.800–1.850 | 1.833 ± 0.019 |
| | 5 | 1 | | 1.765 |
| Mg | 3 | 7 | 2.238–2.288 | 2.257 ± 0.019 |
| | 4 | 20 | 2.187–2.285 | 2.225 ± 0.028 |
| | 5 | 1 | | 2.279 |
| Ca | 3 | 2 | 2.598–2.628 | 2.612 ± 0.021 |
| | 4 | 1 | | 2.644 |
| | 5 | 2 | 2.509–2.582 | 2.547 ± 0.020 |
| | 6 | 8 | 2.518–2.705 | 2.606–0.058 |
| | 7 | 2 | 2.565–2.702 | 2.619–0.045 |

Table 2.3: The coordination number (CN), number of hits and bond lengths of group IIIA metal-imidazol-2-ylidene complexes.

| Metal | CN | No. of Hits | Range D (M–Im) (Å) | Mean ± St.dev |
|-------|----|-------------|-----------------------|---------------|
| B | 2 | 1 | | 1.440 |
| | 3 | 50 | 1.514–1.621 | 1.538 ± 0.025 |
| | 4 | 86 | 1.515–1.710 | 1.618 ± 0.035 |
| | 5 | 11 | 1.526–1.641 | 1.620 ± 0.022 |
| | 6 | 1 | | 1.558 |
| Al | 3 | 1 | | 1.987 |
| | 4 | 45 | 1.964–2.163 | 2.055 ± 0.033 |
| | 5 | 3 | 2.070–2.130 | 2.095 ± 0.025 |
| | 6 | 2 | 2.170–2.198 | 2.185 ± 0.010 |
| Ga | 2 | 2 | 2.189–2.288 | 2.24 ± 0.055 |
| | 4 | 48 | 1.984–2.196 | 2.089 ± 0.053 |
| | 5 | 1 | | 1.978 |

The K–Im complexes have the most varied coordination numbers among the retrieved entries. These complexes are used as transmetallation agents for various transition metals including titanium, vanadium, zirconium and chromium [24, 25]. The coordination numbers range from two (linear) [8] to nine. The relatively large size of the K ion makes it possible to for complexes with varied ligands and different coordination modes including η interactions with π -systems and η with benzylic groups [23]. The mean K–C_{carbene} bond length however ranges from 2.888 to 3.024 Å. The sodium

complexes are in the minority with eight entries in the CSD as at the time of this research. The coordination numbers are two, three and four. These complexes are rare [23] and are used as transmetallation agents in the synthesis of dinuclear gold (I) NHC complexes [26]. The range of the average $\text{Na-C}_{\text{carbene}}$ bond lengths lie between those of $\text{Li-C}_{\text{carbene}}$ and $\text{K-C}_{\text{carbene}}$ as expected in relation to the change in cationic size down group IA. In general, the $\text{M-C}_{\text{carbene}}$ bond lengths are higher than the sum of the covalent radii of the constituent atoms ($\text{M-C} = 1.96 \text{ \AA}$, 2.34 \AA and 2.71 \AA for $\text{M} = \text{Li}$, Na and K) which support predominantly ionic interactions in these complexes [6].

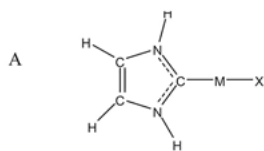
As shown in Table 2.2, a total of 55 group IIA imidazol-2-ylidene complexes were retrieved with varying coordination numbers from 3 to 7 around the metal centres. These compounds are rather scarce with most of the reported complexes concentrated on magnesium. They are usually employed as mild reducing agents due to the stabilizing properties of NHCs for low-valent main group element compounds [23]. The average $\text{M-C}_{\text{carbene}}$ bond length ranges from $1.765\text{--}1.833 \text{ \AA}$ in the Be compounds to $2.547\text{--}2.644 \text{ \AA}$ in the Ca complexes, a downward trend which is similar to those observed in the group IA metal complexes.

Again, the lengths of the $\text{M-C}_{\text{carbene}}$ bonds support the electrostatic interactions between the NHC ligands and the metal centres. This is due to the relatively longer distances of these bonds as compared to the covalent radii of the constituent atoms ($\text{M-C} = 1.64 \text{ \AA}$, 2.06 \AA and 2.44 \AA for $\text{M} = \text{Be}$, Mg and Ca).

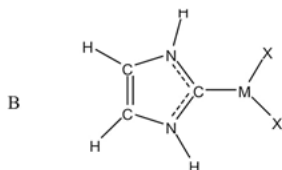
The high stability of group IIIA element compounds emanates from their incomplete octet electronic configurations. They form strong compounds with σ -donating Lewis bases such as amines, phosphines and carbenes due to their Lewis acidic nature. As shown in Table 2.3, a total of 251 entries were retrieved from the database with majority (149) of them being borane adducts with the most varied coordination numbers (from $\text{CN} = 2$ to $\text{CN} = 6$). Generally, the average bond lengths steadily increase down the group with the $\text{M-C}_{\text{carbene}}$ bonding interactions being predominantly electrostatic due to the increase in bonding distances relative to the sum of the covalent radii of the constituent atoms ($\text{M-C} = 1.51 \text{ \AA}$, 1.89 \AA and 1.90 \AA for $\text{M} = \text{B}$, Al and Ga).

The high number of group IIIA entries retrieved from the database could also be due to the fact that NHCs are good candidates for the stabilization of these molecular compounds in all of their possible oxidation states [23]. It can be seen that tetrahedral coordination is the most dominant geometry in the group IIIA compounds which suggests an sp hybridization of the central atoms [8].

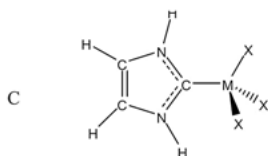
Figure 2.1 shows the structures of H, F and Cl substituted M-Im complexes that were theoretically investigated to understand the effect of nonbonding electrons on the stability of the $\text{M-C}_{\text{carbene}}$ bond. As demonstrated by Abernethy et al. [17], there is a high possibility of lone pair donation from chloride atoms on a high oxidation vanadium ion into the formally vacant $p\pi$ orbital on an N-heterocyclic carbene. This is akin to back-bonding interaction which contributes to a decrease in the $\text{M-C}_{\text{carbene}}$ bond length and hence the stability of the complex.



Im-LiH (M = Li, X = H); Im-LiF (M = Li, X = F); Im-LiCl (M = Li, X = Cl);
 Im-NaH (M = Na, X = H); Im-NaF (M = Na, X = F); Im-NaCl (M = Na, X = Cl);
 Im-KH (M = K, X = H); Im-KF (M = K, X = F); Im-KCl (M = K, X = Cl)



Im-BeH₂ (M = B, X = H); Im-BeF₂ (M = B, X = F); Im-BeCl₂ (M = B, X = Cl);
 Im-MgH₂ (M = B, X = H); Im-MgF₂ (M = B, X = F); Im-MgCl₂ (M = B, X = Cl);
 Im-CaH₂ (M = B, X = H); Im-CaF₂ (M = B, X = F); Im-CaCl₂ (M = B, X = Cl);



Im-BH₃ (M = B, X = H); Im-BF₃ (M = B, X = F); Im-BCl₃ (M = B, X = Cl);
 Im-AlH₃ (M = Al, X = H); Im-AlF₃ (M = Al, X = F); Im-AlCl₃ (M = Al, X = Cl);
 Im-GaH₃ (M = Ga, X = H); Im-GaF₃ (M = Ga, X = F); Im-GaCl₃ (M = Ga, X = Cl);

Figure 2.1: Structures of the (A) group IA, (B) group IIA and (C) group IIIA imidazol-2-ylidene complexes.

In Figure 2.1A, all the substituents on the central metal are *trans* to the M–C_{carbene} bond whereas in 1B, both substituents together with the M–C_{carbene} bond lie in a trigonal plane. However, in Figure 2.1C, one of the substituents lie in a position *cis* to the carbene, a configuration which makes it possible for donation of nonbonding electrons from the substituents into formally vacant p π orbitals of the carbene carbon. The effect of these differences on the M–C_{carbene} bond in different main-group metal-imidazol-2-ylidene complexes is given in Table 2.4.

Generally, the theoretically determined M–C_{carbene} bond lengths are similar to the crystallographically determined experimental values despite the fact that the geometries and coordination numbers of the experimentally determined complexes were not restricted as compared to the theoretically determined structures. It can be observed that for the group IA complexes, the M–C_{carbene} bond length of the chloride substituted

Table 2.4: Mean lengths (Å) of experimentally determined and theoretically calculated M–C bonds in the respective complexes.

| Metal | Experimental | Theoretical | | |
|-------|--------------|-------------|----------|----------|
| | | Hydride | Fluoride | Chloride |
| Li | 2.158 | 2.128 | 2.134 | 2.110 |
| Na | 2.460 | 2.549 | 2.515 | 2.495 |
| K | 2.938 | 3.071 | 2.825 | 2.842 |
| Be | 1.809 | 1.789 | 1.798 | 1.766 |
| Mg | 2.232 | 2.264 | 2.198 | 2.185 |
| Ca | 2.604 | 2.563 | 2.580 | 2.494 |
| B | 1.604 | 1.591 | 1.665 | 1.613 |
| Al | 2.069 | 2.089 | 2.041 | 2.041 |
| Ga | 2.070 | 2.112 | 2.046 | 2.049 |

complexes were the shortest. With the lithium complex for example, the Li–C bond is 2.128 Å for the hydride followed by an increase to 2.134 Å for the fluoride and a decrease to 2.110 Å for the chloride. In the case of sodium, the Na–C bond length is 2.549 Å for the hydride, 2.515 Å for the fluoride and 2.495 Å for the chloride. Similar trends can be observed in the groups IIA and IIIA complexes.

2.3.1 Binding energy

The binding energies of the gas-phase optimized structures were also estimated at the DFT/B3LYP level with diffuse functions added to reduce the basis set superposition error (BSSE). This was done to minimize the overestimation of the binding energy as a result of each fragment utilizing the basis sets of other fragments in the complex [27]. The BSSE of all the complexes was corrected by the method of counterpoise correction introduced by Boys and Bernardi [28]. The counterpoise corrected binding energy (ΔE_{BE}^{CP}) is the difference between the corrected total energy of the optimized complex ($E_{Complex}^{CP}$) and that of the constituent fragments (E_1 and E_2 ; where 1 and 2 represent the imidazol-2-ylidene ligand and the metal hydride/halide respectively)

$$\Delta E_{BE}^{CP} = \Delta E_{Complex}^{CP} - (E_1 + E_2) \quad (2.1)$$

From Equation (2.1), a more negative binding energy gives a more stable complex. Generally, the interaction between the Im and the metal centres have been proposed to be purely ionic with σ -electron donation into vacant orbitals on the central metal ion and insignificant backbonding electron donation onto the imidazol-2-ylidene ligand.

From table 2.5, the binding energy of the hydrides of group IA complexes is in the order Li > Na > K. this order is similar to the electrostatic energy of interaction in these

ions which supports the purely ionic interactions reported for these complexes [23]. In the fluorides and chlorides however, the binding energies are in the order $\text{Li} > \text{Na} < \text{K}$ which suggests that whereas the interactions involving lithium or sodium halides and the Im ligand could be purely electrostatic, there could be other factors influencing the high stability of the potassium halide imidazol-2-ylidene complexes. These variations in binding energies can also be observed in the fluorides of group IIA complexes with values of -38.28 , -38.28 and -30.12 kcal/mol for Be, Mg and Ca respectively. Other values reported for group IIIA chloride complexes include -45.2 , -51.5 and -47.7 kcal/mol for B, Al and Ga respectively.

2.3.2 Natural bond orbital (NBO) analyses

To better understand the contributing factors involved in the high stability of these halide complexes, second-order perturbation analysis of the Fock matrix was evaluated to estimate the level of interaction between occupied (donor) orbitals and formally vacant orbitals. The higher the stabilization energy, the greater the delocalization of electron density from the donor orbitals into the acceptor orbitals. The stabilization energy ($E(2)$) for each donor(i) and acceptor(j) is given as (Equation (2.2))

$$E(2) = \Delta E_{ij} = q_i \frac{F(i, j)^2}{\epsilon_j - \epsilon_i} \quad (2.2)$$

Where q_i is the donor orbital occupancy and ϵ_j and ϵ_i are diagonal elements and $F(i, j)$ is the off diagonal natural bond orbital (NBO) Fock matrix elements. The NBO analyses show that the $\text{M}-\text{C}_{\text{carbene}}$ bond involving the group IA complexes is purely electrostatic with stabilization energies of 35.38 , 35.38 and 33.25 kcal/mol for the complexes involving the hydride, fluoride and chloride of lithium respectively where the donor orbitals are the sp orbitals on the carbene carbon with empty LP^* orbitals on the central

Table 2.5: Binding energies (kcal/mol) of the respective complexes.

| Metal | Hydride | Fluoride | Chloride |
|-------|---------|----------|----------|
| Li | -27.04 | -28.86 | -30.1 |
| Na | -17.21 | -20.08 | -22.6 |
| K | -10.88 | -26.98 | -23.2 |
| Be | -35.59 | -38.28 | -45.2 |
| Mg | -26.35 | -38.28 | -40.8 |
| Ca | -30.75 | -30.12 | -37.7 |
| B | -52.71 | -32.63 | -45.2 |
| Al | -38.28 | -52.71 | -51.5 |
| Ga | -32.63 | -52.71 | -47.7 |

lithium being the acceptor orbitals. Lower stabilization energies of 13.14, 12.85 and 16.13 kcal/mol were reported in the case of the respective sodium complexes. In the case of the potassium complexes, the stabilization energies were 8.15, 8.42 and 9.32 kcal/mol respectively. These trends in stabilization energy correspond to the order of the strength of the $M-C_{\text{carbene}}$ bond length shown in Table 2.1 which increases down the group as a result of the weakening electrostatic interactions between the metal ions and the carbene carbon. Besides these σ -donor interactions involving the carbene carbon and the central metal ions, there were substantial delocalizations of nonbonding lone pair electrons from the fluoride and chloride substituents into antibonding (H2–N8) orbitals on the Im ligand in the potassium complexes. The stabilization energies of these interactions were calculated to be 53.08 and 13.44 kcal/mol for the respective potassium fluoride and chloride complexes. These added back bonding interactions can augment the carbene-to-metal σ -donation to increase the binding energy of the potassium halide complexes as reported in table 2.5. The Be–C bond in the beryllium hydride complex is predominantly polar covalent with bond polarity of 84.14% C and 15.86% Be. In the Mg and Ca complexes however, the $M-C_{\text{carbene}}$ bonds were purely electrostatic with bond stabilization energies of 57.49, 61.74 and 70.13 kcal/mol respectively for the magnesium hydride, fluoride and chloride complexes with minor delocalization of nonbonding electron density from the chloride into the empty antibonding (C1–N8) orbitals on the imidazol-2-ylidene ligand. Results of the NBO analyses of the $M-C_{\text{carbene}}$ bond in the group IIIA complexes show that these bonds are covalent with substantial ionic bond character down the group. Bond polarities of 68.46% C and 31.56% B; 73.06% C and 26.94% B; 69.95% C and 30.05% B were recorded for the respective hydride, fluoride and chloride complexes of boron: 84.70% C and 15.30% Al; 87.26% C and 12.74% Al; 84.44% C and 15.56% Al for the aluminium hydride, fluoride and chloride complexes: 82.15% C and 17.85% Ga; 85.47% C and 14.56% Ga; 81.44% C and 18.56% Ga for the respective gallium complexes. There were minor delocalization of lone pair electrons into antibonding orbitals (BD*) on the respective Im ligands with interaction energy of 0.58 kcal/mol involving LP(3) on Cl and BD*(C1–N9) in the aluminium chloride complex.

2.3.3 Thermodynamic stability

The strength of the interactions was further analysed by determining the free energy change ΔG at 298.15 K. According to the Gibbs energy relation, the free energy change of a thermodynamic process at a given temperature, T , is given as

$$\Delta G = \Delta H - T\Delta S \quad (2.3)$$

Where ΔH is the enthalpy change and ΔS is the entropy change for the process. For a spontaneous change ΔG is negative which implies that exothermic processes with entropy changes greater than zero(0) are always spontaneous. However, a process can be endothermic with relatively high $T\Delta S$ value to make it spontaneous. Therefore, a

Table 2.6: Computed thermodynamic properties for the gas-phase complexes (ΔH and ΔG in kcal mol⁻¹, ΔS in kcal mol⁻¹ K⁻¹).

| | Hydride | | | Fluoride | | | Chloride | | |
|----|------------|------------|------------|------------|------------|------------|------------|------------|------------|
| | ΔH | ΔS | ΔG | ΔH | ΔS | ΔG | ΔH | ΔS | ΔG |
| Li | 1.52 | -0.02 | 8.14 | 0.88 | -0.03 | 10.46 | 1.58 | -0.02 | 8.75 |
| Na | 1.26 | -0.02 | 8.27 | 0.73 | -0.03 | 9.83 | 1.37 | -0.02 | 8.56 |
| K | -0.09 | -0.03 | 8.93 | 0.21 | -0.03 | 9.94 | 1.04 | -0.03 | 10.33 |
| Be | 1.82 | -0.03 | 10.96 | 1.25 | -0.04 | 12.18 | 2.31 | -0.02 | 9.57 |
| Mg | 0.85 | -0.03 | 10.62 | 1.04 | -0.04 | 11.76 | 1.09 | -0.04 | 11.94 |
| Ca | 2.06 | -0.03 | 10.37 | 2.04 | -0.02 | 8.78 | 0.96 | -0.04 | 12.27 |
| B | 2.61 | -0.03 | 12.99 | 1.66 | -0.04 | 12.74 | 2.22 | -0.04 | 13.21 |
| Al | 1.26 | -0.04 | 12.36 | 2.02 | -0.04 | 12.77 | 1.55 | -0.04 | 13.63 |
| Ga | 1.68 | -0.03 | 11.87 | 1.43 | -0.04 | 13.14 | 1.53 | -0.04 | 13.89 |

balance between the enthalpy and entropy changes is key in determining the spontaneity of a reaction. For gas-phase complexes, ΔG is often positive as a result of the relatively large negative values of $T\Delta S$ [29].

As shown in Table 2.6, almost all the processes, with the exception of the formation of the potassium hydride imidazol-2-ylidene complex, are endothermic with ΔH values ranging from 0.85 to 2.31 kcal/mol. There was however, an overall decrease in entropy with ΔS values ranging from -0.02 to -0.04 kcal mol⁻¹ K⁻¹. This reduced entropy of the interactions is as a result of constraints in the freedom of motion with some diminished rotational and translational degree of freedom introduced during the formation of the complexes [30]. For an endothermic process with reduced entropy, the change in Gibbs free energy is always positive and such processes are nonspontaneous at all temperatures. It can be observed from Table 2.6 that the combined enthalpy/entropy effect makes the overall $\Delta G > 0$ meaning that these processes are nonspontaneous in the gas phase.

2.4 Conclusions

This work used a combined crystallographic and density functional theory (DFT) calculations to investigate the M-Ccarbene bond in a series of main group metal imidazol-2-ylidene complexes. A total of 356 entries with at least one imidazol-2-ylidene ligand coordinated to the metal centre were retrieved from the Cambridge Structural Database (CSD) by doing a substructure search using *ConQuest* version 2.1.0. Majority (251) of the candidates were group IIIA metal complexes and the coordination number around the metal centres varied from 2 to 9. The M-Ccarbene bond lengths were higher than the covalent radii of the respective metal and carbene carbon suggesting

predominantly electrostatic interactions. Natural bond orbital (NBO) analysis of a series of metal substituted hydride/halide imidazol-2-ylidene complexes further confirmed a purely electrostatic interaction involving the group IA complexes but the covalent character of the M-Ccarbene bond increases across the period being predominantly polar covalent of varying degrees. Estimation of the thermodynamic stability of the M-Ccarbene bond showed that these processes are mostly endothermic in the gas phase with reduced entropies giving an overall $\Delta G > 0$.

Acknowledgements: The authors would like to thank the organizers of the virtual conference on chemistry and its applications (VCCA-2020) for the opportunity to present this work. ST is grateful to the FAIRE program of the Cambridge Crystallographic Data Centre (CCDC) for the opportunity to use the Cambridge Structural Database (CSD) for substructure searches, molecular visualization and statistical analysis.

Author contributions: All the authors have accepted responsibility for the entire content of this submitted manuscript and approved submission.

Research funding: None declared.

Conflict of interest statement: The authors declare that there is no conflict of interest regarding the preparation and publication of this manuscript.

References

1. Hopkinson MN, Richter C, Schedler M, Glorius F. An overview of N-heterocyclic carbenes. *Nature* 2014;510:485–96.
2. Herrmann WA, Koecher C. N-Heterocyclic carbenes. *Angew Chem Int Ed Engl* 1997;36:2162–87.
3. Díez-González S, Marion N, Nolan SP. N-heterocyclic carbenes in late transition metal catalysis. *Chem Rev* 2009;109:3612–76.
4. Bellemin-Laponnaz S, Despagnet-Ayoub E, Díez-González S, Gade L, Glorius F, Louie J, et al. N-heterocyclic carbenes in transition metal catalysis. *Top Organomet Chem* 2004;21.
5. Marion N, Nolan SP. N-Heterocyclic carbenes in gold catalysis. *Chem Soc Rev* 2008;37:1776–82.
6. Jacobsen H, Correa A, Poater A, Costabile C, Cavallo L. Understanding the M (NHC)(NHC= N-heterocyclic carbene) bond. *Coord Chem Rev* 2009;253:687–703.
7. Nolan SP. N-Heterocyclic carbenes in synthesis. Weinheim: John Wiley & Sons; 2006.
8. Tetteh S. A computational and structural database study of the metal-carbene bond in groups IA, IIA, and IIIA imidazol-2-ylidene complexes. *J Chem* 2019;2019:9.
9. Schumann H, Gottfriedsen J, Glanz M, Dechert S, Demtschuk J. Metallocenes of the alkaline earth metals and their carbene complexes. *J Organomet Chem* 2001;617:588–600.
10. Nakai H, Tang Y, Gantzel P, Meyer K. A new entry to N-heterocyclic carbene chemistry: synthesis and characterisation of a triscarbene complex of thallium (I). *Chem Commun* 2003:24–5.
11. Schumann H, Glanz M, Gottfriedsen J, Dechert S, Wolff D. Lewis-acidic organometallic compounds of the lanthanides and the alkaline earth metals as catalysts for the activation of carbonyl groups. *Pure Appl Chem* 2001;73:279–82.
12. Fröhlich N, Pidun U, Stahl M, Frenking G. Carbenes as pure donor ligands: theoretical study of Beryllium– carbene Complexes¹. *Organometallics* 1997;16:442–8.

13. Doddi A, Peters M, Tamm M. N-heterocyclic carbene adducts of main group elements and their use as ligands in transition metal chemistry. *Chem Rev* 2019;119:6994–7112.
14. Hu X, Tang Y, Gantzel P, Meyer K. Silver complexes of a novel tripodal N-heterocyclic carbene ligand: evidence for significant Metal– carbene π -interaction. *Organometallics* 2003;22:612–4.
15. Hu X, Castro-Rodriguez I, Olsen K, Meyer K. Group 11 metal complexes of N-heterocyclic carbene ligands: nature of the metal carbene bond. *Organometallics* 2004;23:755–64.
16. Cavallo L, Correa A, Costabile C, Jacobsen H. Steric and electronic effects in the bonding of N-heterocyclic ligands to transition metals. *J Organomet Chem* 2005;690:5407–13.
17. Abernethy CD, Codd GM, Spicer MD, Taylor MK. A highly stable N-heterocyclic carbene complex of trichloro-oxo-vanadium (V) displaying novel Cl– Ccarbene bonding interactions. *J Am Chem Soc* 2003;125:1128–9.
18. Bruno IJ, Cole JC, Edgington PR, Kessler M, Macrae CF, McCabe P, et al. New software for searching the Cambridge Structural Database and visualizing crystal structures. *Acta Crystallogr Sect B Struct Sci* 2002;58:389–97.
19. Macrae CF, Edgington PR, McCabe P, Pidcock E, Shields GP, Taylor R, et al. Mercury: visualization and analysis of crystal structures. *J Appl Crystallogr* 2006;39:453–7.
20. Frisch M, Trucks G, Schlegel H, Scuseria G, Robb M, Cheeseman J, et al. Gaussian 09, Revision A. 1 [computer software]. Wallingford, CT, USA: Gaussian; 2009.
21. Frisch A, Nielson A, Holder A. User manual GaussView. Pittsburgh, PA: Gaussian Inc; 2000.
22. Becke AD. Density-functional exchange-energy approximation with correct asymptotic behavior. *Phys Rev* 1988;38:3098.
23. Nesterov V, Reiter D, Bag P, Frisch P, Holzner R, Porzelt A, et al. NHCs in main group chemistry. *Chem Rev* 2018;118:9678–842.
24. Downing SP, Danopoulos AA. Indenyl-and fluorenyl-functionalized N-heterocyclic carbene complexes of titanium and vanadium. *Organometallics* 2006;25:1337–40.
25. Downing SP, Guadano SC, Pugh D, Danopoulos AA, Bellabarba RM, Hanton M, et al. Indenyl-and fluorenyl-functionalized N-heterocyclic carbene complexes of titanium, zirconium, vanadium, chromium, and yttrium. *Organometallics* 2007;26:3762–70.
26. Martínez-Martínez AJ, Fuentes MÁ, Hernán-Gómez A, Hevia E, Kennedy AR, Mulvey RE, et al. Alkali-metal-mediated magnesiations of an N-heterocyclic carbene: normal, abnormal, and “paranormal” reactivity in a single tritopic molecule. *Angew Chem* 2015;127:14281–5.
27. Esrafil MD. Characteristics and nature of the intermolecular interactions in boron-bonded complexes with carbene as electron donor: an ab initio, SAPT and QTAIM study. *J Mol Model* 2012; 18:2003–11.
28. Boys SF, Bernardi F. The calculation of small molecular interactions by the differences of separate total energies. Some procedures with reduced errors. *Mol Phys* 1970;19:553–66.
29. Politzer P, Murray JS, Clark T. Halogen bonding and other σ -hole interactions: a perspective. *Phys Chem Chem Phys* 2013;15:11178–89.
30. Searle MS, Williams DH. The cost of conformational order: entropy changes in molecular associations. *J Am Chem Soc* 1992;114:10690–7.

Liliana Mammino*

3 Educational components in the supervision of chemistry postgraduate students: experiences and reflections

Abstract: This article focuses on the educational aspects of mentoring chemistry postgraduate students, analysing the challenges encountered by students in the transition from undergraduate to postgraduate learning, and throughout the postgraduate projects up to completion of PhD level, and discussing the design of suitable addressing options by the mentor. The mentoring activity is thus viewed within a typical chemistry education paradigm. Some challenges basically continue those encountered at undergraduate level and others are specific to the postgraduate one, thus requiring new approaches. The information presented in the article is mostly based on the author's long experience at the University of Venda (South Africa). The approach utilised in the study is a suitable adaptation of action research. The analysis aims at being comprehensive, considering the major features influencing students' performance, and the strategies that can be adopted to counteract negative impacts and to foster the development of scientific modes of thinking and of research independence. It outlines how known major difficulties, such as diffuse poor language mastery (aggravated by second language instruction), complicate both the undergraduate-postgraduate transition—by affecting the speed and extent to which students learn new approaches—and the further stages, including thesis writing. Writing-related difficulties are given particular attention because they have great impact even for students who have acquired good abilities with the design and practical components of research projects, and because the acquisition of adequate skills in scientific writing is an inherent objective of postgraduate training. Most of the reported observations refer to postgraduate studies in computational chemistry; this enables a broad perspective, by including the common challenges of obtaining, organising and analysing data, as well as the challenges related to learning a new area of chemistry, not encountered in undergraduate studies, and those related to specific demands such as adequate mathematics knowledge, visualization abilities and the ability to abstract thinking.

Keywords: chemistry education, design of research project, language mastery, postgraduate chemistry studies, systems thinking, writing abilities

*Corresponding author: Liliana Mammino, School of Mathematical and Natural Sciences, University of Venda, Thohoyandou, South Africa, E-mail: sasdestria@yahoo.com

This article has previously been published in the journal *Physical Sciences Reviews*. Please cite as: L. Mammino "Educational components in the supervision of chemistry postgraduate students: experiences and reflections" *Physical Sciences Reviews* [Online] 2021, 5. DOI: 10.1515/psr-2020-0116 | <https://doi.org/10.1515/9783110739763-003>

3.1 Introduction

3.1.1 Background information

The formal education and learning process continues as long as a young person is learning, from all the levels of pre-university and undergraduate instruction to the end of postgraduate studies. Different stages have different requirements. The corresponding educational approaches need to be tuned to the characteristics of each stage and of the given group of learners.

The main question of the educational endeavour—at all levels—is how to design and implement approaches that can ensure the best responses and the best results from students. The main objective of postgraduate studies is for students to learn how to do research. The supervision of postgraduate students is mainly tuned to this objective; while doing so, it also constitutes an undertaking continuing and advancing the education of the previous levels, above all in terms of acquisition or enhancement of relevant abilities.

Educational studies for advanced levels of instruction are not frequent; not many studies focus on the advanced chemistry courses of the undergraduate level, and studies focusing on the postgraduate level are even rarer. The current article aims at offering a comprehensive picture of educational questions related to chemistry postgraduate studies and at outlining implementable options. The considered questions stem from diagnoses about the challenges encountered by students. The content is based on the author's more-than-20-years' experience at the University of Venda (UNIVEN), where she has dominantly taught concept-based courses (the first year general chemistry and all the undergraduate and postgraduate physical chemistry courses), and mentored postgraduate students choosing computational chemistry projects.

UNIVEN is a Historically Black University located in a rural area in the North-East of South Africa. The levels of instruction comprise a 3-year B.Sc. degree (undergraduate), and three postgraduate levels, namely B.Sc. Honors (Hons), M.Sc. and Ph.D., with expected durations of one, two and three years respectively. The Hons level marks the transition from undergraduate to postgraduate studies; it includes both standard courses with final exams (aimed at advancing content knowledge in inorganic, organic, analytical and physical chemistry) and a simple research project; it is also the level where students are expected to learn all the components of how to do research. M.Sc. and Ph.D. studies are fully research-based. When their project is complete, Hons. students write a mini-thesis, and M.Sc. and Ph.D. students write a thesis; furthermore, M.Sc. students are expected to write an article in the final stage of their project, and Ph.D. students are expected to write two articles during the three years.

3.1.2 Continuity aspects and novel components in postgraduate mentoring

The postgraduate level educational paradigm comprises continuity and novel aspects with respect to the undergraduate one. Continuity aspects include the need to advance abilities which have not been fully acquired in the undergraduate stage, but constitute essential instruments in postgraduate studies, such as language mastery, logic mastery and abstract reasoning. Novel components are all the components related to learning how to do research.

Learning how to do research involves content-related components (acquiring additional content knowledge that is not part of the undergraduate and Hons courses) and clear attention to the specificities of the selected research area. It also involves fundamental attitude changes: from expecting that the teacher can provide all the answers (as normal for the questions in standard assessment instruments) to acknowledging and internalising that research is a shared task, where the mentor provides guidance, but neither the student nor the mentor knows the answers *a priori*.

An inherent component of the research task is the ability to identify the interconnections among different pieces of information, in order to build a comprehensive and articulated picture of the project and its results; this can be viewed in terms of systems thinking [1–3] and, therefore, in terms of guiding the student to develop adequate systems thinking abilities. Other novel objectives of a mentor's guidance, typical of postgraduate studies, include fostering increasing independence from the student, through carefully planned combinations of suggestions prompting the student to build further steps, and straightforward assistance when needed. They also include expanding the student's scope beyond his/her theme, to ensure readiness to cross-disciplinary tasks, as this is very important in modern research and production activities. An example of the latter is the stimulation of basic familiarization of computational chemistry students with the possible needs of green chemistry research and of green chemistry students with the design potentialities of computational chemistry [4]. The participation of UNIVEN computational chemistry postgraduate students in the IUPAC-endorsed *Summer Schools on Green Chemistry* has proved a fruitful option to this purpose.

3.1.3 General and specific features of learning how to do research in computational chemistry

As already mentioned, the author's direct experience relates to postgraduate studies involving computational chemistry projects. Additional information stems from exchanges of observations and analyses with colleagues running projects in other chemistry areas, in various universities.

The fact that most of the observations and analyses reported in the current work refer to computational chemistry postgraduate studies does not constitute a limitation, or a generality loss. Computational chemistry projects involve the same major challenges as the other areas of chemistry, such as learning how to obtain, organise and analyse data and how to present the obtained results; in addition, they involve specific challenges such as the presence of greater demands in terms of conceptual understanding, mathematics mastery, visualization abilities and abstract thinking abilities. They can, therefore, be considered ideal to comprehensively highlight the challenges of postgraduate chemistry studies and their details, because they can unveil a broader range of them. Furthermore, the fact that, at UNIVEN, only the best-performing students consider computational chemistry as a possible option for their postgraduate studies contributes to single out challenges that will be experienced by a large majority of students (if a best-performing student experiences them, the probability that other students experience them is high).

A computational chemistry project is based on concepts not encountered in undergraduate courses, as the quantum chemistry course has so far been offered at Hons level at UNIVEN. Thus, the postgraduate level also entails the challenges inherent in learning a new area of chemistry. A Hons student doing a computational chemistry project learns the theoretical foundation while already engaging in the project-related research. Even a simple postgraduate project (like the Hons ones) entails broader conceptual knowledge than that provided by the quantum chemistry course. Consequently, mentoring requires extensive contact time for the student to be in a position to learn the new material rapidly enough to use it in the project.

Because of its nature, computational chemistry demands deep conceptual understanding at every stage of the learning or research process. Learning how to use computational software is easy. The crucial components involve clear identification of what one wants to find and of the approaches available to search for it, and clear understanding of the nature of the obtained results. These components also necessitate extensive student-mentor contact time.

3.2 Approaches selected for educational research focusing on the postgraduate level

Educational research focusing on the postgraduate level is inherently different from that concerning the undergraduate one, in terms of both investigation objects and investigation approaches. The difference is determined first of all by the fact that research projects are individual, different for different students. Furthermore, postgraduate learning involves the acquisition of skills of a more holistic nature, as outlined more explicitly in section 3.3.1. The mentor needs to continuously assess a student's progress, in order to provide guidance specifically-tuned to the student's

progress at a given stage, but the assessment needs to respond to the holistic nature of the skills that the student is gradually acquiring. There are no assessment tools comparable to tests and assignments: the assessment stems from the student-mentor interactions. Likewise, educational research cannot rely on something similar to the analysis and comparison of the answers provided by the students of a given group to a specific question, or set of questions (as common for educational studies concerning undergraduate or pre-university levels). Furthermore, some features that are crucial at the postgraduate level are not easy to verify or analyse in a standardised manner (e.g., by defining references or parameters); a clear example is the fostering-independence objective. As a result, educational research concerning the postgraduate level is necessarily qualitative, focusing on the identification of problems and the design of options aimed at addressing them. It aims at responding to the mentor's question "how to provide the best guidance?" and it is based on observations within the experiences of the joint student-mentor work (as also recalled in the title of this article).

The author has been using an action research [5] approach for all her educational research [6], whether for undergraduate courses or for postgraduate supervision. The methodology is apt to support extensive integration of educational research and continuous improvement of teaching approaches; in other words, it is the most suitable strategy for the purpose of using observations and their analysis to improve teaching or mentoring approaches, and to do it with a broad scope (a scope extending to the entire content of a given course for the undergraduate level, and to the entire project and abilities-acquisition for the postgraduate one).

Action research has wide-ranging "experimental" character, if one bases it on direct observations of students' responses in the class and on the evidence provided by students' written works [6]. It enables a holistic approach, since the analysis of responses and evidence is not limited to one or few narrowly-selected issues, but extends to all the aspects characterising a specific learning-topic. Its recursion character makes it suitable for continuous optimisation of the ways a teacher interacts with the students, presents a certain material and guides them to understand it, or guides a postgraduate student through a research project.

The recursion character of action research can be summarised through the steps of its «research + implementation» loop; these, in turn, are more clearly expressed through an instruction-type wording, as if they were instructions in a flow chart describing the loop [6]:

1. identify difficulties encountered by students
2. investigate their details
3. make reasonable guesses about their causes
4. design approaches to address identified problems
5. implement the approaches
6. pay keen attention to students' responses and identify encountered difficulties

7. make reasonable guesses about their causes, distinguishing the pre-existing ones (like those identified in steps 1–3) and those that might highlight weaknesses in the newly-design approaches or their implementation
8. design improved approaches
9. go to step 5 and proceed with a new loop

For the postgraduate level, this loop can be applied to the mentoring of a new student with respect to previous ones, as well as to the mentoring of the same student through subsequent stages or operations, as his/her project progresses.

All the observations reported in the next sections, as well as the outlined addressing options, are the outcomes of action research. It may also be quickly mentioned that the author refrains from the use of questionnaires on ethical bases [7], and this further motivates the adoption of an approach based on professional observations within the learning-context reality.

3.3 Mentoring and learning in postgraduate studies

3.3.1 The main operations in postgraduate work

Different components of postgraduate work present different levels of difficulties and pose different challenges to students. The main operations involved in the conduction of a postgraduate project can be summarised as follows:

1. literature review;
2. project design and preparation of a research proposal;
3. performing the planned activities, both in terms of practical procedures and in terms of reporting, organizing and analysing data;
4. preparation of presentations (e.g., reporting about the progress achieved at a certain stage, or a conference presentation);
5. writing (with various objects: the project proposal; the final report or thesis; articles for publication).

These operations are considered individually in the next subsections.

The term “operations” is not used here to imply a time sequence, but to define types of tasks. Some operations (such as the literature review) pertain mostly to a project initial stages; others, such as writing, are relevant for different actions in different stages. Students may have already acquired partial familiarity with some of these operations, but the mastery-level required for postgraduate studies is substantially greater than for the undergraduate level. Attaining such mastery level is an inherent component of postgraduate learning, and the mentor’s monitoring is essential to guide the acquisition.

3.3.2 The literature review operation

The search for articles relevant to the project (literature review) is carried out on the Internet, and students are very familiar with online searches. The main difficulties concern the selection of articles that are actually pertinent to the given project and the identification of the relationships between the contents of those articles and the details of the project. Selection and identification involve basic systems thinking and rely on prior generation of sufficiently clear ideas about the major features of the project, which, in turn, rely on the mentor's guidance.

Guidance is also crucial to train students to recognise and avoid articles from non-reputable sources, and to recognise conceptual errors that might be present in some sources. The latter is not an easy task, because it requires sufficiently strong conceptual knowledge, which students may not always possess, above all in the early stages of postgraduate studies. Furthermore, students tend to take for granted that whatever is available on the Internet has to be correct, and articulated and detailed explanations are needed to convince them that certain things—although present in an apparently reliable source—are not correct. An example is the “moles of solution” term, found in more than one Internet source; the explanation needs to recall the nature of the mol as the unit of the amount of substance, and the fact that a solution, by definition, does not consist of only one substance. Another example, found by some students in a source that appeared reliable, concerned an illustration (Figure 3.1) regarding the concept of radial probability density in the hydrogen atom, which is defined as the probability of finding the electron in the volume between two spheres with radiuses r and $r + dr$; the direction of the dr increment in the drawing reported in that source was not correct (it should be the same as for r). Events like these offer suitable opportunities to stress the importance of acquiring conceptual knowledge to be able to evaluate encountered materials and recognise possible errors. They also favour the development of critical thinking as an attitude for which the student is encouraged to verify everything against what he/she already knows, and to analyse and discuss discrepancies.

The challenges related to writing the literature review component in a thesis are discussed in section 3.3.6.

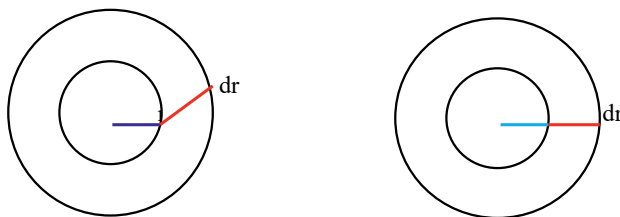


Figure 3.1: Incorrect drawing of the infinitesimal increment dr (left) and correct one (right). The length of dr is exaggerated to better visualise the problem.

3.3.3 Designing a project

The design of a project, and the preparation of the associated proposal, implies the identification of objectives and of what needs to be done to pursue them, both in terms of practical operations and in terms of organizing and analysing obtained data. Thus, the design entails the ability to recognise all the components of the project and their mutual relationships; this, in turn, requires systems thinking for the student to interconnect the components and build the entire picture.

The design may present different levels of difficulties, depending on the familiarity that students have already acquired with the major practices of the selected area of chemistry. It is often easier for projects involving experimental work, because of the familiarization with practical work in the undergraduate courses, although further guidance may be needed, e.g., for the design of synthesis procedures.

The design of a computational chemistry project is more challenging because the underpinning knowledge is mostly new for the students. It requires a variety of reflections on the molecules of interest and on the objectives of the study. One of the crucial issues is the selection of a number of molecules that is adequate for reliable pattern identification and for the possibility of making realistic conclusions. Another crucial issue is the selection of the level of theory for the calculations, requiring reasonable balance between results' accuracy and computational costs involved. The mentor's guidance needs to find a sound balance between direct provision of conceptual information (what is tantamount to teaching) and guiding the student to search for other information, understand its meaning and make inferences pertinent to the project.

3.3.4 Performing the planned activities

Performing the planned activities is initially easier for the practical operations of experimental work, because of already acquired familiarity; guidance is needed to verify the quality of what is obtained at each step and to decide the next steps, or to identify needs for modifications of initially planned routes. In the case of computational work, students acquire reasonable mastery of the basic procedures (input preparation, computation instructions, analysis of optimised geometries) rather fast, but apply them with a sort of "black box" approach, and specific mentoring is needed to develop adequate comprehension of the meaning of each detail.

The organisation and analysis of the obtained data follow different patterns for different research areas and corresponding investigation tools. Like for the earlier-mentioned instances, students acquire familiarity with the treatment of experimental data in previous years, although further guidance is needed in relation to the greater sophistication of some projects.

For computational projects, students have to learn *de novo* which data are relevant and where to find them in a calculation output, or how to calculate them from values present in the output. Guidance is needed for all the aspects of data organisation and analysis: how to build table setups which facilitate analysis; how to analyse the data obtained from molecular calculations, search for possible patterns and make inferences; which comparisons are significant; how to take into account the all-pervasive association with conceptual knowledge.

Given the usually large amount of data to be treated, the author recommends that students enter the data into suitably designed tables (or suitably designed figures for optimised molecular geometries) as soon as they are obtained from calculations, and visualize numerical values through diagrams as soon as a given set of data is complete. This enables the student to keep track of the progress of his/her work and to evaluate how to continue it. Furthermore, it enables early detection of errors which lead to unreasonable results, as an out-of-range value indicates the probable presence of an error, thus requiring verification. Although students should have learnt to evaluate the reasonability of obtained results since the undergraduate level, the reasonability criteria of values concerning the molecular level remain largely challenging.

After the bases for the analysis of the obtained results are laid out through tables and diagrams, the actual analysis needs to be expressed through words. The associated challenges pertain to the realm of the challenges related to writing, and are discussed in section 3.3.6.

3.3.5 Preparation of presentations

At UNIVEN, postgraduate chemistry students are expected to present their progress at least once during the Hons. period, and once per semester for M.Sc. and Ph.D. studies. Preparing a presentation of this type requires the abilities to:

- identify the main results obtained up to the moment of the presentation and their significance for the whole project;
- organize the information, i.e., plan a reasonable sequence of the various pieces of information and their distribution in self-consistent slides;
- write it (in the slides) in a way that is both scientifically correct and understandable.

Substantial guidance is often needed, above all in the terms discussed in section 3.3.6.

Students may also prepare presentations for conferences, more frequently in the form of posters. The preparation needs to take into account that a conference presentation must be self-consistent and sufficiently informative to attract the attention of the other participants. The mentor's guidance mostly responds to the terms discussed in section 3.3.6.

3.3.6 Writing: the most challenging operation

Writing is the most challenging component, where all the inadequacies converge and mutually enhance. It requires the ability to design an outline, i.e., to attain a clear picture of the material concerned (from theoretical aspects to the nature and significance of the obtained results) and to organize the various pieces of information into a logical framework. It also requires the ability to write in a correct and understandable way. Because of the variety and importance of the features involved in the writing operation, their analysis is here organised in a set of subsections, to facilitate readability. The present section (3.3.6.) focuses on writing in the more literal meaning of the term, i.e., the building of sentences, of descriptions, and of the text of individual sections of a larger work (mainly, a thesis); the next section (3.3.7.) focuses on the organization of the material.

3.3.6.1 Writing: students' difficulties and mentor's dilemmas

The writing stage highlights the often unabated impact of the main difficulties students face throughout their studies. The frequently inadequate background preparation engenders difficulties for writing the introduction of articles, or the theoretical background chapter of a thesis, or the analysis of obtained data in a way that relates identified patterns to fundamental concepts and displays the foundation of the conclusions. The poor language mastery (made more serious by second language instruction) affects all the aspects, because it affects the clarity with which concepts are understood, the development of adequate logical abilities, and the ability to express what one would like to express (including the ability to write sentences that have a literal meaning) [8–11]. It is also largely responsible for inadequate development of visual literacy [12], thus bringing additional challenges for projects involving the study of molecules.

The diffuse poverty of students' language mastery creates difficult-to-address problems for a teacher or a mentor. In the levels of instruction involving standard assessment options, such as tests or assignments, the foundations and scope of the assessment become uncertain, because the students' difficulties at expressing their answers constitute a substantial confounding factor [13]. An answer may be incorrect because the student is not able to build a sentence conveying the meaning that he/she would like to convey, but also because language difficulties hamper the clarity with which concepts are understood. There is no way in which a teacher can estimate the extent of the language-mastery impact [14] or differentiate it from the conceptual component of an error. An incorrect answer cannot be given a positive evaluation. On the other hand, when language problems determine poor understanding, the negative assessment is determined by poor language mastery, not by the student's actual

potentialities to understand chemistry. Basic fairness demands urgent attention to ensuring adequate language-mastery development.

At the postgraduate level, the supervisor's dilemma has a totally different nature, because no standard assessment is involved. The student has to write a thesis and the mentor has to offer guidance. The dilemma entails the identification of a reasonable balance between the provision of direct inputs and the need that the student does the writing. If the mentor's inputs are massive, the thesis is not exactly the student's work, and this would defeat the purpose of postgraduate studies. If the mentor's inputs are greatly restricted, the quality of the thesis may suffer severely.

In the case of articles, it is more legitimate that the mentor contributes substantial inputs to the writing of the text (above all in the earlier stages of a postgraduate project), while the student organizes and analyses the data and prepares tentative drafts of the text. The fact that the mentor is co-author of the article contributes to this legitimisation, and the fact that the student prepares tentative drafts is part of the learning process about writing.

A thesis is expected to be entirely the student's work: the mentor is expected to guide the writing, not to do it. However, because of poor language mastery, many students would never be able to write it in a reasonably acceptable way. Leaving the writing task largely to the student may lead to situations in which the external referees infer (and openly comment) that the mentor did not guide or proofread the thesis, or did proofread it only superficially.

The author has opted for an approach that is highly time-demanding, but aims at providing training: proofreading subsequent versions of the thesis together with the student. In practice, the mentor and the student sit together and the mentor reads the draft of the thesis, commenting or asking questions every time there is a problem (which, for some pages, may occur nearly at each and every line). In this way, the student is involved actively, as the mentor's questions engage the student in reflections about what he/she wants to say and the actual meaning conveyed by the written sentence, and in the search for correct assembling of words to convey the wanted meaning. If the student does not answer a given question (what happens frequently, above all in the initial stages), the mentor provides all the explanations about grammar errors, actual meaning conveyed by a sentence (if not the wanted one), or conceptual errors conveyed. The student then re-drafts the given section, or set of sections, and brings the new version to the next session with the mentor. This procedure is repeated until a satisfactory result is obtained. To facilitate and partially speed up the process, the author allows the student to record her questions and explanations, numbering the relevant parts in the text to facilitate correspondence retrieval.

The procedure is time-taking because, given the students' generally poor level of language mastery, it may need to be repeated several times for the same text. On the other hand, it gives the student the opportunity to focus on the correspondence between concepts and their expression and to learn how to write a scientific text. Learning this is extremely important for a young person training to do scientific work,

as is the case of postgraduate students. Through various contacts, the author has come to realise that there are persons who stop publishing after completing their postgraduate studies, not because they are not able to obtain results from their research, but because they are not able to write about the obtained results. A student who does not learn how to write will miss an ability that is likely to be crucial for his/her professional future. Whether in academia, or in the industry, or in other sectors, a highly qualified specialist is expected to write articles or reports. Therefore, fostering this ability is essential. Nevertheless, the option adopted by the author entails two major challenges: the need to devote substantial time to this activity with each individual student, and the need that the mentor has adequate language mastery to be able to perform accurate language analysis on the texts written by the students.

All the illustrative examples included in the next subsections refer to this type of approach. Only comparatively simple errors are selected for illustration, because cases in which no meaning is identifiable—although occurring frequently—would not be suitable for analysis in this text (they require an approach for which the student is invited to explain the desired meaning verbally, analyses its details with the mentor, and then tries to build a new text on this basis).

3.3.6.2 Fostering accuracy through error analysis

The analysis of errors is a powerful explanation tool [14], which can be utilised for all types of errors, from spelling mistakes to largely incorrect sentences or sentences without identifiable literal meaning, and can focus on the language, or on the concept, or simultaneously on both, according to needs. Guiding students to recognise the nature of the errors in their writings needs approaches tailored to the students' language mastery and conceptual understanding.

This section considers errors whose identification does not require specific conceptual knowledge, and that the student could be expected to be able to correct before showing a certain text to the mentor, simply by doing careful proofreading. However, efficient proofreading is also a skill directly linked to language mastery, and its effectiveness sharply decreases when the language mastery is poor, and even more in a second language context.

Spelling should not be expected to be a problem at postgraduate level, but spelling errors still surface [15]. When both the incorrect (for the given text) word and the correct one have a meaning, the mentor can simply ask the student to explain the two meanings; for instance, if a student writes that “complimentary information is provided in Appendix A”, the mentor asks the student to explain the meaning of “complimentary” and “complementary”, and to decide which one is the more appropriate in the given context. Spelling mistakes are also frequent with surnames, such as writing “Moller Plecent” in place of Møller–Plesset; in such cases, the mentor just advises the student to check the spelling in relevant sources.

Spelling errors may also stem from automatic corrections introduced by the computer spell-checker. This may result in incorrect surnames (for instance, “Hartree–Fork” in place of “Hartree–Fock”), or in incorrect technical terms; a frequent example of the latter is the automatic replacement of “solvation” by “salvation”. It becomes important to foster a critical attitude towards what a computer does automatically. This implies the recognition that the computer does not understand the meaning of a sentence, and that many technical terms are not present in its standard dictionary. Therefore, it is necessary to correct the computer’s automatic changes of technical terms, and it is advisable to add relevant technical terms to its dictionary.

The attention to spelling is part of the overall training to accuracy and critical evaluation. Other aspects pertaining to accuracy are the correct use of dimensions (units), the proper numbering of equations, or the correct and complete correspondence between cited and reported references. These are all aspects that do not require specific explanations, and the student is simply invited to double check and correct them whenever errors appear.

3.3.6.3 Correct grammar and the meaning of sentences

Inadequate language mastery is associated with inadequate mastery of grammar and insufficient awareness of its role in conveying the desired information. The regrettably diffuse misconception considering that language is “not so important” in the sciences contributes to insufficient attention to the grammatical and linguistic correctness of the mode of expression and to general insufficient attention to the importance of language mastery in science learning and practice [11].

Some errors are recurrent at all levels of instruction, like the incorrect expression of comparisons. Statements such as “the intramolecular hydrogen bond in conformer A is long than the intramolecular hydrogen bond in conformer B” (where “long” should be replaced by “longer”) are so frequent that, after few cases, they are simply underlined in the joint student-mentor sessions, with comments reminding the student that it is “again the same error”. It can be recalled that comparisons are very important in the analysis of results, for instance, when one tries to identify the factors influencing specific molecular properties (relative energies, preferred geometries, HOMO-LUMO energy gaps, dipole moments, characteristics of intramolecular hydrogen bonds when present, etc.); therefore, expressing comparisons correctly is essential to communicate the reasons for the identification of influencing factors.

Grammar errors appear also with regard to specific functions such as prepositions [16] and logical connectives. In these cases, the mentor usually has to explain the nature of the error.

Errors concerning the association of words with specific roles [17] are also frequent, including incorrect associations of subject and verb, or subject, verb and object. They are more frequent when the subject and the verb are separated by some specifications and are, therefore, at a certain distance. Then the mentor points out the relationships

between them. For instance, the sentence “The relative energies of conformers A, B, C, D, E and F have close relative energies” is analysed by isolating subject, verb and object (“The relative energies ... have close relative energies”), because this highlights that the sentence states that the relative energies have relative energies, which is meaningless. This isolation of the relevant words is frequently adequate for the student to recognise the error.

Errors concerning the roles of clauses in a complex sentence are more difficult to point out, because too often the student’s language mastery is not adequate to grasp the meaning of an explanation given through grammatical terms, even if simplified. An example is offered by the sentence “As optimised geometries are reported in Figure 3.4 showing all the possible geometries which have an intramolecular hydrogen bond”, which lacks the principal clause and, therefore, does not convey a direct meaning. After repeated failures (with a number of analogous cases) to guide the student to identify the problem through various types of explanations, the author has realised that the student recognises the problem if she reads the sentence with an intonation that highlights the incompleteness of the statement; then the student rewords it for the next session.

The correct use of punctuation is partly an issue of accuracy and partly an issue of identifying the different meanings conveyed by different punctuation options. For the latter cases, the just-described option (the mentor reading the sentence with an intonation that highlights the differences) has so far proved the only viable “cure”.

3.3.6.4 The meaning and correctness of descriptions

For errors concerning practical descriptions, it is easy to attract attention to the discrepancies between what is written and reality. An example reported by various colleagues in different institutions can serve as illustration. A student describes a practical procedure roughly with the following pattern: “The dry leaves are crushed and dissolved in dichloromethane; the mixture is then treated with ... the dry crushed leaves must be weighted”. The mentor asks questions related to the feasibility of the sequence of instructions in the described procedure, starting with a simple one like “are you sure that it is possible to follow your instructions in practice?” and, if the student does not identify the problem, proceeding with more focused questions, such as “can you weigh the dry leaves at the stage in which you write this instruction? (i.e., after dissolving them?)”, and, finally, “where should the weighing instruction be written in this sequence?” This case is easy because the reference against which the student is invited to check the meaning of his/her written sentence relates to direct practical experience.

Computational chemistry theses present specific challenges because there are no concrete references against which to check the correctness of the meaning conveyed by a sentence or a description. The correct concepts pertain to a theory that the student is still learning, and are often related to mathematical concepts, which chemistry students tend to find particularly challenging. The mentor has to attract the student’s

attention to the discrepancies between what he/she writes and the theoretical or mathematical concepts, and long explanations are often needed.

A description, or the treatment of a certain issue, need to contain all the pieces of information that can enable the reader to understand it. If relevant pieces of information are missing, the mentor attracts the student's attention on the fact that something is missing, and the student is asked to identify what is missing. For instance, if one lists the solvents selected for the study of certain molecules in solution, one also need to state why they are selected. If certain computational methods are selected for a given study, one also needs to say why they are selected and explain their suitability for the molecules considered, or for the objectives of the study.

Additional problems may appear with regard to the nature of molecular calculations. Most students have not sufficiently internalised the meaning of modelling as simulations providing approximate descriptions of molecular systems and tend to consider each set of results as a reality; for instance, the results of two different calculations methods for the same molecule are viewed as two different, simultaneously existing realities. Fostering the internalization that all results are approximations, being models by their nature, is a demanding task, because it requires a higher level of language and conceptual sophistication than many students have attained.

3.3.6.5 The analysis of obtained results—at the interface between thought and language mastery

Language is the main instrument of thought [18]. This comprises all the activities that require reflection. The analysis of obtained results requires reflection to make comparisons and identify patterns, and to coordinate the various pieces of information into a coherent picture. Major challenges are often observed when students write about the outcomes of the analysis.

A frequent occurrence is that the text simply repeats the values provided in the tables, expressing them through words (e.g., “conformer A has relative energy 0.000 kcal/mol, conformer B has relative energy 0.846 kcal/mol, ...” and the like). Then the mentor has to explain that such repetitions do not contribute any new information (because it is expected that a reader is able to read the tables), and that the text needs to add something new to the tables, such as comparisons, identification of patterns, hypotheses on the factors determining observed trends, and other interpretation components. Inadequate language mastery poses enormous challenges in this regard. The initial drafts of these components are often not sufficiently clear to be understandable on reading. The mentor needs to ask the student to explain (verbally) his/her observations, and then guide him/her to formulate a new text expressing them. The guidance requires continuous analysis of the meaning conveyed by the proposed text and its comparison with the meaning that is to be communicated. It may also entail the cooperative building of a text-skeleton that the student will use as basic framework to prepare improved drafts.

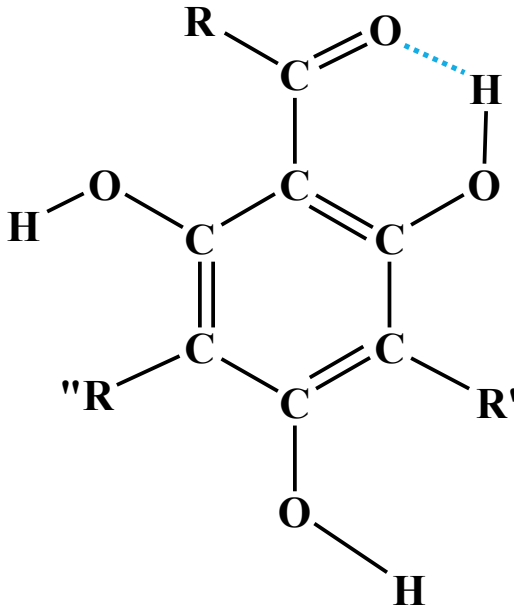


Figure 3.2: Molecular structure of acylphloroglucinols. The intramolecular hydrogen bond mentioned in the text is indicated by a blue dashed segment.

Fundamental logical relationships may prove particularly challenging both in terms of recognition and in terms of expression. For instance, the identification and expression of cause-effect relationships depends simultaneously on conceptual understanding and on language mastery [19], and it is often difficult to untangle the relative weights of these two components. Two illustrative examples can be associated with Figure 3.2 (which shows the general molecular structure of acylphloroglucinols [20]). The statements “the planarity of the carbonyl oxygen in the R–C=O group, which is involved in the hydrogen bond, is determined by the planarity of the R chain” and “the formation of the intramolecular hydrogen bond is determined by the planarity of the carbonyl oxygen in the R–C=O group” do not identify the cause correctly, because the planarity of the carbonyl oxygen is determined by the presence of the intramolecular hydrogen bond (in the absence of this bond, the carbonyl oxygen is not coplanar to the benzene ring); the latter statement actually reverses cause and effect. In both cases, the major problem likely concerns the interpretation level, and they provide opportunity to guide the student to analyse molecular properties and identify what may be responsible for what. On the other hand, analogous cases have been encountered in which the student’s interpretation (as verbally expressed to the mentor) was correct, but its written expression conveyed a different meaning.

3.3.6.6 Writing efficiency and economy

The main objective of a written text is to communicate something, and it is therefore imperative that the text is understandable to the reader. Inviting the student to imagine being in the position of the reader can foster awareness of the importance of communication clarity and completeness.

- Information about the figure showing the geometries of the molecules
- Information about the table reporting the relative energies of the molecules
- Comparison of geometries and relative energies for each subclass:
 - Consider the differences in the geometries of the molecules of subclass I and the corresponding relative energies.
 - ❖ Identify geometrical factors that influence the relative energies.
 - ❖ Compare the effects of the identify geometrical factors (for instance, by how much each of them influences the energy)
 - ❖ Identify a dominant factor, if present (for instance, intramolecular hydrogen bonds can be the dominant energy-influencing factors)
 - Do the same for the molecules of subclass II
 - Do the same for the molecules of subclass III
- Comparison of energy-influencing factors across subclasses
 - Discuss the factors present in all the three subclasses and their effects
 - Discuss the factors present in two of the subclasses but not in the remaining one, and their effects
 - ❖ This may entail one, two or three pairs (the possible pairs being I and II, I and III and II and III)
 - Discuss the factors present in only one of the subclasses
 - ❖ Each subclass may or may not have factors that are not present in the others

Scheme 3.1: Example of basic sketch for the identification of the pieces of information needed in a section discussing the relative energies and conformational preferences of a set of molecules. The example considers the results for the study of a set of molecules pertaining to the same class, and grouped into three subclasses: I, II and III. The sketch also considers the hierarchical organisation of the various issues.

A text must provide all the pieces of information that are needed for the reader to understand the overall discourse and each of its individual components. It is often useful to initially draft a sketch of the pieces of information identified as necessary for a given section, ordering them in a logical framework, so that the sketch can be used as guidance on writing. An illustrative example of a basic sketch of this type is given in Scheme 3.1.

The economy of a text requires conciseness of expression and avoidance of repetitions. The conciseness of expression depends largely on language mastery: the better the language mastery level, the greater the ability to express concepts through sentences containing only the necessary terms and clauses, without dispersions. The previously mentioned recommendation of not repeating through words, in the text, the values provided in the tables, is part of both being concise and avoiding repetitions. Another important component is the avoidance of repetitions of the same pieces of

information in different parts of the text. The student is guided to recognise repetitions and to learn how to refer to the content of other parts of the thesis without repeating it.

3.3.6.7 Writing independence and the ability to summarise

Some parts of a thesis are derived from other sources, above all the literature review and the theoretical background. Writing these parts requires the ability to understand the concepts expressed in the source and to summarise them, i.e., to express them through a much shorter text and with one's own word. Both features pose great challenges to students. The tendency to resort to copy-and-paste (an operation made easy by the electronic format of most sources) is overwhelming. Initial drafts of theses may contain extensive copy-and-pasted portions both in the theoretical background and in the literature review, and the mentor has to identify them, request rewording, and often guide the rewording. In a context with diffuse language challenges, the identification of copy-and-pasted parts is actually immediate, because their mode of expression is correct and has good standard, i.e., has characteristics that do not appear in students' writings.

Besides straightforward copy-and-paste, cases in which students change only few words with respect to the source are frequent. This entails two problems: the fact that, if this concerns an extensive portion of a text, it remains a form of plagiarism; and the fact that the new words are often not correct for the given context. Both aspects are emphasised by the mentor's guidance.

The copy-and-paste option may entail other risks. For instance, students may copy sentences that appear attractive, but are not compatible with the context. For example, the introduction of a sentence like "the experimental data are used to provide evaluation of the results" has no meaning for a computational chemistry work that is not accompanied by experimental work and does not compare computed values with experimental data from literature (something that is not always possible, because experimental data are not always available). On the other hand, the student might have found the sentence in some reference and considered it a "nice" sentence to add to his/her text. The mentor's guidance needs to highlight the importance of consistency between what is written and what has actually been carried out in the research [21].

Like other components inherent in language mastery, summarising a text is one of those abilities that are more effectively learnt at an earlier stage and become more difficult to acquire or promote to a desirable extent after 19–20 years of age. When a student reaches postgraduate studies, it is often too late to attain high levels in language-related abilities; a mentor can only aim at fostering passable levels to meet the requirements of the student's professional future. This can be best pursued in an interactive way. For instance, for the literature review, the mentor asks the student to point out (verbally) the most important pieces of information in a given article, and then to write 1–3 sentences to summarise them; the drafted sentences are analysed and redrafted until a satisfactory result is reached. For the theoretical background, the

mentor guides the student to select the components that are relevant to his/her work from comprehensive sources (ideally, textbooks), to explain their meaning, and then to write about them in a way that maintains the logic of the discourse. The extensive presence of mathematics in the theoretical background of computational chemistry theses poses additional challenges, both in terms of selecting the mathematical treatments that are pertinent to the given project, and because, while equations need to be copied from the source without alterations, the sentences between equations are often very concise in the source and, rather than summarising them, the student may need to expand the explanations, to better highlight the logical steps between subsequent equations.

Independence in writing can be pursued only after a student has acquired sufficient mastery of the basic features, such as writing grammatically correct sentences that convey the wanted meaning, and combining them into larger texts that also convey the wanted meaning. The independence would correspond to reaching sufficient self-confidence for a student to have clear ideas of what and how he/she wants to write. In other words, it corresponds to the acquisition of good mastery of the connections between concepts and the language through which they are expressed, ultimately leading to the acquisition of a personal style. It is however rare that a student who has started with significant language-related difficulties reaches this level by the end of a PhD course (the achievement has been observed with students who had already attained sufficiently good language mastery by the beginning of their postgraduate studies).

3.3.6.8 Writing captions—a task with specific requirements

When they start postgraduate studies, most students have not yet acquired sufficient familiarity with the specificities of writing the captions of figures and tables, and need *ad hoc* guidance even for very basic features, such as the fact that a caption consists of a title and may contain additional information expressed through sentences after the title, or the criteria about *what* to write and *how* to write it. The main criterion about *what* to write is to ensure that the caption provides sufficient information for a reader to understand what the table or the figure is about, without having to read the text. The main criteria about *how* to write are concision and the fact that the title should not consist of an explicit clause (i.e., should not contain a main clause with an explicit verbal form). This latter condition is not easy to explain to students, because most of them do not know the meaning of “clause” or “explicit verbal forms”; therefore, the training has to rely on the correction of errors as they appear, until correct practices are internalised. For instance, if a student writes a caption like “Table 3.3. The lengths of the intramolecular hydrogen bonds are reported here below”, the mentor’s guidance needs to highlight that:

- the title in a caption cannot contain an explicit verbal form and, therefore, “are reported” must be removed;

- “here below” is not appropriate for a caption and must be removed (it would be an actual error if the space distribution in the final version brings the table to the next page);
- it is necessary to specify the “owners” of the intramolecular hydrogen bonds, for the information to be complete.

After these remarks, a correct caption of the type “Table 3.3. Lengths of the intramolecular hydrogen bonds of the calculated molecules” is built.

The specification of the calculation method in the caption is often recommended. For calculations involving a reference value that is not present in the given table, the reference needs to be indicated. For instance, the conformer that is reference for the calculation of relative energies appears in a table of relative energies (its relative energy is 0.000); the vibrational frequency of a free OH group utilised to calculate the red shifts in the vibrational frequencies of OHs which are engaged in hydrogen bonds does not appear in a table of red shifts and, therefore, needs to be specified in the caption.

3.3.7 Planning a thesis and organising its material

A thesis is a rather large overall text, divided into chapters which, in turn, are subdivided into sections and subsections. This requires the design of a framework, and of how the available material is going to be distributed in it. A design of this type is a typical example of systems thinking [1–3], because it requires the recognition of the different sets of information to be considered and of their mutual relationships, so that a plan for their organisation can be built.

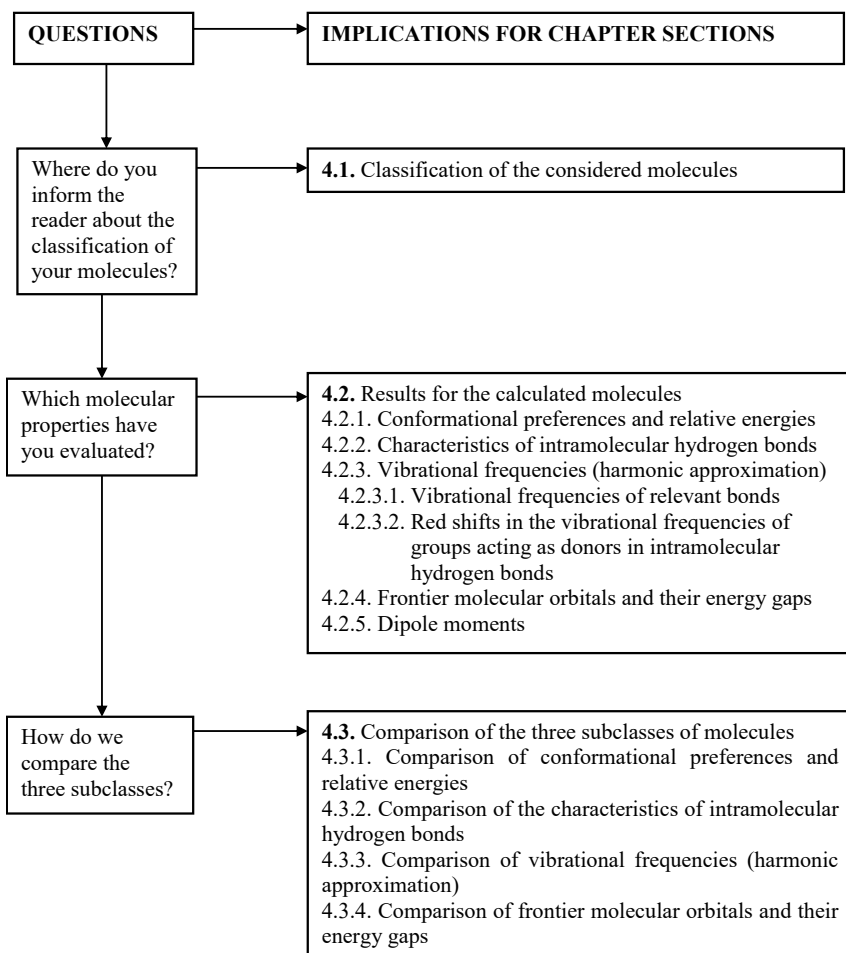
The chapters of a computational chemistry thesis can be rather standard, namely:

- a short introductory chapter;
- a theoretical background chapter, introducing the concepts relevant to the computational study of molecules, with greater focus on the methods selected in the given project and the molecular properties considered in it;
- a literature review chapter on the molecules or class of molecules considered in the given project. If short, it can be combined with the theoretical background chapter;
- chapters presenting the obtained results. Separate chapters may be devoted to different sets of results (e.g., results in vacuo, results in solution, or others);
- a short closing chapter, providing an evaluation of the utilised procedures and the obtained results, and some indications for further studies.

Given this rather standard setup, planning the chapters’ titles does not pose great challenges to students. The major challenges are associated with planning the sections and subsections of each chapter, i.e., planning how to organise the available information (identifying the sequence with which different pieces of information are

suitably presented). The chapters presenting the results appear to be the most challenging, likely because they are to present novel information.

The recommended—and most natural—strategy entails the preparation of an initial plan of each chapter, with tentative titles and subtitles, which are then optimised while writing. The figures and tables in which data have progressively been organised should provide factual guidelines to the organisation of the chapters presenting the results; however, the recognition of these implicit guidelines requires adequate



Scheme 3.2: Example of basic route for the identification of suitable chapter planning, considering the results for the study of a set of molecules pertaining to the same class, and grouped into three subclasses: I, II and III. It is assumed that the molecules can form intramolecular hydrogen bonds. The route identification is expressed through questions; the answers to the question correspond to the titles of sections and subsections. For the sake of section-numbering, it is assumed that the chapter is the fourth chapter of the thesis.

systems thinking abilities, and extensive mentor's guidance is often needed. The guidance is provided in an interactive way, inviting the student to categorise the obtained information, so that the categories can be used to plan the chapters. Scheme 3.2 presents a basic example of categorisation and chapter-planning. Once the chapter layout is thus pre-organised, the student can start writing the text, with the already prepared figures and tables supporting the identification of most of the content.

3.3.8 Fostering independence

The previous sections have frequently mentioned the need for mentor's guidance, and outlined some modes through which it can be provided. On the other hand, one of the central objectives of postgraduate studies is to train the students to become independent researchers and, therefore, the way in which the guidance is provided needs to be tuned to this purpose. Active student's engagement and frequent mentor-student interactions are crucial; they extend the benefits of active learning [22–29] to postgraduate studies and enhance them through specific options made possible by the “doing research” context. Ideally, the guidance about doing research should gradually decrease and the supervisor-student relationship should gradually evolve into a sort of guided collaboration, as the student increasingly acquires expertise, experience and initiative.

The option adopted for the correction of subsequent drafts of articles or the thesis (section 3.3.6.1) enables the student to be in charge of the analysis of results while learning how to write about them, thus trying to build independence both for typically research features and for writing. The fact that it contributes to foster independence is an important reason for which this option is considered preferable to the practice in which the mentor makes the corrections separately.

Independence also comprises the ability to plan and manage time. Time planning for the components of a postgraduate project is actually part of the project proposal and it standardly positions the writing of the thesis at the end because of the assumption that all results must be obtained before writing. The author recommends that the writing of the theoretical background and literature reviews chapters (which do not depend on the results to be obtained) starts since the early stages, because of the challenges posed by material thoroughly intertwined with conceptual demands. This recommendation is rarely followed, because of serious underestimation of the time needed to write those chapters; however, the ensuing difficulties within late writing contribute to building the awareness of the importance of realistic time planning.

3.4 Discussion and conclusions

The previous sections have outlined the major components of the supervision of postgraduate chemistry students, within a perspective viewing supervision as an educational activity. Most of the concrete references and examples were derived from computational chemistry postgraduate activities; this, however, does not entail a limitation of the overall discourse, because they encompass all the relevant components of postgraduate chemistry studies, plus the additional challenges associated with the requirements of attaining substantial theoretical knowledge and working within the paradigm of its conceptual demands. The mentor's guidance needs to address all these demands. Tuning the guidance to the students' needs requires careful identification of these needs, which in turn relies on adequately extensive student-mentor interactions.

The difficulties encountered by postgraduate students provide valuable indications for desirable improvements in undergraduate chemistry education, both for the extent and depth of conceptual knowledge and for the mastery of skills constituting essential tools for the acquisition of knowledge and for its applications. Some of these skills should actually be acquired in pre-university instruction; if they do not reach adequate level, further development needs to be pursued within specifically-focused courses bridging secondary and tertiary instruction. The following paragraphs quickly recall the most crucial skills.

Language mastery is an essential tool for all the components of the learning process and also for the acquisition of other necessary abilities such as logical thinking [8], systems thinking [1–3, 7], and the mastery of communication tools such as visualization [8, 12]. Because of this, developing adequate language mastery is a *conditio sine qua non* to ensure that students can benefit from their studies according to their potentialities, without the heavy hampering effects ensuing from poor language mastery. Initiatives integrating chemistry learning and language learning in secondary-tertiary bridging courses can simultaneously build chemical knowledge and language mastery, through reflections on the correspondence between chemistry concepts and the way in which we express them [30, 31]. Ensuring adequate language training at this stage is crucial. It would benefit many students and make their further studies more profitable (whereas the language training provided through proofreading subsequent thesis-drafts together with a postgraduate student—as outlined in previous sections—benefits only one student at a time, because postgraduate projects are individual). In addition, abilities related to the use and roles of language communication are more effectively acquired by 19–20 years of age, which is largely the age corresponding to bridging courses (this age criterion does not refer to the ability of learning a new language, but to the internalisation of the meaning and usage of language).

Adequate familiarity with mathematics as a tool for description is important in many areas of chemistry, and essential in physical and computational chemistry.

Promoting it at pre-university and bridging levels would facilitate the understanding of concepts and problem solving procedures, and the interpretation of results, throughout undergraduate and postgraduate studies.

Adequate familiarity with the bases of the scientific method is important for students to be able to perform a variety of tasks: analyse all the pieces of information available for a given work and organise them in a functional way; distinguish between aspects pertaining to physical reality and aspects pertaining to our descriptions or models; and being aware of the nature of the obtained results in a given field [32].

In summary, the postgraduate level poses a variety of educational challenges, some of which can be viewed as continuations of challenges that have not been resolved in the undergraduate level, whereas others are novel and relate to the inherent features of postgraduate studies, first of all training students to do research. Decreasing the impact of the formers through timely measures would benefit students' performance in the undergraduate level and enable postgraduate studies to better focus on the training to do research. Then, the student-mentor interactions could more rapidly and extensively develop into collaboration to which the student contributes increasingly more initiatives while simultaneously acquiring increasing independence. Considering the mentoring activity as an object of educational research requiring novel approaches to take into adequate account its inherently creative character could help enhance the quality of mentoring as well as that of pre-university and undergraduate training.

Author contribution: The author has accepted responsibility for the entire content of this submitted manuscript and approved submission.

Research funding: None declared.

Conflict of interest statement: The author declares no conflicts of interest regarding this article.

References

1. Kim DH. Introduction to systems thinking. Waltham (MA): Pegasus Communications; 1999.
2. Arnold RD, Wade JP. A definition of systems thinking: a systems approach. *Procedia Comput Sci* 2015; 44: 669–78.
3. Mahaffy PG, Krief A, Hopf H, Matlin SA, Mehta G. Reorienting chemistry education through systems thinking. *Nat Rev Chem* 2018; 2: 0126.
4. Mammino L. Incorporating information on green chemistry into theoretical chemistry courses. *Curr Opin Green Sustain Chem* 2018; 13: 76–80.
5. Levin R. Frontiers in group dynamics. II. Channels of group life: social planning and action research. *Hum Relat* 1947; 1: 143–59.
6. Mammino L. Chemistry teaching and chemical education research: 30-year experience in integration pathways. In: Mammino L, Apotheker J, editors. *Research in chemistry education*. Cham, Switzerland: Springer; in press.

7. Mammino L. Roles of system thinking within green chemistry education. Reflections from identified challenges in a disadvantaged context. *J Chem Educ* 2019; 96: 2881–7.
8. Mammino L. The mother tongue as a fundamental key to the mastering of chemistry language. In: Lovitt CF, Kelter P, editors. *Chemistry as a second language: chemical education in a globalized society*. Washington. American Chemical Society; 2010.
9. Mammino L. Importance of language mastery and mother tongue instruction in chemistry learning. In: Desai Z, Qorro M, Brock-Utne B, editors. *The role of language in teaching and learning science and mathematics*. Somerset West: African Minds; 2013.
10. Qorro M. Language planning and policy in Tanzania: when practice does not make perfect. In: Desai Z, Qorro M, Brock-Utne B, editors. *The role of language in teaching and learning science and mathematics*. Somerset West: African Minds; 2013.
11. Mammino L. Essential roles of language mastery for conceptual understanding and implications for science education policies. In: Marek T, Karwowski W, Frankowitz M, Kantola J, Zgaga P, editors. *Human factors of a global society: a system of systems perspective*. Rosa Boca (USA). Taylor & Francis, CRC Press; 2014.
12. Mammino L. The interplay between language and visualization: the role of the teacher. In: Eilam B, Gilbert J, editors. *Science teachers' use of visual representations*. Heidelberg. Springer; 2014.
13. Clerk D, Rutherford M. Language as a confounding variable in diagnosing misconceptions. In: *Proceedings of the sixth annual meeting of SAARMSE*. Pretoria, South Africa: UNISA; 1998.
14. Love A, Mammino L. Using the analysis of errors to improve students' expression in the sciences. *Zimbabwe J Educ Res* 1997; 9: 1–17.
15. Mammino L. Language-related difficulties in science learning. II. The sound-concept correspondence in a second language. *J Educ Stud* 2006; 5: 189–213.
16. Mammino L. Language-related difficulties in science learning. IV. The use of prepositions and the expression of related functions. *J Educ Stud* 2009; 8: 142–57.
17. Mammino L. Language-related difficulties in science learning. III. Selection and combination of individual words. *J Educ Stud* 2007; 6: 199–214.
18. Bruner J. Language as an instrument of thought. In: Davies A, editor. *Problems of language and learning*. Edinburgh: Edinburgh University Press; 1975.
19. Mammino L. Cause and effect – a relationship whose nature involves conceptual understanding, scientific method, logic and language. *Anu Latinoam Educ Quím* 2006; XXI:33–7.
20. Singh IP, Bharate SB. Phloroglucinol compounds of natural origin. *Nat Prod Rep* 2006; 23: 558–91.
21. Mammino L. Being consistent with reality: a great challenge for chemistry laboratory reports. In: *ISTE conference on mathematics, science and technology education proceedings*. UNISA Press, Pretoria; 2016.
22. Paulson DR. Active learning and cooperative learning in the organic chemistry lecture class. *J Chem Educ* 1999; 76: 1136–40.
23. Kovac J. Student active learning methods in general chemistry. *J Chem Educ* 1999; 76: 120–4.
24. Hinde RJ, Kovac J. Student active learning methods in physical chemistry. *J Chem Educ* 2001; 78: 93–9.
25. Prince M. Does active learning work? A review of the research. *J Eng Educ* 2004; 93: 223–31.
26. Vera C, Féliz J, Cobos JA, Sánchez-Naranjo MJ, Pinto G. Experiences in education innovation: developing tools in support of active learning. *Eur J Eng Educ* 2006; 31: 227–36.
27. Pinto Cañon G, editor. *Aprendizaje activo de la física y la química*. Madrid: Equipo Sirius; 2007.
28. Oliver-Hoyo MT, Alconchel F, Pinto G. Metodologías activas para el aprendizaje de la Física: un caso de hidrostática para su introducción en la práctica docente. *Rev Esp Física* 2012; 26: 45–50.
29. Mammino L. Enseñanza y aprendizaje activos de la componente teórica: desafíos y reflexiones. In: Pinto Cañon G, editor. *Aprendizaje activo de la física y la química (= Active learning of physics and chemistry)*. Madrid: Equipo Sirius; 2007.

30. Mammino L. Focused language training as a major key for bridging the gap between secondary and tertiary instruction. In: ISTE international conference proceedings. UNISA Press, Pretoria; 2012.
31. Mammino L. Clarifying chemistry concepts through language analysis. In: Lundell J, Aksela M, Tolppanen S, editors. LUMAT special issue of ECRICE, Helsinki, Finland; 2015.
32. Mammino L. Method-related aspects in an introductory theoretical chemistry course. *J Mol Struct* 2005; 729: 39–45.

Miroslava Nedyalkova*, Ralitsa Robeva, Atanaska Elenkova and Vasil Simeonov

4 Chemometric exploratory data analysis for patients with diabetes type 2 and diabetic complications

Abstract: The present study deals with the interpretation and modeling of clinical data for patients with diabetes mellitus type 2 (DMT2) additionally diagnosed with complications of the disease by the use of multivariate statistical methods. The major goal is to determine some specific clinical descriptors characterizing each health problem by applying the options of the exploratory data analysis. The results from the statistical analysis are commented in details by medical reasons for each of the complications. It was found that each of the complications is characterized by specific medical descriptors linked into each one of the five latent factors identified by factor and principal components analysis. Such an approach to interpret concomitant to DMT2 complications is original and allows a better understanding of the role of clinical parameters for diagnostic and prevention goals.

Keywords: complications, DMT2, multivariate statistics

4.1 Introduction

Type 2 diabetes is a heterogeneous disorder, characterized by hyperglycemia and increased risk of acute and chronic complications [1]. Diabetes complications are associated with increased morbidity and mortality among patients along with substantial financial and social costs for the society [2].

The microvascular diabetic complications such as diabetic retinopathy, nephropathy and neuropathy are related to the impairment of small blood vessels [3]. Increased blood glucose levels induce endothelial damage, oxidative stress and aberrant production of sorbitol and glycation end products. The following alterations in endothelial permeability and coagulation facilitate the development of organ damages (reviewed by Vithian et Hurel [4]). Diabetic retinopathy affects about 27% of diabetic patients

***Corresponding author: Miroslava Nedyalkova**, Chair of General and Inorganic Chemistry, Faculty of Chemistry and Pharmacy, University of Sofia “St. Kl. Okhridski”, 1, J. Bourchier Blvd., 1164 Sofia, Bulgaria, E-mail: mici345@yahoo.com

Ralitsa Robeva and Atanaska Elenkova, USHATE “Acad. Iv. Penchev”, Department of Endocrinology, Medical Faculty, Medical University-Sofia, 2, Zdrave Str., 1431 Sofia, Bulgaria

Vasil Simeonov, Chair of Analytical Chemistry, Faculty of Chemistry and Pharmacy, University of Sofia “St. Kl. Okhridski”, 1, J. Bourchier Blvd., 1164 Sofia, Bulgaria

This article has previously been published in the journal *Physical Sciences Reviews*. Please cite as:

M. Nedyalkova, R. Robeva, A. Elenkova and V. Simeonov “Chemometric exploratory data analysis for patients with diabetes type 2 and diabetic complications” *Physical Sciences Reviews* [Online] 2021, 5. DOI: 10.1515/psr-2020-0132 | <https://doi.org/10.1515/9783110739763-004>

worldwide and it is still one of the leading causes of severe visual impairment [5, 6]. The duration and severity of the diabetes, as well as control of hyperglycemia are important factors influencing the onset and progression of the diabetic retinal changes [7, 8]. Diabetic retinopathy is closely associated with diabetic nephropathy both sharing similar pathophysiological pathways. Diabetic nephropathy affects up to 40% of patients with diabetes, and it represents an important factor for the development of end-stage renal disease [9, 10]. The optimal control of hyperglycemia and hypertension is paramount for prevention of the progressive renal impairment [9, 10].

Alterations of the peripheral and autonomic nervous systems are common among diabetic patients. Different risk factors such as increased glucose levels, hypertension, obesity, dyslipidemia, smoking and alcohol abuse might influence the progression of diabetic neuropathy [11, 12]. Considering the irreversibility of neural damage, prevention focusing on improved glucose control and lifestyle changes is of crucial importance for diabetic patients [13].

Macrovascular complications of diabetes reflect the negative impact of hyperglycemia on arteries leading to accelerated atherosclerosis and cardiovascular diseases [3]. Diabetic patients are at increased risk of coronary heart disease, stroke, peripheral artery diseases and vascular death [14–17]. The development of new medical therapies ensuring better glucose control and treatment of concomitant metabolic disturbances has decreased the risk of vascular complications. Nevertheless, the risk remains substantially increased considering the progressive increase of diabetes prevalence worldwide [18, 19].

Diabetic micro- and macrovascular complications might be interrelated and patients with microvascular complications suffer often from accelerated atherosclerosis [20]. For instance, strongly increased cardiovascular morbidity and mortality has been observed in patients with diabetic nephropathy [21]. The search for common and distinct risk factors that could promote the development of micro- and macrovascular diabetic complications is of great clinical importance. Therefore, the present study aims to investigate the possible influence of several metabolic and hormonal parameters on the development of different diabetic complications.

4.2 Methods and results

4.2.1 Input data

The input data set was collected at Department of Endocrinology, Medical University, Sofia, Bulgaria. The Institutional Ethics Committee approved the usage of the data for the scientific purposes. The data set was of dimension $[52 \times 30]$, i.e., 52 patients with diabetes mellitus type 2 (DMT2) were involved as for each of them 30 clinical parameters were recorded. Additionally, data for diabetic complications were registered in order to organize various subsets of patients with DMT2 and specific concomitant diseases.

The clinical records were typical for such types of patients. They include anthropometric indicators age, weight, height, waist circumference, blood pressure – systolic (sysRR) and diastolic (diaRR) readings; blood parameters like erythrocyte sedimentation rate (ESR), hemoglobin (Hgb), erythrocytes (Er), leucocytes (Leu), thrombocytes (Tro); liver and kidney functional parameters for alanine aminotransferase (ALAT), aspartate aminotransferase (ASAT), gamma glutamyl transferase (GGT), alkaline phosphatase (AF), creatinine (Crea), estimated glomerular filtration rate (eGFR), uric acid (UA); lipid profile: high-density lipoproteins (HDL), low-density lipoproteins (LDL), cholesterol (Chol), triglycerides (TG); glucose levels – hemoglobin A1c (HbA1c), estimated average glucose (EAG). Additionally, content of electrolytes (K, Cl, Na, Ca, P) and data for thyroid functional test – thyroid stimulating hormone (TSH) were used.

The input data were separated into nine predetermined groups: all objects are with diagnosis DMT2 but with respect to one concomitant health problem the groups are subdivided as follows:

1. Fifty one patients with AH (arterial hypertension),
2. Forty eight patients with CHD (coronary heart disease),
3. Seven patients with OMI (myocardial infarction),
4. Nine patients with Stroke (ischemic or hemorrhagic stroke),
5. Fifty one patients with DPNP (diabetic polyneuropathy),
6. Seventeen patients with DR (diabetic retinopathy),
7. Sixteen patients with DN (diabetic nephropathy),
8. Forty seven patients with DMA (diabetic macroangiopathy),
9. Twelve patients with steatosis (steatosis hepatis).

For each data set several multivariate statistical methods for data mining were applied in order to reveal similarity patterns between the patients or between the clinical parameters, to identify, if possible, discriminant parameters for each concomitant disease and to compare groups of parameters related both to basic health problem and to the additional disease. This was the major goal of the present study.

4.2.1.1 Chemometric methods

Throughout the study three classical multivariate statistical methods were used – cluster analysis (hierarchical and nonhierarchical), two-way grouping and principal components/factor analysis were used. All methods are well documented and find wide application to need detailed description [22, 23]. Some short outlines of the methods will be presented below.

Hierarchical Cluster Analysis (HCA) is a traditional nonsupervised pattern recognition method trying to detect groups of similarity (clusters) within the structure of the data set with respect both to the objects of interest and to the variables describing the objects. Traditionally, HCA is performed on standardized input data to achieve better clustering and interpretation of the similarity patterns. The similarity is

usually determined by Euclidean distances between the objects or variables. Very suitable for connecting of similar objects is the Ward's method of linkage. The graphical output of the analysis is a tree-like diagram called hierarchical dendrogram. Finally, the statistical significance of the clusters (cut-off point) is determined, very often by the criterion of Sneath.

Nonhierarchical Cluster Analysis (K-means mode) is a supervised pattern recognition approach of clustering based on a priori hypothesizes for a required number of clusters (both for objects and variables). These hypothesizes are due to preliminary information about the system of interest or expert opinions.

Two-way grouping is a chemometric technique of simultaneous linkage of objects and variable on one and the same plot. It makes possible to find the correspondence between certain clusters with certain variables responsible for the cluster formation.

Factor Analysis (FA) and Principal Components Analysis (PCA) are very similar projection techniques leading to dimensionality reduction of the variable space. In the course of the chemometric analysis the real variables are replaced by new (called latent) variables or factors being linear combinations of the old ones. Each latent factor explains a part of the total variance of the system. Thus, the input data matrix is decomposed to a matrix of the factor loadings (representing the new latent variables) and a matrix of the factor scores (representing the new coordinates of the objects in the reduced variable space). The choice of the number of latent factors is related with the amount of variation explained by each of them. It is generally accepted that the selected new latent variables should explain at least 70% of the total variance. The data interpretation gets easier and simpler by the use of the new set of latent variables.

4.3 Results and discussion

In the first stage of the exploratory data analysis PCA was applied to each group of patients as specified above. It was found that five latent factors for each of the analyzed groups of DMT2 patients with specific concomitant disease (out of totally 30 variables) explain over 70% of the total variance for each group of data.

In Table 4.1 a comparison between different outputs for each concomitant disease is presented based on the results from factor analysis. Factor loadings with statistically significant values for each latent factor were included in the Table in order to describe statistically those clinical variables which are characteristic for each concomitant disease.

From the table it is evident that the clinical parameters are linked in such a way that a group of correlated indicators appear in very similar manner for each one of the

Table 4.1: Identified latent factors (variables with statistically significant factor loadings are involved) for each concomitant disease.

| Disease | Factor 1 | Factor 2 | Factor 3 | Factor 4 | Factor 5 |
|-----------|--|-----------------------|-------------------------|------------------|------------------|
| AH | ALAT, ASAT, GGT | Hb1Ac, EAG | Hgb, Er, | SysRR, diaRR | Weight, waist |
| CHD | Leu, eGFR, TSH | ALAT, ASAT | AF, HDL | Weight | SysRR, diaRR |
| OMI | Height, diaRR, crea, chol, Hb1Ac, EAG, Na, TSH | SysRR, Tg, ESR, K | Weight, waist, trom, Ca | Hgb Er, AF, UA | ALAT, ASAT, GGT |
| Stroke | Age, Hgb, Er, ALAT, ASAT, GGT, Na | Waist, Leu, | AF, chol, SUE, TSH | P | UA, Cl |
| DPNP | ALAT, ASAT, GGT | Crea | Hb1Ac, EAG | Waist | SysRRm diaRR, Na |
| DR | Crea, Hb1Ac, EAG, K, Cl | Hgb, Er, SUE, UA | ASAT, GGT, chol, TG | Weight, waist, | DiaRR, Na |
| DN | Age, weight, waist, TG | Tro, ASAT H1bAc, EAG, | AF | Leu, TSH | Crea |
| DMA | Age, ALAT, ASAT, | Leu, TSH | Crea, | waist | AF |
| Steatosis | Hb1A1c, EAG, SUE, Ca | ALAT, ASAT, GGT | Dur, weight, waist, | Age, sysRR, HDL' | Leu |

concomitant disease but with a different impact on the data structure (probably due to the specificity of the disease):

1. **ALAT, ASAT, GGT** group is *Factor 1* for **AH, Stroke, DPNP, DMA**;
2. **ALAT, ASAT, GGT** group is *Factor 2* for **CHD, Steatosis**;
3. **ALAT, ASAT, GGT** group is *Factor 5* for **OMI**;
4. **Hb1Ac, EAG** group is *Factor 1* for **OMI, Steatosis**;
5. **Hb1Ac, EAG** group is *Factor 2* for **AH, DN**;
6. **Hb1Ac, EAG** group is *Factor 3* for **DPNP**;
7. **Weight, Waist** group is *Factor 1* for **DN**;
8. **Weight, Waist** group is *Factor 3* for **OMI, Steatosis**;
9. **Weight, Waist** group is *Factor 4* for **DR**;
10. **SysRR, DiasRR** group is *Factor 4* for **AH**;
11. **SysRR, DiasRR** group is *Factor 5* for **CHD, DPNP**;
12. **Hgb, Er** group is *Factor 3* for **AH**;
13. **Hgb, Er** group is *Factor 4* for **OMI**;
14. **Hgb, Er** group is *Factor 2* for **DR**.

In the next step of the data interpretation the averages for each parameter for each concomitant disease and for all data were calculated. Thus, each disease was described by 30 averages and the input matrix had dimensions [10 × 30]. Applying multivariate statistics to the normalized data set following conclusions could be derived.

4.3.1 Clustering of the parameters (HCA)

Five clusters are formed:

- C4.1 (ASAT, ALAT, GGT, Hgb, Weight)
- C4.2 (Height, K. Crea, Ca, Er, P, TSH)
- C4.3 (TG, AF, Cl, diaRR, UA, Chol, SUE, SysRR)
- C4.4 (Waist, Leu, Na, eGFR, Tro)
- C4.5 (Age, Hb1Ac, EAG, DUR, HDL)

Clustering of the cases (all patients, nine concomitant diseases) (see Figures 4.1 and 4.2).

Three of the associated diseases are quite different (independent) from the rest (stroke, OMI and Steatosis), DR and DN form a small group and the remaining four plus all data set – another big cluster.

K-means clustering with hypothesis of formation of five supervised clusters of variables and three supervised clusters of cases gave the following results:

Cluster 4.1 contains six variables (*visceral obesity and thyroid function*)

Waist, Leu, Tro, eGFR, Na, TSH

Cluster 4.2 contains five variables: (*renal cluster*)

Er, kreatinin, K, Ca, P

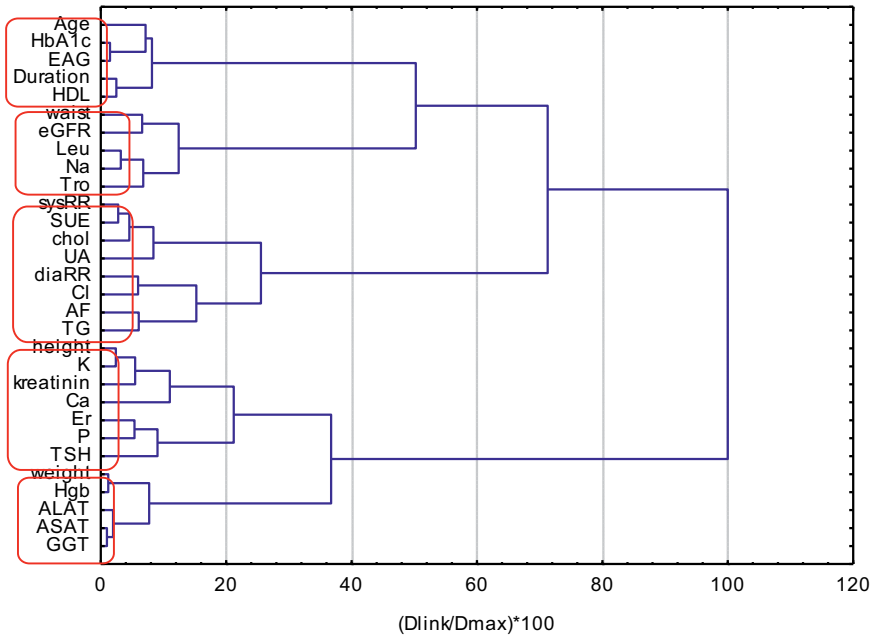


Figure 4.1: Hierarchical dendrogram for 30 parameters for all nine concomitant diseases and the set with all patients.

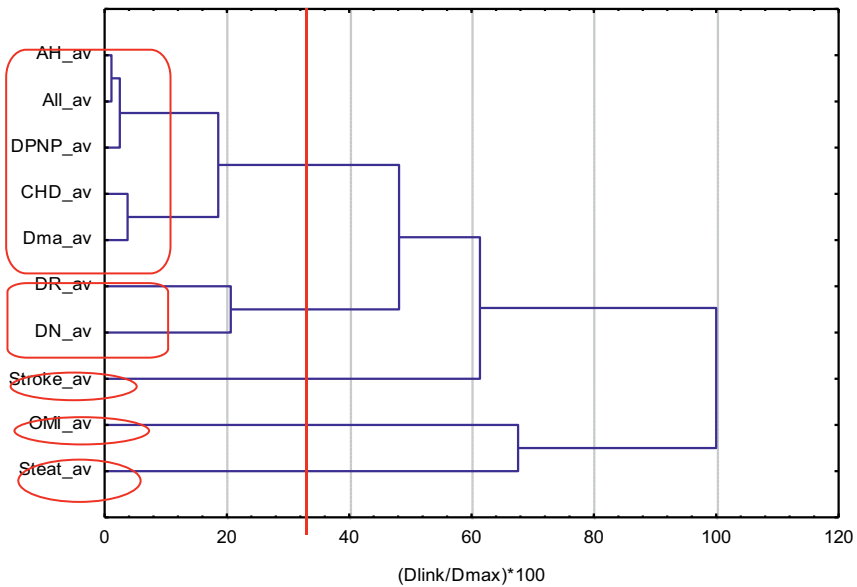


Figure 4.2: Hierarchical dendrogram for cases.

Cluster 4.3 contains nine variables: (*hepatic function and lipid metabolism*)

Height, weight, Hgb, ALAT, ASAT, GGT, AF, TG, Clen

Cluster 4.4 contains five variables: (*hypertension cluster*)

sysRR, diaRR, chol, ESR, UA

Cluster 4.5 contains five variables: (*aging and glucose control cluster*)

Age, Duration, HDL, HbA1c, EAG (see Figure 4.3)

K-means clustering of cases (concomitant diseases):

Three clusters scheme:

Cluster 4.1 contains two cases

| | Distance |
|----------|----------|
| OMI_av | 0.969395 |
| Steat_av | 0.969395 |

Cluster 4.2 contains six cases

| | Distance |
|-----------|----------|
| AH_av | 0.420243 |
| CHD_av | 0.515628 |
| Stroke_av | 1.141340 |
| DPNP_av | 0.361712 |
| Dma_av | 0.487910 |
| All_av | 0.414186 |

Cluster 4.3 contains two cases

| | Distance |
|-------|----------|
| DR_av | 0.535535 |
| DN_av | 0.535535 |

Cluster 4.1 (OMI and Steat) is characterized by *low levels of Age, Duration, blood pressure, cholesterol, HDL, SUE, uric acid* and **high levels of anthropometric parameters, Hgb, Leu, Tro, ASAT, ALAT, GGT, Na, P, TSH**, e.g., younger patients and shorter duration of disease (DMT2), relatively normal blood pressure, cholesterol and renal functions and worsened blood parameters, liver function and hormone level (see Figure 4.4).

Cluster 4.2 (AH, CHD, Stroke, DPNP, Dma, All) is characterized by the lowest levels of most of the clinical parameters but with enhanced values for Hb1Ac, EAG, SUE, eGFR, UA, e.g., worsened level of glucose (effect of DMT2 disease), some of the blood parameters and renal function parameters.

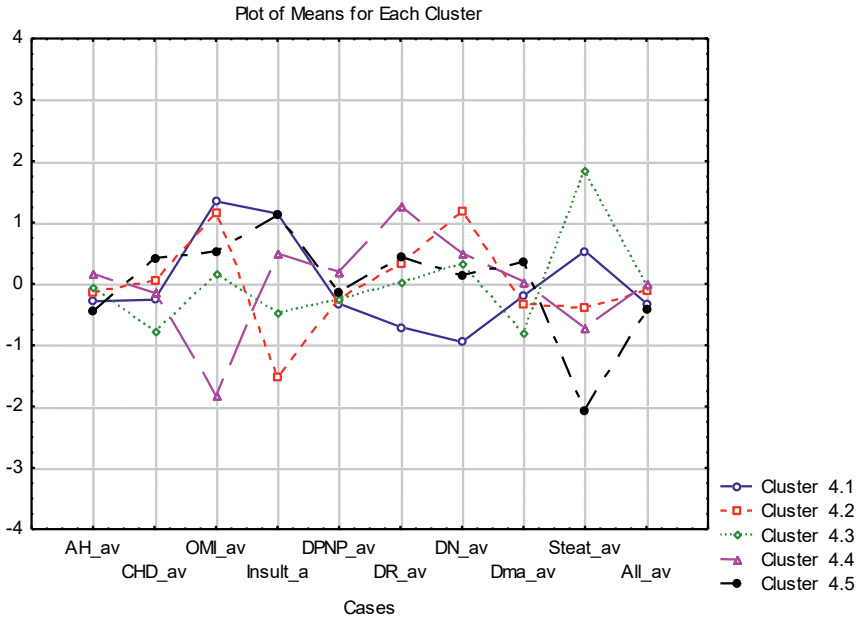


Figure 4.3: Plot of means of each identified cluster of parameters for each disease.

AH – very close averages for all clusters of parameters (no separate parameters seem to be very specific for this concomitant disease);

CHD – the same as previous case with AH but slight impact of parameters from clusters 4.3 (moderately decreased levels of ASAT, ALAT, GGT, AF, Cl, TG, Hgb, height, weight) and 4.5 (moderately increased levels of Age, duration, HDL, EAG, HbAc1);

OMI – very strong negative impact of parameters of cluster 4.4 (blood pressure indicators, chol, SUE and uric acid), significant positive impact of the parameters from clusters 4.1 and 4.2 (waist, LEU, Tro, eGFR, Na, TSH and Er, Crea, K, Ca, P, respectively);

Stroke – very significant negative impact of parameters of cluster 4.2 (Er, Crea, K, Ca, P) and significant positive impact of parameters from clusters 4.1, 4.4, 4.5;

DPNP – similar to AH;

DR – lower levels for parameters of cluster 4.1 and enhanced levels for parameters of cluster 4.4;

DN – lower levels for parameters of cluster 4.1 and enhanced levels for parameters of cluster 4.2;

DMA – similar to AH;

Steat – very strong negative impact for parameters in cluster five and significant negative impact by parameters in clusters 4.2 and 4.4; strong positive impact for parameters in cluster three and moderate positive impact for parameters in cluster 4.1;

All data – similar to AH (see Table 4.2).

Table 4.2: Parameter clusters impact for each concomitant disease (1+, 1- and 0 indicate the highest, the lowest and middle level of clinical indicators typical for each concomitant disease).

| Disease | C1+ | C1- | C1 ₀ | C2+ | C2- | C2 ₀ | C3+ | C3- | C3 ₀ | C4+ | C4- | C4 ₀ | C5+ | C5- | C5 ₀ |
|------------|-----|-----|-----------------|-----|-----|-----------------|-----|-----|-----------------|-----|-----|-----------------|-----|-----|-----------------|
| AH (51) | | | X | | | X | | | X | | | X | | | X |
| CHD (48) | | | X | | X | | | X | | | X | | X | | |
| OMI (7) | X | | | X | | | | | X | | X | | | | X |
| Stroke (9) | X | | | X | | | | | X | X | | | X | | |
| DPNP (51) | | | X | | | X | | X | X | | | X | | | X |
| DR (17) | | X | | | | X | | | X | | | | | | X |
| DN (16) | | X | | | X | | | X | | | X | | | | X |
| Dma (47) | | | X | | | X | | | X | | | X | | | X |
| Steat (12) | X | | | | X | | | | | | X | | | X | |
| All (52) | X | | | | | X | X | | | | X | X | | | X |

Similarity patterns: AH, DPNP, DMA, All.

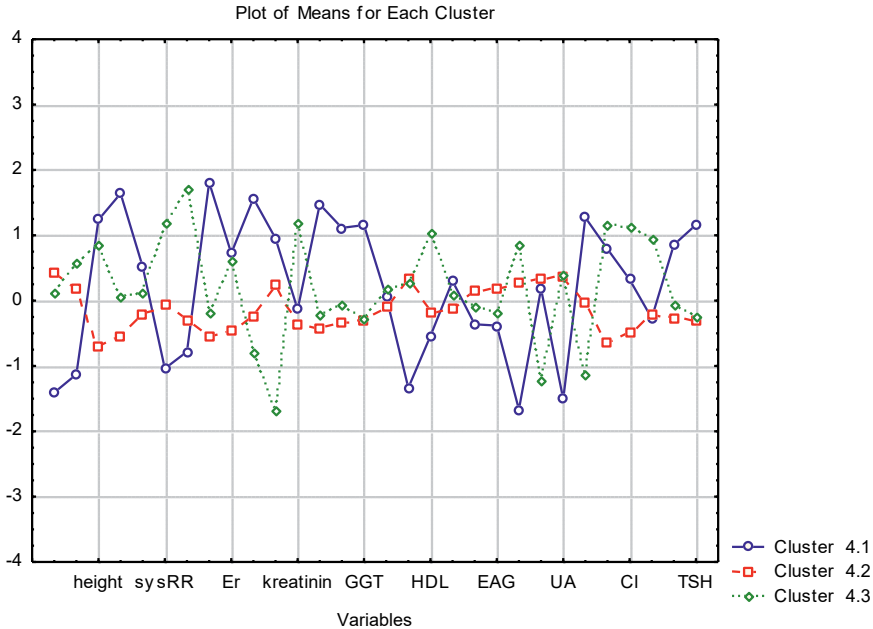


Figure 4.4: Plot of means for each parameter for each identified cluster of cases (diseases).

Cluster 4.3 (DR, DN) is characterized by low levels of Tro and high levels of blood pressure (sysRR and diasRR), creatinine, HDL, SUE, Ca, Cl, K, e.g., impaired renal function and blood circulation.

The two-way clustering confirms in general the results from K-means nonhierarchical cluster analysis (see Figure 4.5).

The factor analysis revealed five hidden factors determining over 90% of the total variance of the system. In Figure 4.6a the biplot Factor 1 versus Factor 2 plane is presented.

The formation of groups of parameters with similar factor loadings is indicated: (ASAT, ALAT, GGT); (duration, age, HDL); (HbA1c, EAG); (diasRR, sysRR, SUE, chol, UA, Ca, AF) etc. Again, as in hierarchical clustering and K-means, one could derive patterns of parameters similarity responsible for conditional latent factors affecting the data structure – enzymatic factor, anthropometric factor, glucose factor, blood and renal function factor.

Next figure from performing principal components analysis show the relationship between the nine concomitant diseases (plus all data results) (see Figures 4.6b and 4.7).

Our study revealed the risk profiles of diabetic patients with different microvascular and macrovascular complications. Almost all included patients were obese and hypertensive and most of them suffered from cardiovascular diseases, e.g., coronary heart disease. Approximately 13.5% of patients have survived myocardial infarction

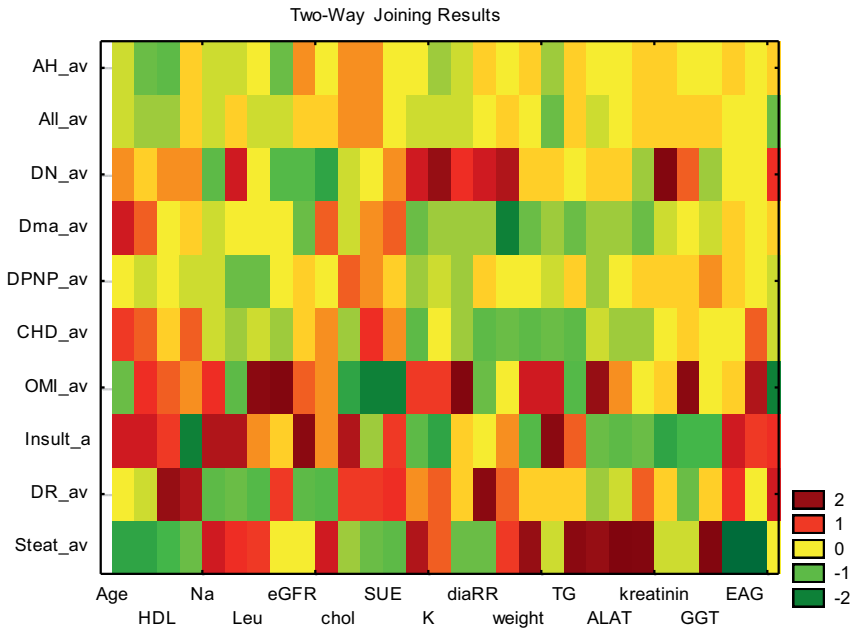


Figure 4.5: Two-way joining results for the correspondence between cases and variables.

and the most specific risk factors in their subgroup were the increased degree of visceral obesity, increased TSH levels suggesting mild thyroid dysfunction and worsened renal function. Abdominal obesity is a well-known risk factor for myocardial infarction that could be especially important in diabetic female patients [24, 25]. Hypothyroidism could promote obesity, hypertension and lipid abnormalities, but it might be also an independent risk factor for the development of atherosclerosis and cardiovascular incidents [26, 27]. Moreover, patients with elevated TSH levels and acute myocardial infarction have shown worse clinical outcome and increased mortality in comparison to patients with normal thyroid function [28]. Thyroid hormone replacement exerts anti-ischemic and cardioprotective effects [29], thus, it could reduce the risk of ischemic heart disease and acute myocardial infarction among hypothyroid diabetic individuals. The chronic kidney disease increases the risk of myocardial infarction and cardiovascular mortality in the general population and among diabetic patients even after adjustment for traditional cardiovascular risk factors [30, 31]. The linkage between diabetes, kidney impairment and cardiovascular diseases might be mediated by different mechanisms including hypertension, hypercoagulability, chronic inflammation, oxidative stress, endothelial dysfunction, disturbances of renin-angiotensin-aldosterone system, sympathetic activity and calcium-phosphate homeostasis [21]. The improvement of glucose control and other metabolic alterations through new therapeutic strategies such as

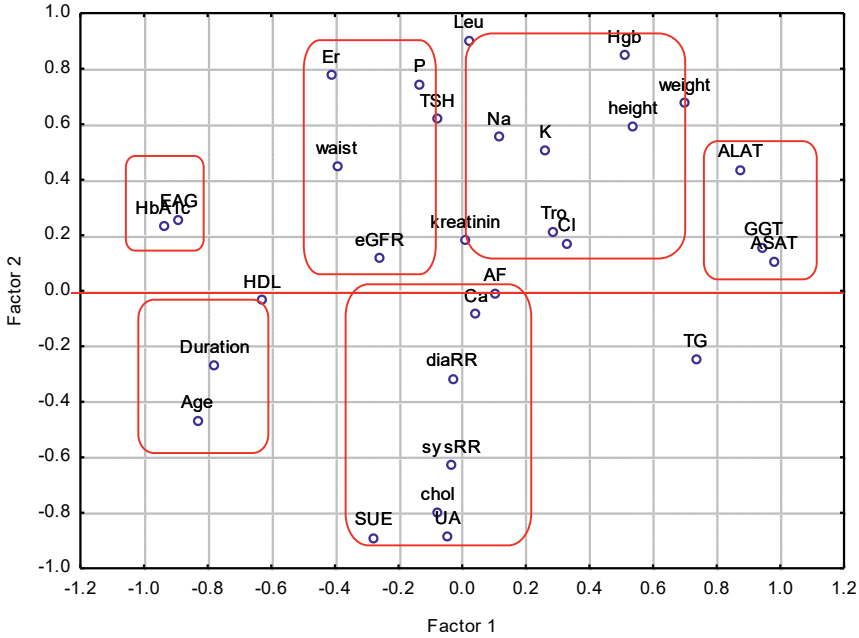


Figure 4.6a: Biplot factor 1 versus Factor 2 (factor loadings).

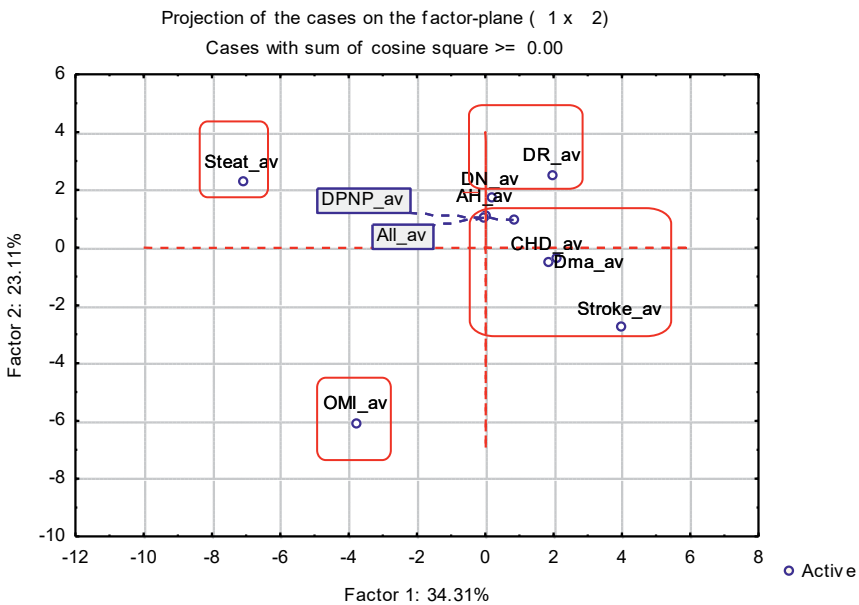


Figure 4.6b: Plot of factor scores for 10 cases.

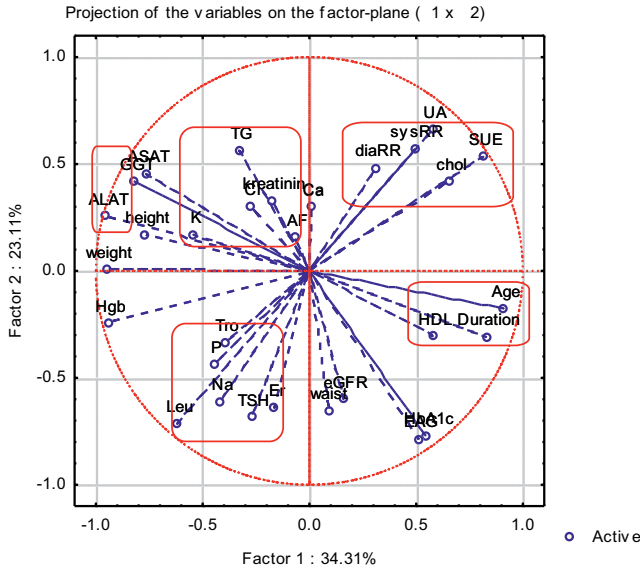


Figure 4.7: Factor loadings plot by PCA.

sodium glucose co-transporter 2 inhibitors and glucagon-like peptide-1 agonists might help to reduce both micro- and macrovascular complications of diabetes [32].

Interestingly, our results showed that the blood pressure and cholesterol levels of patients with MI were lower than in other patients which might be due to a more aggressive treatment and better adherence to lipid-lowering and antihypertensive treatment after the cardiovascular incident. Nonadherence to therapy as well as sub-optimal dosing has been described as main obstacles precluding the reduction of cardiovascular risk in many patients [33]. Therefore, more efforts should be taken to promote the primary cardiovascular prevention in diabetic patients.

Considering the common pathophysiological pathways in the development of diabetic macroangiopathy it might be suggested that similar risk factors predispose to the development of myocardial infarction and stroke. However, slight differences in the risk profile of patients have been observed in some studies [34]; (Naito et al. 2018). Japanese patients with acute coronary syndrome tended to be younger, more obese, and with increased prevalence of diabetes in comparison to patients with stroke who were more often hypertensive. Accordingly, our results showed increased blood pressure levels in diabetic patients with stroke unlike individuals with myocardial infarction. It is not clear if the differences between groups result from intrinsic differences in blood pressure levels or from different adherence to antihypertensives. Nevertheless, control of hypertension is an important strategy for risk reduction in patients. Additionally, age, duration of diabetes and increased HbA1c were all positively related to the presence of stroke. Duration of diabetes is a known risk factor for

stroke, while a U-shaped association between HbA1c and stroke has been described [35, 36]. Therefore, an individualized approach to glucose control instead of intensive glucose lowering has been strongly recommended by current studies [36, 37]. Interestingly, our results showed that the kidney dysfunction was more important risk factor for myocardial infarction than for stroke. Further studies are needed to prove or reject that suggestion.

Diabetic nephropathy was present in one third of the investigated patients. Disturbed renal function was found in that subgroup of patients as expected. The risk profile of individuals with diabetic nephropathy and diabetic retinopathy was similar, but in the latter group the influence of hypertension was more pronounced. These results support the need of aggressive hypertension treatment in order to prevent the development and progression of diabetic microvascular disturbances [38, 39].

Some complications in diabetic patients were not related to specific risk factors. Diabetic polyneuropathy was very common in the investigated group, and therefore, no specific factor could be associated with its development. Recent meta-analysis reported that significant risk factors for the neural alterations among diabetic patients were chronological age, duration of diabetes, poor glucose control and the presence of diabetic retinopathy, while obesity, smoking and dyslipidemia were not so important [40]. On the opposite, other studies considered obesity, smoking, and dyslipidemia as risk factors for the development of diabetic neuropathy [41–43]. Moreover, lipid abnormalities could be involved in the pathogenesis of neural damages in diabetic patients and thus, lipid lowering therapy might be considered as a possible tool in the complex management of diabetic neuropathy [42, 44]. Further studies are needed to identify the most important risk factors for the onset and progression of the diabetic neural damages.

Additional data processing revealed that all investigated complications might be separated in three main groups. Diabetic microvascular complications including retinopathy and nephropathy showed similar risk pattern with pronounced impact of the arterial hypertension. Most diabetic macrovascular complications along with diabetic neuropathy were influenced mainly by the worsening of the glucose control. Interestingly, the development of myocardial infarction and steatosis hepatics showed similar risk profile dominated by the influence of visceral obesity and thyroid dysfunction in relatively young patients with a short duration of diabetes and optimal glucose and blood pressure control. Nonalcoholic fatty liver disease is not considered as a traditional diabetic complication but it is very common among diabetic patients because of the underlying insulin resistance and concomitant obesity [45]. Current studies have reported conflicting results about the possible associations between hypothyroidism and nonalcoholic fatty liver disease (reviewed by Eshraghian et Hamidian Jahromi, [46]). Our results supported the hypothesis that increased TSH might be a risk factor for the development of hepatic steatosis.

A main limitation of our study was the small number of participants. Nevertheless, the present study revealed important differences in the risk profile of different diabetic

complications using a qualitatively new approach. The identifying of risk patterns that could interconnect different subgroups of patients with specific complications might be an important tool in the development of personalized medicine.

4.4 Conclusions

The exploratory data analysis reveals additional options for interpretation and modeling of clinical data. In this attempt to combine formal chemometrics with specific medical expertise a result is obtained which makes it possible to determine clinical descriptors for concomitant complications for group of patients with DMT2. It supports the whole medical protocol for treatment of the patients.

The novel approach not only identifies specific descriptors for medical complications of patients diagnosed with DMT2 but assists in decision making of the therapy options.

Acknowledgements: The authors would like to express their sincere gratitude to the National Science Fund (Project KP06 – OPR - 03/14) for the financial support.

Author contributions: All the authors have accepted responsibility for the entire content of this submitted manuscript and approved submission.

Research funding: This study was supported by National Science Fund (Project KP06 – OPR – 03/14).

Conflict of interest statement: The authors declare no conflicts of interest regarding this article.

References

1. American Diabetes Association. Classification and diagnosis of diabetes: standards of medical care in diabetes—2020. *Diabetes Care* 2020;43(1 Suppl):S14–31.
2. Deshpande AD, Harris-Hayes M, Schootman M. Epidemiology of diabetes and diabetes-related complications. *Phys Ther* 2008;88:1254–64.
3. Forbes JM, Cooper ME. Mechanisms of diabetic complications. *Physiol Rev* 2013;93:137–88.
4. Vithian K, Hurel S. Microvascular complications: pathophysiology and management. *Clin Med* 2010; 10:505–9.
5. Thomas RL, Halim S, Gurudas S, Sivaprasad S, Owens DR. IDF Diabetes Atlas: a review of studies utilising retinal photography on the global prevalence of diabetes related retinopathy between 2015 and 2018. *Diabetes Res Clin Pract* 2019;157:107840.
6. Flaxman SR, Bourne RRA, Resnikoff S, Ackland P, Braithwaite T, Cicinelli MV, et al. Vision Loss Expert Group of the Global Burden of Disease Study. Global causes of blindness and distance vision impairment 1990–2020: a systematic review and meta-analysis. *Lancet Glob Health* 2017;5: e1221–34.
7. Lee R, Wong TY, Sabanayagam C. Epidemiology of diabetic retinopathy, diabetic macular edema and related vision loss. *Eye Vis (Lond)* 2015;2:17.

8. Magliah SF, Bardisi W, Al Attah M, Khorsheed MM. The prevalence and risk factors of diabetic retinopathy in selected primary care centers during the 3-year screening intervals. *J Fam Med Prim Care* 2018;7:975–81.
9. Gross JL, de Azevedo MJ, Silveiro SP, Canani LH, Caramori ML, Zelmanovitz T. Diabetic nephropathy: diagnosis, prevention, and treatment. *Diabetes Care* 2005;28:164–76.
10. Magee C, Grieve DJ, Watson CJ, Brazil DP. Diabetic nephropathy: a tangled web to unweave. *Cardiovasc Drugs Ther* 2017;31:579–92.
11. Feldman EL, Callaghan BC, Pop-Busui R, Zochodne DW, Wright DE, Bennett DL, et al. Diabetic neuropathy. *Nat Rev Dis Prim* 2019;5:42.
12. Callaghan BC, Gao L, Li Y, Zhou X, Reynolds E, Banerjee M, et al. Diabetes and obesity are the main metabolic drivers of peripheral neuropathy. *Ann Clin Transl Neurol* 2018;5:397–405.
13. Pop-Busui R, Boulton AJ, Feldman EL, Bril V, Freeman R, Malik RA, et al. Diabetic neuropathy: a position statement by the American diabetes association. *Diabetes Care* 2017;40:136–54.
14. Kannel WB, McGee DL. Diabetes and cardiovascular disease. The Framingham study. *J Am Med Assoc* 1979;241:2035–8.
15. Emerging Risk Factors Collaboration, Sarwar N, Gao P, Seshasai SR, Gobin R, Kaptoge S, et al. Diabetes mellitus, fasting blood glucose concentration, and risk of vascular disease: a collaborative meta-analysis of 102 prospective studies. *Lancet* 2010;375:2215–22.
16. Murcia AM, Hennekens CH, Lamas GA, Jiménez-Navarro A, Rouleau JL, Flaker GC, et al. Impact of diabetes on mortality in patients with myocardial infarction and left ventricular dysfunction. *Arch Intern Med* 2004;164:2273–9.
17. Thiruvoipati T, Kielhorn CE, Armstrong EJ. Peripheral artery disease in patients with diabetes: epidemiology, mechanisms, and outcomes. *World J Diabetes* 2015;6:961–9.
18. Beckman JA, Creager MA. Vascular complications of diabetes. *Circ Res* 2016;118:1771–85.
19. Gregg EW, Li Y, Wang J, Rios Burrows N, Ali MK, Rolka D et al. Changes in diabetes-related complications in the United States, 1990–2010. *N Engl J Med* 2014;370:1514–23.
20. Orasanu G, Plutzky J. The pathologic continuum of diabetic vascular disease. *J Am Coll Cardiol* 2009;53(5 Suppl):S35–42.
21. Pálsson R, Patel UD. Cardiovascular complications of diabetic kidney disease. *Adv Chron Kidney Dis* 2014;21:273–80.
22. Massart D, Kaufman L. The interpretation of chemical analytical data by the use of cluster analysis. NY: J. Wiley; 1983.
23. Vandeginste B. Chemometrics – general introduction and historical perspective. 2006. https://doi.org/10.1007/3-540-17308-0_1.
24. Cao Q, Yu S, Xiong W, Li Y, Li H, Li J, et al. Waist-hip ratio as a predictor of myocardial infarction risk: a systematic review and meta-analysis. *Medicine (Baltim)* 2018;97:e11639.
25. Peters SAE, Bots SH, Woodward M. Sex differences in the association between measures of general and central adiposity and the risk of myocardial infarction: results from the UK Biobank. *J Am Heart Assoc* 2018;7: e008507.
26. Kahaly GJ. Cardiovascular and atherogenic aspects of subclinical hypothyroidism. *Thyroid* 2000; 10:665–79.
27. Hak AE, Pols HA, Visser TJ, Drexhage HA, Hofman A, Witteman JC. Subclinical hypothyroidism is an independent risk factor for atherosclerosis and myocardial infarction in elderly women: the Rotterdam Study. *Ann Intern Med* 2000;132:270–8.
28. Seo SM, Koh YS, Park HJ, Kim DB, Her SH, Lee JM, et al. Thyroid stimulating hormone elevation as a predictor of long-term mortality in patients with acute myocardial infarction. *Clin Cardiol* 2018;41: 1367–73.
29. von Hafe M, Neves JS, Vale C, Borges-Canha M, Leite-Moreira A. The impact of thyroid hormone dysfunction on ischemic heart disease. *Endocr Connect* 2019;8:R76–90.

30. Meisinger C, Döring A, Löwel H, KORA Study Group. Chronic kidney disease and risk of incident myocardial infarction and all-cause and cardiovascular disease mortality in middle-aged men and women from the general population. *Eur Heart J* 2006;27:1245–50.
31. Amod A, Buse JB, McGuire DK, Pieber TR, Pop-Busui R, Pratley RE, et al. Glomerular filtration rate and associated risks of cardiovascular events, mortality, and severe hypoglycemia in patients with type 2 diabetes: secondary analysis (DEVOTE 11). *Diabetes Ther* 2020;11:53–70.
32. Maqbool M, Cooper ME, Jandeleit-Dahm KAM. Cardiovascular disease and diabetic kidney disease. *Semin Nephrol* 2018;38:217–32.
33. Banach M, Stulc T, Dent R, Toth PP. Statin non-adherence and residual cardiovascular risk: there is need for substantial improvement. *Int J Cardiol* 2016;225:184–96.
34. Uchiyama S, Shibata Y, Hirabayashi T, Mihara B, Hamashige N, Kitagawa K, et al. J-TRACE Investigators. Risk factor profiles of stroke, myocardial infarction, and atrial fibrillation: a Japanese Multicenter Cooperative Registry. *J Stroke Cerebrovasc Dis* 2010;19:190–7.
35. Banerjee C, Moon YP, Paik MC, Rundek T, Mora-McLaughlin C, Vieira JR, et al. Duration of diabetes and risk of ischemic stroke: the Northern Manhattan Study. *Stroke* 2012;43:1212–7.
36. Shen Y, Shi L, Nauman E, Katzmarzyk P, Price-Haywood E, Bazzano A, et al. Association between hemoglobin A1c and stroke risk in patients with type 2 diabetes. *J Stroke* 2020;22:87–98.
37. Action to Control Cardiovascular Risk in Diabetes Study Group, Gerstein HC, Miller ME, Byington RP, Goff DC Jr, Bigger JT, et al. Effects of intensive glucose lowering in type 2 diabetes. *N Engl J Med* 2008;358:2545–59.
38. Hovind P, Tarnow L, Rossing K, Rossing P, Eising S, Larsen N, et al. Decreasing incidence of severe diabetic microangiopathy in type 1 diabetes. *Diabetes Care* 2003;26:1258–64.
39. Cardoso CRL, Leite NC, Dib E, Salles GF. Predictors of development and progression of retinopathy in patients with type 2 diabetes: importance of blood pressure parameters. *Sci Rep* 2017;7:4867.
40. Liu X, Xu Y, An M, Zeng Q. The risk factors for diabetic peripheral neuropathy: a meta-analysis. *PLoS One* 2019;14:e0212574.
41. Ziegler D, Rathmann W, Dickhaus T, Meisinger C, Mielck A, KORA Study Group. Prevalence of polyneuropathy in pre-diabetes and diabetes is associated with abdominal obesity and macroangiopathy: the MONICA/KORA Augsburg Surveys S2 and S3. *Diabetes Care* 2008;31:464–9.
42. Davis TM, Yeap BB, Davis WA, Bruce DG. Lipid-lowering therapy and peripheral sensory neuropathy in type 2 diabetes: the Fremantle Diabetes Study. *Diabetologia* 2008;51:562–6.
43. Papanas N, Ziegler D. Risk factors and comorbidities in diabetic neuropathy: an update 2015. *Rev Diabet Stud* 2015;12:48–62.
44. Perez-Matos MC, Morales-Alvarez MC, Mendivil CO. Lipids: a suitable therapeutic target in diabetic neuropathy? *J Diabetes Res* 2017:6943851.
45. Bhatt HB, Smith RJ. Fatty liver disease in diabetes mellitus. *Hepatobiliary Surg Nutr* 2015;4:101–8.
46. Eshraghian A, Hamidian Jahromi A. Non-alcoholic fatty liver disease and thyroid dysfunction: a systematic review. *World J Gastroenterol* 2014;20:8102–9.

Moses M. Edim, Hitler Louis*, Emmanuel A. Bisong,
Apebende G. Chioma, Obieze C. Enudi, Tomsmith O. Unimuke,
Asuquo B. Bassey, David Prince, Queen O. Sam,
Emmanuel I. Ubana and Tiyati H. Mujong

5 Electronic structure theory study of the reactivity and structural molecular properties of halo-substituted (F, Cl, Br) and heteroatom (N, O, S) doped cyclobutane

Abstract: Cyclobutane and its halo-substituted derivatives and its heteroatom doped derivatives have been extensively investigated in this study because of the vast applications and interesting chemistry associated with them, the vibrational assignments, Natural Bond Orbital (NBO) analysis, Conceptual Density Functional Theory, Quantum Mechanical Descriptors and Molecular Electrostatic Potential (MEP) analysis have been explored in this study. The corresponding wavenumbers of the studied compounds have as well been assigned by Potential Energy Distribution analysis. Several inter and intramolecular hyperconjugative interactions within the studied compounds have been revealed by the NBO analysis with a confirmation of geometric hybridization and electronic occupancy. The compounds reactivity was observed to decrease down the halo group in manners such as the stability, both were observed to decrease from azetidine to thietane. The distribution of charge was observed to be affected by the ring substituent as observed from the charge population analysis; in addition, adjacent atoms are very much affected by the inherent properties of the substituted atoms. The NBO result suggests that the molecules are stabilized by lone pair delocalization of electrons from the substituted atoms and molecular electrostatic potential (MEP) studies revealed that substituted halogens and doped heteroatoms are important and most probable sites of electrostatic interactions.

Keywords: cyclobutane; descriptors; MEP; NBO.

*Corresponding author: Hitler Louis, Computational and Bio-Simulation Research Group, University of Calabar, Calabar, Nigeria, E-mail: louismuzong@gmail.com

Moses M. Edim, Computational and Bio-Simulation Research Group, University of Calabar, Calabar, Nigeria; and Department of Chemistry, Cross River University of Technology, Calabar Nigeria

Emmanuel A. Bisong, Apebende G. Chioma, Obieze C. Enudi, Tomsmith O. Unimuke, Asuquo B. Bassey, David Prince, Queen O. Sam and Emmanuel I. Ubana, Computational and Bio-Simulation Research Group, University of Calabar, Calabar, Nigeria

Tiyati H. Mujong, Universite Claude Bernard, Lyon, France

This article has previously been published in the journal *Physical Sciences Reviews*. Please cite as: M. M. Edim, H. Louis, E. A. Bisong, A. G. Chioma, O. C. Enudi, T. O. Unimuke, A. B. Bassey, D. Prince, Q. O. Sam, E. I. Ubana and T. H. Mujong "Electronic structure theory study of the reactivity and structural molecular properties of halo-substituted (F, Cl, Br) and heteroatom (N, O, S) doped cyclobutane" *Physical Sciences Reviews* [Online] 2021, 7. DOI: 10.1515/psr-2020-0138 | <https://doi.org/10.1515/9783110739763-005>

5.1 Introduction

Lower members of the Cycloalkanes have been of interesting study over the years because of the high reactivity of cyclopropane which seems to have a connected effect with other higher members. Cyclobutane is a colorless gas and commercially available as a liquefied gas with a molecular formula $(\text{CH}_2)_4$ [1]. Cyclobutane is a cycloalkane with carbon atoms attached in the form of a closed ring [2]. An atom or group of atoms that substitute carbon atom gives the compound unique chemical properties and consequently determines its reactivity [3].

The compound cyclopropane easily reacts with bromine to form 1,3-dibromopropane and also with sulfuric acid to give 1-propylsulfuric acid. These cyclobutanes undergo C–C bond cleavage with transition metal species. Series of methods have been used for the synthesis of cyclobutanes. Upon irradiation of UV-light alkenes, dimerization occurs. The dehalogenation of 1,4-dihalobutanes in the presence of reducing metals affords cyclobutanes. This compound was first synthesized in 1907 by the hydrogenation of cyclobutene in the presence of nickel [4].

Cyclobutane is effortlessly available by several techniques of synthesis with better yields. Basically, because of the inherent ring strain, these reactive cleavages of cyclobutane bond are facile; the reaction mechanism determines the reaction rate and cleavage point, also the nature of ring substituents, reagents, and conditions of reactions. Derivatives of cyclobutane are mostly used as starting materials for the production of both cyclic and acyclic systems and heterobicyclic and oligocyclic compounds [5]. The reactivity of cyclobutane can be enhanced when doped [6]. Interestingly, the halogenated cycloalkanes have not been theoretically investigated exhaustively. Several pharmaceuticals and cyclic natural products mostly contain halogenated cycloalkanes and vast information of their properties and synthetic procedures have been investigated and reported in the literature [7].

The need to elucidate the conceptual density functional theory (CDFT), geometrical properties, and other electronic properties of the doped cycloalkane give credence to this study which will eventually widen the horizon for the theoretical study of cycloalkanes in general.

5.2 Computational details

Quantum chemical calculations have been performed using the Gaussian 09W package and Gauss view 6.0 [8, 9], and the vibrational properties of the compounds were rendered by the Vibrational Energy Distribution Analysis (VEDA) 4 software [10]. The natural Bond Orbital (NBO) 7.0 Program was used to calculate the inter and intramolecular hyperconjugative interactions in the molecule whereas the UCA FUKUI software was used to analyze the results accordingly [11]. The Multiwfn program [12]

Table 5.1: Calculated vibrational frequency for cyclobutane and its studied derivatives B3LYP method and 6-311++G(d, p) basic set.

| Unscaled frequency (cm ⁻¹) | Scaled frequency (cm ⁻¹) | Assignments with % of PED |
|--|--------------------------------------|---|
| Cyclobutane | | |
| 3104 | 2984 | ν CH (99) |
| 3088 | 2969 | ν CH asy (18) + ν CH (82) |
| 3059 | 2941 | ν CH (82) + ν CH (18) |
| 3052 | 2934 | ν CH (99) |
| 3052 | 2934 | ν CH (99) |
| 3049 | 2932 | ν CH (100) |
| 1511 | 1453 | β HCH (97) |
| 1475 | 1418 | β HCH (98) |
| 1469 | 1413 | β HCH (99) |
| 1469 | 1413 | β HCH (98) |
| 1273 | 1224 | τ HCCC asy (75) |
| 1273 | 1224 | τ HCCC (73) |
| 1247 | 1199 | β HCC (25) + τ HCCC (59) |
| *1237 | 1189 | τ HCCC (92) |
| 1236 | 1188 | β HCC (43) + τ HCCC (19) + τ HCCC (10) + τ HCCC (11) |
| 1236 | 1188 | β HCC (48) + β CCC asy (12) + τ HCCC asy (13) |
| 1167 | 1122 | β HCC asy (25) + τ HCCC (24) + τ CCCC (46) |
| 1160.08 | 1115 | ν CC (12) + β HCC (27) + τ HCCC (55) |
| 1018 | 978 | ν CC (96) |
| 953 | 916 | β HCC (64) + τ HCCC (100) + τ HCCC (26) |
| 944 | 908 | ν CC asy (82) |
| 911 | 876 | ν CC (81) |
| 879 | 846 | β CCC (41) + β HCC (24) + τ HCCC asy (20) |
| *749 | 720 | β HCC (36) + τ HCCC asy (31) |
| 642 | 617 | β HCC (50) + β HCC asy (27) + τ HCCC (18) |
| Azetidane (N) | | |
| 3508 | 3372 | ν NH (100) |
| 3139 | 3018 | ν CH (98) |
| 3084 | 2965 | ν CH (90) |
| 3069 | 2951 | ν CH (90) |
| 3067 | 2949 | ν CH asy (10) + ν CH (82) |
| 2998 | 2882 | ν CH (92) |
| 2994 | 2878 | ν CH (90) |
| 1524 | 1465 | β HCH (81) |
| 1496 | 1438 | β HCH (93) |
| 1475 | 1413 | β HCH (89) |
| 1368 | 1316 | β HNC (52) + τ HNCC (28) |
| 1335 | 1283 | τ HCNC asy (74) |
| 1262 | 1213 | τ HCNC (69) |
| 1251 | 1203 | τ HCCN asy (78) |
| 1204 | 1157 | β HCN (44) + τ HCCN asy (13) + τ HCNC (20) + τ CNCC (10) |
| 1192 | 1146 | β HCC asy (48) + τ HCCN (33) |

Table 5.1: (continued)

| Unscaled frequency (cm ⁻¹) | Scaled frequency (cm ⁻¹) | Assignments with % of PED |
|--|--------------------------------------|--|
| 1159 | 1115 | β HCN (40) + τ CNCC asy (30) |
| 1102 | 1059 | β HCC (77) |
| 1041 | 1000 | ν CC (86) |
| 1012 | 973 | ν NC (73) + ν CC (10) |
| 975 | 937 | ν CC asy (10) + β CNC (47) + τ HNCC (14) + τ HCNC (10) |
| 930 | 894 | ν CC (27) + β CCN (28) + τ HCCN (25) |
| 919 | 883 | ν CC asy (30) + β CCN (28) + τ HCCN (25) |
| 824 | 792 | β HCC (12) + τ HCNC asy (63) |
| 745 | 716 | β HCC asy (10) + τ HNCC asy (15) + τ HCCN asy (11) + τ HCNC asy (37) |
| 660 | 635 | β CNC asy (32) + β HCH (10) + β HNC asy (13) + τ HNCC (18) + τ HCNC asy (14) |
| 209 | 201 | τ HCCN (22) + τ CNCC (49) |
| Oxetane (O) | | |
| 3139 | 3018 | ν CH asy (96) |
| 3083 | 2964 | ν CH (99) |
| 3073 | 2954 | ν CH asy (10) + ν CH asy (81) |
| 3071 | 2952 | ν CH (95) |
| 3032 | 2915 | ν CH (81) + ν CH asy (10) |
| 3023 | 2907 | ν CH (81) + ν CH (10) |
| 1526 | 1467 | β HCH (10) + β HCH (83) |
| 1499 | 1441 | β HCH (94) |
| 1480 | 1423 | β HCH (87) + β HCH asy (10) |
| 1354 | 1301 | τ HCOC (21) + τ HCCO asy + τ HCOC asy + τ COCC (21) |
| 1291 | 1241 | τ HCOC asy (23) + τ HCCO (23) + τ HCOC asy (21) + τ HCCO (23) |
| 1242 | 1194 | τ HCOC asy (45) + τ HCCO (39) |
| 1223 | 1175 | β HCC (38) + τ HCOC asy (34) |
| 1184 | 1138 | β HCC asy (11) + β HCO (20) + τ HCCO asy (16) + τ HCCO (16) + τ COCC (26) |
| 1146 | 1102 | β HCO (90) |
| 1135 | 1091 | β HCO (78) + τ COCC asy (14) |
| 1042 | 1002 | ν CC (90) |
| 1021 | 981 | ν OC (85) |
| 942 | 905 | ν CC asy (35) + ν OC asy (35) + ν OC(12) + β CCO (40) + β COC (40) |
| 918 | 883 | ν CC (49) + ν OC (49) + β CCO (35) + β COC (35) |
| 831 | 799 | β HCC asy (16) + τ HCOC (14) + τ HCOC asy (20) + τ HCCO asy (20) + τ HCOC asy (20) + τ HCOC asy (13) + τ HCOC asy (20) |
| 809 | 778 | β CCO (94) + β COC (94) |
| 764 | 734 | β HCC (30) + τ HCCO (33) |
| THIETANE (S) | | |
| 3137 | 3015 | ν CH (15) + ν CH (81) |
| 3132 | 3011 | ν CH (96) |
| 3102 | 2983 | ν CH (78) + ν CH asy (14) |

Table 5.1: (continued)

| Unscaled frequency (cm ⁻¹) | Scaled frequency (cm ⁻¹) | Assignments with % of PED |
|--|--------------------------------------|--|
| 3069 | 2951 | ν CH (86) |
| 3068 | 2949 | ν CH (96) |
| 3051 | 2933 | ν CH (88) |
| 1494 | 1436 | β HCH (88) |
| 1468 | 1411 | β HCH asy (92) |
| 1466 | 1409 | β HCH (86) + τ HCSC asy (12) |
| 1299 | 1249 | β HCC asy (21) + β HCS asy (21) + τ HCCS asy (20) + τ HCSC asy (20) + τ HCCS (42) |
| 1241 | 1193 | β HCC asy (14) + β HCS asy (14) + τ HCCS (74) + τ HCSC (74) |
| 1239 | 1191 | τ HCSC asy (45) + τ HCSC (17) |
| 1194 | 1148 | τ HCSC (48) + τ SCCC asy (22) |
| 1179 | 1133 | τ HCSC (76) |
| 1021 | 982 | β HCC asy (63) + β HCS asy (63) + τ HCCS (21) + τ HCSC (21) |
| 989 | 951 | ν CC asy (75) + τ HCCS (14) + τ HCSC (14) |
| 975 | 937 | ν CC asy (19) + ν SC (66) |
| 942 | 906 | ν CC (63) + β HCS (22) |
| 842 | 809 | β CCC (44) + τ HCCS (14) + τ HCSC asy (19) |
| 822 | 791 | β HCC (32) + β HCS (32) + τ HCCS asy (56) + τ HCSC asy (56) |
| 701 | 674 | ν SC (17) + β CCC (38) + τ HCSC (12) |
| 664 | 638 | ν SC (41) + β SCC asy (40) |
| 531 | 510 | ν SC (37) + β SCC (46) |
| Flourocyclobutane | | |
| 3138 | 3017 | ν CH (81) |
| 3127 | 3006 | ν CH (99) |
| 3119 | 2999 | ν CH asy (25) + ν CH (62) |
| 3076 | 2957 | ν CH (87) |
| 3073 | 2955 | ν CH asy (65) + ν CH asy (27) |
| 3069 | 2951 | ν CH (91) |
| 3067 | 2949 | ν CH (99) |
| 1500 | 1442 | β HCH (90) |
| 1474 | 1417 | β HCH asy (93) |
| 1459 | 1403 | β HCH (96) |
| 1366 | 1313 | Opd CCCH asy (83) |
| 1296 | 1246 | β HCC (59) + τ HCCC asy (11) |
| 1258 | 1209 | β HCC asy (18) + τ HCCC (37) |
| 1240 | 1192 | β HCC (17) + τ HCCC (54) |
| 1232 | 1184 | β HCC asy (11) + β HCC (43) + τ HCCC asy (17) |
| 1229 | 1182 | β HCC asy (32) + β HCC asy (14) + τ HCCC (22) |
| 1179 | 1134 | τ HCCC (760) |
| 1144 | 1099 | τ CCCC (52) |
| 1089 | 1047 | ν CC (86) |
| 1061 | 1020 | ν CC (50) + τ HCCC asy (18) |
| 956 | 919 | ν CC (58) + ν FC (58) + β CCC (15) |
| 941 | 904 | ν CC asy (11) + β HCH (11) + β HCC (15) + τ HCCC asy (23) |

Table 5.1: (continued)

| Unscaled frequency (cm ⁻¹) | Scaled frequency (cm ⁻¹) | Assignments with % of PED |
|--|--------------------------------------|--|
| 912 | 876 | ν CC asy (17) + ν CC asy (27) + β CCC (35) |
| 905 | 870 | ν CC (31) + τ HCCC asy (16) |
| 778 | 748 | τ HCCC (40) |
| 754 | 725 | ν CC (11) + β HCC (20) + τ HCCC (40) |
| 607 | 587 | ν CC (14) + ν FC (14) + β CCC (53) |
| 446 | 429 | ν CC asy (10) + ν FC asy (10) + τ HCCC (14) + τ CCCC asy (32) + Opd FCCC asy (32) + τ CCCC (21) |
| 364 | 349 | ν CC asy (10) + β FCC (83) |
| Chlorocyclobutane | | |
| 3144 | 3022 | ν CH (89) |
| 3134 | 3011 | ν CH (99) |
| 3122 | 3002 | ν CH (10) + ν CH asy (80) |
| 3109 | 2989 | ν CH (88) + ν CH (10) |
| 3077 | 2958 | ν CH (16) + ν CH (81) |
| 3072 | 2954 | ν CH (99) |
| 3070 | 2952 | ν CH (81) + ν CH asy (17) |
| 1499 | 1442 | β HCH (92) |
| 1474 | 1417 | β HCH asy (95) |
| 1464 | 1408 | β HCH (96) |
| 1295 | 1245 | Opd CCCH (72) |
| 1280 | 1231 | β HCC (65) |
| 1254 | 1206 | β HCC asy (13) + τ HCCC asy (17) + τ HCCC (21) + Opd CCCH (21) |
| 1239 | 1191 | β HCC (33) + τ HCCC asy (22) + τ HCCC (11) |
| 1235 | 1188 | β HCC asy (12) + τ HCCC (11) + τ HCCC (39) + τ HCCC (15) + Opd CCCH (15) |
| 1219 | 1171 | β HCC asy (18) + τ HCCC asy (25) + τ CCCC asy (10) |
| 1183 | 1137 | β HCC asy (11) + τ HCCC (52) |
| 1110 | 1067 | ν CC (10) + β HCC (10) + τ CCCC (43) |
| 1046 | 1005 | ν CC (60) |
| 1032 | 992 | ν CC (56) + ν CC (14) |
| 946 | 909 | ν CC asy (10) + β CCC asy (12) + β HCC asy (28) |
| 914 | 879 | ν CC asy (46) + β CCC (27) |
| 912 | 877 | ν CC asy (10) + ν CC (19) + β CCC (17) + τ HCCC asy (11) + Opd CCCH asy (11) |
| 835 | 803 | ν ClC (17) + β CCC (51) |
| 778 | 748 | β HCC (23) + τ HCCC (24) |
| 721 | 693 | ν ClC asy (17) + β HCC (14) + τ HCCC (26) |
| 525 | 505 | ν ClC (25) + β CCC asy (16) + τ HCCC asy (18) |
| 363 | 349 | ν ClC (32) + β HCCC (18) + τ CCCC (20) + Opd ClCCC (20) |
| Bromocyclobutane | | |
| 3141 | 3019 | ν CH (87) |
| 3136 | 3015 | ν CH (88) |
| 3129 | 3009 | ν CH (84) + ν CH asy (16) |

Table 5.1: (continued)

| Unscaled frequency (cm ⁻¹) | Scaled frequency (cm ⁻¹) | Assignments with % of PED |
|--|--------------------------------------|--|
| 3120 | 2999 | ν CH asy (90) |
| 3075 | 2957 | ν CH (97) |
| 3057 | 2939 | ν CH (83) |
| 3053 | 2936 | ν CH (15) + ν CH (84) |
| 1489 | 1431 | β HCH (92) |
| 1464 | 1407 | β HCH asy (94) |
| 1453 | 1397 | β HCH (96) |
| 1274 | 1224 | τ HCCC asy (70) |
| 1269 | 1221 | β HCC (12) + τ HCCC (48) |
| 1251 | 1203 | β HCC (14) + τ HCCC (57) + Opd CCCH (57) |
| 1242 | 1194 | β HCC asy (24) + τ HCCC (40) |
| 1238 | 1191 | β HCC asy (10) + β HCC (66) |
| 1195 | 1149 | β HCC asy (34) + τ HCCC (32) + Opd CCCH (32) |
| 1173 | 1127 | ν CC (12) + β HCC (11) + τ HCCC asy (15) + τ HCCC asy (45) |
| 1069 | 1028 | ν CC (12) + τ HCCC asy (11) + τ HCCC asy (15) + Opd CCCH asy (15) + τ CCCC asy (34) |
| 1053 | 1012 | ν CC asy (11) + β HCC asy (10) + τ HCCC (45) |
| 1016 | 976 | ν CC (74) + τ CCCC (10) |
| 951 | 914 | ν CC asy (66) |
| 919 | 884 | ν CC asy (17) + β CCC (12) + β HCC (13) + β CCC (39) |
| 914 | 879 | ν CC (49) + β CCC asy (15) |
| 847 | 815 | β CCC asy (43) + β HCC (12) + β CCC asy (16) |
| 741 | 712 | β HCC (34) + β HCC (10) + β HCC asy (10) |
| 679 | 653 | β CCC (12) + β HCC (31) + τ HCCC asy (18) |
| 523 | 503 | ν BrC (64) + τ CCCC (12) + Opd BrCCC (12) |
| 283 | 272 | ν BrC (30) + τ CCCC (43) |
| 281 | 269 | β BrCC (93) |

was equally used in explaining theoretically the Chemistry and the electronic structural analysis of the CDFT descriptors of cyclobutane. The Gaussian 09W and Gaussview 6.0 software were used for the ground state Geometry optimization of the studied compounds using the DFT/B3LYP method at 6-311++G(d,p) basis set [13].

5.3 Results and discussion

5.3.1 Vibrational analysis

The fundamental modes of cyclobutene and its derivatives in relation to the vibrational assignments connected with hypothetical IR absorbance and normal modes

characterized by PED are listed in Table 5.1. The vibrational calculation is focused on the valuation of the vibrational modes related to the significant and precise skeletal structure of the investigated molecules. The fundamental maximum vibrational modes are equivalent to $(3N - 6)$ for a nonlinear molecule [14] (Table 5.2).

When computational methods are used to theoretically predict normal vibrations of small and complex systems; the idea of scaling is often used to afford computed wavenumbers. This is because of the notion that hybrid DFT functionals overestimate vibrational frequencies under harmonic approximation, thus several literature reports have proposed scale factors for correcting this systematic error [15–17]. Therefore, the B3LYP/6-311++G(d,p) has been adopted in this study to calculate vibrational frequencies according to [18, 19] the computed frequencies were then multiplied by a scale factor as proposed by Scott and Radom to reduce the overall deviations from experimental values. It is worth mentioning that the scale factor does not result in any change in the manner of the calculated intensity patterns of the simulated spectra because the vibrational modes are not affected; both scaled and unscaled vibrational frequencies of the studied systems are reported in Table 5.1, respectively.

C–H vibrations

C–H vibrations are traditionally located around frequencies $2800\text{--}3300\text{ cm}^{-1}$, at which its positions are highly dependent on the hybridization of the carbon atom [19–22]. PED assignments for the optimized and studied cyclobutane structure are compared with results obtained from the NIST database, for correlation [23]. Saturated C–H stretches occurred at $2984, 2669, 2940, 2933,$ and 2932 cm^{-1} , which are within the range of normal sp^3 hybridized C–H stretch. These are comparable with $2895, 2893,$ and 2887 cm^{-1} obtained from the database. H–C–H bends occurred at frequencies; $1453, 1418, 1412,$ and 1188 cm^{-1} , that are also comparable to 1219 cm^{-1} from NIST data [21].

Table 5.2: Calculated quantum descriptors for cyclobutane and its studied derivatives B3LYP method and 6-311++G(d, p) basic set.

| Compound | CBT | BrCB | CICB | FCB | Azetidane | Oxetane | Thietane |
|------------------------------------|---------|---------|---------|---------|-----------|---------|----------|
| HOMO energy (eV) | −8.2519 | −7.4822 | −7.9392 | −8.4860 | −6.2628 | −6.9525 | −6.1039 |
| LUMO energy (eV) | −0.1734 | −0.5795 | −0.3172 | −0.2555 | −0.2482 | −0.2293 | −0.5223 |
| Energy gap (eV) | 8.0785 | 6.9028 | 7.6220 | 8.2305 | 6.0146 | 6.7232 | 5.5815 |
| Electronegativity (eV) | 4.2127 | 4.0308 | 4.1282 | 4.3707 | 3.2555 | 3.5909 | 3.3131 |
| Hardness (eV) | 4.0393 | 3.4514 | 3.8110 | 4.1152 | 3.007 | 3.3616 | 2.7908 |
| Softness (eV) | 0.1238 | 0.1449 | 0.1312 | 0.1215 | 0.1663 | 0.1487 | 0.1792 |
| Electrophilicity Index (eV) | 2.1967 | 2.3538 | 2.2359 | 2.3210 | 1.7621 | 1.9179 | 1.9666 |

From Table 5.1, one can see that the C–H stretches for azetidine (nitrogen-doped cyclobutane) occurred within 3018–2878 cm^{-1} range, those for oxetane (oxygen doped cyclobutane) appeared within 3017–2906 cm^{-1} whereas thietane (nitrogen-doped cyclobutane) gave its C–H stretches from 3015 to 2933 cm^{-1} . This implies that all doped structures' C–H stretches are within natural range, though occurred at higher frequencies equivalent to unsaturated compounds. This is because of the presence of a more electronegative group in the ring, which causes a decrease in electron density around the region. HCH bends for all doped structures occurred at about $1500 \pm 50 \text{ cm}^{-1}$, which is interpreted that their effect is similar on the ring [23].

H–C–Y, C–Y, and C–Y–C VIBRATIONS (where Y = N, O, or S)

From the PED assignments in Table 5.1, we ascertained that HCN bending vibration occurred at 1115 cm^{-1} , this is higher than the position of HCO bend (1102 and 1091 cm^{-1}) in the IR spectrum. Although HCS bending vibrations occurred at 982 cm^{-1} , a lower frequency when compared to those of HCN and HCO bends. We can assert that heavier atoms led to a decrease in vibrational bend frequencies. C–Y–C (CSC) bending frequency is perceived to be absent in the IR of thietane, only azetidine and oxetane gave CNC and COC bending vibrations at 635 and 778 cm^{-1} . On the other hand, Y–C stretches for doped molecules appeared around 1000–500 cm^{-1} . The N–C stretch of azetidine occurred at 973 cm^{-1} , and O–C group of oxetane gave symmetric stretches at 981 cm^{-1} whereas S–C of thietane gave symmetric stretches at 674, 638, and 510 cm^{-1} . As obtained in bending vibrations, an equivalent decrease in vibrational frequencies is noticeable for stretches as you move from Azetidine to thietane.

C–X VIBRATIONS (where X = F, Cl or Br)

Flourocyclobutane gave symmetric C–F stretching vibrations at 919 and 5834 cm^{-1} whereas its asymmetric stretch appeared at 429 cm^{-1} (though at a very low intensity). C–Cl Stretching vibrations for chlorocyclobutane are found at 803, 505, 349 cm^{-1} (symmetric), and 693 cm^{-1} . Although bromocyclobutane gave symmetric C–Br stretches at 503 and 272 cm^{-1} , asymmetric are absent for C–Br bond. One can infer that heavier X-element in the C–X stretching vibrations, whether symmetric or asymmetric, occur at lower frequencies.

5.3.2 Bond Polarity Index (BPI)

The bond polarity index existing in atoms say *A* and *B* can be defined as:

$$\text{BPI}_{AB} = (EI_A - EI_A^{\text{ref}}) - (EI_B - EI_B^{\text{ref}})$$

where EI is energy index, EI_A and EI_B represent C and X, respectively, EI value in C–X interaction derived from the calculation of substituted cyclobutane species and EI^{ref} is the reference value which is obtained by manipulating the homonuclear atoms (Figure 5.1). A greater proportion of the BPI between *A* and *B* signifies the presence of a higher polarity in the respective [24, 25]. To quantitatively appreciate the electronic structures of molecules, BPI is crucial and this can be linked with the concept of electronegativity. Stephan and George in their article proposed a measurable factor of bond polarity by using the electron localization function and QTIAM, they investigated the BPI of X–H bonds and proposed that the bond polarities decrease in the order HF, HCL, and HBr [24]. In this study, we observed that the BPI of the halogen-substituted cyclobutane decreases in the order fluorocyclobutane, chlorocyclobutane, and bromocyclobutane which infers that the BPI decreases down the group as shown in Figure 5.2. Meanwhile, for nitrogen, oxygen, and sulfur substituted cyclobutane, BPI is observed to increase as follows: Oxetane > Thietane > Azetidene as shown in Figure 5.3.

5.3.3 Intrinsic Bond Strength Index (IBSI)

Bond strength seeks to show how strongly each atom is joined to another atom, and as such, shows the minimum energy requirement for bond breakage between the two atoms. The intrinsic bond strength index seeks to quantify the strengths of chemical bonds; it may also be used to compare the strength of weak interactions [12]. The electron density contragradience domains in molecules can be identified precisely with

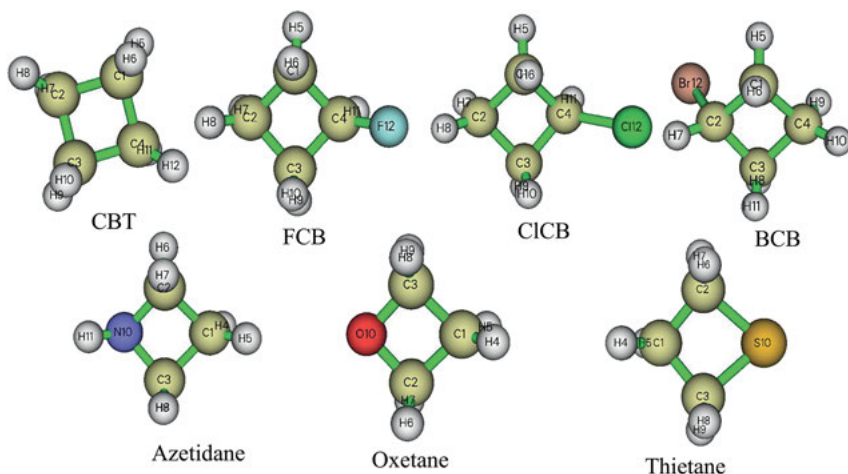


Figure 5.1: Schematic of the molecules investigated showing the numbering system and the abbreviations used (cyclobutane CBT, fluorocyclobutane FCB, chlorocyclobutane ClCB, bromocyclobutane BrCB).

BPI for N, O and S substituted cyclobutane

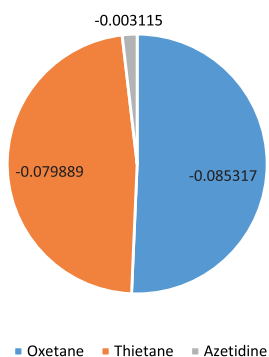


Figure 5.2: Calculated bond polarity index (BPI) for the halogen substituted derivatives of cyclobutane.

BPI for substituted cyclobutane

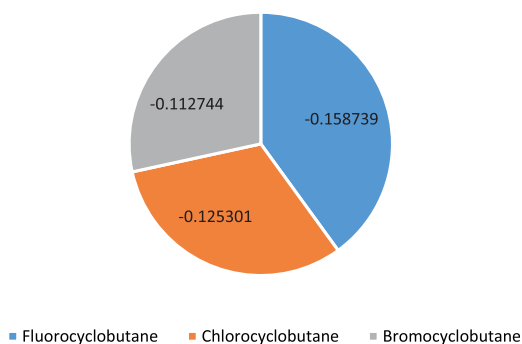


Figure 5.3: Calculated bond polarity index (BPI) for the heteroatom doped derivatives of cyclobutane.

the IGMH-dg descriptor and also this contragradience by the IBSI can be quantified by the contribution of two atomic orbitals in the region [26].

In this section, we have used IBSI which is defined in the framework of the independent gradient model (IGM) because it allows for the connection between the inter- and intra-fragment to be observed individually and thus prevent their cordial meddling and also the involvement of atoms and atomic couples to interfragmentary interactions can be quantified, these features may help to identify “hot” atoms effortlessly.

$$\text{The IBSI is expressed as } \mathbf{IBSI} = \frac{\left(\frac{1}{d^2}\right) \int \delta \mathbf{g}^{pair} d\mathbf{r}}{\left(\frac{1}{d_{H_2}^2}\right) \int d\mathbf{g}H_{2d}\mathbf{r}} \quad (5.1)$$

where d is the space in between the intermingling atoms being studied. The integral in the numerator is equivalent to the atom pair dg index defined between the two atoms, the denominator is the data for the reference system, the dH_2 and the integral are the

bond length and atom pair dg index of H_2 in its equilibrium structure, respectively. It has been demonstrated that the IBSI value correlates modestly positively with the strength of covalent bonds [12]. The results obtained from the IBSI of Halogen substituted cyclobutane using the IGM framework shows that the IBSI of carbon to halogen is $0.32659 \text{ C-F} > 0.18334 \text{ C-Cl} > 0.16136 \text{ C-Br}$ as presented in Figure 5.4. With this, it is proven that carbon to halogen bond strength decreases down the group. The results obtained from the IBSI of carbon to heteroatom bond in azetidine, oxetane, and thietane depicted in Figure 5.5 using the IGM framework shows that the IBSI of carbon to heteroatom is $0.47489 \text{ C-N} > 0.33896 \text{ C-O} > 0.18334 \text{ C-S}$.

5.3.4 CDFT results using Fukui function on cyclobutane and its associated halogenated and doped-ringed structures

CDFT is the concept of predicting chemical reactivity developed some time ago by R. Parr. Several parameters are used in predicting suitable reactive centers and an understanding of the chemical behavior of molecules can be keen-sighted from this

IBSI for Halogen substituted cyclobutane

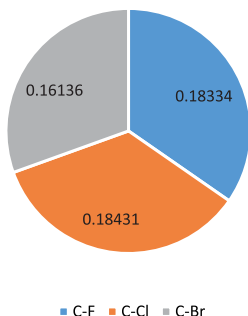


Figure 5.4: Calculated intrinsic bond strength index (IBSI) for the halogen substituted derivatives of cyclobutane.

IBSI for N, O and S substituted cyclobutane

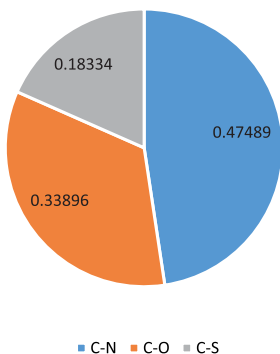


Figure 5.5: Calculated intrinsic bond strength index (IBSI) for the heteroatom doped derivatives of cyclobutane.

observation [27–30]. A very distinctive concept often used in predicting reactive sites as far as the conceptual density functional theory is a concern is the Fukui function whose condensed version has been mathematically defined as:

$$f(r) = \frac{[\delta\mu]}{[\delta v(r)]_N} = \left[\frac{\partial \rho(r)}{\partial N} \right]_{v(r)} \quad (5.2)$$

where the number of electrons is defined by N ; and v the potential. Fukui function can be considered roughly in three determinate ways:

$$\text{Nucleophilic attack : } f^+(r) = \rho_{N+1}(r) - \rho_N(r) \approx \rho^{\text{LUMO}}(r) \quad (5.3)$$

$$\text{Electrophilic attack : } f^-(r) = \rho_N(r) - \rho_{N-1}(r) \approx \rho^{\text{HOMO}}(r) \quad (5.4)$$

$$\text{Radical attack : } f^0(r) = \frac{f^+(r) + f^-(r)}{2} = \frac{\rho_{N+1}(r) - \rho_{N-1}(r)}{2} \approx \frac{\rho^{\text{HOMO}}(r) + \rho^{\text{LUMO}}(r)}{2} \quad (5.5)$$

where, the cationic, neutral, and anionic species are represented as ρ_{N-1} , ρ_N , and ρ_{N+1} , respectively. The electronic concentrations of the HOMO and LUMO orbitals are designated by $\rho^{\text{HOMO}}(r)$ and $\rho^{\text{LUMO}}(r)$ [28–33].

Another important concept used in predicting reactive sites is the dual descriptor put forward by Morell et al. [29], which is defined as

$$f^{(2)}(r) = \frac{[\delta\eta]}{[\delta v(r)]_N} = \frac{[\delta f(r)]}{[\partial N]_{v(r)}} \quad (5.6)$$

where η is the systems' chemical hardness of the system. Considering similar rough calculation as in the case of Fukui function, the dual descriptor can also be expressed as:

$$f^{(2)}(r) = f^+(r) - f^-(r) \approx \rho^{\text{LUMO}}(r) - \rho^{\text{HOMO}}(r) \quad (5.7)$$

The dual descriptor $f^{(2)}(r)$ assumes a positive value to indicate an electrophilic region and negative values nucleophilic regions as proposed in the original work [29] where $\rho^{\text{LUMO}}(r)$, and $\rho^{\text{HOMO}}(r)$ dominates. The dual descriptor can reveal both types of reactive sites at the same time, which makes it a more convenient tool for predicting reactive sites [28, 30]. The condensed dual descriptor can also be defined in like manners as the condensed Fukui function for each individual atom as:

$$f_A^2(r) = f_A^+(r) - f_A^-(r) = 2q_N^A - q_{N+1}^A - q_{N-1}^A \quad (5.8)$$

The aforementioned formulas have been used in this work to designate the electrophilic, and nucleophilic active sites respectively. It is generally accepted that higher Fukui function values at designates centers denote an increased reactivity at specific sites. According to the procedure, the Hirshfeld charges for the carbons in all compounds were calculated in its N , $N + 1$, and $N - 1$ electronic states, respectively. The condensed electrophilicity and nucleophilicity and the dual descriptor were obtained

from the formulae given. From the results, the best possible reactive sites for electrophilic substitution reaction were observed and noted accordingly. The result of the condensed electrophilicity revealed that C1 and C4 would not be suitable for electrophilic substitution as their f -values are the tiniest whereas the dual descriptor prompted that C2 and C4 have stronger positive values than other atoms which makes them unsuitable positions of substitution. The electrophilic factor for C3 is quite more negative compared to other atoms, thus it's a better position of reaction for any electrophile. Though every other atom has negative values, but that of C1 is quite more intense than C2 and C4, therefore the dual descriptor indicates that C3 followed by C1 are preferred points of reaction in electrophilic reactions. The electrophilic descriptor for chlorocyclobutane shows that C3, C2 and C4 were more unfavorable for any electrophilic substitution in like manners, the dual descriptor confirmed the assertion by including C1. Position 1 and 3 have been noted as unfavorable sites of electrophilic attack in fluorecyclobutane whereas, C2 and C4 are identified to be more susceptible to electrophilic attack. In the case of azetidine, C4 and C2 are less susceptible whereas C1 and C3 are more possible to react with any electrophile. The dual descriptor proposed C4 to be the preferred point of electrophilic substitution in oxetane and that of thietane was shown to be C1 and C3, respectively.

5.3.5 Quantum chemical descriptors

Conceptual density functional theory is a chemical reactivity descriptor which aims at evaluating quantum chemical descriptors such as electronegativity (χ), chemical hardness (η), softness (S), chemical potential (μ), electrophilicity index (ω), etc. with the sole aim of giving reasonable insight into the reactive nature and stability of chemical systems. The aforesaid quantum descriptors were calculated using the following equations

$$\chi = -\mu = \frac{I + A}{2} \quad (5.9)$$

$$\eta = \frac{I - A}{2} \quad (5.10)$$

$$S = \frac{1}{2\eta} \quad (5.11)$$

$$\omega = \frac{\mu^2}{2\eta} \quad (5.12)$$

Quantum chemical parameters such as E_{HOMO} , E_{LUMO} , ΔE (LUMO–HOMO energy gap), proton affinity, offers substantial insight into the reactive, and stable nature of compounds and the electrophilicity and nucleophilicity descriptors.

Energy gap: The key parameters in the determination of chemical reactivity of atoms are the HOMO and LUMO. Electrons tend to fill orbitals with the least energy first (HOMO) before those with higher energies (LUMO) as a result, the HOMO is a characteristic nucleophile whereas the LUMO is an electrophile. The HOMO and LUMO values were evaluated using Multiwfn and the difference in energy is a factor of the HOMO and LUMO.

$$\text{Energy gap } (\Delta E) = E_{\text{LUMO}} - E_{\text{HOMO}}$$

where E_{HOMO} and E_{LUMO} represent the HOMO and LUMO energies respectively in (eV). The computed HOMO and LUMO energy values for the studied systems along with their variation in energy gap are presented in Table 5.3. From the observed trends in our results, there is a steady increase in the energy gap between the halogenated rings (BrCB to FCB). This implies that more energy will be required for reactivity as we move from bromocyclobutane to fluorocyclobutane. However, there is an observed decrease in the energy gap between the doped structures, from azetidine to thietane.

Electrophilicity (ω) and nucleophilicity are two valuable chemical reactivity indices proposed by Parr [33] to aid the prediction of chemical reactivity. The electrophilicity index

Table 5.3: Calculated second-order perturbation theory analysis for cyclobutane and its studied derivatives B3LYP method and 6-311++G(d, p) basic set.

| Bromocyclobutane | | | | | | | |
|-------------------|---------------------------|-----------|------------------------|-----------|------------------------|-----------------|----------------------|
| S/N | Donor | Occupancy | Acceptor | Occupancy | $E^{(2a)}$ (kJ/mol) | $E(j) - E(i)^b$ | $F(i, j)^c$ (a.u) |
| 1 | $\sigma\text{C1-C2}$ | 1.98584 | $\sigma\text{C3-H8}$ | 1.98836 | 2.67 | 1.01 | 0.046 |
| 2 | $\sigma\text{C1-C4}$ | 1.98437 | $\sigma\text{C2-H7}$ | 1.99051 | 3.36 | 0.97 | 0.051 |
| 4 | $\sigma\text{C1-H6}$ | 1.97516 | $\sigma\text{C2-Br12}$ | 1.98262 | 4.52 | 0.56 | 0.045 |
| 5 | $\sigma\text{C2-C3}$ | 1.98584 | $\sigma\text{C1-H5}$ | 1.98836 | 2.67 | 1.01 | 0.044 |
| 8 | $\sigma\text{C3-C4}$ | 1.98437 | $\sigma\text{C2-H7}$ | 1.99051 | 3.36 | 0.97 | 0.051 |
| 10 | $\sigma\text{C3-H11}$ | 1.97516 | $\sigma\text{C2-Br12}$ | 1.98262 | 4.52 | 0.56 | 0.045 |
| 11 | $\sigma\text{C4-H9}$ | 1.97516 | $\sigma\text{C1-H6}$ | 1.97516 | 1.85 | 0.90 | 0.036 |
| 32 | $\sigma(2)\text{Br12}$ | 1.98276 | $\sigma\text{C1-C2}$ | 1.98584 | 0.94 | 0.64 | 0.022 |
| 33 | $(3)\text{Br12}$ | 1.97878 | $\sigma\text{C1-C2}$ | 1.98584 | 1.98 | 0.62 | 0.031 |
| Chlorocyclobutane | | | | | | | |
| 1 | $\sigma\text{C1-C2}$ | 1.97340 | $\sigma\text{C4-Cl12}$ | 1.98928 | 7.24 | 0.67 | 0.062 |
| 2 | $\sigma\text{C1-C4}$ | 1.98366 | $\sigma\text{C3-H9}$ | 1.98992 | 2.94 | 1.01 | 0.049 |
| 3 | $\sigma\text{C1-H5}$ | 1.98992 | $\sigma\text{C4-Cl12}$ | 1.98928 | 0.85 | 0.62 | 0.021 |
| 4 | $\sigma\text{C1-H6}$ | 1.98148 | $\sigma\text{C4-H11}$ | 1.98293 | 2.27 | 0.90 | 0.040 |
| 5 | $\sigma\text{C2-C3}$ | 1.97340 | $\sigma\text{C4-Cl12}$ | 1.98928 | 7.24 | 0.67 | 0.062 |
| 6 | $\sigma\text{C2-H7}$ | 1.98613 | $\sigma\text{C1-H6}$ | 1.98148 | 1.92 | 0.91 | 0.037 |
| 8 | $\sigma\text{C3-C4}$ | 1.98366 | $\sigma\text{C1-H5}$ | 1.98992 | 2.94 | 1.01 | 0.049 |
| 9 | $\sigma\text{C3-H9}$ | 1.98992 | $\sigma\text{C4-Cl12}$ | 1.98928 | 0.85 | 0.62 | 0.021 |
| 10 | $\sigma\text{C3-H10}$ | 1.98148 | $\sigma\text{C2-H7}$ | 1.98613 | 2.00 | 0.91 | 0.038 |
| 11 | $\sigma\text{C4-H11}$ | 1.98293 | $\sigma\text{C1-H6}$ | 1.98148 | 2.07 | 0.93 | 0.039 |
| 23 | $(2)\text{Cl12}$ | 1.97929 | $\sigma\text{C1-C4}$ | 1.98366 | 1.24 | 0.65 | 0.025 |
| 24 | $\text{LP}(3)\text{Cl12}$ | 1.96965 | $\sigma\text{C1-C4}$ | 1.98366 | 3.19 | 0.65 | 0.041 |

Table 5.3: (continued)

| Bromocyclobutane | | | | | | | |
|--------------------------|-----------------|------------|-----------------|-----------|------------------------------|-----------------|----------------------|
| S/N | Donor | Occupancy | Acceptor | Occupancy | $\bar{E}^{(2a)}$ (kJ/mol) | $E(j) - E(j)^b$ | $F(i, j)^c$ (a.u) |
| Fluorocyclobutane | | | | | | | |
| 1 | $\sigma C1-C2$ | 1.97670 | $\sigma C4-F12$ | 1.99602 | 6.04 | 0.77 | 0.061 |
| 2 | $\sigma C1-C4$ | 1.98401 | $\sigma C3-H9$ | 1.99053 | 3.12 | 1.00 | 0.050 |
| 3 | $\sigma C1-H5$ | 1.99053 | $\sigma C4-F12$ | 1.99602 | 0.59 | 0.72 | 0.019 |
| 4 | $\sigma C1-H6$ | 1.97997 | $\sigma C4-H11$ | 1.98340 | 2.20 | 2.20 | 0.040 |
| 5 | $\sigma C2-C3$ | 1.97670 | $\sigma C4-F12$ | 1.99602 | 6.04 | 0.77 | 0.061 |
| 6 | $\sigma C2-H7$ | 1.98592 | $\sigma C1-H6$ | 1.97997 | 1.95 | 0.91 | 0.038 |
| 8 | $\sigma C3-C4$ | 1.98401 | $\sigma C1-H5$ | 1.99053 | 3.12 | 1.00 | 0.050 |
| 9 | $\sigma C3-H9$ | 1.99053 | $\sigma C4-F12$ | 1.99602 | 0.59 | 0.72 | 0.019 |
| 10 | $\sigma C3-H10$ | 1.97997 | $\sigma C4-H11$ | 1.98340 | 2.20 | 0.90 | 0.040 |
| 19 | LP (2) F12 | 1.97280 | $\sigma C1-C4$ | 1.98401 | 2.00 | 0.74 | 0.035 |
| 20 | LP (3) F12 | LP (3) F12 | $\sigma SC1-C4$ | 1.98401 | 5.35 | 0.74 | 0.056 |
| Aziritane | | | | | | | |
| 1 | $\sigma C1-C2$ | 1.98419 | $\sigma C3-H8$ | 1.99297 | 3.08 | 0.99 | 0.049 |
| 2 | $\sigma C1-C3$ | 1.98419 | $\sigma C2-H6$ | 1.99297 | 3.08 | 0.99 | 0.049 |
| 3 | $\sigma C1-H4$ | 1.98614 | $\sigma C2-H7$ | 1.99054 | 1.79 | 0.90 | 0.036 |
| 6 | $\sigma C2-H7$ | 1.99054 | $\sigma C1-H4$ | 1.99054 | 1.89 | 0.92 | 0.037 |
| 7 | $\sigma C2-N10$ | 1.99058 | $\sigma C3-H8$ | 1.99297 | 2.23 | 1.08 | 0.044 |
| 9 | $\sigma C3-H9$ | 1.99054 | $\sigma C1-H4$ | 1.99054 | 1.89 | 0.92 | 0.037 |
| 10 | $\sigma C3-N10$ | 1.99058 | $\sigma C2-H6$ | 1.99297 | 2.23 | 1.08 | 0.044 |
| 16 | LP (1) N10 | 1.93095 | $\sigma C2-H7$ | 1.99054 | 4.92 | 0.71 | 0.054 |
| Oxetane | | | | | | | |
| 1 | $\sigma C1-C2$ | 1.98759 | $\sigma C3-O10$ | 1.99329 | 2.74 | 0.85 | 0.043 |
| 2 | $\sigma C1-C3$ | 1.98759 | $\sigma C2-O10$ | 1.99329 | 2.74 | 0.85 | 0.043 |
| 5 | $\sigma C2-H6$ | 1.99274 | $\sigma C2-H7$ | 1.99273 | 0.98 | 0.92 | 0.027 |
| 6 | $\sigma C2-H7$ | 1.99273 | $\sigma C1-H4$ | 1.98953 | 1.25 | 0.93 | 0.030 |
| 7 | $\sigma C2-O10$ | 1.99329 | $\sigma C3-H8$ | 1.99274 | 0.83 | 1.15 | 0.028 |
| 8 | $\sigma C3-H8$ | 1.99274 | $\sigma C1-H4$ | 1.98953 | 1.25 | 0.93 | 0.030 |
| 9 | $\sigma C3-H9$ | 1.99273 | $\sigma C1-H4$ | 1.98953 | 1.25 | 0.93 | 0.030 |
| 10 | $\sigma C3-O10$ | 1.99329 | $\sigma C1-H4$ | 1.98953 | 0.69 | 1.16 | 0.025 |
| 16 | LP π O10 | 1.92572 | $\sigma C2-H6$ | 1.99274 | 5.30 | 0.69 | 0.055 |
| Thietane | | | | | | | |
| 1 | $\sigma C1-C2$ | 1.99074 | $\sigma C3-H9$ | 1.99338 | 2.14 | 1.02 | 0.042 |
| 2 | $\sigma C1-C3$ | 1.99074 | $\sigma C2-H7$ | 1.99338 | 2.14 | 1.02 | 0.042 |
| 3 | $\sigma C1-H4$ | 1.98871 | $\sigma C2-S10$ | 1.98661 | 0.80 | 0.64 | 0.020 |
| 5 | $\sigma C2-H6$ | 1.99131 | $\sigma C1-H5$ | 1.98482 | 1.76 | 0.92 | 0.036 |
| 6 | $\sigma C2-H7$ | 1.99338 | $\sigma C1-H5$ | 1.98482 | 1.76 | 0.92 | 0.036 |
| 7 | $\sigma C2-S10$ | 1.98661 | $\sigma C1-H4$ | 1.98871 | 3.19 | 0.94 | 0.049 |
| 8 | $\sigma C3-H8$ | 1.99131 | $\sigma C1-H5$ | 1.98482 | 1.76 | 0.92 | 0.036 |
| 9 | $\sigma C3-H9$ | 1.99338 | $\sigma C1-C2$ | 1.99074 | 0.57 | 0.87 | 0.020 |
| 10 | $\sigma C3-S10$ | 1.98661 | $\sigma C1-H4$ | 1.98871 | 3.19 | 0.94 | 0.049 |
| 20 | LP π S10 | 1.94731 | $\sigma C3-H8$ | 1.99131 | 3.80 | 0.64 | 0.044 |

is calculated using the formula, $\omega = \frac{\mu^2}{\epsilon} \eta$ depending on the electronegativity and hardness values of chemical species [34]. The electrophilicity index defines the tendency of electron acceptors to attain further electronic charge from the environment whereas nucleophilicity has been described as the multiplicative inverse of electrophilicity ($\omega = 1/\epsilon$). The calculated electrophilicity index of the studied systems as presented in Table 5.3 shows a steady increase in the electrophilicity index in the case of the doped compounds ranging from azetidene = 1.7621, oxetane = 1.9179, and thietane = 1.9666. However, in the halogen-substituted compounds, Bromocyclobutane has the highest electrophilicity index = 2.3538

Koopmans theorem is one of the alternate approaches used to envisage the ionization energy and electron affinity values of chemical species and proposed these two concepts to be negatives of HOMO and LUMO energies respectively. According to Koopmans theorem [35], hardness, softness, and electronegativity can be calculated using: $\eta = \frac{I-A}{2}$ (chemical hardness), $S = \frac{1}{2} \eta$ (softness), and $\chi = -\mu = \frac{I+A}{2}$ (electronegativity) where the hardness of a species defined as IP-EA is the resistance of molecules to exchange electron density with the immediate surroundings whereas the Mulliken electronegativity described as the negative of chemical potential is the degree of the attracting propensity of an atom toward a shared pair of electrons [33–38]. From the observed trends as presented in Table 5.3, the chemical hardness of halogen-substituted compounds increase as an order from BCB (3.4514), ClCB (3.8110), and FCB (4.1153) whereas in the case of the doped compounds, oxetane has the highest chemical hardness value of 3.3616. For chemical softness, there is a decrease from BrCB > ClCB > FCB with 0.145, 0.1312, and 0.1215, respectively. For the doped compounds, thietane is observed to possess the highest softness of 0.1792. Because the stability of molecules is ascertained through its hardness and softness, we can affirm that the stability of the studied systems follows the above trend with FCB and oxetane being the most stable based on hardness values and the compounds with the least values will be the most reactive compounds based on this concept. Observation of the electronegativity results shows a consistent increase in the electronegativity values between the halogen-substituted compounds in the order; (BrCB – 4.03085, ClCB – 4.1282, and FCB – 4.3707) which is in line with common knowledge and inclinations of the said concept for the halogen compounds. Between the doped compounds, the oxetane has the highest electronegativity value of 3.5909 which also is in agreement with several literature reports and the notion that electronegativity increases across the period and decreases down the groups in the periodic table of elements [31–38].

5.3.6 Natural bond orbital analysis (NBO)

The intramolecular and intermolecular hyperconjugative interactions in molecules can be exploited without reasonable doubt from the analysis of natural bond orbital [39]. NBOs majorly consist of natural atomic hybrid orbitals which are orthonormal sets of localized orbitals with maximum occupancy (highest percentage of total electron

density), which gives the most precise plausible natural Lewis structure. NBO analysis makes available substantial evidence about the nature of bonding orbitals, their occupancies and the type and nature of the interaction (inter or intramolecular hyperconjugative or charge transfer) existing between virtual and occupied Lewis orbitals. The analysis is conducted by considering all probable interactions between donor (occupied Lewis NBOs) and acceptors (vacant) non-Lewis NBOs, and approximating their energetic significance by second-order perturbation theory of Fock matrix [18, 40]

$$E(2) = -\eta_{\sigma} \frac{\langle \sigma | \hat{F} | \sigma^* \rangle^2}{\epsilon_{\sigma^*} - \epsilon_{\sigma}}$$

where \hat{F} is the Fock operator, ϵ_{σ} and ϵ_{σ^*} are the energies of the NBO, and η_{σ} is the orbital occupancy.

The result of the analysis is tabulated in Table 5.3. The inference with respect to hybridization is that $\sigma C4-F12$ in flourocycobutane is a product of $sp^{1.00}$ hybrid rendered by 19.05% s , 80.69% p , and 0.25% d orbitals with 1.99602 electrons in the bond which is the highest electron occupancy in the molecule. $\sigma C1-C2$ is seen to have the lowers electron occupancy and is formed by the hybridization of $sp^{3.07}$ hybrid with 24.51% s , 75.19% p , and 0.30% d character. The trend in the electron occupancy across the compounds shows that the highest electron occupancy is found in bonds between the halogen substituents and the heteroatoms. This is in line with the conventional notion of the electronegativity behaviors of these substituents. The result of the second-order perturbation theory analysis is presented in Table 5.3. The inference from this result is the highest stabilization noted is between $\sigma C1-C2$ to $\sigma C4-Cl12$ (7.24 kcal/mol) of chlorocyclobutane and $\sigma C1-C2$ to $\sigma C4-F12$ (6.04 kcal/mol) of flourocyclobutane. The lowest observed stabilization energy is from $\sigma C3-H9$ to $\sigma C4-F12$ (0.59 kcal/mol) of flourocyclobutane and $\sigma C3-O10$ to $\sigma C1-H4$ (0.69 kcal/mol) of oxetane. The high stabilization energy which exists in the compounds can be attributed to the strong ionization energies of the halogen atoms. This high ionization energy gives stability to the compound.

5.3.7 Atomic charge analysis

The ADCH charge of Tian Lu and Feiwu, 2012 [41] are modified Hirshfeld charges that have considered some of the negligence of Hirshfeld charges particularly, the neglect of dipole moment reproducibility [41]. The atomic dipole of each atom has been extended into a correction charge placed at neighboring atoms to give the ADCH charge by summing the original Hirshfeld charge and the correction charge. ADCH charge is very reasonable in chemical sense and is given as $Q_A = q_A + \sum_b^a \Delta q_{bA}$ where Δq_{bA} is correction charge, q_A is the Hirshfeld charge defined as $q_A = - \int \omega_A(r) \Delta \rho(r) dr$ where $\rho(r)$ is the actual electron density of the molecule, $\omega_A(r)$ is the atomic weight function.

The ADCH values of cyclobutane and its substituted compounds were calculated using a combination of Gauss-09 software and multiwfn-3.7-(dev) software. Table 5.4

compares the theoretically calculated ADCH values for cyclobutane (CB), fluorocyclobutane (FCB), chlorocyclobutane (ClCB), bromocyclobutane (BrCB), and cyclobutane doped with oxygen (OCB), nitrogen (NCB) and sulfur (SCB). It is clear from Table 5.4 that the ADCH values for all the halo substituted groups at position C1 are more negative compare to that of C1 for normal cyclobutane with that of FCB (-0.1810) > ClCB (-0.1688) > BrCB (-0.1679) > CB (-0.1673). That of the doped groups is also higher in negative value compare to normal CB except for SCB with that of NCB (-0.1751) > OCB (-0.1708) > CB (-0.1673) > SCB (-0.1524). These differences observed may likely be because of the differences in the electronegative values of the elements attached to the cyclobutane ring which in turn bring about the differences in the pull of electrons through negative inductive effects (-I effect) which decreases with an increase in distance of the element bringing about the electronic effect. Thus, when fluorine with a high electronegative value is attached to one of the carbons of cyclobutane, it pulls electron to itself creating a partial permanent dipole moment δ^- and δ^+ , this effect will be more on the carbons directly attached to fluorine and the effect decreases as the distance increases, this explains why carbon C2 of all the halo substituted cyclobutane showed a lower negative value. The ADCH result presented in this paper is similar to that presented by Tian Lu and Feiwu (2012) [36] on the ADCH for P-toulene sulfuric acid.

5.3.8 Molecular electrostatic potential (MEP)

Molecular electrostatic potential as a quantum reactivity parameter which functions by revealing the sensitivity of a molecular surface toward electrostatic interaction with other molecular structures has been used in this study to probe specific sites of possible interaction. This quantum molecular descriptor is however essential in the sense that correlation between diverse facets of reactions is probable. Notwithstanding this fact, it is also not very appropriate for the estimation of sensitive centers in molecular systems based on the fact that the molecular electrostatic potential is calculated by using the unperturbed geometry and as such does not take into consideration the effect of polarization on the interacting species [42, 43]. The results are, however, presented in Figure 5.6. The ESP around the heteroatoms in the studied systems is very negative because of their evident negative atomic charges, thus very negative molecular electrostatic potential values. On the contrary, the carbon atoms and hydrogen counterparts are characterized by low electron density and low MEP values, the situation becomes quite different when considering the distribution of MEP in cyclobutane, it is rather characterized by a uniform electronic distribution with the carbon atoms possessing higher MEP values than the hydrogen atoms. This clearly shows that the substituted halogens and doped heteroatoms are important and most probable sites of electrostatic interactions.

Table 5.4: ADCH charge analysis result for cyclobutane and its substituted derivatives.

| CB | ADCH | FCB | ADCH | CICB | ADCH | BrCB | ADCH | OCB | ADCH | NCB | ADCH | SCB | ADCH |
|----|---------|-----|---------|------|---------|------|---------|-----|---------|-----|---------|-----|---------|
| C | -0.1673 | C | -0.1810 | C | -0.1688 | C | -0.1679 | C | -0.1708 | C | -0.1751 | C | -0.1524 |
| C | -0.1673 | C | -0.1663 | C | -0.1563 | C | -0.0520 | C | -0.0532 | C | -0.0615 | C | -0.1575 |
| C | -0.1673 | C | -0.1811 | C | -0.1688 | C | -0.1679 | C | -0.0533 | C | -0.0615 | C | -0.1575 |
| C | -0.1673 | C | 0.0532 | C | -0.0312 | C | -0.1625 | H | 0.0986 | H | 0.0956 | H | 0.1003 |
| H | 0.0846 | H | 0.1005 | H | 0.1048 | H | 0.0926 | H | 0.0986 | H | 0.0936 | H | 0.0945 |
| H | 0.0827 | H | 0.0974 | H | 0.0927 | H | 0.1091 | H | 0.0916 | H | 0.0850 | H | 0.1082 |
| H | 0.0827 | H | 0.0891 | H | 0.0904 | H | 0.1055 | H | 0.0915 | H | 0.0792 | H | 0.1123 |
| H | 0.0846 | H | 0.0968 | H | 0.0992 | H | 0.0926 | H | 0.0916 | H | 0.0850 | H | 0.1082 |
| H | 0.0846 | H | 0.1005 | H | 0.1048 | H | 0.0908 | H | 0.0915 | H | 0.0792 | H | 0.1082 |
| H | 0.0827 | H | 0.0975 | H | 0.0927 | H | 0.0983 | O | -0.2862 | N | -0.5188 | S | -0.1685 |
| H | 0.0827 | H | 0.0935 | H | 0.1052 | H | 0.1091 | | | H | 0.2993 | | |
| H | 0.0846 | F | -0.2001 | Cl | -0.1645 | Br | -0.1478 | | | | | | |

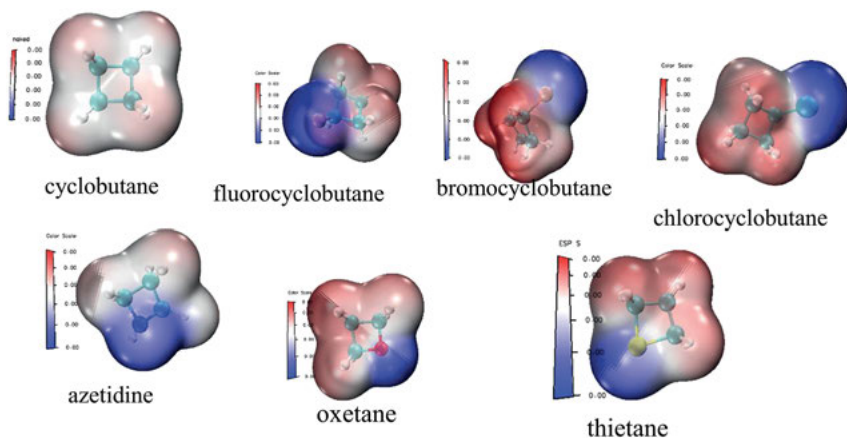


Figure 5.6: Molecular electrostatic potential surface of the studied compounds.

5.4 Conclusions

The vibrational assignments, NBO analysis, CDFT, Quantum mechanical descriptors, and molecular electrostatic potential analysis have been investigated in this study. The corresponding wavenumbers of the studied compounds have as well been assigned by PED analysis. Several inter and intramolecular hyperconjugative interactions within the studied compounds have been revealed by the NBO analysis with a confirmation of geometric hybridization and electronic occupancy. A good correlation between calculated vibrational frequencies and experimental standard data have been observed. Specific suitable and unfavorable sites of electrophilic substitution have been noted by analyzing the Fukui function and dual descriptor as calculated by the CDFT analysis; likewise, the electrostatic interaction regions have similarly been noticed by the molecular electrostatic potential (MEP) analysis. The charge population analysis shows that the type of substituent on the ring influences the charge population and also adjacent atoms are very much affected by the chemical nature of the substituted atoms. The NBO result suggests that the molecules are stabilized by lone pair delocalization of electrons from the substituted atoms and MEP studies revealed that substituted halogens and doped heteroatoms are important and most probable sites of electrostatic interactions.

Acknowledgment: This research was not funded. Our sincere appreciation goes to Emmanuel A. Bisong for the information about the conference proceedings.

Author contributions: All the authors have accepted responsibility for the entire content of this submitted manuscript and approved submission.

Research funding: None declared.

Conflict of interest statement: All authors unanimously declare zero conflict of interest.

References

1. Sakhaee N, Sakhaee S. Pseudorotation in cyclooctane, using spherical conformational landscape model. *Comput Theor Chem* 2020;1184:112845.
2. Hu YJ, Li LX, Han JC, Min L, Li CC. Recent advances in the total synthesis of natural products containing eight-membered carbocycles (2009–2019). *Chem Rev* 2020;120:5910–53.
3. Martins SO, Edna MaO AR, Joseph P, Jorge C, lyndon A, Cornelius M, et al. Synthesis of cyclobutane-fused tetracyclic scaffolds via visible-light photocatalysis for building molecular complexity. *J Am Chem Soc* 2020;142:3094–103.
4. Willstätter R, Bruce J. “Zur Kenntnis der Cyclobutanreihe” [On our knowledge of the cyclobutane series]. *Ber Dtsch Chem Ges* 1907;40:3979–99.
5. de Meijere A, editor. Carbocyclic four-membered ring compounds. In: Houben–Weyl methods of organic chemistry, vol 17e/r. Stuttgart: Thieme; 1997.
6. Zhang X, Nie Y, Yuan Y, Lu F, Geng Z. Density functional theory investigation on the mechanism of dehydrogenation of cyclohexane catalyzed by heteronuclear NiTi. *J Comput Theor Chem* 2020; 1184:112820.
7. Pande JV, Bindwal AB, Pakande YB, Biniwale RB. Application of microwave synthesized Ag–Rh nanoparticles in cyclohexane dehydrogenation for enhanced H₂ delivery. *Int J Hydrogenation Energy* 2018;43:7411–23.
8. Frisch MJ, Trucks GW, Schlegel HB, Scuseria GE, Robb MA, Cheeseman JR, et al. Gaussian 09, Revision C. 02. Wallingford CT: Gaussian, Inc.; 2009.
9. Dennington RD, Keith TA, Millam JM. GaussView 6.0. 16, Semichem. Inc., Shawnee Mission KS; 2016.
10. Jamroz MH. Vibrational energy distribution analysis. Warsaw: VEDA4; 2004. p. 2004–10.
11. Sanchez-Marquez J, Zorrilla D, Sanchez-Coronilla A, Desiree M, Navas J, Fernandez-Lorenzo C, et al. Introducing “UCA FUKUI software; reactivity-index calculations”. *J Mol Model* 2004;20:2492.
12. Tian L, Feiwu CM. A multifunctional analyzer. *J Comput Chem* 2012;33:580–92.
13. Yu HS, He X, Truhlar DG. MN15: a new local exchange–correlation functional for Kohn–Sham density functional theory with broad accuracy for atoms, molecules, and solids. *J Chem Theor Comput* 2016;12:1280–93.
14. Roeges NPG. A guide to complete interpretation of infrared spectra of organic structures. New York: Wiley; 1994.
15. Scott AP, Radom L. Harmonic vibrational frequencies: an evaluation of Hartree–Fock, Moller–Plesset, quadratic configuration interaction, density functional theory, and semiempirical scale factors. *J Phys Chem* 1996;100:16502–13.
16. Kesharwani MK, Brauer B, Martin JML. Frequency and zero-point vibrational energy scale factors for double-hybrid density functionals (and other selected methods): can anharmonic force fields be avoided? *J Phys Chem* 2015;119:1701–14.
17. Houriez C, Ferre N, Flament JP, Masella M, Siri D. Electronic basis of the comparable hydrogen bond properties of small H₂CO/(H₂O)_n and H₂NO/(H₂O)_n systems (n = 1, 2). *J Phys Chem* 2007;111: 11673–82.

18. Bisong EA, Louis H, Unimuke TO, Odey JO, Ubana EI, Edim MM, et al. Vibrational, electronic, spectroscopic properties, and NBO analysis of P-xylene, 3,6-difluoro-p-xylene, 3,5-dichloro-p-xylene and 3,6-dibromo-p-xylene: DFT study. *Heliyon* 2020;6:e05783.
19. Venkatesh G, Govindaraju M, Kamal C, Vennila P, Kaya S. Structural, electronic and optical properties of 2,5-dichloro-p-xylene: experimental and theoretical calculations using DFT method. *RSC Adv* 2017;7:1401.
20. Ahmad MS, Khalid M, Shaheen MA, Tahir MN, Khan MU, Braga AAC, et al. Synthesis and XRD, FT-IR vibrational, UV-vis, and nonlinear optical exploration of novel tetra substituted imidazole derivatives: a synergistic experimental-computational analysis. *J Phys Chem Solid* 2018;115: 265-76.
21. Khalid M, Ullah MA, Adeel M, Khan MU, Tahir MN, Braga AAC. Synthesis, crystal structure analysis, spectral IR, UV-Vis, NMR assessments, electronic and nonlinear optical properties of potent quinoline based derivatives: interplay of experimental and DFT study. *J Saudi Chem Soc* 2019;23: 546-60.
22. Khan MU, Ibrahim M, Khalid M, Jamil S, Al-Saadi AA, Janjua MRSA. Quantum chemical designing of indolo [3, 2, 1-jk] carbazole-based dyes for highly efficient nonlinear optical properties. *Chem Phys Lett* 2019;719:59-66.
23. Shimanouchi T. Tables of vibrational frequencies, consolidated, vol. I. National Bureau of Standards; 1972.
24. Karnan M, Balachandran V, Murugan M, Murali MK, Nataraj A. Vibrational (FT-IR and FT-Raman) spectra, NBO, HOMO-LUMO, Molecular electrostatic potential surface and computational analysis of 4-(trifluoromethyl) benzylbromide. *Spectrochim Acta Mol Biomol Spectrosc* 2013;116:84-95.
25. Raub S, Jansen G. A quantitative measure of bond polarity from the electron localization function and the theory of atoms in molecules. *Theor Chem Acc* 2001;106:223-32.
26. Allen LC, Egoal DA, Knight ET, Liang C. Bond polarity index. *J Phys Chem* 1990;94:5602-7.
27. Klein J, Khartabil H, Boisson J-C, Contreras-García J, Piquemal J-P, Hénon E. New way for probing bond strength. *J Phys Chem* 2020;124:1850-60.
28. Domingo LR, Rios-Gutierrez M, Perez P. Applications of the conceptual density functional theory indices to organic chemistry reactivity. *Molecules* 2016;21:748.
29. Cao J, Ren Q, Chen F, Lu T. Comparative study of the methods for predicting the reactive site of nucleophilic reaction. *Sci China Chem* 2015;58:1845-52.
30. Morell C, Grand A, Toro-Labbe A. New dual descriptor for chemical reactivity. *J Phys Chem* 2004; 109:205-12.
31. Wang B, Rong C, Chattaraj PK, Liu S. A comparative study to predict regioselectivity, electrophilicity and nucleophilicity with Fukui function and Hirshfeld charge. *Theor Chem Acc* 2019;138:124.
32. Parr RG, Yang W. Density functional theory of atoms and molecules. New York, NY, USA: Oxford University Press; 1989.
33. Parr RG, Pearson RG. Absolute hardness: companion parameter to absolute electronegativity. *J Am Chem Soc* 1983;105:7512-6.
34. Parr RG, Szentpaly LV, Liu S. Electrophilicity index. *J Am Chem Soc* 1999;121:1922-4.
35. Vennila P, Govindaraju M, Venkatesh G, Kamal C, Mary SY, Panicker CY, et al. A complete computational and spectroscopic study of 2-bromo-1,4-dichlorobenzene-A frequently used benzene derivative. *J Mol Struct* 2018;1151:245-55.
36. Koopmans T. Über die Zuordnung von Wellenfunktionen und Eigenwerten zu den einzelnen Elektronen eines Atoms. *Physica* 1934;1:104-13.
37. Pearson RG. Hard and soft acids and bases. *J Am Chem Soc* 1963;85:3533-5339.
38. Pearson RG. Absolute electronegativity and hardness: application to inorganic chemistry. *Inorg Chem* 1988;27:734-40.

39. Pearson RG. Absolute electronegativity and hardness correlated with molecular orbital theory. *Proc Natl Acad Sci USA* 1986;83:8440–1.
40. Dunnington BD, Schmidt JR. Generalization of natural bond orbital analysis of periodic systems: applications to solids and surfaces via plane-wave density functional theory. *J Chem Theor Comput* 2012;8:1902–11.
41. Rubarani PG, Sampath KS. Natural bond orbital (NBO) population analysis of 1-azanaphthalene-8-ol. *ACTA Physica Polonica A* 2014;125:18–22.
42. Lu T, Chen F. Atomic dipole moment corrected Hirshfeld population method. *J Theor Comput Chem* 2012;11:163–83.
43. Politzer P, Murray JS. The fundamental nature and role of the electrostatic potential in atoms and molecules. *Theor Chem Acc* 2002;108:132–42.

Emmanuel A. Bisong*, Hitler Louis*, Tomsmith O. Unimuke,
Victoria M. Bassey, John A. Agwupuye, Linda I. Peter,
Francis O. Ekpen and Aderemi T. Adeleye

6 Theoretical investigation of the stability, reactivity, and the interaction of methyl-substituted peridinium-based ionic liquids

Abstract: This research work focuses on the reactivity, stability, and electronic interaction of pyridinium hydrogen nitrate (PHN)-based ionic liquids and the influence of methyl substituent on this class of ionic liquids: *Ortho*- (O-MPHN), *meta*- (M-MPHN), and *para*- (P-MPHN) substitution. Natural bond orbital (NBO) calculations were performed at the density functional theory (DFT) with Becke's Lee Yang and Parr functional (B3LYP) methods and DFT/B3LYP/6-311++G(d,p) as basis set using GAUSSIAN 09W and GAUSSVIEW 6.0 software and the most important interaction between donor (Filled Lewis-type NBO's) and the acceptor (vacant non-Lewis NBOs) were observed. From our natural bond orbital (NBO) result, it could be deduced that the higher the stabilization energy value, the greater the interaction between the donor and acceptor NBOs. The stability of the studied compounds is said to follow the order from O-MPHN > PHN > P-MPHN > M-MPHN based on the hyperconjugative interaction (stabilization energy) of the most significant interaction. The result of the highest occupied molecular orbital (HOMO), shows that PHN has the highest HOMO while the substituted derivatives have similar HOMO values between -7.70 and -7.98 eV thus PHN complex is the best electron donor while the substituted derivatives act as electron acceptors due to the presence of methyl group substituent which is observed to be electron deficient as a result of its withdrawal effect from the aromatic ring. Furthermore, the electron density, real space functions such as energy density and Laplacian of electron density at bond critical point (BCP) of the hydrogen bond interaction of the

*Corresponding authors: **Emmanuel A. Bisong and Hitler Louis**, Department of Pure and Applied Chemistry, Computational and Bio-Simulation Research Group, Faculty of Physical Sciences, University of Calabar, Calabar, Cross River State, Nigeria, E-mail: bisongea@unical.edu.ng (E.A. Bisong) (E.A. Bisong), louismuzong@gmail.com (H. Louis) (H. Louis)

Tomsmith O. Unimuke, Victoria M. Bassey, John A. Agwupuye and Linda I. Peter, Department of Pure and Applied Chemistry, Computational and Bio-Simulation Research Group, Faculty of Physical Sciences, University of Calabar, Calabar, Cross River State, Nigeria

Francis O. Ekpen, Department of Science Education, Faculty of Education, University of Calabar, Calabar, Cross River State, Nigeria

Aderemi T. Adeleye, Dalian Institute of Chemical Physics, University of Chinese Academy of Sciences, Dalian, P. R. China

This article has previously been published in the journal Physical Sciences Reviews. Please cite as: E. A. Bisong, H. Louis, T. O. Unimuke, V. M. Bassey, J. A. Agwupuye, L. I. Peter, F. O. Ekpen and A. T. Adeleye "Theoretical investigation of the stability, reactivity, and the interaction of methyl-substituted peridinium-based ionic liquids" *Physical Sciences Reviews* [Online] 2021, 7. DOI: 10.1515/psr-2020-0137 | <https://doi.org/10.1515/9783110739763-006>

studied compounds were analyzed using Multifunctional Wavefunction analyzer software version 3.7 and it was observed that the hydrogen at position 6 and oxygen at position 11 (H6–O11) of *M*-methyl pyridinium nitrate with bond distance of 4.59 (Å) gave binding energy with the strongest electrostatic interaction between the cation and anion of the compounds under investigation. We also observed from our results that, substitution at the *ortho* position enhances the stability and strengthen the extent of charge transfer. This therefore implies that substitution at *ortho* position is more favorable for inter- and intramolecular interactions resulting to stabilization of the studied molecules.

Keywords: DFT; ionic liquids; NBO; nitrate; pyridine; reactivity.

6.1 Introduction

Ionic liquids (ILs) could be defined in simple terms as liquids composed of ions (cations and anions) only and further expanded to be salts with melting point lower than 100 °C [1, 2]. Pyridinium-based ionic liquids have pyridinium ion as the cation and this class of ionic liquids are widely available due to its stability, reactivity, and catalysis in organic synthesis, pharmaceutical agents and other important applications [3, 4]. In recent decades, ILs are seen to be excellent alternative to the volatile organic solvents because of their environmental friendliness [1, 4]. The structural features and physicochemical properties of ILs give a better understanding of their stability and interactions [5].

ILs found applications in many areas including extraction media for metals [6], materials for dye-synthesized solar cells [7], solvent for separation sciences [8], electrolyte for electrochemical storage device [9]. Furthermore, they are widely applied in organic systems such as but not limited to Diels-Alder reaction, Friedel-Crafts reaction and Michael Protocol [10]. So far, a lot of works on ILs have been reported. In 1992, Wikes and Zaworotko [7] synthesized the first air-stable ILs. This therefore, served as a road map for a wide range of synthesized application of ILs. Rajni [4] reviewed the concept of ILs synthesis and application in catalysis. Irina and Lyubov [5] reported extensively theoretical investigation on the nature of the interactions in triethanolammonium-based ionic liquids. In this work, detail theoretical investigation on the stability, reactivity, and the interactions of methyl-substituted pyridinium-based ILs with nitric acid (HNO₃) in terms of natural bond orbital (NBO), highest occupied molecular orbital (HOMO), lowest unoccupied molecular orbital (LUMO), energy gap, atoms-in-molecule (AIM), atomic dipole moment corrected hirshfeld (ADCH) for atomic charge analysis of pyridine and its interaction with nitric acid, effect of methyl substituent on *meta*, *para*, *ortho* positions have been carried out theoretically which to the best our knowledge have not been reported for methyl-substituted pyridinium-based ILs.

6.2 Computational details

To give a better understanding of the effect of methyl substituent on the various positions of pyridinium-based ILs, pyridinium-based ionic liquid structure was obtained from literature studies [11] and methyl group attached to study its effect on *ortho*, *para*, and *meta* positions. GAUSSIAN 09W [12] and GAUSSVIEW 6.0 [13] software. Natural Bond Orbitals (NBO) 7.0 program [14] and Multifunctional Wavefunction Analyzer version 3.7 software [15] were used. Geometric optimization was done imploring density functional theory (DFT) with Becke's Lee Yang and Parr functional (B3LYP) methods and DFT/B3LYP/6-311++G(d,p) as basis set using GAUSSIAN 09W. The highest occupied molecular orbital (HOMO), lowest unoccupied molecular orbital (LUMO), and energy gap were obtained which give explanation on the stability of the studied compound. NBO explains charge transfer, intra-/intermolecular interaction. Atoms in molecule (AIM) and atomic dipole moment corrected Hirshfeld (ADCH) were carried out with Multifunctional Wavefunction Analyzer software to understand hydrogen bonding interaction and atomic charge analysis of pyridinium ion (cation) and its interaction with nitric acid (anion) respectively.

6.3 Results and discussion

6.3.1 Natural bond orbital (NBO) analysis

NBO analysis offers an efficient method for investigating intra and intermolecular bonding interactions among bonds, and provides the most accurate (natural Lewis structure) representation of orbitals, because all orbital details are mathematically chosen to include the highest possible percentage of the electron density. NBO analysis gives information about interactions in both filled and virtual orbitals which could facilitate the analysis of intra- and intermolecular interactions [16]. This is performed by considering all possible and most significant interactions between filled donor and vacant acceptor orbitals, and estimating their energy contribution by second-order perturbation theory. NBO calculations were performed at the DFT/B3LYP/6-311++G(d,p) levels. The most important interaction between donor (Filled Lewis-type NBO's) and the acceptor (vacant non-Lewis NBOs) is presented in Table 6.1, being the second-order theory resulting from microdisturbances based on the Fock matrix in the NBO basis of the studied compounds. The higher the stabilization energy value, the greater the interaction between the donor and acceptor NBOs. Hyperconjugative interactions in molecules plays an essential role and denotes weak departure from the ideal localized Lewis structure which constitute noncovalent interactions.

The second-order perturbation energies constant with the intramolecular hyperconjugative interactions of *Meta* Pyridinium Hydrogen Nitrate (MPHN), *Ortho* Pyridinium

Table 6.1: Second order perturbation theory analysis of the most interacting NBOs of the studied molecules using B3LYP/6-311++G(d,p) functional ^a $E^{(2)}$ represent the energy of hyperconjugative interaction (stabilization energy), ^benergy difference between donor and acceptor $E(i)$ and $E(j)$ NBO orbitals, ^c $F(i, j)$ is the Fock matrix element between i and j NBO).

| Donor (i) | Occupancy | Acceptor (j) | Occupancy | $E^{(2)a}$ (kcal/mol) | $E(j) - E(i)^b$ (a.u.) | $F(i, j)^c$ (a.u.) |
|------------------|-----------|--------------------|-----------|-----------------------|------------------------|--------------------|
| M-MPHN | | | | | | |
| π C1-C2 | 1.61324 | π^* C3-C4 | 0.32230 | 22.46 | 0.29 | 0.073 |
| | | π^* N5-C14 | 0.42545 | 17.84 | 0.25 | 0.060 |
| π C3-C4 | 1.97480 | π^* C1-C2 | 0.29452 | 18.01 | 0.28 | 0.065 |
| | | π^* N5-C14 | 0.42545 | 30.92 | 0.25 | 0.079 |
| σ C1-C2 | 1.98354 | σ^* C3-H9 | 0.01472 | 2.73 | 1.15 | 0.050 |
| π N5-C14 | 1.74701 | π^* C1-C2 | 0.29452 | 24.20 | 0.34 | 0.081 |
| | | π^* C3-C4 | 0.32230 | 12.12 | 0.34 | 0.058 |
| π^* N5-C14 | 0.42545 | π^* C1-C2 | 0.29452 | 84.99 | 0.03 | 0.078 |
| | | π^* C3-C4 | 0.32230 | 100.59 | 0.04 | 0.088 |
| LP(1)N5 | 1.84011 | σ^* C4-C14 | 0.02876 | 7.44 | 0.93 | 0.077 |
| | | σ^* C1-C2 | 0.02161 | 7.40 | 0.93 | 0.077 |
| | | LP*(1)H6 | 0.49815 | 72.71 | 0.46 | 0.180 |
| CR(1) O10 | 1.99975 | LP*(1) H6 | 0.49815 | 12.17 | 19.07 | 0.496 |
| LP(1)O10 | 1.97930 | LP*(1) H6 | 0.49815 | 17.78 | 0.74 | 0.118 |
| LP(3) O10 | 1.60395 | LP*(1) H6 | 0.49815 | 389.76 | 0.63 | 0.454 |
| σ N12-O13 | 1.99735 | σ^* N12-O13 | 0.63007 | 10.06 | 0.33 | 0.062 |
| LP(2)O10 | 1.83264 | σ^* N12-O13 | 0.63007 | 41.82 | 0.20 | 0.092 |
| LP(2) O11 | 1.87438 | σ^* O10-N12 | 0.16221 | 25.04 | 0.47 | 0.098 |
| | | π^* N12-O13 | 0.05170 | 15.64 | 0.76 | 0.099 |
| LP(3) O11 | 1.51978 | σ^* N12-O13 | 0.63007 | 151.36 | 0.15 | 0.139 |
| LP(2) O13 | 1.86165 | σ^* O10-N12 | 0.16221 | 27.68 | 0.46 | 0.102 |
| | | σ^* O11-N12 | 0.06292 | 17.21 | 0.71 | 0.101 |
| O-MPHN | | | | | | |
| σ C1-C2 | 1.98345 | σ^* C3-H10 | 0.01377 | 2.72 | 1.15 | 0.050 |
| π C1-C2 | 1.62543 | π^* C3-C4 | 0.30589 | 23.85 | 0.28 | 0.075 |
| | | π^* N5-C15 | 0.42601 | 15.62 | 0.26 | 0.057 |
| σ C1-N5 | 1.98591 | σ^* C15-C16 | 0.01867 | 3.19 | 1.25 | 0.056 |
| π C3-C4 | 1.64095 | π^* C1-C2 | 0.28493 | 16.11 | 0.28 | 0.062 |
| | | π^* N5-C15 | 0.42601 | 31.90 | 0.26 | 0.082 |
| π N5-C15 | 1.73414 | π^* C1-C2 | 0.28493 | 26.22 | 0.34 | 0.084 |
| | | π^* C3-C4 | 0.30589 | 10.75 | 0.33 | 0.054 |
| LP(1)N5 | 1.83670 | σ^* C1-C2 | 0.02174 | 7.36 | 0.93 | 0.076 |
| | | σ^* C4-C15 | 0.02942 | 8.44 | 0.93 | 0.082 |
| π^* N5-C15 | 0.42601 | π^* C1-C2 | 0.28493 | 97.86 | 0.03 | 0.076 |
| | | π^* C3-C4 | 0.30589 | 140.98 | 0.02 | 0.087 |
| LP(1) N5 | 1.83670 | LP*(1) H7 | 0.49917 | 73.95 | 0.45 | 0.179 |
| CR(1)O11 | 1.99975 | LP*(1) H7 | 0.49917 | 12.15 | 19.06 | 0.496 |
| LP(1) O11 | 1.97876 | LP*(1) H7 | 0.49917 | 17.97 | 0.74 | 0.118 |
| LP(3) O11 | 1.60768 | LP*(1) H7 | 0.49917 | 384.57 | 0.63 | 0.451 |
| σ N13-O14 | 1.99732 | σ^* N13-O14 | 0.62971 | 10.05 | 0.33 | 0.062 |
| LP(2) O11 | 1.83285 | σ^* N13-O14 | 0.62971 | 41.70 | 0.20 | 0.092 |

Table 6.1: (continued)

| Donor (<i>i</i>) | Occupancy | Acceptor (<i>j</i>) | Occupancy | $E^{(2)a}$ (kcal/mol) | $E(j) - E(i)^b$ (a.u.) | $F(i, j)^c$ (a.u.) |
|--------------------|-----------|-----------------------|-----------|-----------------------|------------------------|--------------------|
| LP(2) O12 | 1.87428 | $\sigma^*O11-N13$ | 0.16258 | 25.02 | 0.47 | 0.098 |
| | | $\pi^*N13-O14$ | 0.05172 | 15.67 | 0.76 | 0.099 |
| LP(3)O12 | 1.51949 | $\sigma^*N13-O14$ | 0.62971 | 151.45 | 0.15 | 0.139 |
| LP(2)O14 | 1.86169 | $\sigma^*O11-N13$ | 0.16258 | 27.68 | 0.46 | 0.102 |
| | | $\sigma^*O12-N13$ | 0.06290 | 17.22 | 0.71 | 0.101 |
| P-MPHN | | | | | | |
| $\sigma C1-C2$ | 1.98225 | $\sigma^*C3-C15$ | 0.01628 | 3.99 | 1.13 | 0.060 |
| $\pi C1-C2$ | 1.63101 | σ^*C3-C4 | 0.02393 | 24.45 | 0.29 | 0.076 |
| $\sigma C1-N5$ | 1.98723 | $\sigma^*N5-C13$ | 0.01829 | 16.14 | 0.25 | 0.058 |
| $\sigma C2-H8$ | 1.97904 | σ^*C1-N5 | 0.01775 | 4.50 | 1.05 | 0.061 |
| | | σ^*C3-C4 | 0.02393 | 4.16 | 1.09 | 0.060 |
| $\pi C3-C4$ | 1.61198 | π^*C1-C2 | 0.27995 | 15.78 | 0.28 | 0.061 |
| | | $\pi^*N5-C13$ | 0.42260 | 33.79 | 0.25 | 0.083 |
| $\pi N5-C13$ | 1.98753 | π^*C1-C2 | 0.27995 | 25.30 | 0.34 | 0.083 |
| | | π^*C3-C4 | 0.32400 | 10.78 | 0.34 | 0.055 |
| LP(1) N5 | 1.83860 | σ^*C1-C2 | 0.02111 | 7.41 | 0.93 | 0.077 |
| | | σ^*C3-C4 | 0.02393 | 7.48 | 0.93 | 0.077 |
| $\pi^*N5-C13$ | 0.42260 | π^*C1-C2 | 0.27995 | 78.09 | 0.03 | 0.077 |
| | | π^*C3-C4 | 0.32400 | 98.29 | 0.04 | 0.086 |
| LP(1)N5 | 1.83860 | $LP^*(1)H6$ | 0.49830 | 73.92 | 0.47 | 0.182 |
| LP(1)O9 | 1.97914 | $LP^*(1)H6$ | 0.49830 | 12.15 | 19.07 | 0.496 |
| | | $LP^*(1)H6$ | 0.49830 | 17.75 | 0.74 | 0.117 |
| LP(3)O9 | 1.60546 | $LP^*(1)H6$ | 0.49830 | 387.85 | 0.63 | 0.454 |
| $\sigma N11-O12$ | 1.99735 | $\sigma^*N11-O12$ | 0.63012 | 10.06 | 0.33 | 0.062 |
| LP(2)O9 | 1.83163 | $\sigma^*N11-O12$ | 0.63012 | 42.09 | 0.20 | 0.092 |
| LP(2)O10 | 1.87487 | $\sigma^*O9-N11$ | 0.16140 | 24.91 | 0.47 | 0.098 |
| | | $\pi^*N11-O12$ | 0.05171 | 15.64 | 0.76 | 0.099 |
| LP(3)O10 | 1.52076 | $\sigma^*N11-O12$ | 0.63012 | 150.92 | 0.15 | 0.139 |
| LP(2)O12 | 1.86195 | $\sigma^*O9-N11$ | 0.16140 | 27.60 | 0.47 | 0.102 |
| | | $\sigma^*O10-N11$ | 0.06306 | 17.24 | 0.71 | 0.101 |
| PHN | | | | | | |
| $\sigma C1-C2$ | 1.98409 | $\sigma^*C3-H12$ | 0.01387 | 2.61 | 1.16 | 0.049 |
| $\pi C1-C2$ | 1.61718 | π^*C3-C4 | 0.30526 | 23.22 | 0.28 | 0.074 |
| | | π^*C5-N6 | 0.41151 | 17.27 | 0.25 | 0.059 |
| $\sigma C1-H10$ | 1.98033 | σ^*C5-N6 | 0.01830 | 5.28 | 1.05 | 0.066 |
| $\pi C3-C4$ | 1.63145 | π^*C1-C2 | 0.28082 | 16.70 | 0.28 | 0.063 |
| | | π^*C5-N6 | 0.41151 | 31.26 | 0.25 | 0.080 |
| $\pi C5-N6$ | 1.98787 | π^*C1-C2 | 0.28082 | 24.81 | 0.34 | 0.082 |
| | | π^*C3-C4 | 0.30526 | 11.55 | 0.33 | 0.056 |
| $\sigma C5-H8$ | 1.98118 | σ^*C1-N6 | 0.01783 | 5.14 | 1.06 | 0.066 |
| LP(1)N6 | 1.84366 | σ^*C1-C2 | 0.02184 | 7.47 | 0.93 | 0.077 |
| | | σ^*C4-C5 | 0.02164 | 7.55 | 0.92 | 0.077 |
| π^*C5-N6 | 0.41151 | π^*C1-C2 | 0.28082 | 79.60 | 0.03 | 0.077 |
| | | π^*C3-C4 | 0.30526 | 112.70 | 0.03 | 0.087 |
| CR(1)O13 | 1.99975 | $LP^*(1)H9$ | 0.49732 | 12.23 | 19.07 | 0.497 |

Table 6.1: (continued)

| Donor (<i>i</i>) | Occupancy | Acceptor (<i>j</i>) | Occupancy | $E^{(2)a}$ (kcal/mol) | $E(i) - E(j)^b$ (a.u.) | $F(i, j)^c$ (a.u.) |
|--------------------|-----------|-----------------------|-----------|-----------------------|------------------------|--------------------|
| LP(1)O13 | 1.97948 | LP*(1)H9 | 0.49732 | 17.84 | 0.74 | 0.118 |
| LP(3)O13 | 1.60105 | LP*(1)H9 | 0.49732 | 394.29 | 0.63 | 0.457 |
| σ N15-O16 | 1.99736 | σ^* N15-O16 | 0.62846 | 10.01 | 0.33 | 0.062 |
| LP(2)O13 | 1.83404 | σ^* N15-O16 | 0.62846 | 41.39 | 0.20 | 0.092 |
| LP(2)O14 | 1.87402 | σ^* O13-N15 | 0.16337 | 25.14 | 0.47 | 0.098 |
| | | π^* N15-O16 | 0.05147 | 15.60 | 0.76 | 0.099 |
| LP(3)O14 | 1.52004 | σ^* N15-O16 | 0.62846 | 150.96 | 0.15 | 0.139 |
| LP(2)O16 | 1.86077 | σ^* O13-N15 | 0.16337 | 27.88 | 0.46 | 0.102 |
| | | σ^* O14-N15 | 0.06292 | 17.23 | 0.71 | 0.101 |

Hydrogen Nitrate (OPHN), *Para* Pyridinium Hydrogen Nitrate (PPHN), and Pyridinium Hydrogen Nitrate (PHN)-based ionic liquid respectively which result in the intermolecular charge transfer (ICT) affecting stabilization of the systems respectively are presented in Table 6.1. The maximum interactions with the highest $E(2)$ energy for MPMH are: $\pi^*(N5 - C14) \rightarrow \pi^*(C3 - C4)$ (100.59 kcal/mol), $\pi^*(N5 - C14) \rightarrow \pi^*(C1 - C2)$ (84.99 kcal/mol), $\pi(C3 - C4) \rightarrow \pi^*(N5 - C14)$ (30.92 kcal/mol), while those of O and P-MPHM are $\pi^*(N5 - C15) \rightarrow \pi^*(C3 - C4)$ (140.98 kcal/mol), $\pi^*(N5 - C15) \rightarrow \pi^*(C1 - C2)$ (97.86 kcal/mol), $\pi(C3 - C4) \rightarrow \pi^*(N5 - C15)$ (31.90 kcal/mol), $\pi(N5 - C13) \rightarrow \pi^*(C1 - C2)$ (78.09 kcal/mol), $\pi(N5 - C13) \rightarrow \pi^*(C3 - C4)$ (98.29 kcal/mol), $\pi(C3 - C4) \rightarrow \pi^*(N5 - C13)$ (33.79 kcal/mol), similarly, the strongest interaction resulting to the highest stabilization observed in PHN are $\pi^*(C5 - N6) \rightarrow \pi^*(C3 - C4)$ (112.70 kcal/mol), $\pi^*(C5 - N6) \rightarrow \pi^*(C1 - C2)$ (79.60 kcal/mol), and $\pi(C3 - C4) \rightarrow \pi^*(C5 - N6)$ (31.26 kcal/mol) this clearly shows that the resonance observed in the system results from the delocalization of electrons principally from the nitrogen atom in the ring to the adjacent carbon antibonding acceptors of the ring and they are related to $\pi \rightarrow \pi^*$ and $\pi^* \rightarrow \pi^*$ interactions. These strong interactions within the pyridine ring system as observed in the results suggest that the compounds are resonance stabilized. The second-order perturbations energies consistent with the inter molecular hyper conjugative interaction between the hydrogen and the anion fragment (N-H and molecular unit 3 NO₃) such as; LP(3)O10 \rightarrow LP*(1)H6 (389.76 kcal/mol) and LP(3)O11 \rightarrow σ^* N12-O13 (151.36 kcal/mol), LP(3)O11 \rightarrow LP*(1)H7 (384.57 kcal/mol), LP(3)O12 \rightarrow σ^* (N13-O14) (151.54 kcal/mol), LP(3)O9 \rightarrow LP*(1)H6 (387.85 kcal/mol), LP(3)O10 \rightarrow σ^* (N11-O12) (150.92 kcal/mol), LP(3)O13 \rightarrow LP*(1)H9 (394.29 kcal/mol), LP(3)O14 \rightarrow σ^* (N15-O16) (150.96 kcal/mol) respectively corresponding to M, O, P-PHN, and PHN are considerably very large and are most responsible for intramolecular hydrogen bonding existing within the molecule. Hydrogen bonds are expected to arise from charge transfer from lone pairs (LP) of proton acceptors to the antibonding of the proton donor and thus the amount of charge transfer and energy of interaction has a significant effect in the strength of the

resulting hydrogen bond. The larger the second-order perturbation energy value (E_2 -value), the greater the extent of charge transfer from the Lewis type donor to the non-Lewis-type acceptors and as such the higher their interaction and strength of hydrogen bond. The result suggest that the strongest charge transfer and hydrogen bond strength occurs in the pyridinium hydrogen nitrate (PHN) and decreases with substitution, the *ortho* substituted methyl-PHN is seen to give the least E_2 energy from the LP \rightarrow LP* (H) interaction and these interactions are observed to give the highest calculated stabilization energy and also the extent of charge transfer for this interaction is higher than that observed for LP \rightarrow σ^* (N-O).

A few nonbonding interactions of 7.44 kcal/mol *meta*-substituted methyl pyridinium hydrogen nitrate (M-MPHN), 8.44 kcal/mol *ortho*-substituted methyl pyridinium hydrogen nitrate (O-MPHN), 7.48 kcal/mol *para*-substituted methyl pyridinium hydrogen nitrate (P-MPHN), and 7.55 kcal/mol (PHN) are obtained for LP(1)N5 \rightarrow σ^* (C4 - C14), LP(1)N5 \rightarrow σ^* (C4 - C15), LP(1)N5 \rightarrow σ^* C3 - C4), LP(1)N6 \rightarrow σ^* (C4 - C5) respectively which increase the stability of the system. The increasing stabilization energy observed for the O-MPHN can be attributed to the electron donation from the methyl group close to the pyridinium nitrogen in the ring which increases the stability by reducing the strong electron withdrawing effect of the oxygen atoms; this is in line with the E_2 values obtained for the intramolecular interaction within the ring by resonance from π^* (N5 - C15) \rightarrow π^* (C3 - C4) which is the strongest interaction. Thus, we can infer from the result that substitution at the *ortho* position enhances the stability and strengthen the extent of charge transfer (*ortho* substitution is more favorable for inter and intramolecular interactions resulting to the stabilization of the system) and the strongest electron donation occurs from the LP orbitals of the oxygen atom of the anion to the antibonding orbitals of the hydrogen atom (*N-H) which shows significant increase in the covalent character of the N-H-O bond. The stability of the molecules is said to follow the order from O-MPHN > PHN > P-MPHN > M-MPHN based on the E_2 energy of the most significant interaction.

The distribution of charge on molecules has significant impact on the vibrational properties. The corresponding NBO charge distribution of the studied compounds is presented in Figure 6.1 obtained at the B3LYP/6311++G(d,p) level. It is noted that the strong negative and positive partial charges on the individual atoms of the studied compounds increase based on the interaction experienced by neighboring atoms [17]. These observed distribution of charges on atoms indicates strong electrostatic repulsive interactions between atoms which contribute to the intra- and intermolecular interactions. The NBO calculated atomic charge values shows that C2, C4, N5, O10, O11 and the methyl carbon atom have large negative values (indicated with red colors) and thus act as electron acceptors while C1, C14 (M-MPHN), C1, C15 (O-MPHN), C1, C13 (P-MPHN), C1, C5 (PHN) have large positive value due to the polarity of C-N bond. The lowest occupancy orbitals π^* N5-C14 (0.42545e), π C1-C2 (1.61324e) (M-MHPN), π^* N5-C15 (0.42601e), π C1-C2 (1.62543e) (O-MPHN), π^* N5-C13 (0.42260e), π C3-C4 (1.61198e) (P-MPHN), π^* C5-N6 (0.41151e), π C1-C2 (1.61718e) (PHN), were expressed via a similar

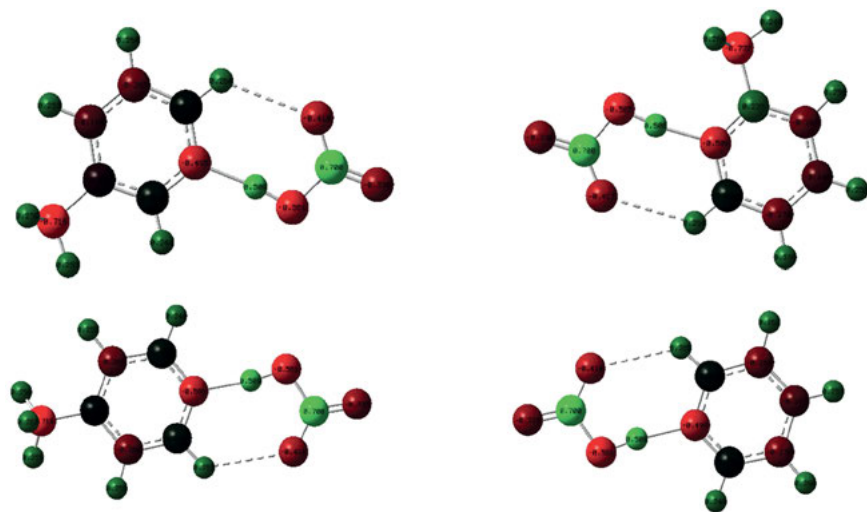


Figure 6.1: NBO charge distribution of the studied compounds obtained at the B3LYP/6311++G(d,p) level.

contribution in the range of 39.71% $sp^{1.72}$ (N5), 60.29% $sp^{2.20}$ (C14), 46.65% $sp^{1.00}$ (C1), and 53.35% $sp^{1.00}$ (C2) respectively.

6.3.2 Analysis of HOMO–LUMO

The highest occupied molecular orbital (HOMO) and the lowest unoccupied molecular orbital (LUMO) give us information about the chemical stability of molecules [18]. Insight into the nature of reactivity of most chemical species as well as their structural and physical properties can be explicitly obtained by investigating molecular orbitals. The HOMO is often associated with the ability to donate electrons while the LUMO represents the tendency to accept electrons. The ground state to the first excited state electronic transitions in molecules as a result of energy absorption is often related with the movement of electrons from the highest occupied molecular orbitals to the lowest unoccupied molecular orbital (LUMO). π -type HOMO and π -type LUMO are inherently localized within and delocalized over the entire ring respectively thus the transition from the HOMO to the LUMO involves energy transfer from the aromatic ring. The difference in energy between the HOMO and LUMO has been extensively utilized in probing the bioactivity of molecules based on charge transfer [19, 20]. It has also been reported in most literature studies that the kinetic stability of compounds is related to the difference in energy between the HOMO and LUMO of such compounds thus, small values of energy gap in molecules signifies a greater tendency for such molecules to be polarized and also denotes high chemical reactivity and low kinetic stability [21–24].

Table 6.2: HOMO, LUMO, energy gap.

| Compound | HOMO | LUMO | Energy gap |
|----------|----------|----------|-------------|
| M-MPHN | -7.90 eV | -1.93 eV | 5.96 kJ/mol |
| O-MPHN | -7.87 eV | -1.89 eV | 5.97 kJ/mol |
| P-MPHN | -7.98 eV | -1.83 eV | 6.15 kJ/mol |
| PHN | -8.08 eV | -2.00 eV | 6.00 kJ/mol |

The HOMO and LUMO energies calculated at the B3LYP/6311++G(d,p) level of theory for the studied compounds are presented in Table 6.2. The result shows that PHN has the highest HOMO while the substituted derivatives have similar HOMO values between -7.70 and -7.98 eV thus PHN complex is the best electron donor while the substituted derivatives act as electron acceptors due to the presence of methyl group substituent which is observed to be electron deficient due to withdrawal effect from the aromatic ring. observation of the energy gap suggest that M-MPHN has the lowest energy gap which suggest that it is the softest complex based on the concept of hardness and softness whereas the complex with the highest energy gap is P-MPHN; thus, it is the hardest molecule and as such more polarizable based on this concept, the chemical hardness and softness of molecules have been demonstrated in previous reports to have a direct correlation with the stability of most systems. The stability of the studied compounds based on the HOMO-LUMO concept and observation of the

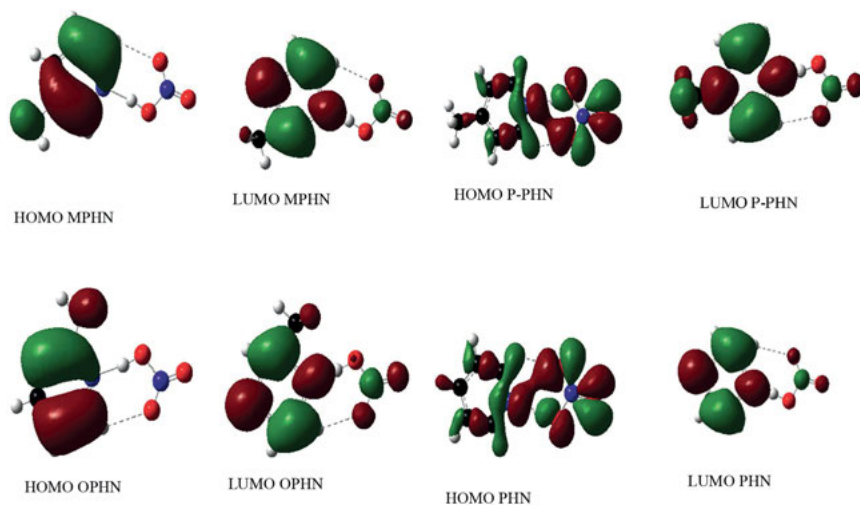


Figure 6.2: Orbitals involved in the electronic transition of *meta* pyridinium hydrogen nitrate (MPHN), *para* pyridinium hydrogen nitrate (PPHN), *ortho* pyridinium hydrogen nitrate (OPHN), and pyridinium hydrogen nitrate (PHN) for the highest occupied molecular orbital (HOMO) and lowest unoccupied molecular orbital (LUMO) respectively.

energy gap difference is seen to follow a trend in the order P -MPHN > PHN > O -MPHN > M -MPHN which shows that substitution at the *para* position enhances the stability of the ionic liquid system and substitution at the meta position slightly distorts the kinetic stability. Figure 6.2 shows orbitals involved in the electronic transition of the studied compounds for the highest occupied molecular orbital (HOMO) and lowest unoccupied molecular orbital (LUMO)

6.3.3 Atomic dipole moment corrected Hirshfeld (ADCH) atomic charge analysis of pyridinium ion and its interaction with hydrogen nitrate: emphasis on the nitrogen charge

In the ADCH method, atomic dipole moment of each atom is expanded to correction charges placed at neighboring atoms and the ADCH charge is the sum of the Hirshfeld charge and correction charge [24]. The charge density on the compounds before and after interaction with hydrogen nitrate Table 6.3, shows that the *para*-substituted position has a charge density of -0.3456 which is more electronegative than that of pyridinium ion which is -0.3318 , implying that the methyl group alters the electron density on the pyridinium ring. This is seen to increase from the *Para*_Pyridinium > *Meta*_Pyridinium > *Ortho*_Pyridinium substitutions. On interaction with hydrogen nitrate, the electron charge density on pyridinium ring is greatly altered as the nitric acid which is more electron withdrawing pulls more electronic charge to itself. This is observed with the higher values of atomic charges after interaction, as compared with those before interaction.

6.3.4 The electrostatic molecular potential (ESP) plot

The ESP plot of the interaction of methyl-substituted pyridine with hydrogen nitrate is reported in Figure 6.3. The heavily colored region of red and blue corresponds to regions of low and high electron charge density respectively. The *para*-substituted ESP has a relatively denser region of electron density (blue) which is as a result of the high amount of charge density located in the hydrogen nitrate fragment [25]. This validates our observation in ADCH charge analysis that the N-atom of the *p*-substituted fragments possess the relatively higher charge density. In general, the NO_3 fragments

Table 6.3: Atomic dipole moment corrected Hirshfeld (ADCH) atomic charge analysis of pyridine and its interaction with nitric acid: emphasis on the nitrogen charge.

| Compound | Before interaction | After interaction |
|--------------------|--------------------|-------------------|
| Pyridine | -0.3318 | -0.0874 |
| <i>O</i> -pyridine | -0.3191 | -0.0888 |
| <i>M</i> -pyridine | -0.3325 | -0.0851 |
| <i>P</i> -pyridine | -0.3456 | -0.0959 |

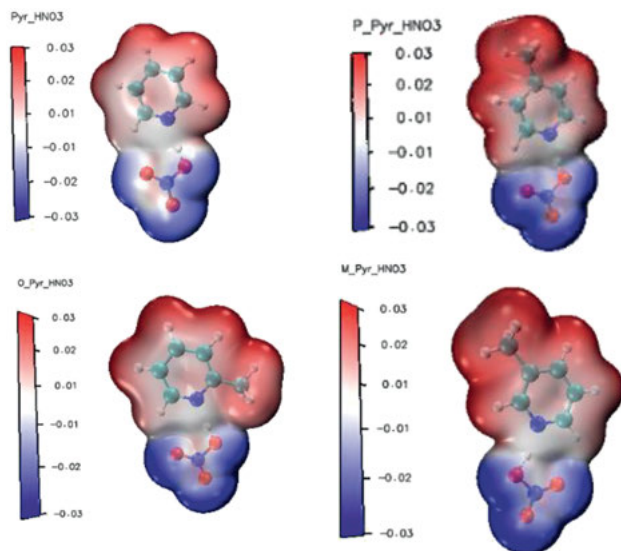


Figure 6.3: The electrostatic molecular potential (ESP) plot.

demonstrated high charge density due to the electron withdrawing power of NO_3^- relative to the pyridinium ion fragment.

6.3.5 Binding energy

As reported in Table 6.4, Binding energy of the *para*-substituted pyridinium ion is -3.23 kJ/mol which shows that *para*-substituted pyridinium interaction with hydrogen nitrate is more stable as compared to the *ortho*- and *meta*-substituted pyridinium ion. The *ortho*, *meta*, and bare pyridinium ILs binding energy follow the pattern: $M(1.42) > O(1.39) > \text{Pyr.}(1.34)$. The binding energy is evaluated according to the equation: Binding Energy (BE) = $E(A) + E(B) - E(A\&B)$, where Fragment A: Pyridine, Fragment B: hydrogen nitrate, and pyridinium complex is (A&B).

Table 6.4: Binding energy.

| Fragment A | Energy of fragment A (Hartree) | Energy of fragment B (Hartree) | Energy of complex (Hartree) | $E(A) + E(B)$ (Hartree) | Binding energy (Hartree) | Binding energy (kJ/mol) |
|------------|--------------------------------|--------------------------------|-----------------------------|-------------------------|--------------------------|-------------------------|
| PHN | -248.34 | -280.95 | -529.35 | -529.30 | 0.04 | 1.34 |
| O-PHN | -287.67 | -280.95 | -568.68 | -568.63 | 0.05 | 1.39 |
| M-PHN | -287.67 | -280.95 | -568.68 | -568.62 | 0.05 | 1.42 |
| P-PHN | -287.67 | -280.95 | -568.51 | -568.63 | -0.11 | -3.23 |

6.3.6 Atoms-in-molecules (AIM) descriptors and H-atom binding energies

The atoms-in-molecules (AIM) were computed to investigate the intermolecular interaction between the cation and anion of the studied compounds. The hydrogen bond designated by X–B...Y–Z in scholarly research papers, connotes an attractive interaction between a hydrogen atom from a molecule (or molecular fragment) X–H where X is more electronegative element than H, and an atom(s) in the same (or different) molecule, in which there is bond formation. One of the most important quantities that characterizes hydrogen bond (HB) is the binding energy (BE) between two species (monomers) in complex geometry [26, 27].

In this study, the electron density, real space functions such as energy density and Laplacian of electron density at bond critical point (BCP) of the HB interaction of the studied compounds were analyzed using Multifunctional Wavefunction Analyzer software version 3.7 [15, 28]. The BE and the wave function-based HB descriptors were calculated for bond critical point (BCP; ρ_{BCP}) of HBs using the approximation;

$$BE \text{ (kcal/mol)} = -223.08 \times \rho_{\text{BCP}}/\text{a.u.} + 0.74235$$

With a mean absolute percentage error (MAPE) of 14.7% [26]. The results of the BEs and classification of the intermolecular HBs for the fully optimized molecules is presented in Table 6.5. In our investigated, the binding energies of –10.36 (N6–H9) and –15.85 (H10–O14); –11.55 (H8–O12) and –10.97 (N5–H7); –10.19 (N5–H6) and –17.83 (H6–O11); –16.42 (N2–H6) and –10.30 (H10–O14) were obtained for pyridinium nitrate, *O*-methyl pyridinium nitrate, *M*-methyl pyridinium nitrate, and *P*-methyl pyridinium nitrate respectively. Interestingly, the bond formed between H10–O14 (in pyridinium nitrate), H6–O11 (in *M*-methyl pyridinium nitrate), and N2–H6 (in *P*-methyl pyridinium nitrate) are strong hydrogen bonds driven by electrostatic interaction. On the other hand, other N–H and H–O bonds of the titled molecules (Table 6.5) are classified as

Table 6.5: Binding energy of the studied molecules and classification of H-bonds calculated at B3LYP/aug-cc-PVDZ level.

| ILs | Structure | Bond distance (Å) | BE (kcal/mol) | Strength | Major nature |
|-------------------------------------|--------------|-------------------|---------------|----------------|---------------|
| Pyridinium nitrate | CN6...H9ON | 3.85 | –10.36 | Weak-to-medium | Electrostatic |
| | CH10...O14NO | 4.29 | –15.85 | Strong | Electrostatic |
| <i>O</i> -methyl pyridinium nitrate | CH8...O12NO | 4.55 | –11.55 | Weak-to-medium | Electrostatic |
| <i>M</i> -methyl pyridinium nitrate | CN5...H7ON | 3.29 | –10.97 | Weak-to medium | Electrostatic |
| <i>P</i> -methyl pyridinium nitrate | CN5...H6ON | 1.34 | –10.19 | Weak-to-medium | Electrostatic |
| Pyridinium nitrate | CH6...O11NO | 4.59 | –17.83 | Strong | Electrostatic |
| | CN2...H6ON | 1.39 | –16.42 | Strong | Electrostatic |
| <i>P</i> -methyl pyridinium nitrate | CH10...O14NO | 5.48 | –10.30 | Weak-to-strong | Electrostatic |

weak-to-medium HBs since the magnitude of each of the molecules BE is larger than 2.5 kcal/mol but lower than 15.0 kcal/mol and are characterized by electrostatic interaction [26]. However, H6–O11 with bond distance of 4.59 (Å) of *M*-methyl pyridinium nitrate gave BE with the strongest electrostatic interaction between the cation and anion of the studied compounds.

6.4 Conclusions

Extensive theoretical evaluation and discussion on the basic chemistry of methyl-substituted pyridinium-based ionic liquids in the aspect of reactivity, stability, and interaction has been provided in this study. Key findings have been made theoretically. However, experimental work is needed to validate the theoretical study. From our findings, methyl substitution on the various positions of pyridinium hydrogen nitrate, shows the *meta* position is least stable while the *ortho* position is the most stable. Moreover, methyl group is electron deficient. Thus, PHN complex is the best electron donor while the substituted derivatives act as electron acceptors due to the presence of methyl group substituent which is observed to be electron deficient as a result of its withdrawal effect from the aromatic ring. Furthermore, we were able to establish an interesting trend in the stability of the studied compounds from *O*-MPHN > PHN > *P*-MPHN > *M*-MPHN based on the hyperconjugative interaction (stabilization energy) of the most significant interaction

Acknowledgments: This research work was not funded by any external organization. However, Dr. Emmanuel A. Bisong and his coauthors are thankful to computation science research group, University of Calabar, Nigeria headed by Dr. Hitler Louis.

Author contributions: All the authors have accepted responsibility for the entire content of this submitted manuscript and approved submission.

Research funding: None declared.

Conflict of interest statement: The authors declare no conflicts of interest regarding this article.

References

1. Rajni R. Ionic liquid synthesis and application in catalysis. *Adv Chem* 2014;729842:1–16.
2. Patricia AH, Claire RA, Richad PM. Hydrogen bonding in ionic liquids. *Chem Soc Rev* 2015;44: 1257–88.
3. Ogomi Y, Kato T, Hayase S. Dye sensitized solar cells consisting of ionic liquid and solidification. *J Photopolym Sci Technol* 2006;19:403–8.
4. Gorlov M, Kloo L. Ionic liquid electrolytes for dye-synthesized solar cells. *Dalton Trans* 2008;28: 2655–66.

5. Irina VF, Lyubov PS. The nature of the interactions in triethanolammonium-based ionic liquids. A quantum chemical study. *J Phys Chem A* 2018;122:4562–70.
6. Alessandrini F, Appetechi GB, Conte M, Passen S. Ionic liquid based electrolytes for high energy electrochemical storage devices. *ECS Trans* 2006;1:67–71.
7. Wikes JS, Zaworotko M. Air and water stable 1-ethyl-3-methylimidazolium based ionic liquids. *J Chem Soc Chem Commun* 1992;13:965–7.
8. Dupont J, de Souza RF, Suarez PA. Ionic liquids (molten salt) phase organometallic catalysis. *Z Chem Rev* 2002;102:3667–92.
9. Welton T. Ionic liquids: a brief history. *Biophys Rev* 2002;10:691–706.
10. Earle M Ionic liquids in synthesis (Wasserebeid P, Weston T, editors.), vol 2. Weinheim: Wiley-Vett; 2008. p. 292–369.
11. Ivaylo T, Romyana Y, Svetlana G, Magdalena M, Dicho S. Density functional theory study on the ionic liquids pyridinium hydrogen sulfate. *J Mol Struct* 2017;1139:400–6.
12. Frisch MJ, Trucks GW, Schlegel HB, Scuseria GE, Robb MA, Cheeseman JR, et al. Gaussian 09, Revision C. 02. Wallingford CT: Gaussian, Inc.; 2009.
13. Dennington RD, Keith TA, Millam JM. GaussView 6.0. 16, Semichem. Inc., Shawnee Mission KS; 2016.
14. Glenedeming ED, Reed AE, Carpenter JE, Weinhold F. NBO version 3.1. TCL-University Wisconsin Madison; 1998.
15. Lu T. Multiwfn manual, version 3.7(dev), Section 3.21.1. Available at: <http://sobereva.com/multiwfn> [Accessed 20 Nov 2019].
16. Theivarasu C, Murugesan R. Natural bond orbital (NBO) population analysis of an energetic molecule 1-phenyl-2-nitroguanidine. *Int J Chem Sci* 2016;14:2029–50.
17. Magdaline JD, Chithambarathanu T. Vibrational spectra (FT-IR, FT-Raman), NBO and HOMO, LUMO studies of 2-thiophene carboxylic acid based on density functional method. *IOSR J Appl Chem* 2015;8:06–14.
18. Bisong EA, Louis H, Unimuke TO, Odey JO, Ubana EI, Edim MM, et al. Vibrational, electronic, spectroscopic, properties and NBO analysis of p-xylene, 3,6-difluoro-p-xylene, 3,6-dichloro-p-xylene, 3,6-dibromo-p-xylene: DFT study. *Heliyon* 2020;6:e05783.
19. De Lile JR, Kang SG, Son Y-A, Lee SG. Do HOMO–LUMO energy levels and band gaps provide sufficient understanding of dye-sensitizer activity trends for water purification. *ACS Omega* 2020.
20. Edim MM, Enudi OC, Asuquo BB, Louis H, Bisong EA, Agwupuye JA, et al. Aromaticity indices, electronic structural properties and fuzzy atomic space investigations of naphthalene and its azo derivatives. *Heliyon* 2021;7:e06138.
21. Ali M, Mansha A, Asim S, Zahid M, Usman M, Ali N. DFT study for the spectroscopic and structural analysis of p-dimethylaminoazobenzene. *J Spectrosc* 2018:15.
22. Abbaz T, Amel B, Villemin D. Density functional theory studies on molecular structure and electronic properties of sulfanilamide, sulfathiazole, E7070 and furosemide molecules. *J Appl Chem* 2019;12:60–9.
23. Magdalene JD, Chithambarathanu T. Vibrational spectra (FT-IR, FT-Raman), NBO and HOMO, LUMO studies of 2-thiophene carboxylic acid based on density functional method. *J Appl Chem* 2015;8:06–14.
24. Lu T, Chen F. Atomic dipole moment corrected Hirshfeld population method. *J Theor Comput Chem* 2012;11:163.
25. Liu Z, Lu T, Chen Q. An *sp*-hybridized all-carboatomic ring, cyclo[18]carbon: bonding character, electron delocalization, and aromaticity. *Carbon* 2020;165:468–75.
26. Emamian S, Lu T, Kruse H, Emamian H. Exploring nature and predicting strength of hydrogen bonds: a correlation analysis between atoms-in-molecules descriptors, binding energies, and energy components of symmetry-adapted perturbation theory. *J Comput Chem* 2019;40:2868–81.

27. Singh I, El-Emam A, Pathak S, Srivastava R, Shukla V, Prasad O, et al. Experimental and theoretical DFT (B3LYP, X3LYP, CAM-B3LYP and M06-2X) study on electronic structure, spectral features, hydrogen bonding and solvent effects of 4-methylthiadiazole-5-carboxylic acid. *Mol Simulat* 2019; 45:1029–43.
28. Arunan E, Desiraju Gautam R, Klein Roger A, Sadlej J, Scheiner S, Alkorta I, et al. Definition of the hydrogen bond (IUPAC Recommendations 2011). *Pure Appl Chem* 2011;83:1637–41.

Tandrima Banerjee and Abhijit Samanta*

7 Chemical computational approaches for optimization of effective surfactants in enhanced oil recovery

Abstract: The surfactant flooding becomes an attractive method among several Enhanced Oil Recovery (EOR) processes to improve the recovery of residual oil left behind in the reservoir after secondary oil recovery process. The designing of a new effective surfactant is a comparatively complex and often time consuming process as well as cost-effective due to its dependency on the crude oil and reservoir properties. An alternative chemical computational approach is focused in this article to optimize the performance of effective surfactant system for EOR. The molecular dynamics (MD), dissipative particle dynamics (DPD) and density functional theory (DFT) simulations are mostly used chemical computational approaches to study the behaviour in multiple phase systems like surfactant/oil/brine. This article highlighted a review on the impact of surfactant head group structure on oil/water interfacial property like interfacial tensions, interface formation energy, interfacial thickness by MD simulation. The effect of entropy in micelle formation has also discussed through MD simulation. The polarity, dipole moment, charge distribution and molecular structure optimization have been illustrated by DFT. A relatively new coarse-grained method, DPD is also emphasized the phase behaviour of surfactant/oil/brine as well as polymer-surfactant complex system.

Keywords: computational modeling, density functional theory, dissipative particle dynamics, interfacial tensions, molecular dynamics simulation, oil–water interface

7.1 Introduction

Energy from various fossil fuels like oil, coal, natural gas, etc. has become an important factor of the global economic development for past century. Among these natural fuels, petroleum remains the main power source [1–3]. It has been predicted that the global energy consumption will increase by 1.7% per annum in barrels of the oil production between 2020 and 2030, as the projected oil utilization is to be reached about 15.3 billion tons yearly. Hence, if this intensity of demand will carry, the availability of crude oil in the reservoirs can fulfill this requirement by around next 40 years [4, 5].

*Corresponding author: **Abhijit Samanta**, School of Engineering and Applied Sciences, The Neotia University, Sarisha, West Bengal 743368, India, E-mail: abhijit.ism08@hotmail.com

Tandrima Banerjee, Department of Chemical Sciences, Indian Institute of Science Education and Research (IISER) Kolkata, West Bengal 741246, India

This article has previously been published in the journal *Physical Sciences Reviews*. Please cite as: T. Banerjee and A. Samanta "Chemical computational approaches for optimization of effective surfactants in enhanced oil recovery" *Physical Sciences Reviews* [Online] 2021, 7. DOI: 10.1515/psr-2020-0098 | <https://doi.org/10.1515/9783110739763-007>

Therefore, it has become crucial to increase the present production efficiency in the next few decades, which can be reached by enhancing the oil production from existing reservoirs or discovering new oil fields. The implicational of conventional oil recovery methods using primary and secondary recovery process is able to produce only ~30–40% of the oil exists in an oil reservoir [6–9]. The primary recovery is the step to use an attempt to recover oil initially from a reservoir by the inherent reservoir pressure. Then remaining trapped oil is recovered by injecting seawater or gas after the dissipation of the initial reservoir pressure (secondary recovery) [10]. Tertiary recovery, also known as enhanced oil recovery (EOR) technology is applied to boost the extraction of residual oil which cannot be recovered after water or brine flooding [11–14]. Among different EOR techniques, chemical enhanced oil recovery (cEOR) becomes an attractive and potential technology existing to boost the recovery of remaining oil and the surfactant flooding process is one of promising cEOR methods implemented globally using different surfactants [15, 16].

Surfactants consist of both the hydrophilic and hydrophobic groups and have capacity to decrease the surface tension of air/water and oil/water interfaces; consequently it reduces the capillary forces between water and oil within the reservoir pores, which leads to recover the trapped oil easily [17–21]. Other oil recovery mechanisms by application of surfactants also include formation of microemulsification, the wettability alteration of reservoir rock, and improvement of the interfacial rheological properties [22–27]. Several researchers have been described about the application of a large number of surfactants in both the laboratory and field tests [28–30]. Selection of appropriate surfactants is the key factor for surfactant flooding which depends on a series factors such as surfactant architecture, physicochemical properties of reservoir like salinity, pH, temperature, formation type, permeability and porosity of rock; and other factors for example surfactant cost, adsorption of the surfactant, and, ultimately, oil recovery efficiency. Applications of commercial synthetic surfactants with high concentration have high cost effect to achieve satisfactory results [14, 31].

Therefore oil industry is facing the challenges today to predict numerous fundamental characteristics of the interfaces of surfactant–solvent systems such as surface properties, IFT, contact angles and adsorption isotherms etc. Now-a-days, chemical computational approaches become one of the most interesting methods with the advancement of computational capacities of modern PCs. The surfactant adsorption isotherm, surface activity and contact angle can be predicted through the first principles molecular modeling computations. Advanced computational chemistry research has been developed in such a ways that the experimental results of a systems can also be described with a satisfactory solution and supplemented with molecular dynamics (MD) simulation [32–35], density gradient [36, 37] and density functional theory (DFT) [38], dissipative particle dynamics (DPD) methods within coarse-grained approach [39, 40], and self-consistent field theory [41]. Several research reports have been exemplified about the applications of MD, DPD and DFT simulation modeling to determine the molecular structure, IFT and different thermodynamics properties of surfactant

molecules. The microscopic structures and IFT of the mixed surfactant from sodium dodecyl sulfate (SDS)/C₄mimBr were studied at the water/hexane interface by MD simulation [42]. Different thermodynamic parameters of the anionic, nonionic, zwitterionic and gemini surfactants were determined by MD modeling, where it has been observed that the micellization process is an entropy-driven process and decreases with increasing temperature [43]. The MD studies of zwitterionic surfactant like sulfobetaine type surfactant were performed by GROMACS, which showed that the IFT was reached up to 1.6 mN·m⁻¹, when the number of surfactants was up to 134 at the decane/water interface [44]. The MD simulation studies of aqueous solution of curcumin and dodecyl-trimethylammonium bromide (DTAB) showed that two different aggregation states namely monomer and pre-micelle state of DTAB were interacted with curcumin through electrostatic and hydrophobic interactions, respectively [45]. The DPD simulation study of the phase transition of aqueous solution of SDS has performed using the coarse-gained models of SDS and obtained a comparative result on critical micelle concentration (CMC) value of SDS with experimentally observed value [46]. The DPD simulation has showed that the average aggregation numbers (AN) of micelles in aqueous solutions of surfactant oligomers raise with a power law of AN ~ c^a while the surfactant concentration c ≫ CMC and the self-diffusion coefficients (D) also decrease with a power law of D ~ c^{-a} while wormlike micelles are formed [47]. The classical DFT, also known as interfacial statistical associating fluid theory, has been applied for a better understanding of effect of the molecular architecture of surfactant on micellization and interfacial properties [48]. Chen et al. [49] have optimized that the formation of an anionic surfactant complexes CH₃(CH₂)₇OSO-3(H₂O)_n (n = 0–6) with DFT method and also calculated their molecular frequencies at the air/water interface. Some primary thermodynamic parameters of a binary mixture containing SDS in aqueous tartrazine (TAR) have been evaluated by calculating the frequency of molecular orbital energies in relation to pre- and post-micellization processes using computational DFT approach [50]. The adsorption and surface tension isotherms at the air/water or oil/water interface with different nonionic surfactants have been calculated using the DFT [51]. Therefore, this article reviewed the modern computational modeling methods to optimize the performance of best surfactant at the oil/water interfaces from the perspective of its applications in EOR using the MD, DPD and DFT simulations.

7.2 Fundamentals of use of surfactant in EOR

The oil recovery (N_P) in cEOR can be represented by Eq. (7.1):

$$N_P = E_D E_A E_{VI} \left(\frac{S_O V_P}{B_O} \right) \quad (7.1)$$

where E_D is the pore to pore displacement efficiency (microscopic efficiency) which can improve by the addition of alkali and surfactant; E_A is the areal displacement efficiency

which can improve by addition of polymer [52–54]; E_{VT} is the vertical displacement efficiency which can also improve by polymer addition; both the E_A and E_{VT} are known as macroscopic efficiencies [55–58] and $\left(\frac{S_{oVf}}{B_o}\right)$ the stock tank oil saturation.

Water or brine flooding during secondary recovery can't displace the trapped oil due to high capillary forces. The pore to pore displacement efficiency can be enhanced by reducing the capillary forces and IFT of oil/water interface. Equation (7.2) describes the correlation between the viscous forces and the capillary forces by a dimensionless number, known as capillary number [59].

$$\text{Capillary number } (N_{ca}) = \frac{\mu v}{\gamma \cos \theta} \quad (7.2)$$

where μ , v , γ and θ denote the viscosity of the aqueous phase, velocity, IFT between oil and water, and contact angle respectively. The oil recovery and sweeping of residual oil are directly dependent on capillary number which is generally ranges from 10^{-7} to 10^{-6} in case of conventional brine flooding. It has been reported that if N_{ca} increases from 10^{-4} to 10^{-3} , the residual oil saturation reduces to 90% [60], and when N_{ca} reaches 10^{-2} , the residual oil saturation approaches to zero [61]. Application of surfactants with brine during cEOR process can reduce the IFT from 20 to 30 mN/m to a range of 10^{-2} – 10^{-3} to achieve sufficient oil recovery [62, 63].

7.3 Chemical computational approaches for surfactant

This part of the article describes the fundamental theory of different chemical computational approaches used for oil recovery research such as MD and DPD simulation methods.

7.3.1 Molecular dynamics (MD) simulation

The MD simulation is an important chemical computational approach widely applied in the fields of structure, dynamics and thermodynamics of molecular systems. This method has attracted the oil recovery research community rapidly as it can greatly relate and interpret experimental results with the simulated processes of the model system at a microscopic level under the controlled conditions [64–67]. This MD simulation method helps to formulate a new effective surfactant system without costly laboratory experiments. The formulation of effective surfactant is often a time consuming process as the physicochemical properties of surfactant mainly depends on the composition of the crude oil and surfactant system. The main objective of MD simulation is to link between experimental results and theoretical model, by which the interactions between molecules and their bulk properties can be predicted. One of the main advantages of this

method is it can be applied on systems even under difficult or impossible in laboratory conditions like very high temperature and pressure. The basic theory and fundamental equations of MD simulation approach is discussed in the next part.

7.3.1.1 Equations of motion and potential energy

The MD method is based on the solution of Newton's equation of motion of a set of interacting atoms and calculations of the microscopic and macroscopic properties using the resulting trajectories of interactions. Applying Newton's equations of motion for a set of interacting atoms represents (Eq. (7.3)):

$$\left. \begin{aligned} \frac{d\vec{r}_i}{dt} &= \vec{v}_i \\ m_i \frac{d^2\vec{r}_i}{dt^2} &= m_i \frac{d\vec{v}_i}{dt} = \vec{F}_i \end{aligned} \right\} \quad (7.3)$$

where \vec{r}_i , \vec{v}_i , m_i and \vec{F}_i are the positions, velocity, mass, and force vectors of i -th atom respectively.

Firstly one has to give the details of initial positions and velocities of the atoms to start a simulation. To specify the initial positions may be assigned arbitrarily and positioned in a simple cube and its value may taken from a theoretical model or sometimes obtained from laboratory investigation. On the other hand, the initial velocities can also be chosen arbitrarily from Boltzmann distribution at the temperature of concern [68].

7.3.1.2 Force fields

Considering N numbers of atoms are interacting in a system, the force, \vec{F}_i is obtained from the potential energy gradient function (Eq. (7.4)):

$$\vec{F}_i = -\nabla_{\vec{r}_i} U(\vec{r}_1, \vec{r}_2, \vec{r}_3 \dots \vec{r}_n) \quad (7.4)$$

The potential energy $U(\vec{r}_1, \vec{r}_2, \vec{r}_3 \dots \vec{r}_n)$ is calculated from the summation of bonded and non-bonded interaction energies which are generally due to intermolecular, Van der Waals (vdW) and electrostatics forces [69]:

$$\begin{aligned} U(\vec{r}_1, \vec{r}_2, \vec{r}_3 \dots \vec{r}_n) &= \sum_{\text{bonds}} \frac{a_i}{2} (r_i - r_{i0})^2 + \sum_{\text{angles}} \frac{b_i}{2} (\theta_i - \theta_{i0})^2 + \sum_{\text{torsions}} \frac{c_i}{2} [1 + \cos(n\omega_i - \gamma)_i] \\ &+ \sum_{\text{atom pairs}} 4\epsilon_{ij} \left[\left(\frac{\sigma_{ij}}{r_{ij}} \right)^{12} - \left(\frac{\sigma_{ij}}{r_{ij}} \right)^6 \right] + \sum_{\text{atom pairs}} \frac{q_i q_j}{4\pi\epsilon_0 \epsilon_r r_{ij}} \end{aligned} \quad (7.5)$$

The first term in the equation (Eq. (7.5)) describes the bonded potential modeling for all the covalent bonds present in a molecular configuration, where r_i and r_{i0} denote the bond length and equilibrium bond length respectively. The angle of potential modeling is described by second term for the angle formation between two bonds sharing a common atom, where θ_i = the corresponding bond angle and θ_{i0} = its equilibrium value. a_i and b_i are describes as the force constants for the bonded and angle potentials. The third term denotes for the torsion angle potential, which is used to restrict the circular movement of four consecutive bonded atoms around the chemical bond. In this term the periodic energy can be determined by the periodicity n , the rotational energy barriers is given by c_i and the current dihedral angle and the phase angle are given by ω_i and γ_i respectively.

The Van der Waals (vdW) repulsive and attractive inter-atomic forces are described by the fourth term, where ϵ_{ij} , r_{ij} and σ_{ij} are the minimum (well depth) of the potential, distance and collision diameter for atoms i and j respectively. The vdW interactions are calculated by applying the Lorentz–Berthelot combination rules, which are represented by $\epsilon_{ij} = \sqrt{\epsilon_i \epsilon_j}$ and $\sigma_{ij} = \left(\frac{\sigma_i + \sigma_j}{2}\right)$ [70]. Here, the terms ϵ_i , ϵ_j , σ_i and σ_j indicate the well depths and the collision diameters for the atoms i and j respectively.

The Coulomb potential is illustrated by the last term in Eq. (7.5), where q_i and q_j are charges of the atoms, and ϵ_0 and ϵ_r are the dielectric permittivity of vacuum and the relative dielectric constant of a medium in which the atoms i and j are located, respectively.

7.3.1.3 Leap-frog algorithm

The leap-frog algorithm is used for integrating the equations of motion during the MD simulation process [68, 71]. Approximation for the position and dynamic properties (velocities and accelerations) is given by Eqs. (7.6) and (7.7).

$$\vec{r}_i(t + \Delta t) = \vec{r}_i(t) + \Delta t \vec{v}_i\left(t + \frac{1}{2}\Delta t\right) \quad (7.6)$$

$$\vec{v}_i\left(t + \frac{1}{2}\Delta t\right) = \vec{v}_i\left(t - \frac{1}{2}\Delta t\right) + \Delta t \vec{a}_i(t) \quad (7.7)$$

To apply the leap-frog algorithm, at first the velocities $\vec{v}_i\left(t + \frac{1}{2}\Delta t\right)$ are computed from the velocities at time $\left(t - \frac{1}{2}\Delta t\right)$ and the accelerations at time t together with Δt (Eq. (7.7)).

Then the positions $\vec{r}_i(t + \Delta t)$ are determined from the positions at time t and the calculated velocities together with Δt (Eq. (7.6)). Therefore, the velocity at time t can be determined by Eq. (7.8).

$$\vec{v}_i(t) = \frac{1}{2} \left[\vec{v}_i \left(t + \frac{1}{2} \Delta t \right) + \vec{v}_i \left(t - \frac{1}{2} \Delta t \right) \right] \quad (7.8)$$

As a result the velocities leap-frog over the positions is given by the values at $\left(t + \frac{1}{2} \Delta t \right)$ and the positions then leap over the velocities at time $t + \Delta t$. Then the user can specify the integration time step Δt . The simulation becomes unstable with too large time step due to increase the energy whereas a large amount of computational time requires for too small time step. The best possible alternative of the time step in the system is considered roughly as a factor of one-tenth of the fastest time scale.

7.3.1.4 Treatment of non-bonded interactions

Force calculation is the most prolonged process in MD modeling, particularly computation of the vdW and electrostatic interactions for each pair of interacting atoms [72]. A cut-off distance can be used to save the time and costs of computational procedures by the approximation of the calculation. That means the interactions between two atoms have taken apart by a distance greater than the given cut-off distance are not considered. This is the best method for computation of the vdW forces, which rapidly disappear at longer distance. However the electrostatic interactions gradually reduce with the distance. Significant errors can be occurred after they are computed at the cut-off distance. A number of approximation algorithms are available to control this issue, and example of one method is to split it into two components viz. short-range and long-range. The short-range component can be measured in real space, whereas the long-range component can be determined using Fourier space. The Fourier-based particle-mesh Ewald (PME) method can be employed in the MD simulations [73, 74].

7.3.1.5 Boundary condition

To calculate the macroscopic properties of any system, at first one has to simulate small system under proper boundary condition in MD simulation and then compute for bulk properties. There are a number of methods can apply the boundary condition in MD simulation.

The periodic boundary condition (PBC) is widely applied in MD simulation to eliminate boundary effects for the reason of finite size [75, 76]. The PBC simulation cell is schematically represented in all directions to shape an infinite lattice as depicted in Figure 7.1. The particle in the central cell is only accounted during simulation process, when a central cell particle shifts and its periodic image in the every adjoining cell also moves in the similar way. When a particle leaves the central cell its periodic representation approaches from the opposite face. Therefore, it may consider that the number of particles in the central cell is conserved and no rigid boundaries are required during the simulation process. So, a range of cell sizes and shapes can be used as PBC to perform

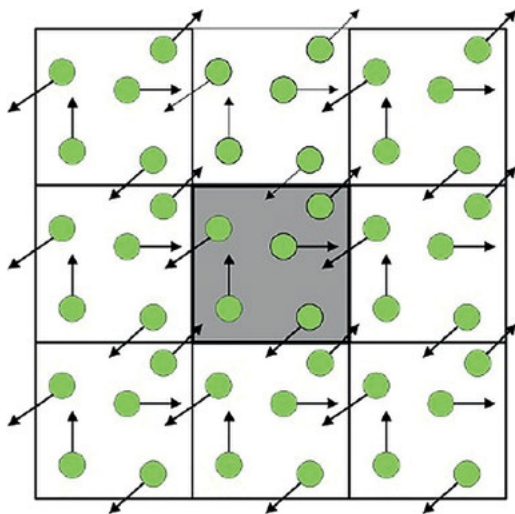


Figure 7.1: Schematic representation of PBC. Central cell is highlighted for simulation and surrounded by neighbouring periodic images.

simulations and this has also important implication to compute the interaction energy and hence forces.

7.3.1.6 Ensemble

In MD simulation if the number of atoms (N), box volume (V), and total energy (E) are set as constant then it is considered as microcanonical (NVE) ensemble [77, 78]. Generally, the small part of a large simulation system is considered as a canonical system. Temperatures may be considered approximately constant if the temperature fluctuations for large NVE systems are small. Sometimes the canonical ensembles in simulating system are required either constant temperature (NVT) or constant pressure and temperature (NPT). Sometimes the controlled Hamiltonian equation of motion needs to be solved for the simulation in canonical ensemble to obtain the required ensemble. Nose and Hoover have formulated an extended system Hamiltonian dynamics to simulate the NVT and NPT ensembles [79].

7.3.2 Dissipative particle dynamics (DPD) simulation

The DPD simulation is applied to simulate to equilibrium and dynamical properties of fluids [80–83]. This type of mesoscopic simulation procedure was first introduced by Hoogerbrugge and Koelman in the year 1992 [84, 85] and consequently modified by Groot et al. [80, 81, 86]. This technique has been used in diverse systems including aqueous solutions of surfactants and polymer [87–89], colloidal suspensions [90], fluid flow in porous media [91], and many more over last two decades. The term “bead” in DPD simulation is known for different atoms those are coarse-grained into one particle. These

beads act together with one another through pair wise additive forces that conserve the momentum and contribute exact hydrodynamic behaviour. The time of evolution of DPD beads is controlled by the Newton's equations of motion like MD simulation (Eq. (7.3)).

The force \vec{F}_i exerted on i -th bead is the summation of a conservative force (\vec{F}_{ij}^C), a dissipative force (\vec{F}_{ij}^D) and a random force (\vec{F}_{ij}^R) as shown in Eq. (7.9). These entire forces generally work within a sphere of interaction which is known as the cut-off length of a DPD system (r_c).

$$\vec{F}_i = m_i \frac{d\vec{v}_i}{dt} = \sum_{j \neq i} \left(\vec{F}_{ij}^C + \vec{F}_{ij}^D + \vec{F}_{ij}^R \right) \quad (7.9)$$

7.3.2.1 Soft and repulsive potential

The conservative force (\vec{F}_{ij}^C) is given by

$$\vec{F}_{ij}^C = \begin{cases} a_{ij} (1 - r_{ij}/r_c) \hat{r}_{ij}, & r_{ij} < r_c \\ 0, & r_{ij} \geq r_c \end{cases} \quad (7.10)$$

where a_{ij} = the strength of the repulsive interaction between beads i and j , $\vec{r}_{ij} = \vec{r}_j - \vec{r}_i$ (\vec{r}_i and \vec{r}_j are positions vectors of beads i and j), $r_{ij} = |\vec{r}_{ij}|$ and $\hat{r}_{ij} = \vec{r}_{ij}/|\vec{r}_{ij}|$. Note that \vec{F}_{ij}^C is finite when $\vec{r}_j = 0$ (i.e. overlapping of two DPD beads totally with one another) which indicates that the DPD method is a soft potential. The main characteristic of this soft potential permits a larger time scale in DPD application in comparison with MD method where a theoretical-molecular model of the physical system is used to derive the soft potential. A plot of conservative force (\vec{F}_{ij}^C) versus distance (r_{ij}) is shown in Figure 7.2, which shows that \vec{F}_{ij}^C is modelled as a linear function of r_{ij} and $\vec{F}_{ij}^C = 0$ at the cut-off length (r_c). In the figure, the repulsion between the interacting beads is maximum, when a_{ij} is constant.

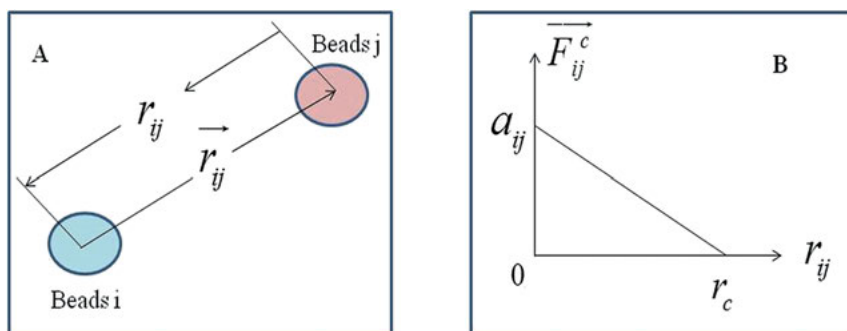


Figure 7.2: (A) definition of distance r_{ij} and (B) plot of the conservative force versus distance r_{ij} .

The dissipative force (\vec{F}_{ij}^D) is expressed in terms of friction and energy dissipation as bead i passes bead j and given by:

$$\vec{F}_{ij}^D = -\gamma\omega^D(r_{ij})\left(\vec{r}_{ij} \cdot \vec{v}_{ij}\right)\hat{r}_{ij} \quad (7.11)$$

where γ = the friction coefficient parameter, $\omega^D(r_{ij})$ = the dissipative weight function vanishing for $r_{ij} > r_C$, and $\vec{v}_{ij} = \vec{v}_j - \vec{v}_i$.

The random force (\vec{F}_{ij}^R) illustrates the loss of kinetic energy from dissipation and expresses as

$$\vec{F}_{ij}^R = \sigma\omega^R(r_{ij})\theta_{ij}\hat{r}_{ij} \quad (7.12)$$

where σ = strength of the random force, $\omega^R(r_{ij})$ = random weight function which is vanishing for $r_{ij} > r_C$, and θ_{ij} = randomly fluctuating variable with uniform distribution and unit variance (Gaussian Statistics): $\langle\theta_{ij}(t)\theta_{kl}(t')\rangle = (\delta_{ik}\delta_{jl} + \delta_{il}\delta_{jk})\delta(t - t')$, where δ_{ij} is the Kronecker delta and $\delta(t - t')$ is the Dirac delta function.

Any one of the two weight functions (ω^D and ω^R) can be determined by the relationship $\omega^D(r_{ij}) = [\omega^R(r_{ij})]^2$, when another is selected arbitrarily [92]. The weight function may be usually chosen as [80]:

$$\omega^D(r_{ij}) = \begin{cases} (1 - r_{ij})^2, & \text{for } r_{ij} < r_C \\ 0, & \text{for } r_{ij} \geq r_C \end{cases} \quad (7.13)$$

The friction coefficient (γ) is expressed by the relation $\sigma^2 = 2\gamma k_B T$ that relates the strength of random and the friction coefficient that implies that a constant temperature maintained during simulation. Where T = absolute temperature of the system and k_B = the Boltzmann constant. Generally $k_B T$ is set as one during DPD simulations processes.

7.3.2.2 Spring force

The DPD simulations can be applied to configure surfactant architectures by modification of hydrophilic head and hydrophobic tail beads. A spring force (\vec{F}_{ij}^S) has been set into the simulations to illustrate the limitations between the bonded successive beads within a surfactant molecule and is expressed by

$$\vec{F}_{ij}^S = -k_S\left(1 - \frac{r_{ij}}{r_0}\right)\hat{r}_{ij} \quad (7.14)$$

where k_S = spring constant and r_0 = equilibrium bond length.

Therefore the total force (\vec{F}_{ij}) on the DPD beads is expressed by the combination of the spring force as below (Eq. (7.15))

$$\vec{F}_{ij} = \sum_{j \neq i} \left(\vec{F}_{ij}^{\rightarrow C} + \vec{F}_{ij}^{\rightarrow D} + \vec{F}_{ij}^{\rightarrow R} + \vec{F}_{ij}^{\rightarrow S} \right) \quad (7.15)$$

7.3.2.3 Modified velocity Verlet algorithm

The modified velocity Verlet algorithm is applied to solve the equations of motions as describes below [80].

$$\left. \begin{aligned} \vec{r}_i(t + \Delta t) &= \vec{r}_i(t) + \Delta t \vec{v}_i(t) + \frac{1}{2}(\Delta t)^2 \vec{f}_i(t) \\ \vec{v}'_i(t + \Delta t) &= \vec{v}_i(t) + \lambda \Delta t \vec{f}_i(t) \\ \vec{f}_i(t + \Delta t) &= \vec{f}_i \left[\vec{r}_i(t + \Delta t), \vec{v}'_i(t + \Delta t) \right] \\ \vec{v}_i(t + \Delta t) &= \vec{v}_i(t) + \frac{1}{2} \Delta t \left[\vec{f}_i(t) + \vec{f}_i(t + \Delta t) \right] \end{aligned} \right\} \quad (7.16)$$

where $\vec{r}_i(t)$ = position for bead i at time t , $\vec{f}_i(t)$ = force for bead i at time t , $\vec{v}'_i(t)$ = predicted velocities at time t , $\vec{v}_i(t)$ = corrected velocities at time t , Δt = integration time step and λ = an adjustable parameter in the range 0–1, most preferable value is found as 0.5.

7.3.2.4 Units of length and time

Application of the reduced units of length and times are very much important for calculations of all parameters in DPD simulation. The unit of length is signified by the DPD cut-off length r_C , unit of energy is denoted by $k_B T$ and the unit of mass is considered as masses of beads. For example, if the degree of coarse graining of water $N_m = 5$ represents that each water bead contains five water molecules and has volume $V_b \approx 150 \text{ \AA}^3$ [93]. During DPD simulation, the reduced density of one DPD bead (i.e. the average number of beads in $1r_C^3$) is set to $\rho = 5$ and consequently $r_C = \sqrt[3]{5 \times 150} = 9.0856 \text{ \AA}$. The time scale can be estimated by comparing the self-diffusion constant of water and the calculated time constant of the simulation is given as [81]

$$\tau = \frac{(N_m D_{\text{sim}} r_C^3)}{D_{\text{Water}}} \quad (7.17)$$

where τ = DPD time constant

D_{sim} = simulated water self-diffusion coefficient, and

D_{Water} = experimental water self-diffusion coefficient

When $a_{ii} = 15k_B T/r_C$, $D_{\text{sim}} = 3.0615r_C^2/\tau$.

For $D_{\text{Water}} = 2.43 \times 10^{-3} \text{ cm}^2/\text{s}$ calculated $\tau = 5.2 \text{ ps}$.

7.4 Application of chemical computational approaches

7.4.1 Application of MD and DFT Simulation in EOR

The molecular dynamics (MD) technique has been extensively applied to model the complex systems like oil/brine/surfactant and hence it is rapidly gaining importance in EOR process [94–100]. It relates the experimental results at a microscopic level with the simulated processes under control of components and conditions. MD simulations are helpful in modeling of a new surfactant based on the change of nature of IFT, interface formation energy and interfacial thickness due to water and surfactant interaction. It also provides an idea about the mechanism of influence of molecular configuration on IFT [101]. Atomistic molecular dynamics simulations are also used for wettability alteration of oil-wet carbonate reservoirs, which is one of the significant mechanisms in EOR using non-ionic and anionic surfactants [102]. The micellization ability and calculation of thermodynamic properties of anionic, nonionic, zwitterionic and gemini surfactants can also be investigated through MD simulations. This study also helps to provide detailed information about the effects of molecular arrangement of surfactant and their physicochemical characteristics in aqueous medium on micelle formation [103]. The simulations of self-assembled micelles of anionic (SDS) and cationic surfactants (CTAB) have been performed to obtain detailed atomistic information of micellar structures through MD simulations with COSMOmic (an extension of COSMO-RS) [104].

7.4.1.1 Different computational methods of MD simulations

The adsorption of surfactant molecules on the oil/water interface creates a self-aggregated monolayer that increases the interfacial interactions like interaction between water and surfactant hydrophilic head group, and oil and surfactant hydrophobic tail [105–110]. In general these interactions can reduce the oil/water IFT. In order to investigate the interfacial characteristics of surfactant/oil/water systems, several laboratory investigational and theoretical researches have been conducted. One of MD simulation software, Materials Studio 4.0 software is used for simulating and modeling of surfactant molecules of using PCFF force field [111]. Sometimes short NPT ensembles MD simulations have been conducted to frozen the surfactant head groups and water molecules under certain temperature and the molecules are unfrozen to conduct NVT ensembles MD simulation for statistical property calculation. Other computational tools like Verlet algorithm used for integration [112], Andersen thermostat for temperature control [113, 114] and Berendsen method for pressure control [114] are applied for simulation. Charge Group method is applied for the calculation of non-bond interactions [115].

DFT is generally applied for calculation of the electron distribution and molecular polarity of a molecule. The electron distribution of a molecule can be estimated by GGA/PBE method based on a set of a double zeta plus polarization (DNP) function

[116, 117]. For example, the molecular polarity has been calculated by a water solvation model with real space cut-off radius of 0.37 nm and the lowest end of the potential energy surface is obtained by a frequency analysis.

Xu et al. [101] has investigated the the influences of head group structure on oil–water IFT of four anionic surfactants viz. SDS, sodium dodecyl sulfonate (SDSn), sodium dodecyl benzene sulfonate (SDBS) and sodium dodecyl-di(oxyethylene) ether sulfate (AES). In order to get an idea about the mechanism of interaction, a combination of MD simulations technique and quantum mechanical calculations have been conducted to find interfacial energy, interfacial thickness and interaction between surfactant and water molecule. It has been observed from the simulation studies that the decreasing capability of IFT of these four surfactants follow the order: SDSn < SDS < SDBS < AES (Figure 7.3). Since with decrease in the IFT of crude oil on rock, the work of adhesion decreases that leads to easy desorption of the crude oil from the rock surface and helps in EOR.

Since IFT has direct relationship with the interface formation energy (IFE), the interfacial thickness and interactions among surfactant, oil and water, hence these three parameters have been investigated by MD simulation studies. The IFE of single surfactant molecule defined by Eq. (7.18) and the corresponding calculated values have been tabulated in Table 7.1. The IFE values of four anionic surfactants obey the sequence as AES > SDBS > SDS > SDSn, therefore the IFTs observe the reverse order as AES < SDBS < SDS < SDSn. Another important parameter that effect IFT is interfacial thickness of surfactants and pure oil/water system which can also be calculated by MD simulation. If t_{oil} and t_{water} are the interfacial thickness of pure oil/water systems, then t_{water} follows the sequence as SDSn < SDS < SDBS < AES and t_{oil} follows the order as SDSn < SDS < AES < SDBS.

$$\text{Interface formation energy (IFE)} = \frac{E_{\text{total}} - (n \times E_{\text{surfactant, single}} \times E_{\text{dodecane-water}})}{n} \quad (7.18)$$

where E_{total} = energy of the whole system

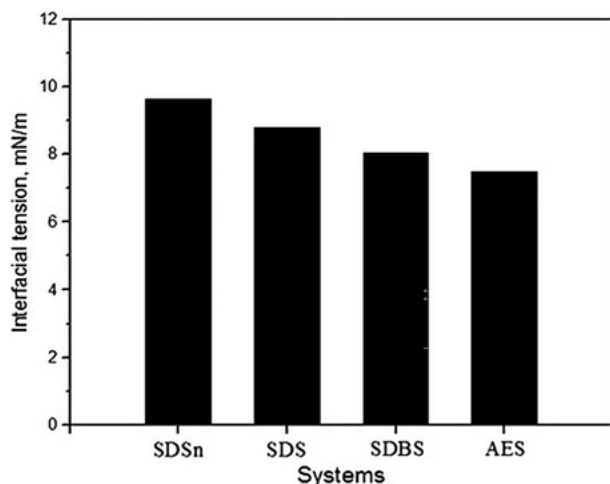


Figure 7.3: IFT of the four anionic surfactant systems [101]. Copyright © 2013 Elsevier.

Table 7.1: IFE of different oil–water and surfactant mixtures [101]. Copyright © 2013 Elsevier.

| Systems | Energy (kJ/mol) | | | |
|---------|---------------------------------|------------------------|--------------------|-----------|
| | $E_{\text{Surfactant, single}}$ | $E_{\text{Oil-water}}$ | E_{Total} | IFE |
| SDSn | -326.420 | -7671.309 | -50624.228 | -1015.859 |
| SDS | -222.176 | -8328.570 | -48898.660 | -1045.640 |
| SDBS | 97.356 | -10094.970 | -42286.905 | -1103.354 |
| AES | -188.260 | -9438.300 | -52936.538 | -1171.060 |

$E_{\text{surfactant, single}}$ = energy of one single surfactant molecule and

$E_{\text{dodecane-water}}$ = energy of pure dodecane/water system (n is the number of surfactant molecules).

Reduction of IFT also depends on the interaction between hydrophilic head group of surfactant molecules and water which is mainly due to the contribution of polar atoms present in both water and surfactant head group. The polarity of the surfactants is obtained from DFT calculations and observes the sequence as AES > SDBS > SDS > SDSn. Since the total hydration number of surfactant depends on the polarity hence the order of total hydration number of surfactants must follow the sequence as AES > SDBS > SDS > SDSn. Again greater the hydration number stronger will be the interaction which will lead to lowering of IFT, hence IFTs obey the order SDSn > SDS > SDBS > AES, which is accordance with previous results. The charge distribution of the anionic parts of above four surfactants have been calculated which suggest that the polarity of those surfactants may follow the sequence as AES > SDBS > SDS > SDSn and these are verified by their dipole moment calculations (Figure 7.4).

The mechanism of surfactant flooding in EOR process in oil-wet carbonate reservoirs is mainly depends on the wettability alteration of the reservoir rock. The wetting nature of the carbonate rock is oil-wet due to adsorption of the polar components in crude oil on the rock surfaces. The reservoir rock becomes oil-wet to water-wet on addition of surfactant as the hydrophilic head groups are adsorbed on the rock surfaces and hydrophobic segments are adsorbed on the non-polar oil phase. The wettability of a system is investigated through the GROMACS 5.1.2 software using CHARMM36 force field in the MD simulations process [118, 119]. PBC are implemented in all directions. The Van der Waals interactions are obtained from Lennard–Jones (LJ) potentials with a certain cut-off distance and the long-range electrostatic forces are calculated applying the PME algorithm. Bai et al. [102] have constructed some realistic models to understand the influence of surfactant on the wettability of calcite surfaces using a calcite pore and a crude oil. They have used SPCFW model for water [120] and simulations were performed at 1 bar pressure and constant temperature at 300 K controlled by the Nosé–Hoover thermostat. The pressure was managed either by the Parrinello–Rahman barostat for NPT type simulation or by pistons made of dummy atoms for NVT type simulation. The MD simulations with forced flooding has been investigated by combing

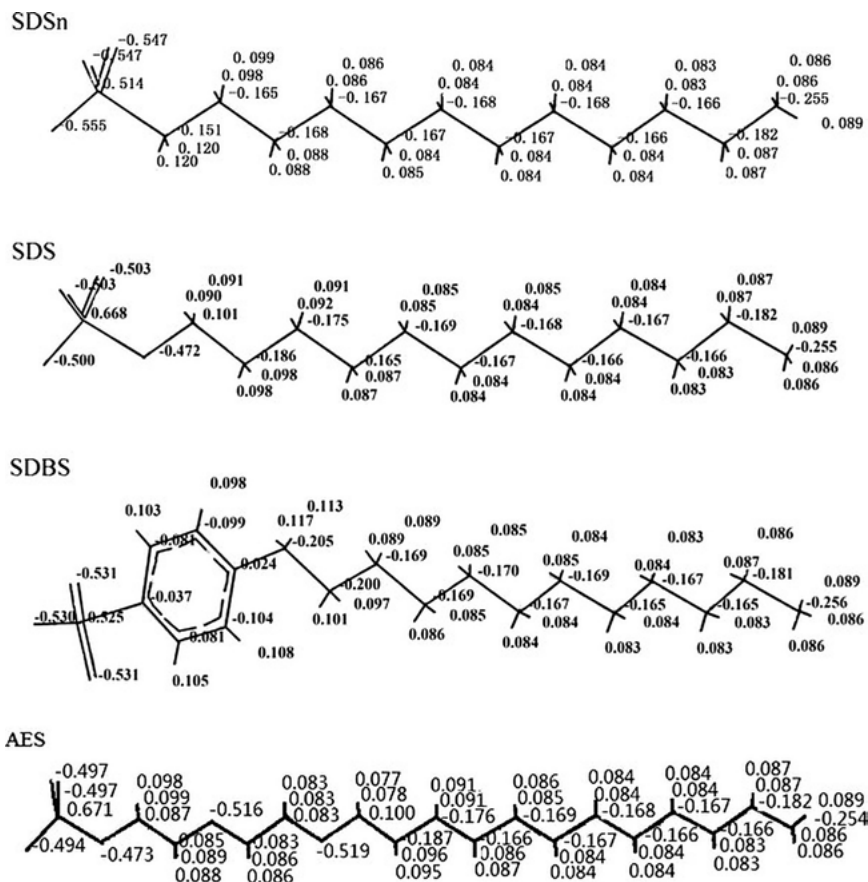


Figure 7.4: Charge distributions of the anionic parts of surfactants [101]. Copyright © 2013 Elsevier.

the calcite surface in the corner geometry and a multi-components oil model based on GC–MS analysis of a real crude oil. The simulation studies for flooding have described that the wettability alteration of a corner system are observed both for an anionic surfactant, octadeca ethylene glycol monodecyl ether ($\text{CH}_3(\text{CH}_2)_{12}(\text{OCH}_2\text{CH}_2)_{18}\text{OH}$) and a nonionic surfactant, ammonium decylsulfate ($\text{CH}_3(\text{CH}_2)_9\text{OSO}_3^- (\text{NH}_4)^+$).

Another software Gaussian 09 using the B3LYP/6-31G was used for DFT calculations to know the effect of the microscopic charge distribution on the surfactant molecule. Here the polarized continuum model (PCM) is used to simulate water (solvent) molecules. Fully optimized molecular geometries with the Merz–Singh–Kollman (MK) scheme were used for determining the partial charges [121, 122].

The ability of the wettability alteration of both the anionic and non-ionic surfactants can be determined by comparing the surfactant flooding with just brine flooding. Figure 7.5 compares different surfactant flooding after brine flooding on different calcite models. The figure illustrates that the images for (i) brine flooding are

represented by A–C, (ii) non-ionic surfactant flooding by D–F and (iii) anionic surfactant flooding by G–I. The snapshots of the cross section of the corner models of upper, middle and lower images are taken at 0, 10, and 20 ns from the beginning of the simulations studies respectively. The orange and green colours signify for surfactants and oil, and water molecules are not represented for clearness.

The ratio of polar to non-polar molecules in the remaining oil is also responsible for wettability alteration. Figure 7.6 represents the mole percentage of the ratios between polar and non-polar constituents of the residual oil with simulation timing during surfactant and brine flooding. It reveals that the surfactant molecules facilitate the extraction of polar components from the reservoir surface compared to the brine known as the “surface cleaning mechanism”. It has been observed that neither anionic nor nonionic surfactants can configure the ion pairs with carboxylic acids, these kind of effects can only

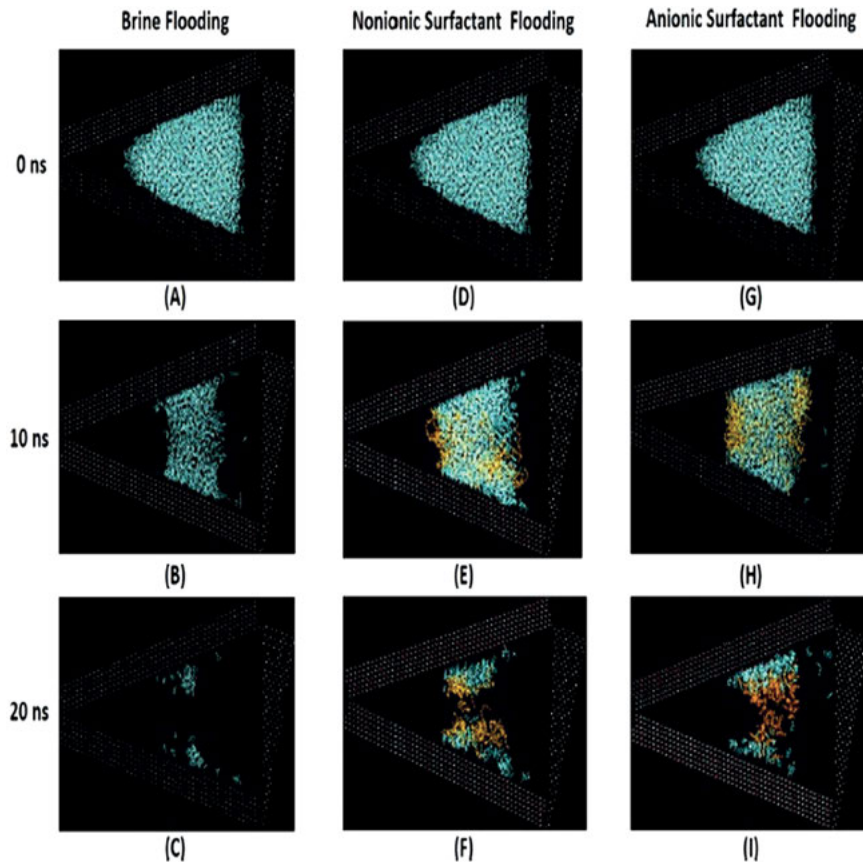


Figure 7.5: Screenshots of the model calcite corner geometry during simulation at 0, 10, and 20 ns of brine and surfactant flooding from beginning of the simulation [102]. Copyright © 2020 American Chemical Society.

be originated by the Van der Waals and weak electrostatic interactions among the surfactant molecules and carboxylic acids, which provides a “drag” effect operating along with the aqueous phase. Terrón-Mejía et al. [123] have also informed similar type of mechanism in a coarse-grained DPD simulation study. The polar to non-polar of anionic surfactant is higher than that of the non-ionic surfactant due to the weaker intermolecular interaction of anionic surfactant within the oil compared to the non-ionic one.

Along with Interfacial interaction and wettability, the self-assembling of surfactant molecules has taken part as a significant role in EOR techniques. The micelles formation and the configuration of micelles are governed by thermodynamic properties. The thermodynamic properties of anionic, nonionic, zwitterion and gemini surfactants are calculated by MD simulation [103]. The entropy is the key factor for the development of micellization and the entropy-driven contribution reduces with rising of temperature. To calculate the thermodynamics properties of micellization, at first different surfactants are drawn by the ChemDraw software, subsequently the structures are optimized applying the B3LYP/6-31+g(d) basis set in GAMESS (US) [124] and the charge distribution is determined by the MK approaches [125]. GROMACS (5.1.2) is the simulation tool using GROMOS 53a6 force field [126, 127]. The force field parameters are corrected through the Automated Topology Builder (ATB) [128]. Then SD frog hopping algorithm is applied for simulation calculations. Langevin piston method is used for temperature coupling. NVT and NPT ensembles are selected and then ΔG_m^θ , ΔH_m^θ and ΔS_m^θ are calculated at different temperature for different types of surfactant.

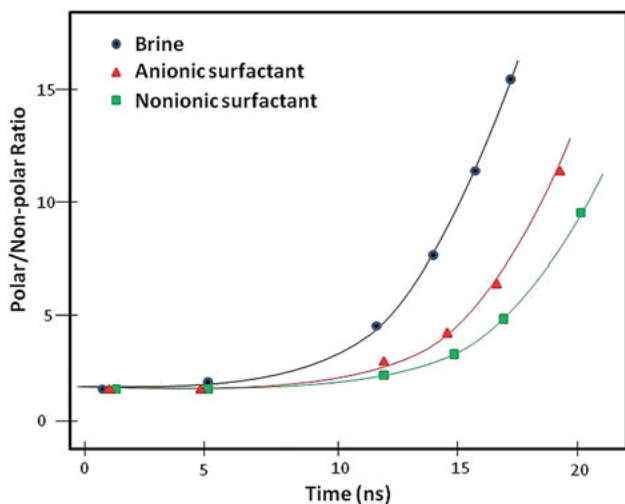


Figure 7.6: Progression of % of molar ratio between polar and non-polar components in the residual oil during surfactant flooding simulations [102].

ΔG_m^θ is related to the critical micelle concentration (CMC) by the following relation:

$$\left. \begin{aligned} \Delta G_m^\theta &= 2RT \ln \text{CMC} \text{ or } \Delta G_m^\theta = 2RT \ln \text{CMC} \\ \Delta H_m^\theta &= -2RT^2 \left(\frac{\partial \ln \text{CMC}}{\partial T} \right) \text{ or } \Delta H_m^\theta = -RT^2 \left(\frac{\partial \ln \text{CMC}}{\partial T} \right) \\ \Delta S_m^\theta &= \frac{(\Delta H_m^\theta - \Delta G_m^\theta)}{T} \end{aligned} \right\} \quad (7.19)$$

where R is the universal gas constant and T is the absolute temperature.

Thus smaller the value of change in Gibbs free energy, greater is the stability of the surfactant molecules. With rise in temperature, the hydrogen bonding between the oxygen atom of the head group of surfactant molecule and water is ruptured and enhances micelle formation. Thus comparisons of the properties of several surfactant molecules have been described that the sequence of micellization at the same temperature follows as gemini surfactant > zwitterionic surfactant > non-ionic surfactant > anionic surfactant (Figure 7.7). The entropy plays a major role in micelle formation at different temperatures, but with increase in temperature the contribution of entropy decreases and enthalpy increases.

Storm et al. [104] have investigated the size, shape and density profile of multiple self-assembled micelles of an anionic (SDS) and a cationic surfactant (Cetyltrimethyl ammoniumbromide, CTAB) at different concentration in order to find their influences on partition equilibria. For these purposes they have combined all atoms in MD simulation with COSMOmic software, which is an extension of COSMO-RS [129]. For simulation in GROMACS 4.5.3 with CHARMM36 additive force field is also carried out to reproduce quantum mechanical (QM) energies modifying Lennar–Jones (LJ) potentials [130]. A short simulation process in the NVT ensemble has performed using the Nosé–Hoover thermostat. After these initialization steps, all simulations are performed in the NPT ensemble using the Nosé–Hoover thermostat and the Parrinello–Rahman barostat. For

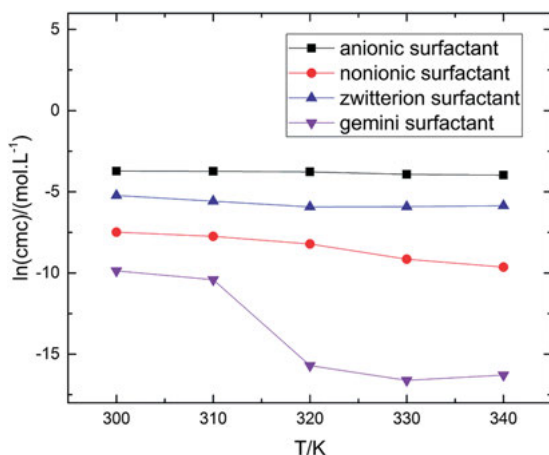


Figure 7.7: The plot of $\ln(\text{CMC})$ versus T/K of four different types of surfactant [103]. Copyright © The Royal Society of Chemistry 2019.

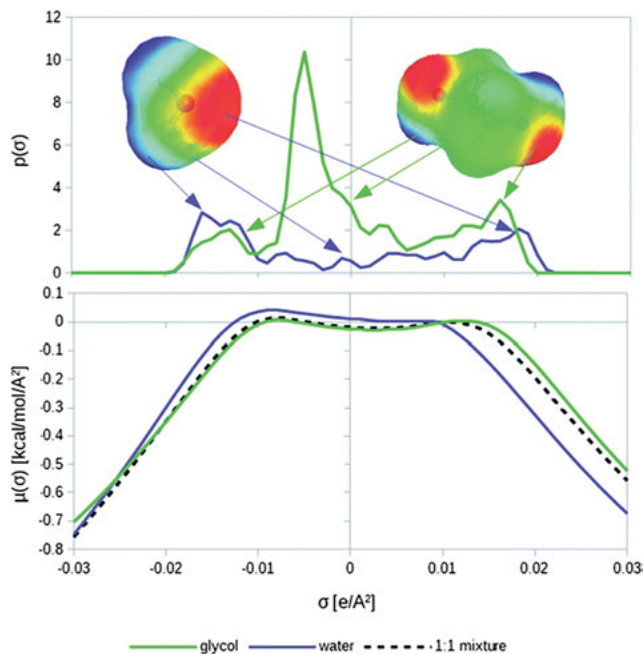


Figure 7.8: Schematic diagram of the COSMO-RS method: upper diagram is a histogram for σ -profile and lower diagram is for solvent σ -profile [134]. Copyright © the Owner Societies 2019.

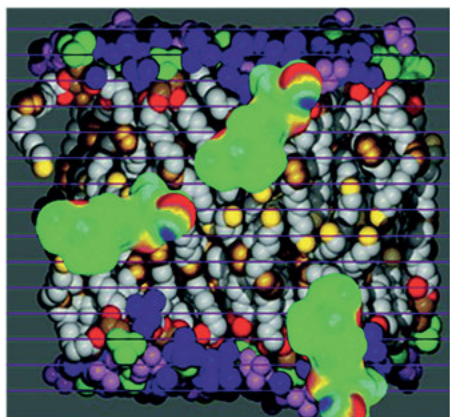


Figure 7.9: Schematic diagram of COSMOmic method [134]. Copyright © the Owner Societies 2019.

COSMOmic DFT/COSMO files were worked out with Turbomole 5.10 on the BPTZVP level using RI (resolution of the identity) approximation [131–133]. The schematic snaps of the COSMO-RS and COSMOthe COSMO-RS are presented in Figures 7.8 and 7.9. In the case of the COSMO-RS figure, a histogram of the COSMO surface polarization charge densities of the surface fragments is shown in the upper diagram (σ -profile). Here σ is the conductor

polarization charge density. The lower diagram signifies the solvent σ -profile diagram where calculation of the chemical potential of each molecule is done by the solvent σ -potential to the surface segments of the solute. In COSMO σ -profiles and σ -potentials of the layers are estimated considering all positions and orientations of a solute molecule are calculated from the state specific free energy from the local σ -potentials. A new method of rigorous extension of COSMO-RS is COSMOplex, which is applied to predict the structure and properties of much broader range of complex, self-aggregating inhomogeneous systems like micelles, microemulsions and liquid–liquid interfaces [134].

7.4.2 Application of DPD simulation in EOR

As in MD simulations all atomic degrees of freedom are taken into account, it became a time consuming process especially for complex system with many molecules. The DPD simulation is chosen for surfactant molecule. The properties polymer-surfactant aggregation can be investigated using DPD method for a polymer-surfactant-water system. In order to achieve the chemical potential of a surfactant molecule, the Wisdom Insertion Method is used. It was observed from the experiment that on addition of small amount of surfactant, the polymer shrink and then with increase in the surfactant concentration it passes through the minimum (Figure 7.10).

Depending upon the polymer-surfactant interaction, the surfactant adsorption on polymer is occurred by two modes – (i) continuous adsorption and (ii) adsorption of surfactant by discrete micelles. When the polymer and surfactant interaction is governed

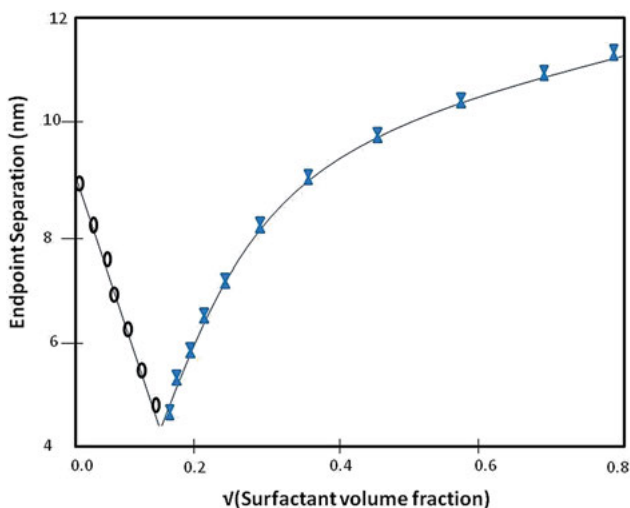


Figure 7.10: Plot of Polymer endpoint separation versus square root of added volume fraction of surfactant in the simulation box [133].

by tail group of surfactant then mechanism (i) is followed and if the interaction depends on surfactant head group then mechanism (ii) is followed. In that case, the size of micelle decreases with increase in hydrophobic groups in polymer.

The microemulsion properties such as optimum salinity can be efficiently calculated and implemented on DPD level by a new method called Method of Moments [135]. The surfactant/oil/brine interface is simulated to determine the (lateral) stress profile and its moments by this method. This method is computationally fast, flexible and can apply for the mixtures of surfactants, solvents, complex oils, etc. Culgi software package is used in DPD simulation. The capabilities of the DPD method to simulate oil/brine/surfactant systems are illustrated below with a few examples of simulations.

An entire molecule or a molecular fragment is represented as one particle or “bead” in DPD method. The DPD simulation study by Buijse et al. [135] has considered the SDS molecule is represented by five connected beads: four tail-beads and one head-bead, hexane molecule as two beads, octadecane as six beads and water is represented by three molecules per bead. The simulations have been performed in a simulation box of size $5 \times 5 \times 12$ nm for SDS in hexane/water and octadecane/water at $T = 298$ K. The IFT is calculated as a function of the area occupied by an SDS molecule at the interface of oil/water with ~ 100 SDS molecules, ~ 900 hexane molecules and ~ 4500 water molecules (total number of beads: ~ 3800).

A mixture of oil components can also be simulated by DPD method. The DPD density profile study of an oil as a mixture of octadecane (C_{18}) and propane (C_3) in 60/40% and brine solution (0.5 M NaCl) shows that the total density fluctuates close to the interfaces, due to the repulsion between oil and water beads. From the density contributions of the individual components it is clear the surfactant get adsorbed at the interface, while the Na^+ ions concentrate in a layer close to the anionic surfactant heads, as expected. One of the interesting aspects of this simulation is the separation of oil components close to the interface. The C_3/C_{18} concentration ratio is significantly higher at the interface, compared to bulk. This result reflects the different affinities of different oil components towards the surfactant. Especially in crude oils, which are complex mixtures of many components, this preferential partitioning of oil components at the interface can have a significant effect on the IFT. Coarse grained simulation methods like DPD are quite suitable to study these effects because complex systems, with many (different) molecules, can be simulated in a relatively fast way. The constituents of system and number of surfactant molecules have played an important role to examine the properties of interfacial regions between oil, water and different surfactant molecules. The interactions between a nonionic surfactants (octaethylene glycol monododecyl ether, C12E8), an anionic surfactants (SDS) and oil/water have been reported using the coarse-grained modeling technique in DPD simulations [136]. In this study, the ionic surfactant has been modelled by adjusting the interface parameters as head-head and head-water interactions. The DPD modeling of SDS at oil/water interface has revealed that IFT is depended on the total concentration of SDS and shown in Figure 7.11. It has been clearly observed that the IFT value does not change beyond the micelle formation after CMC, which indicates that the

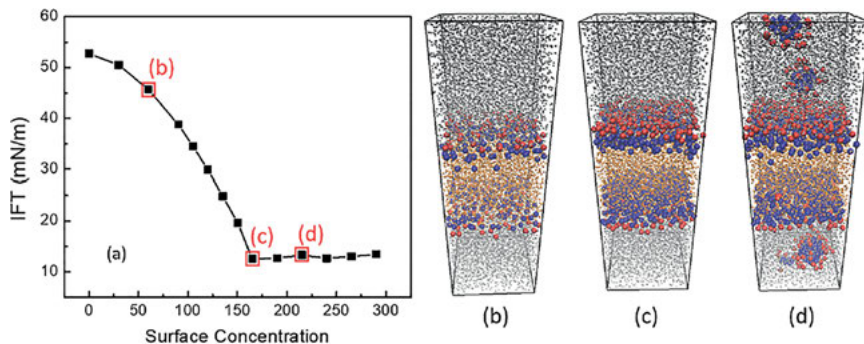


Figure 7.11: Plot of IFT versus total concentration of SDS. Images of DPD simulations for interactions between surfactant molecules and oil/water interface (where surfactant heads and tails are revealed in red and blue beads, and oils and water molecules are shown as orange and gray beads) [136]. Copyright © 2018 AIP Publishing.

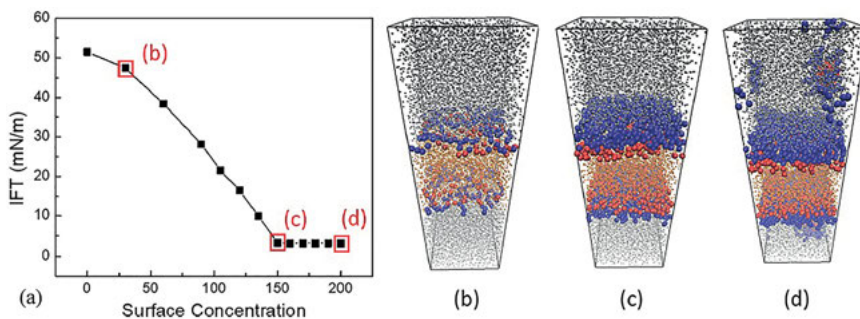


Figure 7.12: Plot of IFT versus total concentration of C12E8. Images of DPD simulations for interactions between surfactant molecules and oil/water interface (where surfactant heads and tails are revealed in red and blue beads, and oils and water molecules are shown as orange and gray beads) [136]. Copyright © 2018 AIP Publishing.

interface becomes saturated at CMC and further addition of SDS can't reach at the interface. The simulation results also describes that the IFT value reduces linearly with the concentration below its CMC. A typical plot of IFT as a function of total surfactant concentration is also presented here. The simulation process with longer surfactant like C12E8 becomes more complicated due to the steric effect; hence intramolecular angles are required to incorporate during simulation in DPD model. During this study the surface excess value is taken quite similar as SDS (3.3 and 2.4×10^{-10} mol/cm²) and the number of surfactant beads is considered as double of SDS on the interface as the length of C12E8 is twice compared to SDS length. The simulation results have shown that the variation of IFT with concentration of C12E8 is comparable to that of SDS, but the CMC is observed at lower than SDS (Figure 7.12). This study is consistent with the Gibbs adsorption equation. The

figure also shows that all the added surfactant forms micelles in water phase after the CMC and the IFT does not change with rising surfactant concentration due the saturation of the interface with surfactant micelles.

7.5 Conclusions

Optimization of effective surfactant for cEOR is laboratory intense and time-consuming mainly because of the complex nature of the crude oil and reservoir rock matrix. The MD simulations reveal that the head group structure of surfactant have influence on interface formation energy, interfacial thickness and the character of surfactants and water interaction, these three parameters are the crucial factors for reduction of the interfacial tensions. Some observations from simulation process specify that the inferred interfacial tension obeys an order which is just reverse of the interfacial thickness, interface formation energy and interaction behaviours of water and those surfactant molecules. The polarity of surfactant molecules strongly depends on the molecular structure and the polarity can be enhanced by adding oxygen, oxyethyl group and benzene ring to the molecular structure of surfactants. A Novel, coarse grained, molecular modeling methods such as DPD have the potential to support and significantly speed up the surfactant screening process and the development of new surfactant structures. Multi-component surfactants and oils can be simulated accurately and relatively fast. Fine tuning of the DPD parameters describing the particle-particle interaction potentials is required to obtain a good match with experimental results. The DPD models for coarse-grained methods are also applied to find the appropriate parameters to explain the behaviour of surfactants on oil/water interface. Still there have several questions to fix the optimization of the effective surfactant for EOR such as which head group configuration has the best effective hydrophilic ability; what is the best surfactant polarity for IFT reduction; how physical parameters like temperature and pressure influence the surfactant head group structure and consequently the IFT; and which will be best ratio of hydrophilicity to hydrophobicity of a surfactant molecule etc. Therefore, there will be enormous scopes of study to develop better molecular structure of different surfactants by computational approaches. A deeper perceptive of the connection between surfactant configuration and its effectiveness will attract the oil researchers extensively in a new direction of this research.

Author contribution: All the authors have accepted responsibility for the entire content of this submitted manuscript and approved submission.

Research funding: This research received no specific grant from any funding agency in the public, commercial, or not-for-profit sectors.

Conflict of interest statement: The authors declare no conflicts of interest regarding this article.

References

1. Okoliegbe IN, Agarry OO. Application of microbial surfactant (a review). *Sch J Biotechnol* 2012;1: 15–23.
2. Silva RCFS, Almeida DG, Rufino RD, Luna JM, Santos VA, Sarubbo LA. Applications of biosurfactants in the petroleum industry and their mediation of oil spills. *Int J Mol Sci* 2014;15:12523–42.
3. Najafi-Marghmaleki A, Kord S, Hashemi A, Motamedi H. Experimental investigation of efficiency of MEOR process in a carbonate oil reservoir using *Alcaligenes faecalis*: impact of interfacial tension reduction and wettability alteration mechanisms. *Fuel* 2018;232:27–35.
4. Elraies KA, Tan IM. The application of a new polymeric surfactant for chemical EOR. In: Book: Introduction to Enhanced Oil Recovery (EOR) processes and bioremediation of oil-contaminated sites. Rijeka: InTech; 2012:45–70 pp.
5. Santos DKF, Rufino RD, Luna JM, Santos VA, Sarubbo LA. Biosurfactants multifunctional biomolecules of the 21st century. *Int J Mol Sci* 2016;17:401.
6. Hirasaki G, Miller C, Puerto M. Recent advances in surfactant EOR. *SPE J* 2011;16:889–907.
7. Kaster KM, Hiorth A, Kjeilen-Eilertsen G, Boccadoro K, Lohne A, Berland H, et al. Mechanisms involved in microbially enhanced oil recovery. *Transport Porous Media* 2012;91: 59–79.
8. Rabiei A, Sharifnik M, Niazi A, Hashemi A, Ayatollahi S. Core flooding tests to investigate the effects of IFT reduction and wettability alteration on oil recovery during MEOR process in an Iranian oil reservoir. *Appl Microbiol Biotechnol* 2013;97:5979–91.
9. Abramov VO, Abramova AV, Bayazitov VM, Altunina LK, Gerasin AS, Pashin DM, et al. Sonochemical approaches to enhanced oil recovery. *Ultrason Sonochem* 2015;25:76–81.
10. Daghljan Sofla SJ, Sharifi M, Hemmati Sarapardeh A. Toward mechanistic understanding of natural surfactant flooding in enhanced oil recovery processes: the role of salinity, surfactant concentration and rock type. *J Mol Liq* 2016;222:632–9.
11. Brown LR. Microbial enhanced oil recovery (MEOR). *Curr Opin Microbiol* 2010;13:316–20.
12. Samanta A, Mandal A, Sarkar A. Design of alkali-surfactant-polymer flooding for Enhanced Oil Recovery. Germany: LAP LAMBERT Academic Publishing GmbH & Co. KG; 2011.
13. Khajepour H, Mahmoodi M, Biria D, Ayatollahi S. Investigation of wettability alteration through relative permeability measurement during MEOR process: a micromodel study. *J Petrol Sci Eng* 2014;120:10–7.
14. Fernandes PL, Rodrigues EM, Paiva FR, Ayupe BAL. Biosurfactant, solvents and polymer production by *Bacillus subtilis* RI4914 and their application for enhanced oil recovery. *Fuel* 2016;180:551–7.
15. Samanta A, Bera A, Mandal A, Ojha K. Mobility control and enhanced oil recovery using partially hydrolyzed polyacrylamide (PHPA). *J Petrol Explor Prod Technol* 2012;2:67–74.
16. Nabipour M, Ayatollahi S, Keshavarz P. Application of different novel and newly designed commercial ionic liquids and surfactants for more oil recovery from an Iranian oil field. *J Mol Liq* 2017;230:579–88.
17. Khan MY, Samanta A, Ojha K, Mandal A. Design of alkaline/surfactant/polymer (ASP) slug and its use in enhanced oil recovery. *Petrol Sci Technol* 2009;27:1926–42.
18. Zhang QQ, Cai BX, Xu WJ, Gang H. Novel zwitterionic surfactant derived from castor oil and its performance evaluation for oil recovery. *Colloids Surf A Physicochem Eng Asp* 2015;483:87–95.
19. Kumar A, Mandal A. Synthesis and physicochemical characterization of zwitterionic surfactant for application in enhanced oil recovery. *J Mol Liq* 2017;243:61–71.
20. Bera A, Mandal A, Belhaj H, Kumar T. Enhanced oil recovery by nonionic surfactants considering micellization, surface, and foaming properties. *Petrol Sci* 2017;14:362–71.

21. Pal N, Verma A, Ojha K, Mandal A. Nanoparticle-modified gemini surfactant foams as efficient displacing fluids for enhanced oil recovery. *J Mol Liq* 2020;310:113193.
22. Ahmadi MA, Shadzadeh SR. Implementation of a highperformance surfactant for enhanced oil recovery from carbonate reservoirs. *J Petrol Sci Eng* 2013;110:66–73.
23. Ahmadi MA, Arabsahebi Y, Shadzadeh SR, Shokrollahzadeh BS. Preliminary evaluation of mulberry leaf-derived surfactant on interfacial tension in an oil-aqueous system: EOR application. *Fuel* 2014;117:749–55.
24. Ahmadi MA, Galedarzadeh M, Shadzadeh SR. Wettability alteration in carbonate rocks by implementing new derived natural surfactant: enhanced oil recovery applications. *Transport Porous Media* 2015;106:645–67.
25. Sahu A, Choudhury S, Bera A, Kar S, Kumar S, Mandal A. Anionic–nonionic mixed surfactant systems: micellar interaction and thermodynamic behavior. *J Dispersion Sci Technol* 2015;36:1156–69.
26. Mohammed M, Babadagli T. Wettability alteration: a comprehensive review of materials/methods and testing the selected ones on heavy-oil containing oil-wet systems. *Adv Colloid Interface Sci* 2015;220:54–77.
27. Fu L, Zhang G, Ge J, Liao K, Pei H, Jiang P, et al. Study on organic alkali-surfactant-polymer flooding for enhanced ordinary heavy oil recovery. *Colloids Surf, A* 2016;508:230–9.
28. Liyanage PJ, Lu J, Arachchilage GWP, Weerasooriya UP, Pope GA. A novel class of large-hydrophobe tristyrylphenol (TSP) alkoxy sulfate surfactants for chemical enhanced oil recovery. *J Petrol Sci Eng* 2015;128:73–85.
29. Goudarzi A, Delshad M, Mohanty KK, Sepehrnoori K. Surfactant oil recovery in fractured carbonates: experiments and modeling of different matrix dimensions. *J Petrol Sci Eng* 2015;125:136–45.
30. Karambeigi MS, Abbassi R, Roayaei E, Emadi MA. Emulsion flooding for enhanced oil recovery: interactive optimization of phase behavior, microvisual and core-flood experiments. *J Ind Eng Chem* 2015;29:382–91.
31. Cerón-Camacho R, Martínez-Palou R, Chávez Gómez B, CuéllarCésar FHB, JorgeAburto JCC. Synergistic effect of alkyl-O-glucoside and -cellobioside biosurfactants as effective emulsifiers of crude oil in water. A proposal for the transport of heavy crude oil by pipeline. *Fuel* 2013;110:310–7.
32. Tikhonov AM, Patel H, Garde S, Schlossman ML. Tail ordering due to headgroup hydrogen bonding interactions in surfactant monolayers at the water-oil interface. *J Phys Chem B* 2006;110:19093–6.
33. Vácha R, Roke S. Sodium dodecyl sulfate at water–hydrophobic interfaces: a simulation study. *J Phys Chem B* 2012;116:11936–42.
34. Holte LK, Kuran BA, Richmond GL, Johnson KE. Computational modeling of lauric acid at the organic–water interface. *J Phys Chem C* 2014;118:10024–32.
35. Hantal G, Sega M, Horvai G, Jedlovsky P. Contribution of different molecules and moieties to the surface tension in aqueous surfactant solutions. *J Phys Chem C* 2019;123:16660–70.
36. Rehner P, Gross J. Predictive density gradient theory based on nonlocal density functional theory. *Phys Rev E* 2018;98:063312.
37. Mu X, Xi S, Alpak FO, Chapman WG. Modified density gradient theory for surfactant molecules applied to oil/water interfaces. *Ind Eng Chem Res* 2018;57:7643–54.
38. Prabhakar S, Melnik R. Influence of Mg^{2+} , SO_4^{2-} and Na^+ ions of sea water in crude oil recovery: DFT and ab initio molecular dynamics simulations. *Colloid Surface Physicochem Eng Aspect* 2018;539:53–8.
39. Herdes C, Ervik Å, Mejía A, Müller EA. Prediction of the water/oil interfacial tension from molecular simulations using the coarse-grained SAFT- γ Mie force field. *Fluid Phase Equil* 2018;476:9–15.
40. Vu TV, Papavassiliou DV. Oil–water interfaces with surfactants: a systematic approach to determine coarse-grained model parameters. *J Chem Phys* 2018;148:204704.

41. Ginzburg VV, Chang K, Jog PK, Argenton AB, Rakesh L. Modeling the interfacial tension in oil–water-nonionic surfactant mixtures using dissipative particle dynamics and self-consistent field theory. *J Phys Chem B* 2011;115:4654–61.
42. Liu H, Liu Y, Shang Y, Liu H. Molecular simulation and experimental studies on the interfacial properties of a mixed surfactant SDS/C4mimBr. *Mol Simulat* 2019;45:223–9.
43. Peng S, Hui Z, Lin L, Chunhui S, Qingguo C, Zesheng L. Molecular dynamics simulation of four typical surfactants in aqueous solution. *RSC Adv* 2019;9:3224–31.
44. Xue C, Qu G, Han Y, Li S, Gao X, Ding W. Molecular dynamics simulations of sulfobetaine -type zwitterionic surfactant at the decane/water interface. *J Dispersion Sci Technol* 2016;37:1480–5.
45. Liu Y, Yan H, Liu H, Liu J, Sun B, Liu M. Molecular dynamics simulation studies on the concentration-dependent interaction of dodecyltrimethylammonium bromide with curcumin. *J Dispersion Sci Technol* 2020;0:1–11.
46. Choudhary M, Kamil SM. Phase diagram study of sodium dodecyl sulfate using dissipative particle dynamics. *ACS Omega*; 2020, 5:22891–900 pp.
47. Wu H, Xu J, He X, Zhao Y, Wen H. Mesoscopic simulation of self-assembly in surfactant oligomers by dissipative particle dynamics. *Colloid Surface Physicochem Eng Aspect* 2006;290:239–46.
48. Le W, Amin H, Jinlu L, Shun X, George JH, Clarence AM, et al. Modeling micelle formation and interfacial properties with iSAFT classical density functional theory. *J Chem Phys* 2017;146:124705.
49. Chen M, Wang Z, Wang H, Zhang G, Tao F. Investigation of adsorption of surfactant at the air-water interface with quantum chemistry method. *Chinese Sci Bull* 2007;52:1451–5.
50. Itoo FA, Mir JM, Malik NA, Ali A. Density functional aspects and thermodynamic evaluation of sodium dodecyl sulphate in aqueous tartrazine. *J King Saud Univ Sci* 2020;32:2505–12.
51. Stoyanov SD, Rehage H, Paunov VN. Novel surface tension isotherm for surfactants based on local density functional theory. *Phys Rev Lett* 2003;91:086102.
52. Kamal MS, Hussien IA, Sultan AS, Han M. Rheological study on ATBS-AM copolymer-surfactant system in high-temperature and high-salinity environment. *J Chem* 2013;2013:801570.
53. Kamal MS, Sultan AS, Al-Mubaiyeh UA, Hussein IA. Review on polymer flooding: rheology, adsorption, stability, and field applications of various polymer systems. *Polym Rev* 2015;55: 491–530.
54. Saboorian-Jooybari H, Dejam M, Chen Z. Heavy oil polymer flooding from laboratory core floods to pilot tests and field applications: half-century studies. *J Petrol Sci Eng* 2016;142:85–100.
55. Samanta A, Bera A, Ojha K, Mandal A. Effects of alkali, salts, and surfactant on rheological behavior of partially hydrolyzed polyacrylamide solutions. *J Chem Eng Data* 2010;55:4315–22.
56. Samanta A, Bera A, Ojha K, Mandal A. Comparative studies on enhanced oil recovery by alkali–surfactant and polymer flooding. *J Pet Explor Prod Technol* 2012;2:67–74.
57. Bera A, Kumar T, Ojha K, Mandal A. Screening of microemulsion properties for application in enhanced oil recovery. *Fuel* 2014;121:198–207.
58. Olajire AA. Review of ASP EOR (alkaline surfactant polymer enhanced oil recovery) technology in the petroleum industry: prospects and challenges. *Energy* 2014;77:963–82.
59. Ayirala SC, Rao DN. Multiphase flow and wettability effects of surfactants in porous media. *Colloids Surf A* 2004;241:313–22.
60. Howe AM, Clarke A, Mitchell J, Staniland J, Hawkes L, Whalan C. Visualising surfactant enhanced oil recovery. *Colloids Surf A* 2015;480:449–61.
61. Hou J, Liu Z, Zhang S, Yue XA, Yang J. The role of viscoelasticity of alkali/surfactant/polymer solutions in enhanced oil recovery. *J Petrol Sci Eng* 2005;47:219–35.
62. Song B, Hu X, Shui X, Cui Z, Wang Z. A new type of renewable surfactants for enhanced oil recovery: dialkylpolyoxyethylene ether methyl carboxyl betaines. *Colloids Surf, A* 2016;489:433–40.
63. Pal N, Babu K, Mandal A. Surface tension, dynamic light scattering and rheological studies of a new polymeric surfactant for application in enhanced oil recovery. *J Petrol Sci Eng* 2016;146:591–600.

64. Lemasson FA, Strunk T, Gerstel P, Hennrich F, Lebedkin S, Barner-Kowollik C, et al. Selective dispersion of single-walled carbon nanotubes with specific chiral indices by poly(*N*-decyl-2,7-carbazole). *J Am Chem Soc* 2010;133:652.
65. McDonald TJ, Engtrakul C, Jones M, Rumbles G, Heben MJ. Kinetics of PL quenching during single-walled carbon nanotube rebundling and diameter-dependent surfactant interactions. *J Phys Chem B* 2006;110:25339.
66. Tan Y, Resasco DE. Dispersion of single-walled carbon nanotubes of narrow diameter distribution. *J Phys Chem B* 2005;109:14454.
67. Yurekli K, Mitchell CA, Krishnamoorti R. Small-angle neutron scattering from surfactant-assisted aqueous dispersions of carbon nanotubes. *J Am Chem Soc* 2004;126:9902.
68. Van Der Spoel D, Lindahl E, Hess B, Groenhof G, Mark AE, Berendsen HJC, et al. Fast, flexible, and free. *J Comput Chem* 2005;26:1701.
69. Monticelli L, Tieleman DP. Force fields for classical molecular dynamics. In: Monticelli L, Salonen E, editors. *Biomolecular simulations. Methods in molecular biology (methods and protocols)*. Totowa, NJ: Humana Press; 2013:924p.
70. Delhommelle J, Millie P. Inadequacy of the Lorentz–Berthelot combining rules for accurate predictions of equilibrium properties by molecular simulation. *Mol Phys* 2001;99:619–25.
71. Elbeltagi E, Hegazy T, Grierson D. Comparison among five evolutionary-based optimization algorithms. *Adv Eng Inf* 2005;19:43–53.
72. Stone A. *The theory of intermolecular forces*, 2nd ed. UK: Oxford University Press; 2013.
73. Ballenegger V, Cerdà JJ, Holm C. How to convert SPME to P3M: influence functions and error estimates. *J Chem Theor Comput* 2012;8:936–47.
74. Guo X, Liu X, Xu P, Du Z, Chow E. Efficient particle-mesh spreading on GPUs. *Proc Comput Sci* 2015; 55:120–9.
75. Kasahara K, Sakuraba S, Fukuda I. Enhanced sampling of molecular dynamics simulations of a polyalanine octapeptide: effects of the periodic boundary conditions on peptide conformation. *J Phys Chem B* 2018;122:2495–503.
76. Sharma S. Chapter 2 – overview of BIOVIA materials Studio, LAMMPS, and GROMACS. In: *Molecular dynamics simulation of nanocomposites using BIOVIA materials studio, lammmps and gromacs*. UK: Elsevier; 2019:39–100 pp.
77. Zheng L, Alhossary AA, Kwoh CK, Mu Y. Molecular dynamics and simulation. In: *book: encyclopedia of bioinformatics and computational biology*. USA: Academic Press, Elsevier; 2019:550–66 pp.
78. Hammonds KD, Heyes DM. Shadow Hamiltonian in classical NVE molecular dynamics simulations: a path to long time stability. *J Chem Phys* 2020;152:024114.
79. Kumar K, Maity PK. Chapter 6: Introduction to molecular dynamics simulation. In: *Computational statistical physics*. Switzerland: Springer Nature 2011: 173–213 pp.
80. Groot RD, Warren PB. Dissipative particle dynamics: bridging the gap between atomistic and mesoscopic simulation. *J Chem Phys* 1997;107:4423.
81. Groot RD, Rabone KL. Mesoscopic simulation of cell membrane damage, morphology change and rupture by nonionic surfactants. *Biophys J* 2001;81:725.
82. Maiti A, McGrother S. Bead–bead interaction parameters in dissipative particle dynamics: relation to bead-size, solubility parameter, and surface tension. *J Chem Phys* 2004;120:1594.
83. Moeendarbary E, Ng TY, Zangeneh M. Dissipative particle dynamics: introduction, methodology and complex fluid applications – a review. *Int J Appl Mech* 2009;01:737–63.
84. Hoogerbrugge PJ, Koelman J. Simulating microscopic hydrodynamic phenomena with dissipative particle dynamics. *Europhys Lett* 1992;19:155.
85. Koelman JMVA, Hoogerbrugge PJ. Dynamic simulations of hard-sphere suspensions under steady shear. *Europhys Lett* 1993;21:363.

86. Groot RD, Madden TJ, Tildesley DJ. On the role of hydrodynamic interactions in block copolymer microphase separation. *J Chem Phys* 1999;110:9739.
87. Shelley JC, Shelley MY. Computer simulation of surfactant solutions. *Curr Opin Colloid Interface Sci* 2000;5:101.
88. Arai N, Yasuoka K, Zeng XC. Self-Assembly of surfactants and polymorphic transition in nanotubes. *J Am Chem Soc* 2008;130:7916–20.
89. Liu Y, Yu C, Jin H, Jiang B, Zhu X, Zhou Y, et al. A supramolecular Janus hyperbranched polymer and its photoresponsive self-assembly of vesicles with narrow size distribution. *J Am Chem Soc* 2013; 135:4765–70.
90. Boek ES, Coveney PV, Lekkerkerker HNW, van der Schoot P. Simulating the rheology of dense colloidal suspensions using dissipative particle dynamics. *Phys Rev E* 1997;55:3124.
91. Meakin P, Tartakovsky AM. Modeling and simulation of pore scale multiphase fluid flow and reactive transport in fractured and porous media. *Rev Geophys* 2009;47:RG3002.
92. Espanol P, Warren P. Statistical mechanics of dissipative particle dynamics. *Europhys Lett* 1995; 30:191.
93. Lu JR, Li ZX, Thomas RK, Staples EJ, Tucker I, Penfold J. Neutron reflection from a layer of monododecyl hexaethylene glycol adsorbed at the air–liquid interface: the configuration of the ethylene glycol chain. *J Phys Chem* 1993;97:8012–20.
94. Lowry E, Sedghi M, Goual L. Molecular simulations of NAPL removal from mineral surfaces using microemulsions and surfactants. *Colloids Surf A* 2016;506:485–94.
95. Yuan S, Wang S, Wang X, Guo M, Wang Y, Wang D. Molecular dynamics simulation of oil detachment from calcite surface in aqueous surfactant solution. *Comput Theor Chem* 2016;1092: 82–9.
96. Li X, Xue Q, Wu T, Jin Y, Ling C, Lu S. Oil detachment from silica surface modified by carboxy groups in aqueous cetyltriethylammonium bromide solution. *Appl Surf Sci* 2015;353:1103–11.
97. Liu Q, Yuan S, Yan H, Zhao X. Mechanism of oil detachment from a silica surface in aqueous surfactant solutions: molecular dynamics simulations. *J Phys Chem B* 2012;116:2867–75.
98. Yan H, Yuan S. Molecular dynamics simulation of the oil detachment process within silica nanopores. *J Phys Chem C* 2016;120:2667–74.
99. Sedghi M, Piri M, Goual L. Molecular dynamics of wetting layer formation and forced water invasion in angular nanopores with mixed wettability. *J Chem Phys* 2014;141:194703.
100. Pivkin IV, Caswell B, Karniadakis GE. *Reviews in computational chemistry*. USA: John Wiley & Sons, Inc.; 2010:85–110 pp.
101. Xu J, Zhang Y, Chen H, Wang P, Xie Z, Yao Y, et al. Effect of surfactant headgroups on the oil/water interface: an interfacial tension measurement and simulation study. *J Mol Struct* 2013;1052:50–6.
102. Bai S, Kubelka J, Piri M. Atomistic molecular dynamics simulations of surfactant-induced wettability alteration in crevices of calcite nanopores. *Energy Fuels* 2020;34:3135–43.
103. Shi P, Zhang H, Lin L, Song C, Chen Q, Li Z. Molecular dynamics simulation of four typical surfactants in aqueous solution. *RSC Adv* 2019;9:3224–31.
104. Storm S, Jakobtorweihen S, Smirnova I, Panagiotopoulos AZ. Molecular dynamics simulation of SDS and CTAB micellization and prediction of partition equilibria with COSMOmic. *Langmuir* 2013;29:11582–92.
105. Zorbakhsh A, Querol A. Neutron reflection from the liquid–liquid Interface: adsorption of hexadecylphosphorylcholine to the hexadecane–aqueous solution interface. *Langmuir* 2005;21: 11704–9.
106. Lawrence FS, Geraldine LR. Isolated molecular ion solvation at an oil/water interface investigated by vibrational sum-frequency spectroscopy. *J Phys Chem B* 2004;108:12518–28.
107. Knock MM, Bell GR, Hill EK, Turner HJ, Bain CD. Sum-frequency spectroscopy of surfactant monolayers at the oil–water interface. *J Phys Chem B* 2003;107:10801–14.

108. Zarbakhsh A, Querol A, Bowers J, Webster JRP. Structural studies of amphiphiles adsorbed at liquid–liquid interfaces using neutron reflectometry. *Faraday Discuss* 2005;129:155–67.
109. Zarbakhsh A, Webster JRP, Eames J. Structural studies of surfactants at the Oil–Water interface by neutron reflectometry. *Langmuir* 2009;25:3953–6.
110. Song Y, Lee JH, Jung I, Seo B, Hwang H. Molecular dynamics simulations of micelle properties and behaviors of sodium lauryl ether sulfate penetrating ceramide and phospholipid bilayers. *J Phys Chem B* 2020;124:5919–29.
111. Guan Y, Chi MH, Sun WF, Chen QG, Wei X-L. Molecular dynamics simulations of molecular diffusion equilibrium and breakdown mechanism of oil-impregnated pressboard with water impurity. *Polymers* 2018;10:1274.
112. Omelyan IP, Mryglod IM, Folk R. Optimized Verlet-like algorithms for molecular dynamics simulations. *Phys Rev E* 2002;65:056706.
113. Hünenberger PH. Thermostat algorithms for molecular dynamics simulations. In: Book: advanced computer simulation. Advances in polymer science. Berlin, Heidelberg: Springer; 2005:173p.
114. Lippert RA, Predescu CP, Ierardi DJ, Mackenzie KM, Eastwood MP, Dror RO, et al. Accurate and efficient integration for molecular dynamics simulations at constant temperature and pressure. *J Chem Phys* 2013;139:164106.
115. Adcock SA, McCammon JA. Molecular dynamics: survey of methods for simulating the activity of proteins. *Chem Rev* 2006;106:1589–615.
116. Mohallem JR, Coura TO, Diniz LG, Castro G, Assafrão D, Heine T. Adiabatic corrections to density functional theory energies and wave functions. *J Phys Chem A* 2008;112:8896–901.
117. Ciezak JA, Trevino SF. Inelastic neutron scattering spectrum of Cyclotrimethylenetrinitramine: a comparison with solid-state electronic structure calculations. *J Phys Chem A* 2006;110:5149–55.
118. Lindahl E, Hess B, van der Spoel D. GROMACS 3.0: a package for molecular simulation and trajectory analysis. *J Mol Model* 2001;7:306–17.
119. Brooks B, Brooks CL, MacKerell AD, Nilsson L, Petrella RJ, Roux B, et al. CHARMM: the biomolecular simulation program. *J Comput Chem* 2009;30:1545–614.
120. Wu Y, Tepper HL, Voth GA. Flexible simple point-charge water model with improved liquid-state properties. *J Chem Phys* 2006;124:024503.
121. Singh UC, Kollman PA. An approach to computing electrostatic charges for molecules. *Comput Chem* 1984;5:129–45.
122. Prasetyo N, Hofer TS. Structure, dynamics, and hydration free energy of carbon dioxide in aqueous solution: a quantum mechanical/molecular mechanics molecular dynamics thermodynamic integration (QM/MM MD TI) simulation study. *J Chem Theory Comput*; 2018, 14: 6472–83 pp.
123. Terrón-Mejía KA, López-Rendón R, Goicochea AG. Desorption of hydrocarbon chains by association with ionic and nonionic surfactants under flow as a mechanism for enhanced oil recovery. *Sci Rep* 2017;7:9586.
124. Malde AK, Zuo L, Breeze M, et al. An automated force field Topology builder (ATB) and repository: version 1.0. *J Chem Theor Comput* 2011;7:4026–37.
125. Dykstra C, Frenking G, Kim K, Scuseria G. Theory and applications of computational chemistry: the first forty years. Amsterdam, Netherlands: Elsevier Science; 2011.
126. Kutzner C, van Der Spoel D, Fechner M, et al. Speeding up parallel GROMACS on high-latency networks. *J Comput Chem* 2007;28:2075–84.
127. Hess B, Kutzner C, Van Der Spoel D, Lindahl E. GROMACS 4: algorithms for highly efficient, load-balanced, and scalable molecular simulation. *J Chem Theory Comput* 2008;4:435–47.
128. Pronk S, Pall S, Schulz R, et al. GROMACS 4.5: a high-throughput and highly parallel open source molecular simulation toolkit. *Bioinformatics* 2013;29:845–54.

129. van der Spoel D, Lindahl E, Hess B, Groenhof G, Mark AE, Berendsen HJC. GROMACS: fast, flexible, and free. *J Comput Chem* 2005;26:1701–8.
130. Khan HM, MacKerell AD, Reuter N. Cation- π interactions between methylated ammonium groups and tryptophan in the CHARMM36 additive force field. *J Chem Theory Comput*: 2019, 15:7–12 pp.
131. Schäfer A, Klamt A, Sattel D, Lohrenz JCW, Eckert F. COSMO implementation in TURBOMOLE: extension of an efficient quantum chemical code towards liquid systems. *Phys Chem Chem Phys* 2000;2:2187–93.
132. Jakobtorweihen S, Ingram T, Smirnova I. Combination of COSMOmic and molecular dynamics simulations for the calculation of membrane–water partition coefficients. *J Comput Chem* 2013; 34:1332–40.
133. Groot RD. Mesoscopic simulation of polymer-surfactant aggregation. *Langmuir* 2000;16: 7493–502.
134. Klamt A, Schwöbel J, Huniar U, Koch L, Terzi S, Gaudin T. COSMOplex: self-consistent simulation of self-organizing inhomogeneous systems based on COSMO-RS. *Phys Chem Chem Phys* 2019;21: 9225–38.
135. Buijse MA, Tandon K, Jain S, et al. Surfactant optimization for EOR using advanced chemical computational methods. *SPE Improved Oil Recovery Symposium*. Tulsa, Oklahoma, USA; 2012. SPE 154212-MS.

Olugbenga Morayo Oshakuade* and Oluseyi Ezekiel Awe

8 Determination of bulk and surface properties of liquid Bi-Sn alloys using an improved quasi-lattice theory

Abstract: The thermodynamic properties of Bi-Sn were studied at 600 and 900 K using a quasi-lattice theory. After successful fitting of Gibbs free energies of mixing and thermodynamic activities, the fitting parameters were used to investigate the enthalpy of mixing, the entropy of mixing, concentration fluctuations, Warren-Cowley short-range-order parameter, surface concentrations and surface tensions of the binary systems. Positive and symmetrically shaped enthalpies of mixing were observed in all composition range, while negative excess entropies of mixing were observed. Bi-Sn showed a slight preference for like-atoms as nearest neighbours in all composition range. The nature of atomic order in Bi-Sn at 600 and 900 K appeared similar. The highest tendency for homocoordination exists at composition where mole fraction of Bi is about 40%. It was also observed that Bi (whose surface tension is lower than that of Sn) has the highest surface enrichment in the Bi-Sn systems. Unlike many previous applications of the quasi-lattice theory where constant values were used to approximate coordination numbers, temperature and composition-dependent coordination numbers were applied in this work.

Keywords: average coordination number; concentration fluctuations; lead-free solder; surface concentration; surface tension.

8.1 Introduction

Before the last two decades, the eutectic Pb-Sn alloy has been the major soldering material in the electronics industry. However, the toxic nature of Pb has led to the restriction in the use of Pb-based materials, hence, the need for substitutes [1, 2]. Bi-Sn and Bi-Sn-based ternary systems have been identified as Pb-free solder candidates, due to the low liquidus temperature of Bi-Sn [1]. Moreover, the determination of a good solder candidate requires several other assessments, such as wettability, solidification behaviour, solder joint strength, safety to the environment, electrical conductivity and chemical stability [3]. Some researchers expect ternary and multi-component alloys to be better solder candidates because they possess lower liquidus temperatures than

*Corresponding author: **Olugbenga Morayo Oshakuade**, Department of Physics, University of Ibadan, Ibadan, Nigeria, E-mail: om.oshakuade@ui.edu.ng. <https://orcid.org/0000-0001-9971-1213>

Oluseyi Ezekiel Awe, Department of Physics, University of Ibadan, Ibadan, Nigeria, E-mail: oluseyi.awe@ui.edu.ng

This article has previously been published in the journal *Physical Sciences Reviews*. Please cite as:

O. M. Oshakuade and O. E. Awe "Determination of bulk and surface properties of liquid Bi-Sn alloys using an improved quasi-lattice theory" *Physical Sciences Reviews* [Online] 2021, 5. DOI: 10.1515/psr-2020-0095 | <https://doi.org/10.1515/9783110739763-008>

their binary counterparts [4]. Notwithstanding, the understanding of the thermodynamics of binary alloy systems is important in the study of their ternary and multi-component systems [4, 5].

The thermodynamic properties of the Bi-Sn binary system have been studied both experimentally and theoretically [6–13]. Some scientists have also worked on Bi-Sn-based ternary and multi-component systems [3, 7, 8, 14–16]. Experimental thermodynamic data (Gibbs free energies of mixing, entropies and enthalpies of mixing, thermodynamic activities) of Bi-Sn for 600 K is available in binary alloy repository [9]. Also, Katayama et al. [7] have studied the Bi-Sn and Bi-Sb-Sn systems at 900 K via EMF method. However, a literature search on the nature of atomic order and surface properties of Bi-Sn shows that research work is deficient in that area.

Amongst several existing thermodynamic models, the quasi-lattice theory (QLT) [17] is preferred for its ability to describe alloy systems in terms of the relative bonding energies between atom pairs and success in the study of concentration-concentration fluctuations in the long-wavelength limit. Unlike the widely used approximations of the Complex formation model by Bhatia and Hargrove [18] (where coordination number is either two or infinity), QLT [17] depends on more physically reasonable coordination numbers. In many previous applications of QLT [17], constants have been used to approximate coordination number.

In this work, the bulk and surface properties of Bi-Sn is studied using an improved quasi-lattice theory, introduced in our previous work [19], where more physically realistic coordination numbers have been incorporated into the popular quasi-lattice theory [17]. A model for estimating temperature-dependent coordination numbers of pure liquid metals, developed by Tao [20], is adopted for the estimation of nature and temperature-dependent coordination numbers in this work. Bi-Sn is studied at 600 and 900 K to provide information on the temperature dependence of the bulk and surface properties, and also help in Bi-Sb-Sn studies via QLT, in future. This work will contribute to the knowledge on the thermodynamic properties of the Bi-Sn system which is important in understanding its process metallurgy and further materials development.

Section 2 gives details on QLT, its improvement, and application to Gibbs free energy of mixing, thermodynamic activity, enthalpy of formation, entropy of formation, concentration fluctuations, Warren-Cowley chemical short-range-order parameter and surface properties calculation. Section 3 contains results and discussions on the computed thermodynamic properties while Section 4 contains summary and conclusions.

8.2 Theoretical framework

8.2.1 Average coordination number (\widehat{Z})

The average coordination number of liquid alloys, \widehat{Z} , is depends on the nature, composition and temperature of the system [20–23]. Equation is introduced to account

for the composition-dependent nature of Coordination number (Z) in liquid alloys [24]. Where Z_i is the coordination number of pure element i and c_i is the molar concentration of component i in the system.

$$\widehat{Z} = \sum_{i=1}^2 Z_i c_i \quad (8.1)$$

The model of Tao [20], which estimates temperature-dependent coordination numbers for pure liquid metals (Z_i) from their physical properties, defined in Eq. (8.2), is used in this work.

$$Z_i = \frac{4\sqrt{2\pi}}{3} \left(\frac{r_{mi}^3 - r_{oi}^3}{r_{mi} - r_{oi}} \right) \frac{0.6022 r_{mi}}{V_{mi}} \exp\left(\frac{\Delta H_{mi} (T_{mi} - T)}{Z_c R T T_{mi}} \right) \quad (8.2)$$

where T is the temperature of the system under study, ΔH_{mi} and T_{mi} are the melting enthalpy and melting temperature of component i , respectively, Z_c is the close-packed coordination number of magnitude 12, V_{mi} is the molar volume of component i at T , r_{oi} and r_{mi} are the beginning and first peak values of radial distance distribution function near the melting point of liquid metal i , respectively. The relevant parameters used in this work to estimate Z_i are presented in Table 8.1 [25].

Expanding Eqs. (8.1) and (8.2) for Bi-Sn binary system gives Eq. (8.3), an expression for average coordination number that is dependent on nature, composition and temperature.

$$\widehat{Z}(c_{Bi}, T) = \frac{4 \times 0.6022 \sqrt{2\pi}}{3} \left[\left(\frac{r_{mBi}^3 - r_{oBi}^3}{r_{mBi} - r_{oBi}} \right) \frac{r_{mBi}}{V_{mBi}} \exp\left(\frac{\Delta H_{mBi} (T_{mBi} - T)}{Z_c R T T_{mBi}} \right) c_{Bi} + \left(\frac{r_{mSn}^3 - r_{oSn}^3}{r_{mSn} - r_{oSn}} \right) \frac{r_{mSn}}{V_{mSn}} \exp\left(\frac{\Delta H_{mSn} (T_{mSn} - T)}{Z_c R T T_{mSn}} \right) (1 - c_{Bi}) \right] \quad (8.3)$$

Subscripts Bi and Sn in Eq. (8.3) correspond to the two components (Bi and Sn) in the Bi-Sn binary system.

The Average coordination number (\widehat{Z}), defined in Eq. (8.3), is adopted in this work to apply quasi-lattice theory to the study of Bi-Sn systems.

Table 8.1: Calculated Z_i of each component and essential parameters related to its calculation.

| Metal i | V_{mi}^a (cm ³ /mol) | T_{mi}^a (K) | ΔH_{mi}^a (kJ/mol) | $r_{mi}^{a,b}$ | $r_{oi}^{a,b}$ | Z_i (T) ^c | |
|--------------|-----------------------------------|-------------------|-------------------------------|----------------|----------------|------------------------|--------|
| | | | | | | 600 K | 900 K |
| Bi | 20.80 [1 + 0.000117 (T - 544)] | 544 | 10.88 | 3.34 | 2.78 | 8.8770 | 8.0736 |
| Sn | 17.00 [1 + 0.000087 (T - 505)] | 505 | 7.07 | 3.14 | 2.68 | 9.1799 | 8.6028 |

^aThese parameters were obtained from [25]. ^bUnit is 10⁻⁸ cm. ^cThe various values for different temperatures were obtained using Eq. (8.2).

8.2.2 Quasi-lattice theory for compound forming liquid alloys (QLT)

Following the assumptions by Bhatia and Singh [17] on QLT, it can be deduced that N_{Bi} moles of Bi and N_{Sn} moles of Sn will mix to form a pseudo-ternary mixture comprising of n_1 moles of unassociated Bi atoms (specie 1), n_2 moles of unassociated Sn atoms (specie 2) and n_3 moles of $\text{Bi}_\mu\text{Sn}_\nu$ complex (specie 3). Where μ and ν are small integers obtained from stoichiometric information while c_{Bi} and c_{Sn} are the molar concentrations of Bi and Sn, respectively ($c_{\text{Bi}} + c_{\text{Sn}} = 1$). If the total number of moles in the mixture is N , then Eqs. (8.4)–(8.8) can be equivalent to the laws of conservation of matter. The average coordination number (\bar{Z}) described in Section 8.2.1 is used in this section to replace the nominal Z , which is common in previous works on QLT.

$$N_{\text{Bi}} + N_{\text{Sn}} = N \quad (8.4)$$

$$N_{\text{Bi}} = Nc_{\text{Bi}} \quad (8.5)$$

$$N_{\text{Sn}} = N - N_{\text{Bi}} = N - Nc_{\text{Bi}} = N(1 - c_{\text{Bi}}) \quad (8.6)$$

$$n_1 = Nc_{\text{Bi}} - \mu n_3 \quad (8.7)$$

$$n_2 = N(1 - c_{\text{Bi}}) - \nu n_3 \quad (8.8)$$

The expressions for Gibbs free energy of mixing (G_M) given as Eq. (8.9) can be written as Eq. (8.10) [18, 26].

$$G_M = G - Nc_{\text{Bi}} G_{\text{Bi}}^{(0)} - Nc_{\text{Sn}} G_{\text{Sn}}^{(0)} \quad (8.9)$$

$$G_M = -n_3 g + G' \quad (8.10)$$

where $G_i^{(0)}$ is the chemical potential for species i in the mixture, G is the free energy of the mixture, g is the free energy of formation of chemical complex, the term “ $-n_3 g$ ” denotes the lowering of free energy as a result of chemical complex formation, G' is the free energy of mixing of the pseudo-ternary mixture assumed to interact weakly, and G' depends on the underlying relevant theory being applied to study weakly interacting mixtures. Generally, g and G' is defined as Eqs. (8.11) and (8.12).

$$g = \mu G_{\text{Bi}}^{(0)} + \nu G_{\text{Sn}}^{(0)} - G_{\text{BiSn}}^{(0)} \quad (8.11)$$

$$G' = G - \left(n_1 G_{\text{Bi}}^{(0)} + n_2 G_{\text{Sn}}^{(0)} + n_3 G_{\text{BiSn}}^{(0)} \right) \quad (8.12)$$

For an ideal mixture, G' can be defined as Eq. (8.13), where R and T are the molar gas constant and temperature, respectively.

$$G' = RT \left(n_1 \ln \frac{n_1}{n_1 + n_2 + n_3} + n_2 \ln \frac{n_2}{n_1 + n_2 + n_3} + n_3 \ln \frac{n_3}{n_1 + n_2 + n_3} \right) \quad (8.13)$$

Assuming only one type of complex is formed, the QLT by Bhatia and Singh [17] gives the expression for G_M as Eq. (8.14), where ζ and \aleph are defined in Eqs. (8.15) and (8.16), respectively.

$$G_M = -n_3g + RT \left[n_1 \ln \frac{n_1}{N} + n_2 \ln \frac{n_2}{N} + n_3 \ln \frac{(\mu + \nu)n_3}{N} - \frac{1}{2} \hat{Z} n_3 (\mu + \nu - \zeta) \ln \frac{\mu + \nu}{\mu + \nu - \zeta} - \frac{1}{2} \hat{Z} \aleph \ln \frac{\aleph}{N} \right] + \frac{1}{\aleph} \left(\frac{n_1 n_2}{N} v_{12} + \frac{n_1 n_3}{N} v_{13} + \frac{n_2 n_3}{N} v_{23} \right) \quad (8.14)$$

$$\zeta = \frac{2(\mu + \nu - 1)}{\hat{Z}} \quad (8.15)$$

$$\aleph = n_1 + n_2 + \left(\mu + \nu - \frac{2(\mu + \nu - 1)}{\hat{Z}} \right) n_3 = N - \frac{2(\mu + \nu - 1)}{\hat{Z}} n_3 = N - \zeta n_3 \quad (8.16)$$

The v_{ij} s gives information on the inter-specie energetics of species i and j in the pseudo-ternary mixture. Interaction parameters g , v_{12} , v_{13} and v_{23} are determined by fitting, until Eq. (8.14) conforms to experimental thermodynamic data. The equilibrium condition of n_3 at a specified temperature is given in Eq. (8.17) [17].

$$\left(\frac{\partial G_M}{\partial n_3} \right)_{T,P,N,\zeta} = 0 \quad (8.17)$$

When Eq. (8.14) is substituted for G_M in Eq. (8.17), it gives Eq. (8.18) (where Q is defined in Eq. (8.19)).

$$n_1^\mu n_2^\nu = (\mu + \nu) n_3 e^{(Q-g/RT)} \aleph^{\mu+\nu-1} \quad (8.18)$$

$$Q = \frac{1}{\aleph RT} \left(-(\nu n_1 + \mu n_2) v_{12} + (n_1 - \mu n_3) v_{13} + (n_2 - \nu n_3) v_{23} + \frac{\zeta}{\aleph} (n_1 n_2 v_{12} + n_1 n_3 v_{13} + n_2 n_3 v_{23}) - \frac{1}{2} \hat{Z} (\mu + \nu - \zeta) \ln \frac{\mu + \nu}{\mu + \nu - \zeta} \right) \quad (8.19)$$

The directly observed thermodynamic activity can be derived from thermodynamic function in Eq. (8.20), where i refers to Bi or Sn [17, 27]. Simplification of Eq. (8.20) for components Bi and Sn while considering the composition-dependent nature of \hat{Z} gives Eqs. (8.21) and (8.22). Where Z_{Bi} and Z_{Sn} are the coordination numbers of pure liquid Bi and Sn at the specified T , respectively.

$$\ln a_i = \frac{1}{RT} \left(\frac{\partial G_M}{\partial N_i} \right)_{T,P,N} \quad (8.20)$$

$$\ln a_{Bi} = \ln\left(\frac{n_1}{N}\right) - \frac{1}{2}\widehat{Z}\ln\left(\frac{N}{N}\right) + \frac{n_2v_{12} + n_3v_{13}}{NRT} - \frac{n_1n_2v_{12} + n_1n_3v_{13} + n_2n_3v_{23}}{N^2RT} - \frac{Z_{Bi} - \widehat{Z}}{2N} \left[N \ln\left(\frac{N}{N}\right) + n_3(\mu + \nu)\ln\left(\frac{\mu + \nu}{\mu + \nu - \zeta}\right) \right] \quad (8.21)$$

$$- \frac{n_3\zeta}{N^2RT} \frac{Z_{Bi} - \widehat{Z}}{\widehat{Z}N} (n_1n_2v_{12} + n_1n_3v_{13} + n_2n_3v_{23})$$

$$\ln a_{Sn} = \ln\left(\frac{n_2}{N}\right) - \frac{1}{2}\widehat{Z}\ln\left(\frac{N}{N}\right) + \frac{n_1v_{12} + n_3v_{23}}{NRT} - \frac{n_1n_2v_{12} + n_1n_3v_{13} + n_2n_3v_{23}}{N^2RT} - \frac{Z_{Sn} - \widehat{Z}}{2N} \left[N \ln\left(\frac{N}{N}\right) + n_3(\mu + \nu)\ln\left(\frac{\mu + \nu}{\mu + \nu - \zeta}\right) \right] \quad (8.22)$$

$$- \frac{n_3\zeta}{N^2RT} \frac{Z_{Sn} - \widehat{Z}}{\widehat{Z}N} (n_1n_2v_{12} + n_1n_3v_{13} + n_2n_3v_{23})$$

Equation (8.18) is solved numerically to obtain n_3 at each concentration of study, having set the interaction parameters to convenient start values. The corresponding n_1 and n_2 for each n_3 are obtained from Eqs. (8.7) and (8.8). Thereafter, n_1 , n_2 and n_3 are used in Eqs. (8.14), (8.21) and (8.22), and to compute G_M and thermodynamic activities of Bi and Sn (a_i s). The computed G_M and a_i s are then compared with experimental G_M and a_i s, and adjustment of interaction parameters (g , v_{12} , v_{13} , v_{23}) is made in order to obtain a good fit. The final set of interaction parameters that give satisfactory agreement between experimental and computed data are then used to compute other thermodynamic quantities.

Mean absolute percentage error (Er_i) estimation, as defined in Eq. (8.23), was used to measure the agreements between two sets of data [28].

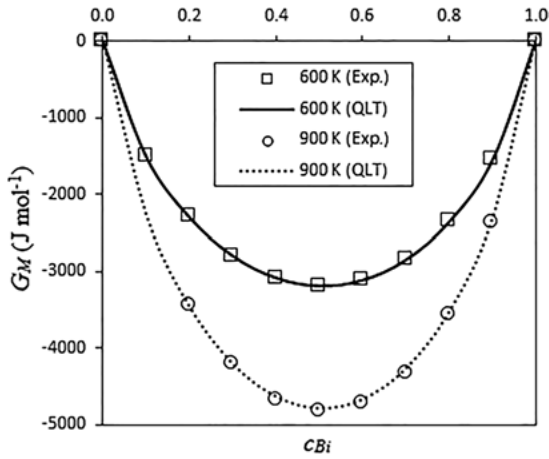
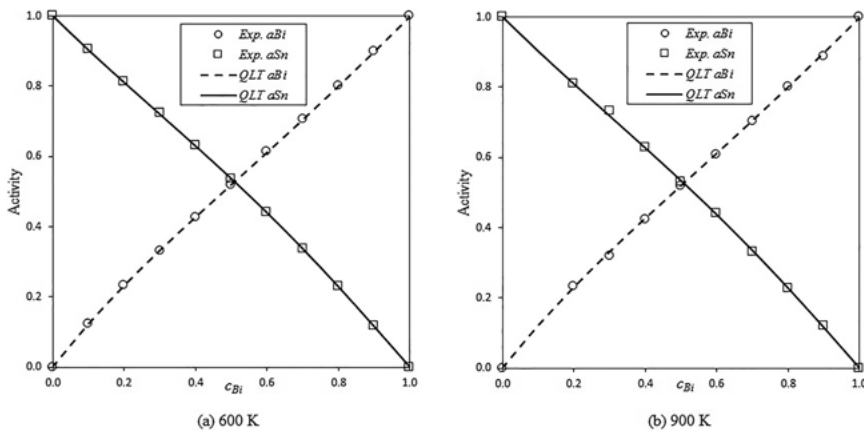
$$Er_i = \pm \frac{100}{t} \sum_{i=1}^t \left[\frac{d_{i,ex} - d_{i,pr}}{d_{i,ex}} \right] \quad (8.23)$$

where $d_{i,ex}$ and $d_{i,pr}$ are the existing and predicted values, respectively, while t is the size of data set.

The assumed complex obtained from stoichiometric information [7, 9] is Bi_1Sn_1 . Table 8.2 shows the interaction parameters obtained for Bi-Sn at 600 and 900 K and the corresponding mean absolute percentage error in QLT computation. Bi-Sn can be described as weakly interacting because their values of g/RT is small compared to strongly interacting systems like Mg-Bi, Tl-Te, K-Te and Na-Sn with interaction parameters ranging from 16.7 to 47.8 [18, 29]. The negative v_{ij} s imply attractive interactions between the species. The theoretically fitted G_M and a_i s, with corresponding experimentally observed values [7, 9], for Bi-Sn at both temperatures are plotted in Figure 8.1 and Figure 8.2. The small Er_i values in Table 8.2 and the plots presented in Figure 8.1 and Figure 8.2 show that the interaction parameters for both temperatures give good fits. Hence, the interaction parameters, listed in Table 8.2, will be used in further thermodynamic studies in this work.

Table 8.2: Interaction parameters for each binary system and their corresponding mean absolute percentage error.

| System | μ | ν | $\frac{g}{RT}$ | $\frac{V_{12}}{RT}$ | $\frac{V_{13}}{RT}$ | $\frac{V_{23}}{RT}$ | Er_i (%) | |
|----------------|-------|-------|----------------|---------------------|---------------------|---------------------|------------|---------|
| | | | | | | | G_M | $a_i s$ |
| Bi-Sn at 600 K | 1 | 1 | -1.8 | 0.5 | -0.2 | 0.3 | 0.19 | 0.25 |
| Bi-Sn at 900 K | 1 | 1 | -1.8 | 0.5 | -0.2 | 0.2 | 0.83 | 1.23 |

**Figure 8.1:** G_M in Bi-Sn at 600 and 900 K.**Figure 8.2:** Activities of all components in Bi-Sn at 600 and 900 K.

8.2.2.1 Enthalpy and entropy of mixing

To study the enthalpy and entropy of mixing within the quasi-lattice theory, the knowledge of the partial differentials of the interaction parameters with respect to temperature is required. The enthalpy of mixing, H_M , can be defined from thermodynamic relations [26, 30] as given in Eq. (8.24). Differentiating G_M , Eq. (8.14), which contains the temperature-dependent g , v_{ij} s and \hat{Z} , and substituting in Eq. (8.24) gives Eq. (8.25).

$$H_M = G_M - T \left(\frac{\partial G_M}{\partial T} \right)_p \quad (8.24)$$

$$H_M = -n_3 \left(g - T \frac{\partial g}{\partial T} \right) + \frac{1}{2} \frac{\partial \hat{Z}}{\partial T} RT^2 \left(n_3 (\mu + \nu) \ln \frac{\mu + \nu}{\mu + \nu - \zeta} + N \ln \frac{N}{N} \right) \\ + \frac{1}{N} \sum_{i < j}^3 n_i n_j \left(v_{ij} - T \frac{\partial v_{ij}}{\partial T} \right) + T \frac{\partial \hat{Z}}{\partial T} \frac{n_3 \zeta}{N^2 \hat{Z}} \sum_{i < j}^3 n_i n_j v_{ij} \quad (8.25)$$

$$S_M = \frac{H_M - G_M}{T} \quad (8.26)$$

$$S_M = n_3 \frac{\partial g}{\partial T} - R \left(n_1 \ln \frac{n_1}{N} + n_2 \ln \frac{n_2}{N} + n_3 \ln \frac{(\mu + \nu)n_3}{N} \right) \\ - \frac{1}{2} \hat{Z} n_3 (\mu + \nu - \zeta) \ln \frac{\mu + \nu}{\mu + \nu - \zeta} - \frac{1}{2} \hat{Z} N \ln \frac{N}{N} \\ + \frac{1}{2} \frac{\partial \hat{Z}}{\partial T} RT \left(n_3 (\mu + \nu) \ln \frac{\mu + \nu}{\mu + \nu - \zeta} + N \ln \frac{N}{N} \right) \\ - \frac{1}{N} \sum_{i < j}^3 n_i n_j \frac{\partial v_{ij}}{\partial T} + \frac{\partial \hat{Z}}{\partial T} \frac{n_3 \zeta}{N^2 \hat{Z}} \sum_{i < j}^3 n_i n_j v_{ij} \quad (8.27)$$

$$\frac{\partial \hat{Z}}{\partial T} = -Z_{Bi} C_{Bi} \left(\frac{\Delta H_{mBi}}{Z_c RT^2} + \frac{1}{T - T_{mBi} + 1} \right) - Z_{Sn} C_{Sn} \left(\frac{\Delta H_{mSn}}{Z_c RT^2} + \frac{1}{T - T_{mSn} + 1} \right) \quad (8.28)$$

The entropy of mixing, S_M , is defined in Eq. (8.26) [26, 30]. The expression for S_M is simplified and given in Eq. (8.27). Eq. (8.27) is obtained by substituting Eqs. (8.14) and (8.25) and for G_M and H_M , respectively, in Eq. (8.26). The partial differential of the average coordination number with respect to system temperature ($\partial \hat{Z} / \partial T$) in Eqs. (8.24) and (8.27) and is defined in Eq. (8.28). The $\partial \hat{Z} / \partial T$ in Eq. (8.28) is based on the model of Tao [20], which is used in this work to compute coordination numbers of pure liquid metals. Since the interaction parameters are temperature dependent, the partial differentials: $\partial g / \partial T$, $\partial v_{12} / \partial T$, $\partial v_{13} / \partial T$ and $\partial v_{23} / \partial T$, were fitted to conform with experimental H_M and S_M for Bi-Sn at 600 K. Excess entropy of mixing (S_M^{XS}) was estimated from real and ideal entropies of mixing, using thermodynamic relations given in Eq. (8.29) [26, 30].

$$S_M^{xs} = S_M + NR \sum c_i \ln c_i \quad (8.29)$$

8.2.2.2 Concentration-concentration fluctuations in the long-wavelength limit and Warren-Cowley short-range-order parameter

Concentration-concentration fluctuations in the long-wavelength limit ($S_{cc}(0)$) is a microscopic function that is useful in the study of the nature of atomic order. It provides information that determines the phase-separating or compound-forming nature of alloys. The $S_{cc}(0)$ is related to G_M and thermodynamic activities, as defined in Eq. (8.30). The measured $S_{cc}(0)$ values are compared with their ideal values ($S_{cc}^{id}(0)$) (Eq. (8.31)) at specified compositions to make useful deductions [27, 31]. When $S_{cc}(0) < S_{cc}^{id}(0)$ for a certain composition, it implies a tendency for heterocoordination, while $S_{cc}(0) > S_{cc}^{id}(0)$ implies a tendency for homocoordination [27, 31].

$$S_{cc}(0) = RT \left/ \left(\frac{\partial^2 G_M}{\partial c_{Bi}^2} \right)_{T,P,N} \right. = c_{Sn} a_{Bi} \left/ \left(\frac{\partial a_{Bi}}{\partial c_{Bi}} \right)_{T,P,N} \right. = c_{Bi} a_{Sn} \left/ \left(\frac{\partial a_{Sn}}{\partial c_{Sn}} \right)_{T,P,N} \right. \quad (8.30)$$

$$S_{cc}^{id}(0) = c_{Bi} c_{Sn} \quad (8.31)$$

The second-order differential in Eq. (8.30) can be solved numerically to obtain $S_{cc}(0)$.

The Warren-Cowley short-range-order parameter, α_1 , is used to determine the extent of order in the liquid alloy [32, 33]. The α_1 can be deduced from the knowledge of the concentration-concentration and number-number structure factors from diffraction experiments. However, experimental structure factors are not easily measured during diffraction. Furthermore, α_1 can be determined from the knowledge of $S_{cc}(0)$ and $S_{cc}^{id}(0)$ as defined in Eq. (8.35) [31–33]. When $\alpha_1 > 0$, it implies like-atom pairing as nearest neighbours, whereas $\alpha_1 < 0$ corresponds to unlike-atom pairing as nearest neighbours, while $\alpha_1 = 0$ denotes random distribution of atoms. The limiting values for α_1 when $c_{Bi} \leq 1/2$ and $c_{Bi} \geq 1/2$ are given in Eqs. (8.32) and (8.33), respectively. Eqs. (8.32) and (8.33) reduces to Eq. (8.34) when $c_{Bi} = c_{Sn} = 1/2$ [31].

$$-\frac{c_{Bi}}{c_{Sn}} \leq \alpha_1 \leq 1 \quad (8.32)$$

$$-\frac{c_{Sn}}{c_{Bi}} \leq \alpha_1 \leq 1 \quad (8.33)$$

$$-1 \leq \alpha_1 \leq +1 \quad (8.34)$$

When the value of α_1 is maximum (+1), it implies complete phase separation of components in the mixture, while its minimum value (−1) implies complete ordering of unlike-atoms as nearest neighbours. The relationship between α_1 , $S_{cc}(0)$ and $S_{cc}^{id}(0)$ are provided in Eq. (8.35) [31–33].

$$\alpha_1 = \frac{(Scc(0)/Scc^{id}(0)) - 1}{Scc(0)/Scc^{id}(0)(\widehat{Z} - 1) + 1} \quad (8.35)$$

The Average coordination number, \widehat{Z} , used in Eq. (8.35) was computed using Eq. (8.3).

8.2.3 Surface concentration and surface tension

A statistical mechanical approach to the modelling of surface properties, using the concept of a layered structure near the interface is known to be useful in binary alloys [27, 34]. The grand partition functions setup for the surface layer and the bulk provides a relation between surface and bulk compositions, given in Eq. (8.36) [35]. In Eq. (8.36), σ is the surface tension of the mixture, c_i^s , σ_i , γ_i and γ_i^s , are the surface concentration, surface tension, bulk activity coefficient and surface activity coefficient of component i at temperature T , respectively, A_0 is the mean surface area of the mixture (defined in Eq. (8.37)), N_0 is Avogadro's number and k_B is Boltzmann's constant. The surface activity coefficient, γ_i^s , is defined in Eq. (8.38), where $\gamma_i(c_i^s)$ implies the use of c_i^s in place of c_i in the computation of activity coefficient. Similar to bulk properties (where $a_i = c_i \times \gamma_i$), surface activity (a_i^s) is a product of c_i^s and γ_i^s .

Equation is solved numerically to obtain surface concentration and surface tension for Bi-Sn at 600 and 900 K.

$$\sigma = \sigma_{Bi} + \frac{k_B T}{A_0} \ln \frac{c_{Bi}^s}{c_{Bi}} + \frac{k_B T}{A_0} \ln \frac{\gamma_{Bi}^s}{\gamma_{Bi}} = \sigma_{Sn} + \frac{k_B T}{A_0} \ln \frac{c_{Sn}^s}{c_{Sn}} + \frac{k_B T}{A_0} \ln \frac{\gamma_{Sn}^s}{\gamma_{Sn}} \quad (8.36)$$

$$A_0 = 1.102 N_0^{-2/3} [c_{Bi} V_{mBi}^{2/3} + c_{Sn} V_{mSn}^{2/3}] \quad (8.37)$$

$$\ln \gamma_i^s = p \ln \gamma_i \left(\frac{c_i^s}{c_i} \right) + q \ln \gamma_i \quad (8.38)$$

In Eq. (8.38), p and q are surface coordination functions such that $p + 2q = 1$ (p and q are 1/2 and 1/4, respectively, for closed packed structures). Where p and q can be defined as fractions of the total number of nearest neighbours made by an atom within the layer in which it lies and that in the adjoining layer, respectively.

Table 8.3 gives the surface tension for pure Bi and Sn at 600 and 900 K, and these values are applied in the solution of Eq. (8.36).

Table 8.3: Surface tension for pure components.

| Metal | σ_i^a (N m ⁻¹) | |
|-------|-----------------------------------|--------|
| | 600 K | 900 K |
| Bi | 0.3741 | 0.3531 |
| Sn | 0.5515 | 0.5245 |

^aObtained from [25].

8.3 Results and discussion

Based on the theoretical formalism described in Section 8.2, it is important to note that the fitted interaction parameters will remain unchanged in the calculations of enthalpy and entropy of formation for Bi-Sn at 600 K; concentration fluctuations, Warren-Cowley short-range-order parameter, surface concentrations and surface tension at 600 and 900 K. The fitted parameters will form the basis for understanding the energetics of the alloys.

8.3.1 Enthalpy and entropy of mixing

The partial differentials of interaction parameters for Bi-Sn at 600 K were fitted while retaining the interaction parameters presented in Table 8.2. Satisfactory partial differentials, presented in Table 8.4, give good predictions of enthalpy and entropy mixing (H_M and S_M) [9]. Parameter g in Table 8.2 agrees with $\partial g/\partial T$ (Table 8.4), in the sense that the negative $\partial g/\partial T$ suggests decreased energy of formation of chemical complexes with temperature increase. The positive $\partial v_i/s/\partial T$ values can be interpreted as increasing repulsion between pseudo-ternary species as system temperature increases. Conversely, negative $\partial v_i/s/\partial T$ values can be interpreted as decreasing repulsion between pseudo-ternary species as system temperature increases. The agreements between the theoretical fitting and experimentally observed values of H_M and S_M were quantified by estimating Er_i (Eq. (8.23)). Excess entropy of mixing (S_M^{xs}) was estimated by applying Eqs. (8.27) and (8.29).

Furthermore, H_M/RT and S_M^{xs}/R for all concentration range were estimated and the results are graphically represented with plots in Figure 8.3. The Er_i values, presented in Table 8.4, and the H_M/RT and S_M^{xs}/R plots in Figure 8.3 show good agreements between the fitted theoretical values and experiments [9].

The H_M/RT plot in Figure 8.3 shows that Bi-Sn at 600 K is symmetric about the equiatomic composition and exhibits positive deviation from Raoultian behaviour across all concentration range. Also, the S_M^{xs} plot in Figure 8.3 reveals negative values in all composition range and asymmetry around the equiatomic composition.

Table 8.4: Partial differentials of interaction parameters obtained from experimental data [9].

| System | $\frac{\partial g}{\partial T}$ | $\frac{\partial v_{12}}{\partial T}$ | $\frac{\partial v_{13}}{\partial T}$ | $\frac{\partial v_{23}}{\partial T}$ | Er_i (%) | |
|----------------|---------------------------------|--------------------------------------|--------------------------------------|--------------------------------------|------------|-------|
| | | | | | H_M | S_M |
| Bi-Sn at 600 K | -15.0 R | 2.6 R | -0.1 R | 5.2 R | 2.90 | 0.23 |

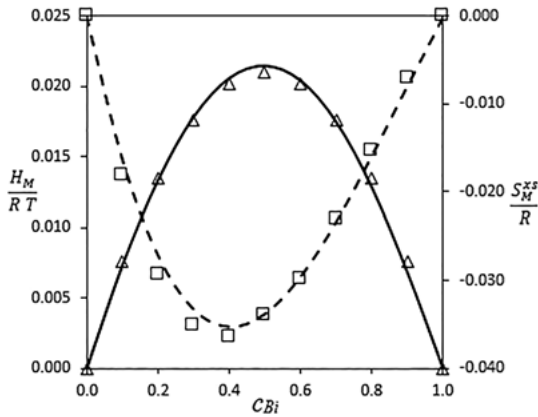


Figure 8.3: Concentration dependence of H_M/RT and S_M^{xs}/R at 600 K. Triangles represent H_M/RT obtained from experiments [9], squares represent S_M^{xs}/R obtained from experiments [9], solid line represents QLT-computed H_M/RT while dashed line represents QLT-computed S_M^{xs}/R .

8.3.2 Concentration-concentration fluctuations in the long-wavelength limit and Warren-Cowley short-range-order parameter

The $S_{cc}(0)$ for Bi-Sn at 600 and 900 K, were computed and the results were plotted and presented in Figure 8.4. The interpretation of the $S_{cc}(0)$ results depends on the corresponding ideal values at every composition. Figure 8.4 shows homocoordination tendency in the entire composition range of Bi-Sn at 600 and 900 K.

The α_1 for the Bi-Sn systems were computed and the results were plotted and presented in Figure 8.5. Figure 8.5 shows that $\alpha_1 > 1$ for all compositions and at both temperatures, which corroborates the $S_{cc}(0)$ results. The peak value of α_1 is about

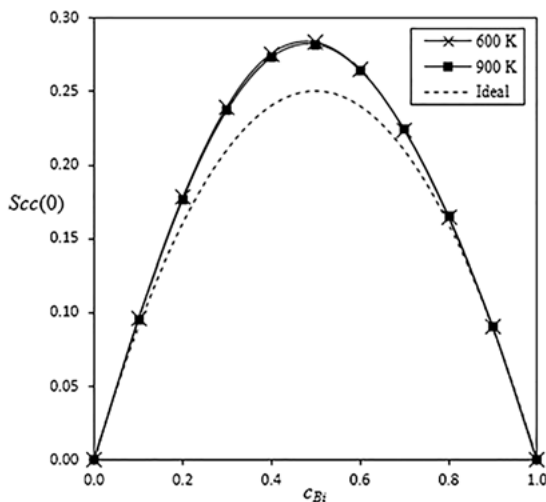


Figure 8.4: $S_{cc}(0)$ for Bi-Sn at 600 and 900 K.

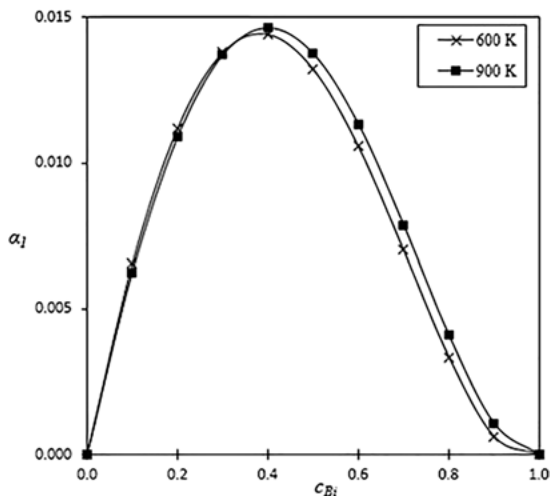


Figure 8.5: α_i for Bi-Sn at 600 and 900 K.

+0.015, this implies that a slight homocoordination property exists in the Bi-Sn systems, in other words, there is a slight preference for like-atoms as nearest neighbours. It can also be observed that, at about $c_{Bi} \geq 0.35$, segregation tendency increases with a rise in temperature, while the reverse is the case at about $c_{Bi} < 0.35$.

8.3.3 Surface concentration and surface tension

The surface concentrations of Bi and Sn, as well as the surface tension of the Bi-Sn system, were obtained simultaneously, as functions of bulk concentrations by solving Eq. (8.36), and the results are presented as plots in Figure 8.6 and Figure 8.7. The plots in Figure 8.6 show an expected trend, particularly, the surface concentration increases with an increase in bulk concentration for Bi and Sn at 600 and 900 K. Also, Figure 8.6 shows that the surface of the Bi-Sn system is enriched with Bi-atoms within 600 and 900 K, for example, when $c_{Bi} \approx 0.1$, $c_{Bi}^s \approx 0.4$ at 900 K and $c_{Bi}^s \approx 0.6$ at 600 K. The surface concentration of Bi decreases as temperature of Bi-Sn rises. Since $c_{Bi}^s + c_{Sn}^s = 1$, it can also be deduced that the surface concentration of Sn increases as temperature of Bi-Sn rises.

The computed surface tension of Bi-Sn at 600 and 900 K, presented in Figure 8.7, reduces as temperature rises. This surface tension plots have a concave-like shape which agrees with many studies on surface properties that the component with lower surface tension, that is, Bismuth, has the greatest surface enrichment.

Experimental surface tension data of Bi-Sn at 600 K [10–13] were also plotted in Figure 8.7, and they show similar trend with computed data. The computed and experimental data show satisfactory agreement, with the difference between the various data sets indicating an acceptable difference of less than 5.1%.

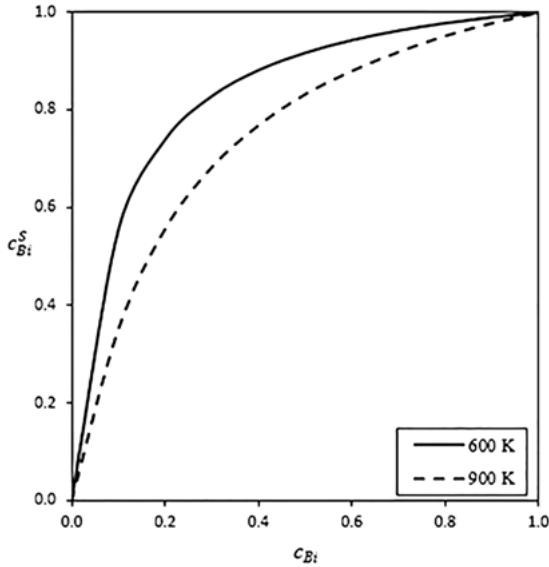


Figure 8.6: c_{Bi}^S versus c_{Bi} for Bi-Sn at 600 and 900 K.

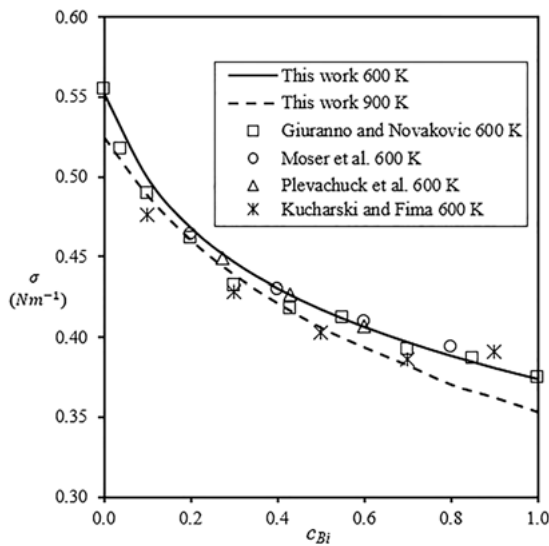


Figure 8.7: Concentration dependence of surface tension for Bi-Sn at 600 and 900 K. Solid and dashed lines represent QLT computation at 600 and 900 K, respectively. Experimental values at 600 K are represented by squares [10], circles [11], triangles [12] and stars [13].

8.4 Conclusions

The improved QLT [19], which applies nature, composition and temperature-dependent coordination numbers, has been successfully applied to model the thermodynamic properties of Bi-Sn at 600 and 900 K.

The fitted parameters were observed to reliably predict the Gibbs free energies of mixing and thermodynamic activities of alloy components. The same set of interaction parameters were used while fitting their temperature derivatives, to model the integral enthalpies and entropies of mixing of Bi-Sn at 600 K. The integral enthalpies of mixing exhibited positive deviation from Raoultian behaviour and is symmetric about the equiatomic composition, while the integral excess entropies of mixing is negative in all composition range and asymmetric about the equiatomic composition. The $S_{cc}(0)$ and α_1 computations for Bi-Sn at 600 and 900 K revealed slight segregation tendencies. Surface property studies reveal that Bi atoms segregate to the Bi-Sn surface, and the enrichment of Bi atoms at the surface reduces with temperature. The surface tension for Bi-Sn at 600 and 900 K was also predicted. The information provided in this work will help in the prediction of bulk and surface properties of Bi-Sn-based ternary and multi-component systems.

Author contribution: All the authors have accepted responsibility for the entire content of this submitted manuscript and approved submission.

Research funding: None declared.

Conflict of interest statement: The authors declare no conflicts of interest regarding this article.

References

1. Wang F, Chen H, Huang Y, Liu L, Zhang Z. Recent progress on the development of Sn–Bi based low-temperature Pb-free solders. *J Mater Sci Mater Electron* 2019;30:3222–43.
2. Abtew M, Selvaduray G. Lead-free solders in microelectronics. *Mater Sci Eng R Rep* 2000;27:95–141.
3. Awe OE, Oshakuade OM. Theoretical prediction of thermodynamic activities of liquid Au-Sn-X (X=Bi, Sb, Zn) solder systems. *Phys B Condens Matter* 2017;507:84–94.
4. Akinlade O, Sommer F. Concentration fluctuations and thermodynamic properties of ternary liquid alloys. *J Alloys Compd* 2001;316:226–35.
5. Tao DP. A new model of thermodynamics of liquid mixtures and its application to liquid alloys. *Thermochim Acta* 2000;363:105–13.
6. Asryan NA, Mikula A. Thermodynamic properties of Bi-Sn melts. *Inorg Mater* 2004;40:386–90.
7. Katayama I, Živković D, Manasijević D, Tanaka T, Živković Ž, Yamashita H. Thermodynamic properties of liquid Sn-Bi-Sb alloys. *Netsu Sokutei* 2005;32:40–4.
8. Awe OE, Oshakuade OM. Theoretical prediction of thermodynamic activities of all components in the Bi-Sb-Sn ternary lead-free solder system and Pb-Bi-Sb-Sn quaternary system. *Thermochim Acta* 2014;589:47–55.
9. Hultgren R, Desai PD, Hawkins DT, Geiser M, Kelley KK, editors. Selected values of the thermodynamic properties of binary alloys. Metals Park, OH: ASM; 1973.
10. Giuranno D, Novakovic R. Surface and transport properties of liquid Bi–Sn alloys. *J Mater Sci Mater Electron* 2020;31. <https://doi.org/10.1007/s10854-020-03118-y>.
11. Moser Z, Gasior W, Pstrus J. Surface tension measurements of the Bi-Sn and Sn-Bi-Ag liquid alloys. *J Electron Mater* 2001;30:1104–11.

12. Plevachuk Y, Sklyarchuk V, Gerbeth G, Eckert S. Thermophysical properties of liquid tin-bismuth alloys. *Int J Mater Res* 2010;101:839–44.
13. Kucharski M, Fima P. The surface tension and density of liquid Ag-Bi, Ag-Sn, and Bi-Sn alloys. *Monatsh Chem* 2005;136:1841–6.
14. Manasijević D, Minić D, Živković D, Katayama I, Vřešťál J, Petković D. Experimental investigation and thermodynamic calculation of the Bi-Ga-Sn phase equilibria. *J Phys Chem Solid* 2009;70:1267–73.
15. Katayama I, Tanaka T, Akai S, Yamazaki K, Iida T. Activity measurement of liquid Sn-Ag-Bi alloys by fused salt EMF method. *Mater Sci Forum* 2005;502:129–38.
16. Plevachuk Y, Sklyarchuk V, Gerbeth G, Eckert S, Novakovic R. Surface tension and density of liquid Bi-Pb, Bi-Sn and Bi-Pb-Sn eutectic alloys. *Surf Sci* 2011;605:1034–42.
17. Bhatia AB, Singh RN. A quasi-lattice theory for compound forming molten alloys. *Phys Chem Liq* 1984;13:177–90.
18. Bhatia AB, Hargrove WH. Concentration fluctuations and thermodynamic properties of some compound forming binary molten systems. *Phys Rev B* 1974;10:3186.
19. Oshakuade OM, Awe OE. Modification of the quasi-lattice theory for liquid alloys on the basis of varying the coordination number and its application to Al-Sn, Al-Zn and Sn-Zn. Submitted for publication. n.d. arXiv:2102.08516 [cond-mat.mtrl-sci].
20. Tao DP. Prediction of the coordination numbers of liquid metals. *Metall Mater Trans* 2005;36:3495–7.
21. Simon SH. *The Oxford solid state basics*. Oxford: Oxford University Press; 2013.
22. Wilson JR. The structure of liquid metals and alloys. *Metall Rev* 1965;10:381–590.
23. Cahoon JR. The first coordination number for liquid metals. *Can J Phys* 2004;82:291–301.
24. Saffarini G. Glass transition temperature and molar volume versus average coordination number in Ge_{100-x}Sx bulk glasses. *Appl Phys Solid Surface* 1994;59:385–8.
25. Iida T, Guthrie RIL. *The physical properties of liquid metals*. Oxford: Clarendon Press; 1988.
26. Ansermet J-P, Brechet SD. *Principles of thermodynamics*. Cambridge: Cambridge University Press; 2019.
27. Novakovic R, Giuranno D, Caccia M, Amore S, Nowak R, Sobczak N, et al. Thermodynamic, surface and structural properties of liquid Co-Si alloys. *J Mol Liq* 2016;221:346–53.
28. Khair U, Fahmi H, Al Hakim S, Rahim R. Forecasting error calculation with mean absolute deviation and mean absolute percentage error. In: *Proceedings of an international conference on information and communication technology (IconICT 2017) 25–26 August 2017, Medan, Indonesia*. Institute of Physics Publishing; 2017. <https://doi.org/10.1088/1742-6596/930/1/012002>.
29. Akinlade O, Singh RN. Bulk and surface properties of liquid In–Cu alloys. *J Alloys Compd* 2002;333:84–90.
30. Sekerka RF. *Thermal physics: thermodynamics and statistical mechanics for scientists and engineers*. Waltham: Elsevier; 2015.
31. Singh RN. Short-range order and concentration fluctuations in binary molten alloys. *Can J Phys* 1987;65:309–25.
32. Warren BE. *X-ray diffraction*. Reading: Addison-Wesley; 1969.
33. Cowley JM. An approximate theory of order in alloys. *Phys Rev* 1950;77:669–75.
34. Novakovic R, Delsante S, Lee J, Borzone G. Surface and transport properties of liquid Ag–Sn alloys and a case study of Ag–Sn eutectic solder. *J Mater Sci Mater Electron* 2018;29:17108–21.
35. Prasad LC, Singh RN, Singh GP. The role of size effects on surface properties. *Phys Chem Liq* 1994;273:179–85.

Kayode E. Adewole*, Ahmed A. Ishola and Blessing O. Omolaso

9 Identification of potential histone deacetylase inhibitory biflavonoids from *Garcinia kola* (Guttiferae) using *in silico* protein-ligand interaction

Abstract: Overactivity of histone deacetylases (HDACs) is the underlying cause of some cancers, thus, inhibiting their overactivities is a rational treatment option. However, endeavors to employ current anti-HDACs agents in cancer treatment have yielded limited success. Consequently, there is need to explore anti-HDACs natural products, especially from plants sources, because of the intimate relationship plant products and drug discovery have enjoyed over the centuries. To identify possible HDACs inhibitors, *Garcinia kola* (Guttiferae) seed-derived compounds were screened *in silico* for HDAC-inhibitory tendencies because of their reported anticancer potentials. Fifteen *G. kola*-derived compounds and givinostat were docked with five selected HDACs using AutodockVina, while the binding interactions of the compounds with high binding affinities for the five HDACs were viewed with Discovery Studio Visualizer BIOVIA, 2016. Results indicated that four of the compounds studied, including amentoflavone, *Garcinia* biflavonoid 1, *Garcinia* biflavonoid 2 and kolaflavanone have higher binding propensity for all the five HDACs relative to givinostat, the standard HDAC inhibitor. This study indicated that inhibition of HDAC might be another key mechanism accountable for the bioactivities of *G. kola* and its intrinsic compounds. The results from this study implied that the compounds could be further investigated as drugable HDAC inhibitors with potential pharmacological applications in the treatment of cancers.

Keywords: biflavonoids, cancer, *Garcinia kola*, histone deacetylase, kolaviron, molecular docking

9.1 Introduction

Aberrations in the activities of histone deacetylases (HDACs) have been linked with a range of negative health outcomes, including cancer which is currently a major leading cause of death globally [1, 2]. HDACs and histone acetyl-transferases

***Corresponding author: Kayode E. Adewole**, Department of Biochemistry, Faculty of Basic Medical Sciences, University of Medical Sciences, Ondo City, Ondo State, Nigeria,
E-mail: kayowolemi@gmail.com

Ahmed A. Ishola, Central Research Laboratories Limited, University Road, Ilorin, Kwara State, Nigeria
Blessing O. Omolaso, Department of Physiology, Faculty of Basic Medical Sciences, University of Medical Sciences, Ondo City, Ondo State, Nigeria

This article has previously been published in the journal *Physical Sciences Reviews*. Please cite as: K. E. Adewole, A. A. Ishola and B. O. Omolaso "Identification of potential histone deacetylase inhibitory biflavonoids from *Garcinia kola* (Guttiferae) using *in silico* protein-ligand interaction" *Physical Sciences Reviews* [Online] 2021, 5. DOI: 10.1515/psr-2020-0099 | <https://doi.org/10.1515/9783110739763-009>

regulate the acetylation of histones in post translational modifications that control chromatin packing and gene expression [3]. In addition to histone modification, HDACs also regulate some cellular activities, including the stability of non-histone proteins, protein-DNA interaction and protein-protein interactions [4, 5], thereby regulating cellular activities, examples of which include cell propagation, apoptosis, aging, cancer plus other disease conditions [3]. The 18 HDACs already characterized in human are grouped into four classes; class I which include HDACs 1, 2, 3 and 8; class II which include HDACs 4, 5, 6, 7, 9 and 10; class III, which are referred to as sirtuins (SIRT) include SIRTs 1, 2, 3, 4, 5, 6 and 7; and class IV which include HDAC 11 [6, 7]. Overexpression of HDAC1 has been reported in lung [8], breast [9] and colon cancers [10], while overexpression of HDAC2 is seen in colon [11], gastric [12] and cervical cancers [13]. Elevation of HDAC3 has been reported in prostate cancer [14], HDAC8 in neuroblastoma [15], HDAC7 in lung cancer [16], pancreatic adenocarcinoma [17] and salivary mucoepidermoid carcinoma [18]. Thus, HDAC inhibitors are now seen as important options in the treatment of cancers, including nature-derived agents, such as phytochemicals because of the intimate relationship natural products have enjoyed with drug discovery over the centuries, coupled with concerns over the toxicity of approved synthetic anticancer HDAC inhibitors [19–21].

Garcinia kola (Guttiferae) seed has enjoyed great patronage in Central and West Africa, where it is cherished and consumed as a snack and for medicinal purposes [22, 23]. Various bioactive compounds have been isolated from this seed, including kolaviron, a combination of *Garcinia* biflavonoid 1 (GB1), *Garcinia* biflavonoid 2 (GB2), and kolaflavanone [24], garcinoic acid [25], 9,19-cyclolanost-24-en-3-ol, 9,19-cyclolanostan-3-ol, lanosterol [26], lupeol [27], kolanone [28], hexadecanoic acid, linoleic acid, 9-octadecenoic acid, 2,3-Dihydro-3,5-dihydroxy-6-methyl ester, 9-Octadecenamamide [29], amentoflavone, 24-methylenecyclartenol, cycloartenol [30], δ -tocotrienol, gacinianin and garcinal [31, 32].

Some of the pharmacological activities that have been credited to *G. kola* seed-derived extracts and compounds include antioxidative, antiinflammatory, antigenotoxic, hepatoprotective, neuroprotective and cardioprotective activities [33, 34]. Also, the modulatory effect of *G. kola* seed extracts on antiproliferative- and anticancer-related pathways are also well documented [35–38]; these include up-regulating antioxidant defense power [32, 39, 40], suppressing the expression of cyclooxygenase-2 (COX-2), inducible nitric oxide synthase (iNOS), inhibiting the activation of nuclear factor kappa B (NF- κ B), activator protein-1 (AP-1) [41], stress-inducible proteins clusterin, heat shock proteins, caspase-3 and caspase-9, p53, Bax and Bcl-2 in various experimental models [22, 40].

In spite of the battery of pharmacological activities attributed to *G. kola*-derived extracts and compounds, the HDAC-inhibitory activity of *G. kola*-derived compounds is unknown. This study was therefore aimed at investigating the HDAC-inhibitory potentials of *G. kola*-derived compounds via *in silico* docking methods.

9.2 Materials and methods

9.2.1 Ligand preparation

The Spatial Data File (SDF) structures of givinostat, the standard HDAC inhibitor, and fifteen *G. kola*-derived compounds, including 3- β -2,4-methylenecycloartan-3-ol, amentoflavone, cycloartenol, δ -tocotrienol, elaidamide, elaidic acid, garcinal, GB1, GB2, garcinoic acid, hexadecanoic acid, kolaflavanone, kolanone, lanosterol and lupeol were downloaded from <http://www.pubchem.ncbi.nlm.nih.gov> (the PubChem database). The compounds were changed to Protein Data Bank (PDB) format with Discovery Studio Visualizer, BIOVIA, 2016. Polar hydrogen charges of the Gasteiger-type were assigned while the nonpolar hydrogens were combined with the carbons, followed by setting the internal degrees of freedom and torsions. The ligands were then converted to the dockable PDB, Partial Charge and Atom Type (PDBQT) format using Autodock tools.

9.2.2 Protein preparation

The structures of the selected proteins (HDAC1, 2, 3, 7 and 8) with PDB IDs of 4BKX, 4LY1, 4A69, 3C10 and 5FCW, respectively, were obtained from <http://www.rcsb.org>. The crystal structures were prepared one by one by deleting the attached water and ligands molecules, and the missing hydrogen atoms added with the aid of Scripps Research Institute's Autodock v4.2. Subsequently, nonpolar hydrogens were combined as polar hydrogen where added to each enzyme. The proteins were thereafter saved as PDBQT format to be used for molecular docking.

9.2.3 Molecular docking

Docking of compounds with selected HDACs was achieved by using AutodockVina [42]. The PDBQT format of each proteins and compounds were dropped in the appropriate columns, followed by running of the software. A cluster examination, dependent on root mean square deviation figures relative to the starting geometry was then carried out and the smallest energy conformation of the more populated cluster was taken to be the most dependable option. The binding propensities of the compounds for the selected HDACs were recorded and graded by their energy values. To compare the docking scores, the molecular associations of the compounds and HDACs, the binding energy ranked higher than that of givinostat were analyzed using Discovery Studio Visualizer, BIOVIA, 2016 to get the details of the residues contributing significantly toward their stability at the various binding sites.

9.3 Results

The binding affinities of *G. kola*-derived compounds for the selected HDACs are shown in Table 9.1. From the result obtained, four compounds have notably higher binding affinity for the five selected HDACs relative to givinostat. Givinostat formed three hydrogen bonds with HDAC1 via Asp306, Asp209 and Gln26 in addition to hydrophobic interaction i.e. π -alkyl interaction with Pro29 and π - π stacking with

His28 and Phe150. GB2 has the most negative binding affinity for HDAC1 and 2, -12.3 and -13.3 kcal/mol, respectively, compared to the respective values of -9.8 and -10.5 kcal/mol for givinostat. Amentoflavone and GB1 recorded the highest binding affinity (-12 kcal/mol) for HDAC3 compared to -10.4 kcal/mol of givinostat (Table 9.1), while GB2 has the highest binding affinity for HDAC7, i.e. -13.8 kcal/mol compared to -10.4 kcal/mol recorded for givinostat (Table 9.1). The duo of amentoflavone and GB2 have equal binding affinity of -12.9 kcal/mol for HDAC8, outscoring the -10.5 kcal/mol recorded for givinostat.

From the molecular binding interaction profiles, results showed that amentoflavone exhibited π -cation interaction with Arg36 and Asp256 in the HDAC1 binding site, in addition to two π -alkyl interaction with Ile249 and Val198 (Figure 9.1a). Similar to amentoflavone, GB1 has a π -cation interaction with Arg36, with extra hydrogen bond formation with His39 and Glu325 (Figure 9.1b). Also, π -alkyl interactions were observed between amentoflavone and Arg55, and Ile249 of HDAC1. A combination of hydrogen bonds with Tyr15, Asn40, Ile249, π -alkyl interactions with Arg55, Val198, π - π stacking with Try15, Phe252 and a single donor-donor interaction with Lys260 were observed in the binding interaction of GB1 with HDAC1 (Figure 9.1c). GB2 was seen to interact with Asn40, Asp332 and Lys260 via hydrogen bonds, Ile249 via π -sigma bond, Arg36 via π -cation interaction and Phe252 via π - π stacking (Figure 9.1d).

Table 9.1: Binding affinity of *Garcinia kola*-derived compounds to HDAC1, HDAC2, HDAC3, HDAC7 and HDAC8.

| S/N | Compounds | Binding affinity (kcal/mol) | | | | |
|-----|------------------------------------|-----------------------------|--------------|--------------|--------------|--------------|
| | | HDAC1 | HDAC2 | HDAC3 | HDAC7 | HDAC8 |
| 5 | Givinostat | -9.8 | -10.5 | -10.4 | -10.4 | -10.5 |
| 1 | 3beta 2,4-methylenecycloartan 3-ol | -8.6 | -9.7 | -9.5 | -9.9 | -11.4 |
| 2 | Amentoflavone | -10.6 | -12.8 | -12.0 | -13.7 | -12.9 |
| 3 | Cycloartenol | -8.4 | -8.7 | -9.4 | -9.5 | -11.5 |
| 4 | δ -tocotrienol | -8.6 | -9.2 | -10.0 | -9.3 | -11.1 |
| 5 | Elaidamide | -6.4 | -7.2 | -7.9 | -7.7 | -8.3 |
| 6 | Elaidic acid | -7.2 | -7.4 | -8.2 | -6.6 | -8.3 |
| 7 | Garcinal | -8.7 | -9.5 | -9.4 | -9.8 | -11.2 |
| 8 | Garcinia biflavonoid 1 | -11.5 | -12.4 | -12.0 | -13.5 | -12.8 |
| 9 | Garcinia biflavonoid 2 | -12.3 | -13.3 | -11.2 | -13.8 | -12.9 |
| 10 | Garcinoic acid | -8.9 | -9.4 | -10.3 | -9.8 | -11.3 |
| 11 | Hexadecanoic acid | -7.1 | -6.1 | -7.4 | -6.1 | -7.8 |
| 12 | Kolaflavanone | -11.7 | -13.5 | -11.2 | -13.6 | -12.8 |
| 13 | Kolanone | -9.6 | -10.1 | -9.9 | -11.4 | -11.7 |
| 14 | Lanosterol | -8.5 | -9.1 | -11.1 | -10.1 | -11.7 |
| 15 | Lupeol | -8.8 | -8.5 | -9.0 | -9.8 | -11.1 |

For HDAC2 and givinostat, a combination of hydrogen bonds with Glu151, Lys252, Lys268, π -alkyl interactions with Pro248, Ala221 and π - π stacking with Phe372 were observed in the binding interactions. The binding of amentoflavone to HDAC2 revealed a total of five hydrogen bonds with Lys148, Glu151, Lys252 and Ser153, π -anion interactions with Glu190 and Asp218 and an π -sigma interaction with Thr213 (Figure 9.2a). GB1 had a donor-donor interaction with Lys148 and Gly220 in addition to hydrogen bond formation with Thr193, Arg217 and Ser251 of HDAC2 (Figure 9.2b). Some similarities

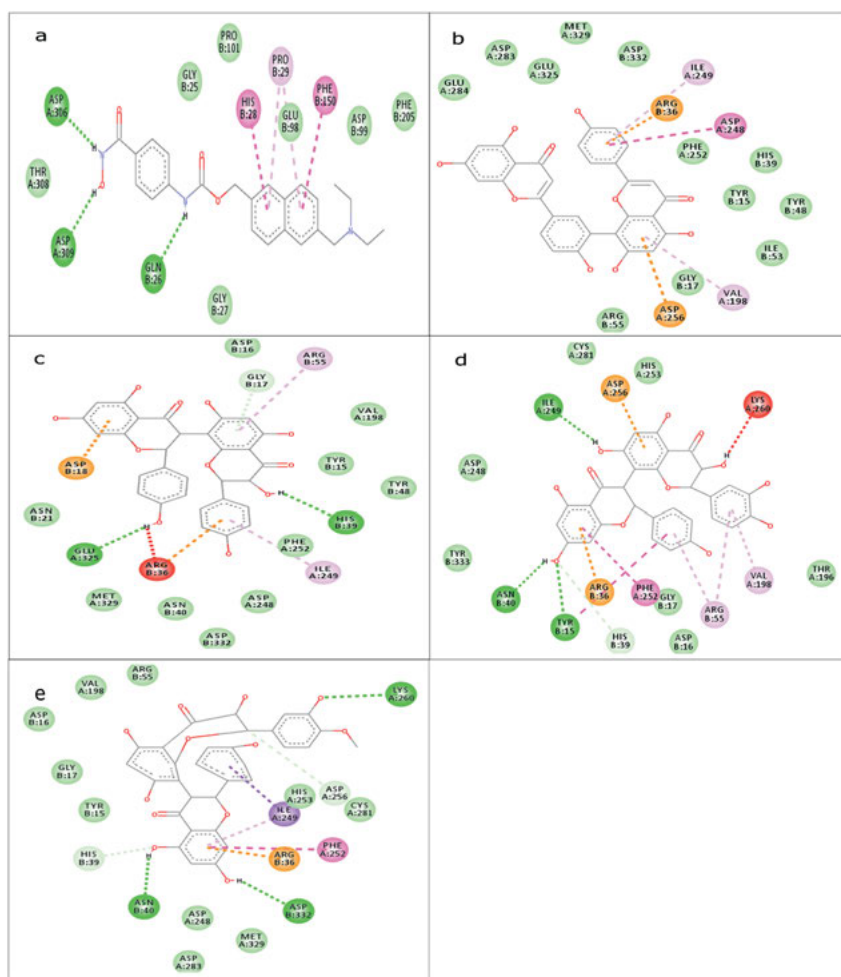


Figure 9.1: Interaction between amino acids in the binding site of HDAC1 and (a) Givinostat, (b) Amentoflavone, (c) Garcinia biflavonoid 1, (d) Garcinia biflavonoid 2, (e) Kolaflavanone. Green dotted line: hydrogen bond, purple dotted line: π -sigma bond, orange dotted line: π -cation/anion bond, pink dotted line: π - π stacking, faint pink dotted line: π -alkyl bond, red dotted line: donor-donor interaction, cyan dotted line: carbon-hydrogen bond.

were observed in the binding profiles of GB1, GB2 and kolaflavanone with identical interactions with Lys247 (π - π stacking), Thr193 (hydrogen bond), Pro248 (π -alkyl bond) (Figure 9.2c and 9.2d).

Electrostatic force of attraction (π -cation/ π -anion) was visible between Glu156 and Lys474 of HDAC3 and givinostat in addition to a single π - π stacking with Phe444, π -alkyl interaction with Lys159 and Arg441. Molecular interactions between HDAC3 and the compounds revealed different binding patterns with amino acids in the

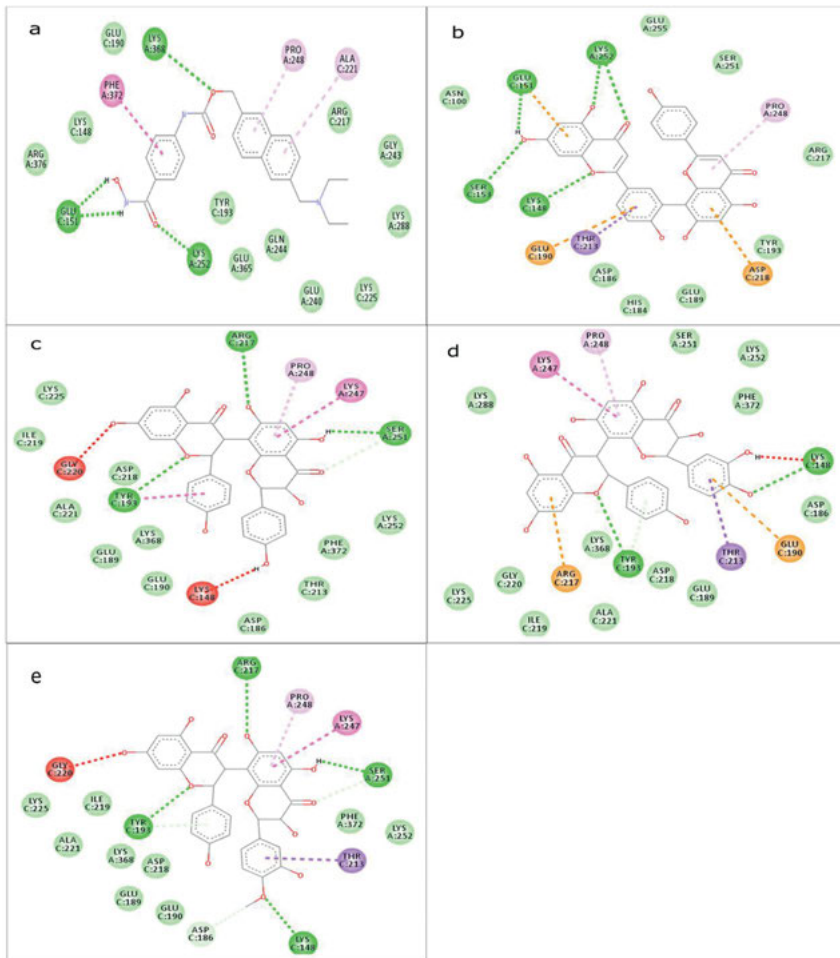


Figure 9.2: Interaction between amino acids in the binding site of HDAC2 and (a) Givinostat, (b) Amentoflavone, (c) Garcinia biflavonoid 1, (d) Garcinia biflavonoid 2, (e) Kolaflavanone. Green dotted line: hydrogen bond, purple dotted line: π -sigma bond, orange dotted line: π -cation/anion bond, pink dotted line: π - π stacking, faint pink dotted line: π -alkyl bond, red dotted line: donor-donor interaction, cyan dotted line: carbon-hydrogen bond.

binding sites of the enzyme. Amentoflavone exhibited hydrophobic interaction in the form of π -anion bond with Arg224 and Glu465 as well as π - π stacking and π -alkyl interaction with Tyr354 and Met429, respectively (Figure 9.3a). A total of six hydrogen bonds were formed between GB1 and Tyr195, Asn197, Tyr354, Gln357 and Met431 of HDAC3 (Figure 9.3b). GB2 and kolaf flavanone have similar binding pattern with HDAC3 which include hydrogen bond formation with Thr4, Tyr18, Asp92, Asn450, carbon-hydrogen bond with Gly19 and hydrophobic interaction (π -alkyl bond) with Pro95 and Ile122 (Figure 9.3c and 9.3d).

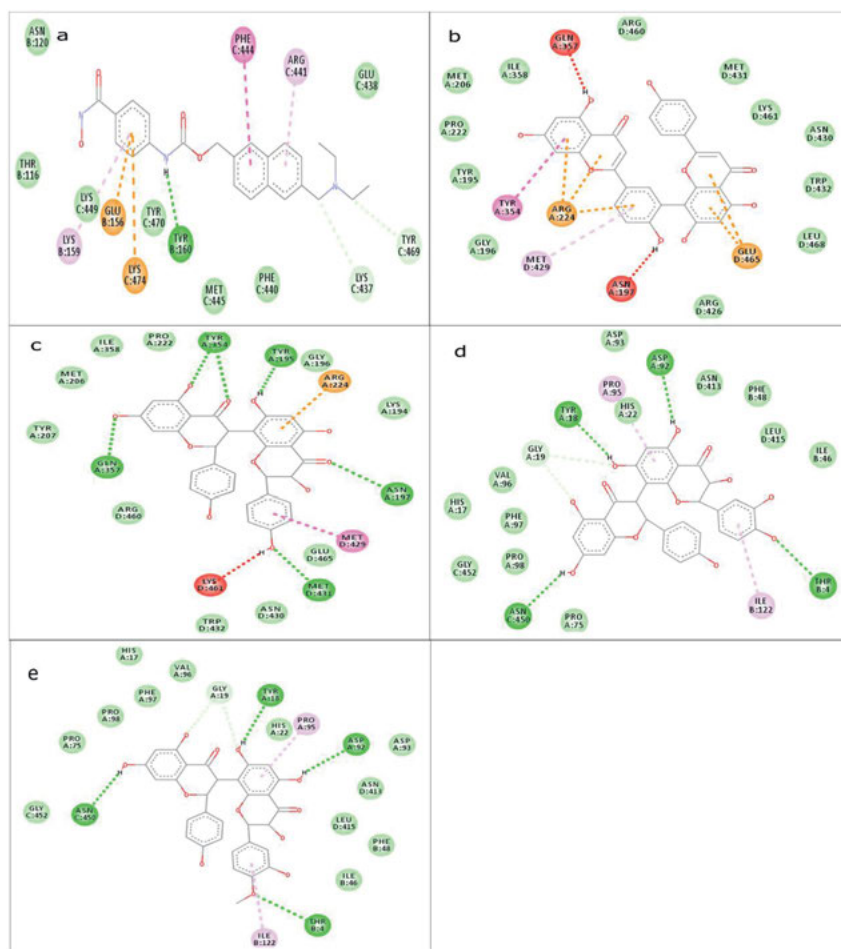


Figure 9.3: Interaction between amino acids in the binding site of HDAC3 and (a) Givinstat, (b) Amentoflavone, (c) Garcinia biflavonoid 1, (d) Garcinia biflavonoid 2, (e) Kolaf flavanone. Green dotted line: hydrogen bond, purple dotted line: π -sigma bond, orange dotted line: π -cation/anion bond, pink dotted line: π - π stacking, faint pink dotted line: π -alkyl bond, red dotted line: donor-donor interaction, cyan dotted line: carbon-hydrogen bond.

Givinostat exhibited π -sigma interactions with Leu588 and Leu604 of HDAC7 together with π -alkyl interactions with Pro593, Leu607 and Leu608, carbon-hydrogen bonds with Leu607 and Trp629. Hydrophobic interaction consisting of mainly π -sigma bond with Arg655, π - π stacking with Phe518, Trp552, π -alkyl interactions with Arg568 and Arg655 were identified in the binding profile of amentoflavone with HDAC7 (Figure 9.4a). Hydrophobic interaction played a prominent role in the binding of GB1 with HDAC7, forming π - π stacking with Phe518, with π -cation interaction with Arg561

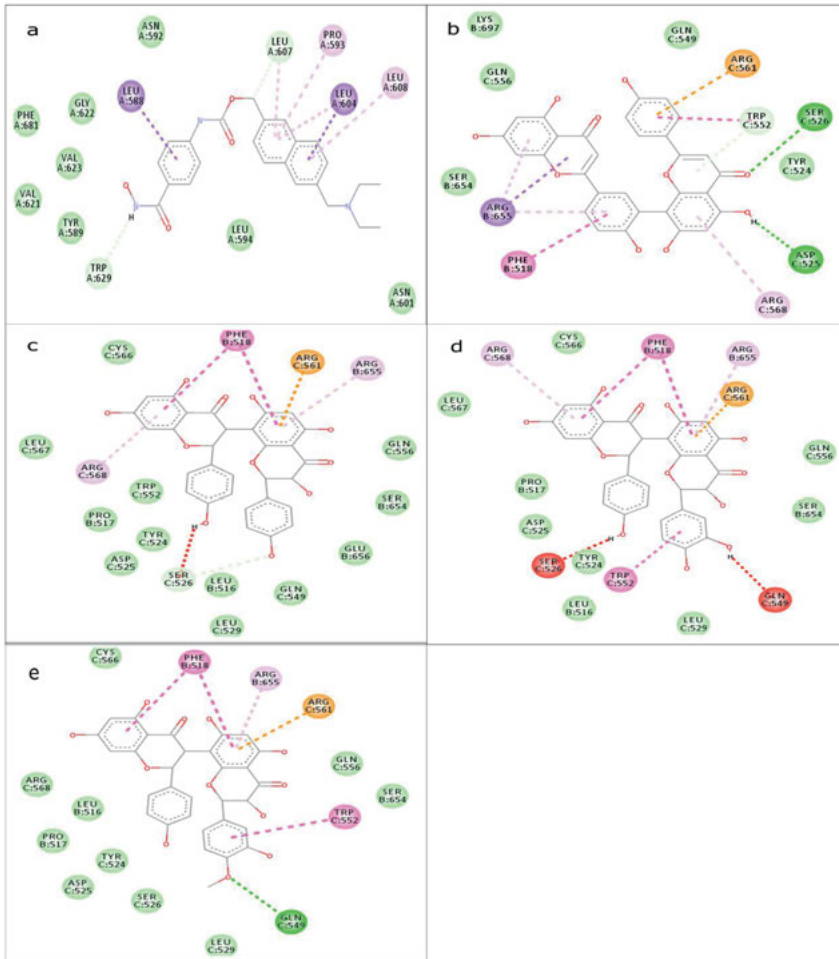


Figure 9.4: Interaction between amino acids in the binding site of HDAC7 and (a) Givinostat, (b) Amentoflavone, (c) Garcinia biflavonoid 1, (d) Garcinia biflavonoid 2, (e) Kolaflavanone. Green dotted line: hydrogen bond, purple dotted line: π -sigma bond, orange dotted line: π -cation/anion bond, pink dotted line: π - π stacking, faint pink dotted line: π -alkyl bond, red dotted line: donor-donor interaction, cyan dotted line: carbon-hydrogen bond.

and π -alkyl interactions Arg568 and Arg655 (Figure 9.4b). As observed for HDAC3, similarities were seen in the binding profile of GB2 and kolaflavanone where π - π stacking with Phe518 and Trp552 adds to π -anion interaction with Arg561 and π -alkyl interaction with Arg655. However, the distinguishing feature in the interaction of the two compounds is the donor-donor interactions with Gln549 and Ser526 recorded by GB2 (Figure 9.4c) and the hydrogen bond formation seen between kolaflavanone and HDAC7 (Figure 9.4d).

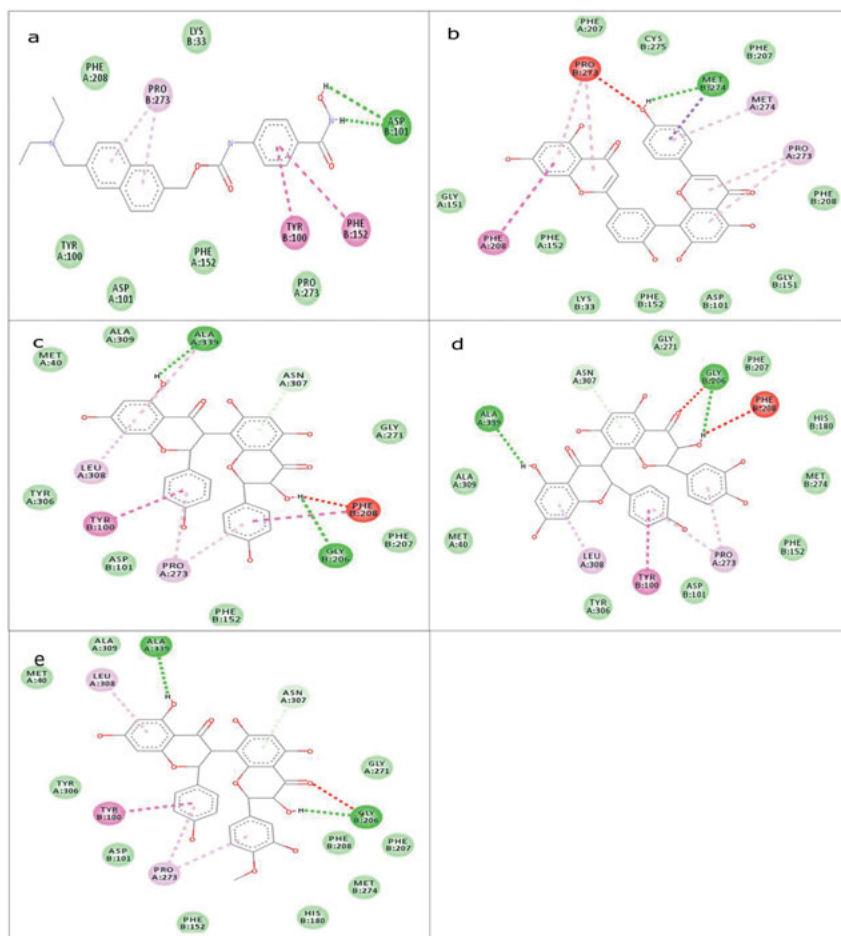


Figure 9.5: Interaction between amino acids in the binding site of HDAC8 and (a) Givinostat, (b) Amentoflavone, (c) Garcinia biflavonoid 1, (d) Garcinia biflavonoid 2, (e) Kolaflavanone. Green dotted line: hydrogen bond, purple dotted line: π -sigma bond, orange dotted line: π -cation/anion bond, pink dotted line: π - π stacking, faint pink dotted line: π -alkyl bond, red dotted line: donor-donor interaction, cyan dotted line: carbon-hydrogen bond.

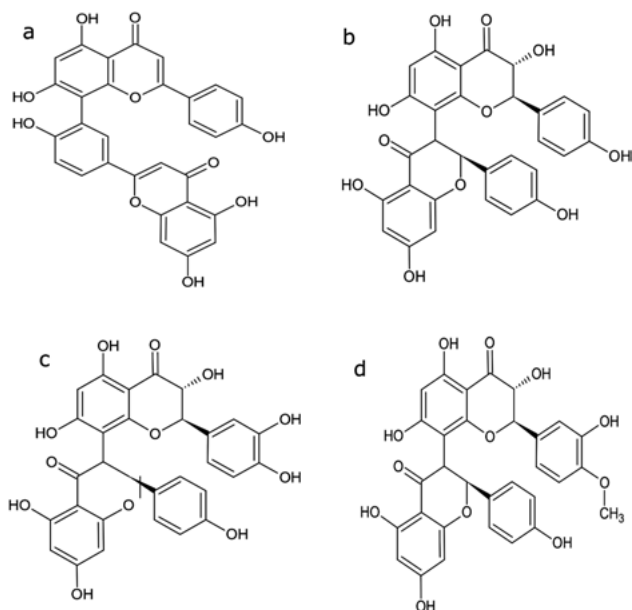


Figure 9.6: Structures of promising HDAC inhibitors identified from *Garcinia kola*; (a) amentoflavone, (b) Garcinia biflavonoid 1, (c) Garcinia biflavonoid 2, (d) kolaflavanone.

Hydrogen bond formation between an amine and hydroxyl group in the side chain of givinostat and HDAC8 were seen, coupled with two π - π stacking with Tyr100 and Phe152 as well as an π -alkyl interaction with Pro273. Multiple bonds were observed between HDAC8 and amentoflavone, with hydrophobic interactions (π -alkyl bonds) with Pro273 and Met274 as well as π - π stacking with Phe208 (Figure 9.5a). The binding of GB1, GB2 and kolaflavanone to HDAC8 followed a similar pattern, in addition to hydrogen bond formations with Gly206 and Ala339, the three compounds formed π -alkyl bonds with Pro273 and Leu308 as well as a carbon-hydrogen bond with Asn307 in the HDAC8 binding site (Figure 9.5b, 9.5c, and 9.5d). The observed similarities between the compounds may be due to presence of the same ring systems in the compounds (Figure 9.6).

9.4 Discussion and conclusions

9.4.1 Discussion

Identification of targets and their inhibitors by computational studies is one of the strategies employed for resource optimization in drug development [43, 44]. To identify more promising and non-toxic HDACs inhibitors, 15 bioactive compounds identified

from *G. kola* were docked with HDAC1, HDAC2, HDAC3, HDAC7 and HDAC8. From the results obtained, four compounds, amentoflavone, GB1, GB2 and kolaflavanone, stood out as potential HDAC inhibitors. The higher negative binding affinities of these compounds relative to givinostat indicate that they might be better HDACs inhibitors compared to givinostat. Interestingly, three out of these compounds, GB1, GB2 and kolaflavanone, are the constituents of kolaviron, the biflavonoid complex from *G. kola* seed, reportedly the most active phytochemical from this plant product [22]. Several pharmacological activities have been attributed to this biflavonoid complex. The complex is also reported to have several pharmacokinetic advantages over simple monomeric flavonoids because of its ability to survive first-pass metabolism which inactivates most flavonoids [45]. The cellular mechanisms responsible for the chemopreventive ability of kolaviron include antioxidant and free radical scavenging activity, thus protecting DNA, lipids and proteins from oxidative damage [46]. Other mechanisms underlying the chemopreventive activities of kolaviron include inhibition of the expression of COX-2 and iNOS, abrogation of the DNA binding activity of NF- κ B and AP-1, induced by dimethyl nitrosamine [41]. From the results obtained in this study, inhibition of HDACs might be another important mechanism underlying the anticancer potential of this biflavonoid. The fourth notable compound, amentoflavone, which is also a well-known plant-derived biflavonoid [47] have also been credited with a battery of pharmacological activities, including antioxidant effect, via attenuation of, ROS, malondialdehyde and augmentation of the activity of antioxidant enzymes in experimentally induced oxidative stress conditions [48, 49]. Other bioactivities attributed to amentoflavone include antiinflammatory effect, via inhibition of tumor necrosis factor- α (TNF- α), suppression of the production of prostaglandin E-2, and the nuclear translocation of c-Fos, interleukin-1 β and IL-6 [47], antitumor effect, through caspase 3 activation, diminution of mitochondrial membrane potential, release of mitochondrial cytochrome c in breast cancer MCF-7 cells, inhibition of cell division and growth (progression from G0/G1 to S phase) and regulatory effect on genes controlling apoptosis and cell cycle, including Bax and caspase 9 [47, 50]. Other mechanisms underlying the anticancer activity of amentoflavone include inhibition of fatty acid synthase expression in human epidermal growth factor receptor 2 (HER2)-positive human breast carcinoma SKBR3 cells, upregulation of polyoma enhancer activator 3 (PEA3), which represses HER2 at the level of transcription to impede phosphorylation of protein kinase B (PKB), mechanistic target of rapamycin and c-Jun N-terminal kinases [51, 52]. However, despite the plethora of studies investigating the pharmacological activities of amentoflavone, to the knowledge of the authors, the HDAC-inhibitory effect of this compound has not been reported. Interestingly, with the high docking energy of this compound with the selected HDACs, it very likely that the compound is a potential HDAC inhibitor and qualifies for further studies.

9.4.2 Conclusions

Inhibition of HDAC is a critical strategy in the search for anticancer therapeutics. However, endeavors to employ current anti-HDACs agents in cancer treatment have yielded limited success, prompting the need to explore anti-HDACs natural products, especially from plants sources. The outcome of this *in silico* study indicated that four compounds from *G. kola* seed including amentoflavone, GB1, GB2, and kolaflavanone have high binding tendencies for the selected HDACs compared with givinostat, the standard HDAC inhibitor. These results indicated that four *G. kola*-derived compounds are potential inhibitors of the selected HDACs. However, further investigations using *in vitro* and *in vivo* studies are required to validate these compounds as inhibitors of the selected HDAC isoforms.

Author contribution: All the authors have accepted responsibility for the entire content of this submitted manuscript and approved submission.

Research funding: None declared.

Conflict of interest statement: The authors declare no conflicts of interest regarding this article.

References

1. Steven S, Frenis K, Oelze M, Kalinovic S, Kuntic M, Teresa M, et al. Vascular inflammation and oxidative stress: major triggers for cardiovascular disease. *Oxid Med Cell Longev* 2019;2019:1–26.
2. Singh A, Bishayee A, Pandey A. Targeting histone deacetylases with natural and synthetic agents: an emerging strategy. *Nutrients* 2018;10:731.
3. Yoon S, Eom GH. HDAC and HDAC inhibitor: from cancer to cardiovascular diseases. *Chonnam Med J* 2016;52:1–11.
4. Zhu C, Chen Q, Xie Z, Ai J, Tong L, Ding J, et al. The role of histone deacetylase 7 (HDAC7) in cancer cell proliferation: regulation on c-Myc. *J Mol Med* 2011;89:279–89.
5. Minucci S, Pelicci P. Histone deacetylase inhibitors and the promise of epigenetic (and more) treatments for cancer. *Nat Rev Canc* 2006;6:38–51.
6. Bagchi RA, Weeks KL. Histone deacetylases in cardiovascular and metabolic diseases. *J Mol Cell Cardiol* 2019;130:151–9.
7. Cavaşin MA, Stenmark KR, Mckinsey TA. Emerging roles for histone deacetylases in pulmonary hypertension and right ventricular remodeling (2013 Grover conference series). *Pulm Circ* 2015;5: 63–72.
8. Wang W, Liu Y, Zhao L. Tambulin targets histone deacetylase 1 inhibiting cell growth and inducing apoptosis in human lung squamous cell carcinoma. *Front Pharmacol* 2020;12:1188.
9. Sukocheva O, Lukina E, Friedemann M, Menschikowski M, Hagegans A, Aliev G. The crucial role of epigenetic regulation in breast cancer anti-estrogen resistance: current findings and future perspectives. *Semin Canc Biol* 2020 Dec 7. <https://doi.org/10.1016/j.semcancer.2020.12.004> [Epub ahead of print].

10. Sanaei M, Kavooosi F. Investigation of the effect of zebularine in comparison to and in combination with trichostatin A on p21Cip1/Waf1/Sdi1, p27Kip1, p57Kip2, DNA methyltransferases and histone deacetylases in colon cancer LS 180 cell line. *Asian Pac J Cancer Prev* 2020;12:1819–28.
11. Patel M, Patel B. Repurposing of sodium valproate in colon cancer associated with diabetes mellitus: role of HDAC inhibition. *Eur J Pharmaceut Sci* 2018;30:188–99.
12. Zhang L, Kang W, Lu X, Ma S, Dong L, Zou B. Weighted gene co-expression network analysis and connectivity map identifies lovastatin as a treatment option of gastric cancer by inhibiting HDAC2. *Gene* 2019;10:15–25.
13. Anantharaju P, Reddy D, Padukudru M, Chitturi C, Vimalambike MG, Madhunapantula S. Induction of colon and cervical cancer cell death by cinnamic acid derivatives is mediated through the inhibition of histone deacetylases (HDAC). *PLoS One* 2017;12:e0186208.
14. Beaver L, Löhr C, Clarke J, Glasser S, Watson G, Wong C, et al. Broccoli sprouts delay prostate cancer formation and decrease prostate cancer severity with a concurrent decrease in HDAC3 protein expression in transgenic adenocarcinoma of the mouse prostate (TRAMP) mice. *Curr Dev Nutr* 2017;2:nzy002.
15. Zhao G, Wang G, Bai H, Li T, Gong F, Yang H, et al. Targeted inhibition of HDAC8 increases the doxorubicin sensitivity of neuroblastoma cells via up regulation of miR-137. *Eur J Pharmacol* 2017; 5:20–6.
16. Lei Y, Liu L, Zhang S, Guo S, Li X, Wang J, et al. HDAC7 promotes lung tumorigenesis by inhibiting Stat3 activation. *Mol Canc* 2017;16:1–13.
17. Ouaisi M, Silvy F, Loncle C, DaSilva D, Abreu C, Martinez E, et al. Further characterization of HDAC and SIRT gene expression patterns in pancreatic cancer and their relation to disease outcome. *PLoS One* 2014;9:e108520.
18. Ahn M-Y, Yoon J-H. Histone deacetylase 7 silencing induces apoptosis and autophagy in salivary mucoepidermoid carcinoma cells. *J Oral Pathol Med* 2017;46:276–83.
19. Ishola A, Adewole K. Phytosterols and triterpenes from *Morinda lucida* Benth. exhibit binding tendency against class I HDAC and HDAC7 isoforms. *Mol Biol Rep* 2019;46:2307–25.
20. Ganai SA, Farooq Z, Bandy S, Altaf M. *In silico* approaches for investigating the binding propensity of apigenin and luteolin against class I HDAC isoforms. *Future Med Chem* 2018;10: 1925–45.
21. Negmeldina AT, Knoffa JR, Pflum MKH. The structural requirements of histone deacetylase inhibitors: C4-modified SAHA analogs display dual HDAC6/HDAC8 selectivity. *Eur J Med Chem* 2018;143:1790–806.
22. Oyagbemi AA, Bester D, Esterhuysen J, Farombi EO, Farombi EO, Metabolism D, et al. Kolaviron and *Garcinia kola* seed extract protect against ischaemia/reperfusion injury on isolated rat heart. *Drug Res* 2018;68:286–95.
23. Adedara IA, Awogbindin IO, Maduako IC, Ajeleti AO, Owumi SE, Owoeye O, et al. Kolaviron suppresses dysfunctional reproductive axis associated with multi-walled carbon nanotubes exposure in male rats. *Environ Sci Pollut Res* 2021;28:354–64.
24. Iwu M. Antihepatotoxic constituents of *Garcinia kola* seed. *Experientia* 1985;41:699–700.
25. Wallert M, Bauer J, Kluge S, Schmözl L, Chen Y, Ziegler M, et al. The vitamin E derivative garcinoic acid from *Garcinia kola* nut seeds attenuates the inflammatory response. *Redox Biol* 2019;24: 101166.
26. Penduka D, Buwa L, Mayekiso B, Basson AK, Okoh AI. Identification of the anti listerial constituents in partially purified column chromatography fractions of *Garcinia kola* seeds and their interactions with standard antibiotics. *Evid Base Compl Alternative Med* 2014;2014:1–9.
27. Amaechi NC, Okonkwo U. Identification of compounds in *Garcinia kola* (Heckel) fruit pulp using gas chromatography-mass spectrometry. *Arch Curr Res Int* 2017;10:1–11.

28. Hussain RA, Owegby AG, Parimoo P, Waterman PG. Kolanone, a novel polyisoprenylated benzophenone with antimicrobial properties from the fruit of *Garcinia kola*. *Planta Med* 1982;44: 78–81.
29. Seanego CT, Ndip RN. Identification and antibacterial evaluation of bioactive compounds from *Garcinia kola* (Heckel) seeds. *Molecules* 2012;17:6569–84.
30. Iwu MM, Diop A, Meserole L, Okunji C. *Garcinia kola*: a new look at an old adaptogenic agent. In: Wootton I, editor. *Ethnomedicine and drug discovery*. Europe: Elsevier Science B.V.; 2002:191–9 pp.
31. Terashima K, Shimamura T, Tanabayashi M, Aqiu M, Akinniji J, Niwa M. Constituents of the seeds of *Garcinia kola*: two new antioxidants, garcinoic acid and garcinal. *Heterocycles* 1997;45: 1559–66.
32. Okoko T. *In vitro* antioxidant and free radical scavenging activities of *Garcinia kola* seeds. *Food Chem Toxicol* 2009;47:2620–3.
33. Alabi QK, Akomolafe RO, Olukiran OS, Nafiu AO, Omole JG, Adefisayo AM, et al. Assessment of haematological and biochemical effects of kolaviron in male Wistar rats. *Br J Pharmaceut Res* 2017; 16:1–14.
34. Farombi E, Awogbindin I, Farombi T, Oladele J, Izomoh E, Aladelokun O, et al. Neuroprotective role of kolaviron in striatal redoinflammation associated with rotenone model of Parkinson's disease. *Neurotoxicology* 2019;73:132–41.
35. Oyagbemi A, Omobowale T, Adedapo A, Oyekan A, Yakubu M. Antiproliferative effect of kolaviron, a biflavonoid complex from the seed of *Garcinia kola* on vascular smooth muscle cells (VSMs) and A549 cancer cell line. *FASEB J* 2015;29(1 Suppl):945–17.
36. Onasanwo SA, Velagapudi R, El-Bakoush A, Olajide O. Inhibition of neuroinflammation in BV2 microglia by the biflavonoid kolaviron is dependent on the Nrf2/ARE antioxidant protective mechanism. *Mol Cell Biochem* 2016;414:23–36.
37. Oyagbemi AA, Omobowale TO, Adedapo AA, Yakubu MA. Kolaviron, biflavonoid complex from the seed of *Garcinia kola* attenuated angiotensin II- and lypopolysaccharide-induced vascular smooth muscle cell proliferation and nitric oxide production. *Pharmacogn Res* 2016;8(1 Suppl):S50.
38. Olaleye B, Onasanwo S, Ige A, Wu K, Cho C. Anti-inflammatory activities of a kolaviron-inhibition of nitric oxide, prostaglandin E2 and tumor necrosis factor-alpha production in activated macrophage-like cell line. *Afr J Med Med Sci* 2010;39(Suppl):41–6.
39. Farombi EO, Adedara IA, Ajayi BO, Ayepola OR, Egbeme EE. Kolaviron, a natural antioxidant and anti-inflammatory phytochemical prevents dextran sulphate sodium-induced colitis in rats. *Basic Clin Pharmacol Toxicol* 2013;113:49–55.
40. Omole JG, Ayoka OA, Alabi QK, Adefisayo MA, Asafa MA, Olubunmi BO, et al. Protective effect of kolaviron on cyclophosphamide-induced cardiac toxicity in rats. *J Evidence-Based Med* 2018;23: 1–11.
41. Farombi EO, Shrotriya S, Surh Y. Kolaviron inhibits dimethyl nitrosamine-induced liver injury by suppressing COX-2 and iNOS expression via NF- κ B and AP-1. *Life Sci* 2009;84:149–55.
42. Trott O, Olson AJ. AutoDock Vina: improving the speed and accuracy of docking with a new scoring function, efficient optimization, and multithreading. *J Comput Chem* 2010;31:455–61.
43. Adewole KE, Ishola AA. Phytosterols and triterpenes from *Morinda lucida* Benth (Rubiaceae) as potential inhibitors of anti-apoptotic BCL-XL, BCL-2, and MCL-1: an in-silico study. *J Recept Signal Transduct* 2019;39:87–97.
44. Tripathi H, Khan F. Identification of potential inhibitors against nuclear Dam1 complex subunit Ask1 of *Candida albicans* using virtual screening and MD simulations. *Comput Biol Chem* 2017;72: 33–44.
45. Iwu M. Biflavanones of *Garcinia*: pharmacological and biological activities. In: Cody V, Middleton E, editors. *In plant flavonoids and medicine: biochemical, pharmacological and structure activity relationships*. New York, NY, USA: Alan R. Liss Inc.; 1986:485–8 pp.

46. Farombi EO, Owoeye O. Antioxidative and chemopreventive properties of *Vernonia amygdalina* and *Garcinia biflavonoid*. *Int J Environ Res Publ Health* 2011;8:2533–55.
47. Yu S, Yan H, Zhang L, Shan M, Chen P, Ding A. A review on the phytochemistry, pharmacology, and pharmacokinetics of amentoflavone, a naturally-occurring biflavonoid. *Molecules* 2017;22:1–23.
48. Gan L, Ma J, You G, Mai J, Wang Z, Yang R, et al. Glucuronidation and its effect on the bioactivity of amentoflavone, a biflavonoid from *Ginkgo biloba* leaves. *J Pharm Pharmacol* 2020;72:1840–53.
49. Arwa P, Zeraik M, Ximenes V, da Fonseca L, Bolzani V, Silva DHS. Redox-active biflavonoids from *Garcinia brasiliensis* as inhibitors of neutrophil oxidative burst and human erythrocyte membrane damage. *J Ethnopharmacol* 2015;174:410–8.
50. Ndongo J, Issa M, Messi A, Mbing J, Cuendet M, Pegnyemb D, et al. Cytotoxic flavonoids and other constituents from the stem bark of *Ochna schweinfurthiana*. *Nat Prod Res* 2015;29:1684–7.
51. Lee J, Sul J, Park J, Lee M, Cha E, Song I, et al. Fatty acid synthase inhibition by amentoflavone suppresses HER2/neu (erbB2) oncogene in SKBR3 human breast cancer cells. *Phytother Res* 2013; 27:713–20.
52. Zha X, Xu Z, Liu Y, Xu L, Huang H, Zhang J, et al. Amentoflavone enhances osteogenesis of human mesenchymal stem cells through JNK and p38 MAPK pathways. *J Nat Med* 2016;70:634–44.

Medinat O. Osundiya*, Segun E. Olaseni, Rasaq A. Olowu and Olanrewaju Owoyomi

10 Thermodynamics of the micellization of quaternary based cationic surfactants in triethanolamine-water media: a conductometry study

Abstract: The effect of triethanolamine, a solvent with wide technical and industrial benefit on the micellization of an aqueous mixture of cationic surfactants, dodecyltrimethylammonium bromide (DETAB) and hexadecyltrimethylammonium bromide (HATAB) was studied to examining the stability of the mixed micelles at 298.1, 303.1, 308.1 and 313.1 K using the electrical conductance method. The values of the critical micelle concentration (C^*) were found to decrease with an increase in the concentration of triethanolamine (TEA). The values of the free energy of micellization (ΔG_m) were negative at a particular temperature, and the extent of spontaneity was discovered to increase when the concentration of TEA was increased. However, an increase in temperature was observed to have a negative linear relationship with the spontaneity of the process. The formation of the mixed micelles was an exothermic process, and it was also TEA and temperature-dependent with a trend similar to those observed in the free energy of micellization (ΔG_m). The degree of disorderliness of the system was also found to be entropy driven at a higher concentration of TEA. The synergistic interaction between the molecules of DETAB–HATAB in the presence of TEA (0.4% v/v) and the spontaneity of the system was at the maximum at 0.1:0.9 mol fraction ratio and the energetics of the system was discussed based on hydrophobic–solvophobic interaction of the monomers in TEA at elevated temperatures.

Keywords: cationic surfactants; monomers; solvophobic; thermodynamics.

*Corresponding author: **Medinat O. Osundiya**, Department of Chemistry, Lagos State University, Ojo, Nigeria, E-mail: medinat.osundiya@lasu.edu.ng

Segun E. Olaseni, Department of Chemical Sciences, Adekunle Ajasin University, Akungba-Akoko, Nigeria, E-mail: segunolaseni@aaua.edu.ng

Rasaq A. Olowu, Department of Chemistry, Lagos State University, Ojo, Nigeria, E-mail: Rasaq.olowu@lasu.edu.ng

Olanrewaju Owoyomi, Department of Chemistry, Obafemi Awolowo University, Ile-Ife, Nigeria, E-mail: oowoyomi@oauife.edu.ng

This article has previously been published in the journal *Physical Sciences Reviews*. Please cite as: M. O. Osundiya, S. E. Olaseni, R. A. Olowu and O. Owoyomi "Thermodynamics of the micellization of quaternary based cationic surfactants in triethanolamine-water media: a conductometry study" *Physical Sciences Reviews* [Online] 2021, 7. DOI: 10.1515/psr-2020-0131 | <https://doi.org/10.1515/9783110739763-010>

10.1 Introduction

Surfactant molecule possesses a water-loving segment and a hydrophile [1]. This amphiphilic nature of the surface-active agent is responsible for their (a) adsorption at an interface in an orientation such that the hydrophobic tail points upwardly from the aqueous medium, and the hydrophilic part resides in water [2]. This sequence leads to a decrease in surface free energy of the system [3–5]. At saturation (b) surfactant self-assemble into an entity called micelle or mixed-micelles as in the case of monomeric or mixture of surfactant species, respectively [6]. These dual, incompatible unusual but notable characteristics of surfactant (amphiphile) play vital roles in processes of interest such as dye solubilization, fabric softening, improve drug solubilization detergency, oil recovery [7, 8] and as a catalyst to enhance the rate of chemical and biological reactions [9–11].

Cationic surfactants have a net positive charge that is independent of the pH of the system localized at the head group are of immense value [3]. A mixture of surfactant yielding micelles that comprised of the two surfactants in different proportion (x) are more efficient and cost-effective than micelles from a single monomer [12, 13].

The formation of micelles which is majorly as a result of hydrophobic interactions originated from the hydrocarbon segments, and which must be strong enough to overcome the opposing electrostatic forces from the hydrophilic portion of the surfactant molecules [8, 9, 11] occurs at a well-defined concentration [6, 9, 14] called the critical concentration called the critical micelle concentration (CMC). The CMC is the concentration of economic importance [15] especially in the case of favourable interaction [16] (synergism) in the mixed state, hence the structural, thermodynamics and kinetic properties of surfactants involved in industrial and technical processes are defined at a specific concentration (C) which corresponds to the concentration of optimal performance ($C > \text{CMC}$) as micelles are present [8, 11, 17].

The micellization process and the CMC have been reported to be significantly influenced by solvents, temperature and a broad range of solutes [8, 17, 18]. The effects of additives to surfactants which may result in improved performance of the products [3] have also been reported to be because of the solvent structural features and behaviour in terms of reinforcing water structure or otherwise, hydration phenomenon (temperature) and reduction in electrostatic repulsion by ionic electrolytes [19].

Previous studies on cationic-cationic mixtures are very scanty, as a lot of researchers focused on cationic surfactants that have bulky head groups (TPPB, TTPyB). Very few have, however, tried to study the effect of co-solvent/additives such as DMSO, DMF, MeOH, THF, DO, EG among other co-solvents on the aggregation properties, and the effects of the aforementioned co-solvents based on their reports are largely inhibitory [8, 20–22]. A lot of reports is also available in the literature on binary mixtures of cationic surfactants in aqueous and aqueous–organic media [15, 19, 23, 24], however, investigations of the effect of temperature on the micellization of mixed

cationic surfactants especially those of the linear quaternary ammonium halides in triethanolamine has not been mentioned.

The co-solvent of choice, TEA, with OH and NH functional groups (Figure 10.1), are used in the formulations of herbicides, cleaning and soil dispersing (laundering) agents, drug carriers and a host of other industrial processes [25]. The presence of the OH group in its structure can allow the formation of multiple hydrogen bonds, a condition which according to Evan [26, 27] stands as a prerequisite for micelle formation. Additionally, the OH can also be incorporated into the mixed-micellar core by acting as a bridge [23] thereby minimizing the electrostatic repulsive force among the polar head groups, and at the same time increase the van der Waals interaction through the large hydrophobic volume in the structure.

Mixed-micelles of cationic surfactants consisting of OH segments can preserve aquatic lives as it has been reported to be efficient in reducing water pollution by emulsification of oil spills in the aquatic system [28].

Considering the widespread application of mixed micelles of dodecyltrimethylammonium bromide (DETAB) and hexadecyltrimethylammonium bromide (HATAB) in Triethanolamine (TEA), information on the overall stability and feasibility of the process of the potential products is of value, and need to be ascertained through the evaluation of the energetics of the aggregation process. The structure of the surfactants and the co-solvent (TEA) are shown in Figure 10.1.

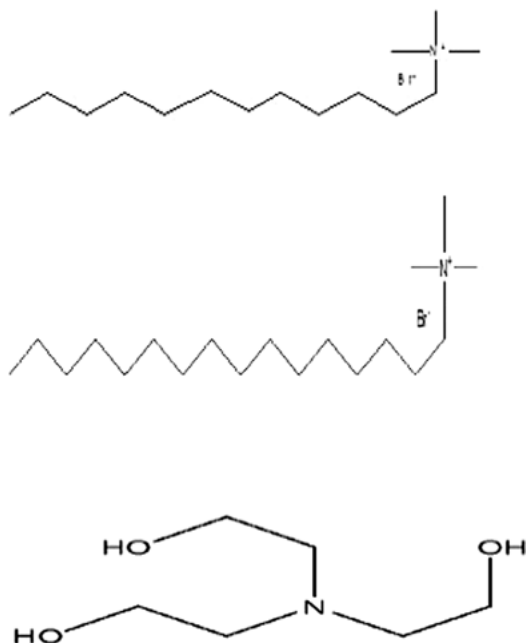


Figure 10.1: Structure of a: DETAB
b: HATAB c: TEA.

Conductance measurement has been described by many researchers to be the ideal diagnostic technique for probing changes in concentration of ionic surfactants in aqueous and aqueous–organic media [29, 30].

10.2 Materials and methods

10.2.1 Materials

The n-alkyl, dodecyltrimethylammonium bromide (DETAB-C₁₂) and hexadecyltrimethylammonium bromide (HATAB-C₁₆) were purchased from Sigma Aldrich company. These cationic surfactants are of the highest purity, that are commercially available, and they are therefore used without further purification. The TEA was of analytical grade also purchased from Sigma Aldrich and used as received. The water used for this work was re-distilled, with a specific conductivity value that ranged between 1 and 3 $\mu\text{s cm}^{-1}$ at room temperature. The concentration of the mixture was expressed in mole fraction in accordance with ideal mixing system at temperatures 298.1, 303.1, 308.1 and 313.1 K.

Jenway conductivity meter of model 4510 with a dip-type probe of 1.0 cm^{-1} cell constant was used for the experiment. The electrode was calibrated before use with an aqueous solution of 0.01 mol l^{-1} KCl which is of known conductivity.

10.2.1.1 Methods

The conductance of the mixture DETAB–HATAB solution based on mole fractional ratio in 0.0, 0.2 and 0.4% v/v was measured using the titrimetric method at temperatures of 293.1 through 313.1 K at an interval of 5.1 K. A thermostated water bath was used for the experiment at the working temperatures. The solution of the surfactant mixture was prepared (mole fraction) in accordance with Clint's [31] model which is based on the ideal mixing system as shown in Eq. (10.1).

$$\frac{1}{id_{\text{CMC}}} = \sum_{i=1}^{N=2} \frac{\alpha_i}{\text{CMC}_i} \quad (10.1)$$

The id_{CMC} is the critical concentration for the ideal mixture, CMC_i , its critical micelle concentrations of the pure forms (DETAB and HATAB), and is related to the CMC_1 and CMC_2 of the pure components and α_i the bulk mole fraction. The experimental details have been described in our previous work [3].

Table 10.1: Thermodynamic behaviour of micellization of DTAB–HTAB in 0.2% v/v TEA.

| α | $C^*(\text{mmol l}^{-1})$ | $\frac{-\Delta G_{\text{mx}}}{\text{kJ mol}^{-1}}$ | $\frac{-\Delta H_{\text{mx}}}{\text{kJ mol}^{-1}}$ | $\frac{\Delta S_{\text{mx}}}{\text{J mol}^{-1} \text{K}^{-1}}$ |
|----------------|---------------------------|--|--|--|
| 298.1 K | | | | |
| 0.1 | 0.790 | 2.299 | 1.300 | 3.352 |
| 0.2 | 0.874 | 2.215 | 1.151 | 3.572 |
| 0.3 | 0.947 | 1.376 | 1.207 | 3.919 |
| 0.4 | 1.028 | 2.593 | 1.319 | 4.273 |
| 0.5 | 1.127 | 2.838 | 1.464 | 4.610 |
| 0.6 | 1.245 | 3.118 | 1.646 | 4.938 |
| 303.1 K | | | | |
| 0.1 | 0.838 | 1.915 | 1.006 | 3.001 |
| 0.2 | 0.915 | 1.946 | 0.944 | 3.306 |
| 0.3 | 0.969 | 2.294 | 1.133 | 3.829 |
| 0.4 | 1.063 | 2.475 | 1.214 | 4.161 |
| 0.5 | 1.139 | 2.841 | 1.449 | 4.591 |
| 0.6 | 1.295 | 2.908 | 1.428 | 4.882 |
| 308.1 K | | | | |
| 0.1 | 0.874 | 1.582 | 0.766 | 2.648 |
| 0.2 | 0.945 | 1.747 | 0.797 | 3.084 |
| 0.3 | 1.017 | 2.041 | 0.935 | 3.586 |
| 0.4 | 1.098 | 2.349 | 1.104 | 4.042 |
| 0.5 | 1.141 | 2.876 | 1.465 | 4.582 |
| 0.6 | 1.329 | 2.982 | 1.491 | 4.841 |
| 313.1 K | | | | |
| 0.1 | 0.885 | 1.499 | 0.705 | 2.534 |
| 0.2 | 0.958 | 1.776 | 0.810 | 3.084 |
| 0.3 | 1.044 | 1.903 | 0.831 | 3.427 |
| 0.4 | 1.119 | 2.277 | 1.038 | 3.957 |
| 0.5 | 1.177 | 2.783 | 1.373 | 4.503 |
| 0.6 | 1.337 | 3.005 | 1.494 | 4.824 |

10.3 Results and discussion

10.3.1 Results

10.3.1.1 Determination of the critical mixed micelle concentration

The electrical conductivity of 0.1:0.9, 0.2:0.8, 0.3:0.7, 0.4:0.6, 0.5:0.5 and 0.6:0.4 of different mole fractional combinations where the first value in each mixture (0.1, 0.2, 0.3, 0.4, 0.5 and 0.6 represent the fraction of the first components in the mixture) of DETAB–HATAB following ideal mixing with and without different percentage of TEA was measured to determine the critical micelle concentration (C_{12}) of the mixture and

Table 10.2: Thermodynamic behaviour of micellization of DTAB–HTAB in 0.4% v/v TEA.

| α | $C^*(\text{mmol}^{-1})$ | $\frac{-\Delta G_{\text{mix}}}{\text{kJ mol}^{-1}}$ | $\frac{-\Delta H_{\text{mix}}}{\text{kJ mol}^{-1}}$ | $\frac{\Delta S_{\text{mix}}}{\text{J mol}^{-1}\text{K}^{-1}}$ |
|----------------|-------------------------|---|---|--|
| 298.1 K | | | | |
| 0.1 | 0.764 | 2.531 | 1.479 | 3.529 |
| 0.2 | 0.785 | 2.831 | 1.633 | 4.018 |
| 0.3 | 0.909 | 2.598 | 1.383 | 4.078 |
| 0.4 | 1.029 | 2.584 | 1.313 | 4.263 |
| 0.5 | 1.083 | 2.994 | 1.595 | 4.693 |
| 0.6 | 1.141 | 3.437 | 1.923 | 5.057 |
| 303.1 K | | | | |
| 0.1 | 0.818 | 2.094 | 1.136 | 3.165 |
| 0.2 | 0.827 | 2.591 | 1.431 | 3.829 |
| 0.3 | 0.916 | 2.593 | 1.368 | 4.042 |
| 0.4 | 1.047 | 2.556 | 1.273 | 4.217 |
| 0.5 | 1.098 | 2.988 | 1.574 | 4.666 |
| 0.6 | 1.184 | 3.357 | 1.837 | 5.014 |
| 308.1 K | | | | |
| 0.1 | 0.828 | 2.038 | 1.088 | 3.084 |
| 0.2 | 0.838 | 2.555 | 1.391 | 3.777 |
| 0.3 | 0.970 | 2.319 | 1.143 | 3.816 |
| 0.4 | 1.101 | 2.333 | 1.092 | 4.030 |
| 0.5 | 1.157 | 2.822 | 1.419 | 4.553 |
| 0.6 | 1.220 | 3.301 | 1.769 | 4.969 |
| 313.1 K | | | | |
| 0.1 | 0.835 | 1.997 | 1.051 | 3.017 |
| 0.2 | 0.843 | 2.567 | 1.393 | 3.750 |
| 0.3 | 0.998 | 2.188 | 1.035 | 3.683 |
| 0.4 | 1.147 | 2.317 | 1.067 | 3.994 |
| 0.5 | 1.224 | 2.611 | 1.232 | 4.402 |
| 0.6 | 1.260 | 3.232 | 1.691 | 4.922 |

other thermodynamically dependent mixed micellar parameters. The conductance values, k , obtained were plotted as a function of surfactants (mol L^{-1}), and the plot yielded a straight-line graph with an inflection point which corresponds to a single break C^* . The graph has two different slopes representing pre (A_1) and post (A_2) mixed micellar regions. The ratio of the slopes (α_1) gives information about the counter ion dissociation $\left(\beta_1 = \frac{A_2}{A_1}\right)$, whereas the fraction of counter-ion binding (β_{12}) to the mixed micellar surface was calculated by subtracting the value of β_1 from unity. However, the use of the conventional plots for the determination of micellar CMC has remained elusive owing to the presence of curvatures which is largely because of the gradual transition from monomer to micelle especially at higher surfactant concentration, aqua-co-solvent media and temperature greater than 298.1 K has been taken as

the second CMC [32]. To surmount the problem of uncertainty in locating the breakpoint, the values of the critical micelle concentration of the mixed micelle (C_*) of DETAB–HATAB were determined graphically with the aid of the method proposed by Carpena et al. [33] which involved mathematical fittings to the conductance data to obtain a nonlinear function followed by the integration of the Boltzmann-type Sigmoid equation (Eq. 10.2).

$$k = A_0 + A_1 C + A_3 (A_2 - A_1) \ln \left[\frac{1 + \exp(C - A_4/A_3)}{1 + \exp(-A_4/A_3)} \right] \quad (10.2)$$

A_0 represents the initial conductivity of water, A_1 and A_2 are the slopes for low (pre micelle) and high (post micelle) regions, A_3 is the width of transition between the two regions, and the central point of the transition, respectively. The values of A_4 corresponds to the centre of transition, and it is equal to the experimental critical micelle concentration of the mixed micelles (C^*). The summary of results of the mixed micellar parameters in aqueous-TEA (0.2 and 0.4% v/v) at different temperatures were presented in Tables 10.1 and 10.2. The plot of differential conductivity (κ) versus mixed surfactant concentration using Eq. (10.1) was shown in Figure 10.2.

10.3.2 Mixed micelle formation. And Solvent Effect

The micellization process was discovered to deviate from ideality in TEA at 0.2% v/v, and the enhancement of the aggregation process was seen when the percentage concentration of TEA was increased to 0.4% v/v as the values of the critical mixed micelle concentration (C^*) became markedly smaller than that predicted by assuming an ideal

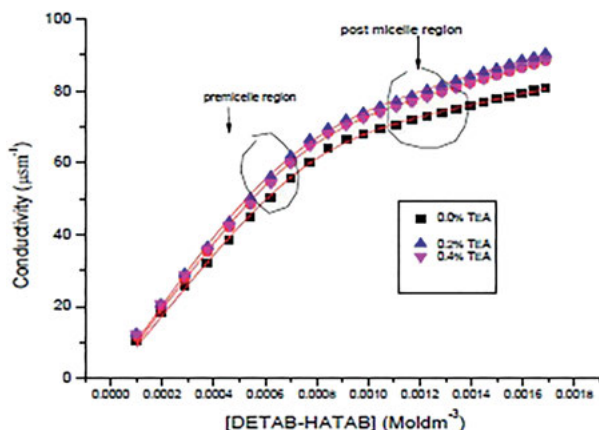


Figure 10.2: Plot of the differential conductivity against the concentration of DETAB-HATAB in Water-TEA at 298.1K.

mixing system indicating a favourable (synergism) interaction between the mixed surfactants in TEA at higher solvent addition.

Several factors could be responsible for this nonconformity to ideality. A decrease in the values of C^* of DETAB-HATAB in aqueous-triethanolamine mixed-media could be ascribed to the argumentation of the 3-D structure of water by TEA through hydrophobic-solvophobic interaction. The hydrophobicity (driving force for aggregation) of the process was strengthened in a manner that TEA was able to infiltrate the mixed micellar core, intercalating such that the distance between the hydrophile was increased with a concomitant reduction in ion-ion repulsion, hence early mixed micelle formation. The deviation of C^* from ideality was a result of the synergistic interaction between the mixed surfactants in the aqueous –TEA system. Figure 10.3 depicted the extent of deviation from ideal behaviour.

10.3.3 Effect of Temperature on the Mixed micelle formation

Mixed-micelle that has a linear relationship with temperature was obtained as the values of C^* increased with an increase in temperature, a behaviour that is characteristic of ionic surfactants [34] because of (a) dehydration of the head group at a higher temperature which led to an increase in repulsion among the polar head groups and the disruption of the palisade layer of the mixed-micelles which shifted the equilibrium position in favour of the surfactant monomers are factors that came to play with the aggregation behaviour at elevated temperature [35, 36]. Figure 10.4 showed the variation of the C^* with solution mole fraction (α_i) as a function of temperature.

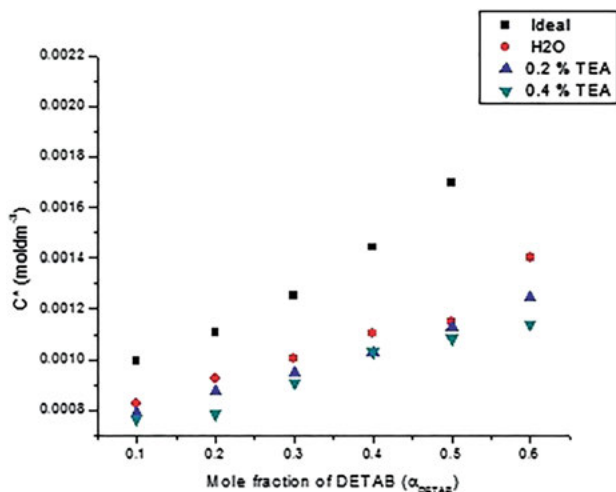


Figure 10.3: The plot of (C^*) of DETAB-HATAB in TEA-Water mixture as a function of the mole fraction of DTABr. at 298K (Extent of deviation from ideality).

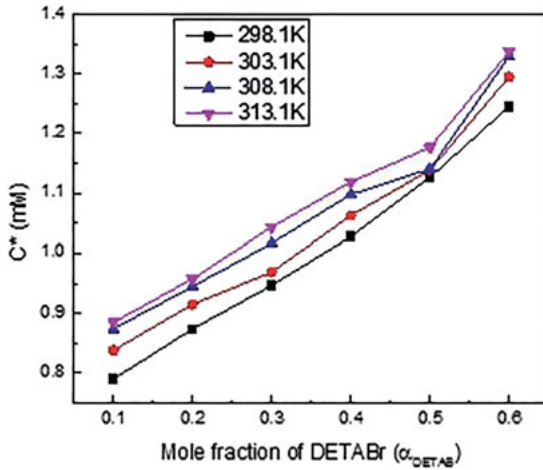


Figure 10.4: Representative Plot of C^* versus mole fraction in TEA-Water (0.2%) at different temperatures.

Consequential adjustment to Clint's equation [31] was inevitable (Eq. 10.1) and this was carried out by Rubingh [37] through the introduction of activity coefficients to account for non-ideality in surfactant mixtures. Equation (10.3) gave the modified form of Clint's equation

$$\frac{1}{CMC^{ideal}} = \sum_{i=1}^{N-2} \frac{\alpha_i}{\sigma_i CMC_i} \quad (10.3)$$

The activity coefficients (σ_i) of the components can be expressed as follows

$$\sigma_1 = \exp \beta_x (1 - \chi_1)^2 \quad (10.4a)$$

$$\sigma_2 = \exp \beta_x (\chi_1)^2 \quad (10.4b)$$

Where σ_1 and σ_2 represent the activity coefficients for the first component (DETAB) and the second component (HATAB), respectively of the mixed micelles. The values of the activity coefficients of σ_1 were found to be below unity, with the values of σ_2 closer to the standard state than the values of σ_1 .

10.3.4 Thermodynamics of Mixed-Micelles

The energetic of the micellization process with organic co-solvent was examined by evaluating relevant thermodynamic quantities using the phase separation model [37] According to the regular solution theory, the relationship between the excess free energy (G^E) the excess enthalpy (H^E) and the changes in Gibb's free energy and enthalpy of micellization are given by

$$G^E = H^E = \Delta H_m = RT (\chi_1 \ln \sigma_1 + (1 - \chi_1) \ln \sigma_2) \quad (10.5)$$

$$\Delta G_M = RT(\chi_1 \ln(\chi_1 \sigma_1) + (1 - \chi_1) \ln((1 - \chi_1) \sigma_2)) \quad (10.6)$$

$$\Delta S_m = \frac{\Delta H_m - \Delta G_m}{T} \quad (10.7)$$

The values of Gibb's free energy of micellization (ΔG_m) for DETAB-HATAB were negative at 0.2% v/v cosolvent addition. The spontaneity of the process, however, decreased when the temperature > 298.1 K. When the concentration of the cosolvent was increased to 0.4% v/v, the hydrophobic-solvophobic interaction was found to increase as less work (ΔG_m) was expended to achieve the desire results, the values of the free energy of the mixed micelle became more negative, and these values were also temperature-dependent., because of solubility of some of the hydrophobic part [34, 36] and an increase in the K.E of the system at a higher temperature. Furthermore, the negative values obtained indicated that the mixed micelles were more stable than the micelle formed from the individual surfactant components. Similar findings have been reported in the literature [19, 20].

The process of aggregation was exothermic, and the results obtained were also shown in Tables 10.1 and 10.2. When TEA (0.2%) was added to the mixture of C_{12} TAB- C_{16} TAB, the values of enthalpy of micellization were negative, However, the formation of the mixed micelle became more exothermic when the medium was further fortified with a higher concentration of TEA (0.4% v/v) as the values became more negative because of reinforcement of the three-dimensional structure of water with TEA own to its structural making capacity. These values ($-\Delta H_m$) also decreased with an increase in temperature. On the overall, the process was exothermic in nature.

The values of the entropy of micellization (ΔS_m) were discovered to be positive at a given composition of the organic co-solvent used (TEA). An increase in the percentage composition (0.4 v/v %) further enhanced the motional freedom of the ordered structure of water by broken more of the 'Frank-Evan icebergs' during the formation of mixed micelles. However, there was a loss of water structure at a higher temperature. Although the mixed micelle is an ordered entity, but the process of concealment of the tail group into the interior of the mixed micelle, along site the intercalation of the cosolvent involved liberation of water/in the vicinity of the aggregation zone, a process that is largely random in nature.

10.4 Conclusion

Micellization of cationic surfactants that differ in the hydrocarbon segments were examined in the presence of an organic cosolvent (TEA) as a function of temperature was studied with a view to examining the stability of the product in terms of energetics of the process.

From the results it was discovered that when a mixture of DETAB-HATAB was accentuated with varying concentrations of organic additive such as TEA, the critical

micelle concentration values that would be lower than that predicted by ideal behaviour could be obtained. This synergistic interaction is of industrial value as C^* values represent in practice, the smallest concentration at which maximum benefit, because of cost-effectiveness could be obtained. Furthermore, the energetics of the process was found to be thermodynamically feasible at the studied temperature.

Author contributions: All the authors have accepted responsibility for the entire content of this submitted manuscript and approved submission.

Research funding: The research is not funded.

Conflict of interest statement: There is no conflict of interest.

References

1. Aswal V K, Goyal P S. Role of counterion distribution on the structure of micelles in aqueous salt solutions: small angle neutron scattering study. *Chem Phys Lett* 2002;357:491–7.
2. Shah S K, Bhattaral A, Chatterjee S K. Applications of surfactants in modern science and technology. *Modern Trends Sci Technol* 2013;147–58.
3. Osundiya M O, Olowu R A, Olaseni S E, Aboluwoye C O. Micellization and interaction of cationic surfactants with different hydrophobic group in polar organic solvent. *Am J Phys Chem* 2020;9:86–92.
4. Animesh P, Satya P M. Surface tension of binary liquid mixtures including ionic liquids and the gibbs surface excess. *J Surf Technol* 2015;3:1–8.
5. Zia Ul H, Rehman N, Farman A, Nasir M K, Ullah H. Physico-chemical properties of cationic surfactant cetytrimethylammonium bromide in the presence of electrolyte. *J Mater Environ Sci* 2017;8:1029–38.
6. Tennouga L, Mansri A, Medjahed K, Chetouani A, Warad I. The micelle formation of cationic and anionic surfactants in aqueous medium: determination of CMC and thermodynamic parameters at different temperatures. *J Mater Environ SC* 2015;6:2711–6.
7. Sachin KM, Karpe SA, Singh M, Bhattarai A. An interaction of anionic- and cationic-rich mixed surfactants in aqueous medium through physico-chemical properties at three different temperatures. *J Chem* 2018;1–17.
8. Koya PA, Kabir-ud-Din, Ismail K. Micellization and thermodynamic parameters of butanediyl-1,4-bis(tetradecyldimethylammonium bromide) Gemini Surfactant at different temperatures: effect of the addition of 2-methoxyethanol. *J Solut Chem* 2012;41:1271–81.
9. Fernandez I, Perez-Juste J, Herves P. Cationic mixed micelles as reaction medium for hydrolysis reactions. *J Solut Chem* 2015;44:1866–74.
10. Das D, Das D, Das P K. Improved activity of enzymes in mixed cationic reverse micelles with imidazolium-based surfactants. *Biochimie* 2008;90:820–9.
11. Khan M N, Fagge I I. Kinetics and mechanism of cationic micelle/flexible nanoparticle catalysis: a review. *Prog React Kinet Mech* 2018;43:1–20.
12. Mandal A, Kar S. A Thermodynamic assessment of micellization for a mixture of sodium dodecylbenzene sulfonate and Tween 80 surfactant for ultralow interfacial tension. *Fluid Ph Equilibria* 2016;40:212–22.
13. Owoyomi O, Ige O O, Ogunlusi G O, Ayinde O. Micellization behaviour of mixtures of sodium dodecylsulphate and sodium lauroyl surcosinate in water. *Phys Chem Liq* 2013;1–8.
14. Chatterjee A, Moulik S p, Sanyal S K, Mishra B K, Puri P P. Thermodynamics of micelle formation of ionic surfactants: a crical assessment for sodium dodecyl sulfate, cetyl pyridinium chloride and

- dioctyl sulfosuccinate (Na salt) by microcalorimetric, and tensiometric measurements. *J Phys Chem B* 2001;105:12823–31.
15. Nighat N, Mohammed S, Arif A. Micellization of cationic cetyltrimethylammonium bromide in mixed water-alcohol media. *J Dispersion Sci Technol* 2009;30:51–5.
 16. Malik A R, Naved A, Abudulah M A. Binary mixtures of sodium salt of ibuprofen and selected bile salts: interface, micellar, thermodynamic, and spectroscopic study. *J Chem Eng* 2017;62:3216–28.
 17. Santos M S, Tavares F W, Biscaia Jr. Molecular thermodynamics of micellization: micelle size distributions and geometry transitions. *Braz J Chem Eng* 2016;33:515–23.
 18. Gracie K, Turner D, Palepu R. Thermodynamic Properties of micellization of sodium dodecyl sulfate in binary mixtures of ethylene glycol with water. *Can J Chem* 1996;74:1616–25.
 19. Olaseni S E, Oladoja N A, Ololade I A, Aboluwoye C O, Osundiya M O. Micellization of cetyltrimethylammonium bromide in aqueous-organic media. *Chem Sci J* 2012;52:1–11.
 20. Kallol K G, Vidvacharam B. Micellar properties of benzyldimethyldodecylammonium bromide in aquo-organic solvent media. *Indian J Chem* 2008;47A:1230–3.
 21. Ray G B, Chakraborty I, Ghosh S, Moulik S P. A critical and comprehensive assessment of interfacial and bulk properties of aqueous binary mixtures of anionic surfactants, sodiumdodecyl sulfate and sodium dodecylbenzene sulfonate. *J Colloid Polym Sci* 2007;285:457–69.
 22. Prasad M, P Moulik S, Palepu P. Self-aggregation of binary mixtures of alkyltriphenylphosphonium bromides: a critical assessment in favor of more than one kind of micelle formation. *J Colloid Interface Sci* 2005;284:658–66.
 23. Ashish S, Kallol K G. Micellization of CethylTriPhenylPhosphonium Bromide surfactant in binary aqueous solvents. *J Surfactant Deterg* 2008;11:287–92.
 24. Misra P K, Mishra B K, Bebera G B. Micellization of ionic surfactants in tetrahydrofuran-water and acetonitrile-water mixed solvent systems. *Colloid Surf* 1991;57:1–10.
 25. Bijay K M, Partha M, Sukalyan D, Sabita P, Hari N P. Alkylation of ethanolamine: an approach to a novel class of functional surfactants. *Taylor & Francis* 2009;39:2529–39.
 26. Evans D F, Wennestrom H. The colloidal domain where physics, chemistry and biology meets. *New York: VCH; 1994:515–6 pp.*
 27. Fenta A D. Surface and thermodynamic studies of micellization of surfactants in binary mixtures of 1,2-ehanediol and 1,2,3-propanetriol with water. *Int J Phys Sci* 2015;10:276–88.
 28. Ziyafaddin B A, Ravan A R, Shafiga M N, Ahmadova G A. Surface activity, thermodynamics of micellization and adsorption properties of quarternary salt based on ethanolamines and decyl bromide. *J Surfactants Deterg* 2010;13:459–64.
 29. Ana K, Bojan S, Marija B R. What affect the degree of micelle ionization: conductivity study of alkyltrimethylammonium chloride. *Acta Chim Slov* 2012;59:564–70.
 30. Prasad M, Chakraborty I, Rakshit A K, Moulik S P. Critical evaluation of micellization behavior of nonionic surfactant MEGA 10 in comparison with ionic surfactants tetradecyltriphenylphosphonium bromide studies by calorimetric method in aqueous medium. *J Phys Chem B* 2006;110:9815–21.
 31. Clint J H. Mixed micelle theory as an aid to surfactant formulation' in the structure, dynamics and equilibrium properties of colloidal systems, Bloor D M, editor. *London: Kluwer Academic; 1990:184 p.*
 32. Owoyomi O, Ige J, Soriyan O O. Thermodynamics of micellization of n-alkyltriphenylphosphonium bromide: a conductometric study. *Chem Sci J* 2011;25:1–13.
 33. Carpena P, Aguiar J, Bemaola-Garvan P. *Langmuir* 2002;18:60546.
 34. Al-Wardian A, Glenn K M, Palepu R M. Thermodynamic and interfacial properties of binary cationic mixed systems. *Colloids Surf, A Physicochem Eng Asp* 2004;247:115–23.
 35. Sansanwal P K. Effect of co-solutes physico-chemical properties of surfactant solutions. *J Sci Ind Res* 2006;6:57–64.

36. Bakashi MS, Sachar S. Influence of hydrophobicity on the mixed micelles of pluronic F127 and P103 plus cationic surfactant mixtures. *Colloids Surf A* 2006;276:146–54.
37. Holland H D, Rubingh D, editors. Chapter 1, Mixed surfactant system: an overview, 501st ed. Washington, D. C.: ACS Symposium Series An Overview. American Chemical Society Symposium Series; 1992:2–30 pp.

Index

- ability to summarise 52
- absorbance 85
- accentuated 190
- action research 39
- active learning 56
- active student involvement 45
- active student's engagement 56
- activity coefficients 189
- ADCH charge 96
- additive 190
- amphiphilic 182
- anticancer 175
- aromatic ring 103, 110, 115
- aromaticity 3
- atomic hybrid orbitals 95
- automatic corrections by the computer 47
- avoidance of repetitions 51
- azetidine 79
- biflavonoid 175
- binding energy 104, 113–114
- binding interaction 168
- binding tendencies 176
- bond breakage 88
- bond polarity index 87
- bond strength 88
- bridging secondary and tertiary instruction 57
- building of descriptions 44
- building of sentences 44
- Cambridge structural database 23
- cationic surfactants 182
- CDFT 80, 85, 90, 99
- charge transfer 104–106, 108–110
- charge transport 8
- chemical complex 152, 159
- chemical hardness 92
- chemical potential 92
- chemical reactivity 93
- chemometric 64
- chemopreventive 175
- clinical parameters 61–64, 68
- clinical variable 64
- cluster 63–64, 66, 68, 71
- comparisons 49
- computational chemistry postgraduate studies 37–38
- computational chemistry thesis 54
- computational chemistry 38, 48, 53
- concealment 190
- concentration fluctuations 157, 160
- conceptual density functional theory 91
- conceptual knowledge 41
- conceptual understanding 38, 46
- condensed dual descriptor 91
- conductance 184
- coordination number 150, 158
- critical micelle concentration 181–182, 185, 187, 191
- critical thinking 41
- curvatures 186
- cycloalkanes 80
- cyclopropane 80
- delocalization 108, 116
- density functional theory 21, 23, 119–120, 143–144
- description of practical operations 48
- designing a project 42
- development of logical abilities 44
- DFT 119–120, 130, 132–133, 137, 143
- dimerization 80
- dissipative particle dynamics 119–120, 126, 144–146
- docking 167
- docking energy 175
- dodecyltrimethylammonium bromide 183
- doped 79, 80, 87, 90, 93, 95, 97, 99
- DPD 119–120, 122, 126–129, 135, 138–139, 141
- dual descriptor 91
- economy of a text 51
- educational research 38, 39, 58
- educational studies for advanced levels 36
- electrode 184
- electron density 103, 105, 112, 114
- electron localization function 88
- electronegativity 88, 92, 95–96, 101
- electrophilic 91, 99
- electrophilic substitution 92, 99
- electrophilicity 91–93, 101
- electrophilicity index 92–93
- electrostatic interaction 97, 99
- energy gap 104–105, 110
- ensemble 126, 136
- enthalpy of mixing 156, 159
- entropy of mixing 156, 159

<https://doi.org/10.1515/9783110739763-011>

- EOR 119–121, 130–132, 135, 138, 141–144, 148
 ESP plot 112
 expression of comparisons 47
 familiarization with the scientific method 58
 flavonoids 175
 force fields 123
 fostering independence 37, 53, 56
 free energy of formation 152
 free energy of mixing 152
 frequencies 87
 fukui function 91, 99
 fundamental 85, 101
 garcinia biflavonoid 1 166
 garcinia biflavonoid 2 166
 GAUSS VIEW 103, 105
 gaussian 09W 80, 103, 105
 gibbs free energy of mixing 152
 givinostat 167
 global hardness 2
 grammar errors 47
 grouping 63–64
 HDAC inhibitor 167
 HDAC1 175
 HDAC2 175
 HDAC3 173
 HDAC7 173
 HDAC8 174
 heteroatoms 79, 96–97, 99
 heterocoordination 157
 hexadecyltrimethylammonium bromide 183
 hirshfeld charges 91, 96
 histone deacetylases 165
 HOMO 91–93, 95, 100
 homocoordination 157, 160, 163
 homonuclear atoms 88
 hydrogen bond 168
 hydrogen bonds 108
 hydrophobic interaction 171
 hydrophobicity 188
 ideal mixing 184–185, 188
 identification of patterns 49
 IFT 120, 122, 130–132, 139, 141–142
 importance of learning scientific writing 45
 independent gradient model 89
 infiltrate 188
 inflection point 186
 inherent ring 80
 inhibitors 174
 integrating chemistry learning and language
 learning 57
 interaction parameters 154, 156
 interactions 80, 88–89, 95, 97, 99
 interfragment 89
 intramolecular 79, 80, 96, 99
 intermolecular hyperconjugative 95
 intrinsic bond strength index 88, 90
 ionic liquids 104, 116
 kolaflavanone 166
 kolaviron 166
 language mastery 37, 44, 46, 51, 57
 learning how to do research 36–37
 ligands 167
 literature review 41, 52, 54
 logic mastery 37
 logical relationships 50
 logical thinking 57
 LUMO 92–93, 95, 100
 making inferences 43
 mathematics as a tool for descriptions 57
 MD 119–120, 122–127, 130–132, 135–136, 138,
 141, 147
 mean absolute percentage error 154
 mole fraction 181, 184, 188
 molecular calculations 43
 molecular dynamics 119–120, 122, 130, 143,
 145–148
 molecular electrostatic potential 97, 100
 molecular electrostatic potential surface 4
 multifunctional 104–105, 114
 natural bond orbital 80, 103
 natural products 166
 nature of molecular calculations 49
 nucleophilic 91, 101
 number of nearest neighbours 158
 ordered entity 190
 organisation and analysis of obtained
 data 42
 organisation and analysis of the obtained
 data 42
 oxetane 87
 palisade layer 188
 PED 86, 99
 periodic boundary condition 125
 perturbation theory 105
 phase separation 157
 phytochemicals 166

- planning a thesis 54
- postgraduate studies 36, 52, 58
- presentations for conferences 43
- proofreading 46
- pyridinium ion 112–113
- QLT 154
- QTIAM 88
- quantum 79–80, 92, 99, 100
- quantum chemical descriptors 92
- Raoult's law 159, 163
- reactivity 79–80, 90–93, 97, 100–101, 103–104, 110, 115
- recursion character of action research 39
- regular solution theory 189
- reinforcement 190
- reorganization energy 3
- roles of clauses in a complex sentence 48
- rubingh 189
- searching for possible patterns 43
- second language instruction 44
- second order perturbation 105
- segregation 163
- selection of the level of theory 42
- short range order parameter 157, 160
- sigmoid equation 187
- soldering material 149
- solubility 190
- spelling errors 46
- stability 79, 92, 95–96, 103–105, 109–110, 115
- stabilization energy 103, 105, 109, 115
- symmetric stretches 87
- synergism 182, 188
- systems thinking 37, 41, 57
- technical terms 47
- the hyperconjugative interaction 103, 115
- the mentor's guidance 57
- theoretical background 52, 54
- theoretically 80, 85–86, 97
- thermodynamic activity 153–154
- thermodynamic model 150
- thermodynamic properties 162
- thermodynamic relations 156
- thietane 79, 87, 90, 92–93, 95
- time planning 56
- triethanolamine 181, 183
- undergraduate chemistry education 57
- verlet algorithm 129–130
- vibrational energy distribution analysis 80, 100
- vibrations 86–87
- visualization abilities 38
- withdrawal effect 103, 111, 115
- writing 44

